THESE

Aix-Marseille Université

ED352 : Ecole doctorale de Physique et Sciences de la Matière

Centre Interdisciplinaire de Nanoscience de Marseille

Thèse présentée pour l'obtention du grade de Docteur de l'université

Spécialité : Nanosciences et Matières condensées

Volkan KILINC

« Development of Organic Field-Effect Transistor for the detection of cesium in seawater »

Soutenance prévue le 14 Mai 2020

Composition du jury

Prof. Fabio Biscarini (LEO - University of Modena and Reggio Emilia)	**Rapporteur**
Prof. Olivia Reinaud (LCBPT – Université Paris Descartes)	**Rapporteur**
Prof. Marc Bendahan (IM2NP – Aix-Marseille Université)	**Membre**
Dr. Catherine Henry-de-Villeneuve (PMC – Ecole Polytechnique)	**Membre**
Dr. Anne Charrier (CINaM – Aix-Marseille Université)	**Co-Directrice**
Prof. Jean-Manuel Raimundo (CINaM – Aix-Marseille Université)	**Co-Directeur**

THESE

Aix-Marseille Université

ED352 : Ecole doctorale de Physique et Sciences de la Matière

Centre Interdisciplinaire de Nanoscience de Marseille

Thèse présentée pour l'obtention du grade de Docteur de l'université

Spécialité : Nanosciences et Matières condensées

Volkan KILINC

« Development of Organic Field-Effect Transistor for the detection of cesium in seawater »

Soutenance prévue le 14 Mai 2020

Composition du jury

Prof. Fabio Biscarini (LEO - University of Modena and Reggio Emilia)	**Rapporteur**
Prof. Olivia Reinaud (LCBPT – Université Paris Descartes)	**Rapporteur**
Prof. Marc Bendahan (IM2NP – Aix-Marseille Université)	**Membre**
Dr. Catherine Henry-de-Villeneuve (PMC – Ecole Polytechnique)	**Membre**
Dr. Anne Charrier (CINaM – Aix-Marseille Université)	**Co-Directrice**
Prof. Jean-Manuel Raimundo (CINaM – Aix-Marseille Université)	**Co-Directeur**

Acknowledgment :

Je remercie tout d'abord Monsieur Frédéric Fages, directeur du CINaM lors de mon arrivé, ainsi que Monsieur Pierre Muller, son successeur, pour m'avoir accueilli dans leur laboratoire et m'avoir ainsi donné la possibilité de réaliser ce travail.

J'aimerais exprimer toute ma gratitude aux membres du jury qui ont acceptés d'évaluer ce travail de thèse. Je pense à Monsieur Marc Bendahan, qui m'a fait l'honneur de présider ce jury. Je remercie par ailleurs Madame Olivia Reinaud de l'Université Paris Descartes et Monsieur Fabio Biscarini de l'Université de Modène et Reggio d'Emilie en Italie pour avoir jugé mon travail de thèse en qualité de rapporteur.

Je tiens à témoigner ma plus sincère reconnaissance à Anne Charrier et Jean-Manuel Raimundo qui ont codirigés ma thèse. Au-delà de votre disponibilité et de votre rigueur, je vous remercie de m'avoir fait profiter de vos compétences scientifiques. L'autonomie dont j'ai pu bénéficier durant ces trois années n'aurait pu être possible sans votre confiance. Je vous remercie également de m'avoir partagé des moments riches en connaissances dans les multiples conférences et workshops que j'ai pu participer. Vous êtes au top !

J'adresse également mes remerciements à Catherine Henry-de-Villeneuve de l'Ecole Polytechnique pour ses conseils. Je voudrais l'a remercié pour tous les échanges scientifiques que j'ai pu avoir avec elle mais également pour son soutien lors de mes longues expérimentations au PMC. Un grand merci à l'équipe du PMC !

Je n'oublie pas bien sûr nos collaborateurs du Japon. Merci Tin Phan Nguy pour toute l'aide que tu m'as apporté au Japon et aussi pour m'avoir fait partager ta culture Vietnamienne ! Je remercie également Monsieur Yutaka Wakamaya. Merci Sencei pour vos conseils et votre encadrement. Je vous dois toujours un restaurant !

Je voudrais également exprimer mon amitié à Matthieu Petit. Merci pour ton enthousiasme et ta bonne humeur lors des expériences interminables menées au SAINT-CROTRON hahaha.

Je remercie tous les PI de PIV, Annie, Emmanuel, Keya, Didier et Carole, vous formez une très bonne équipe avec beaucoup d'énergie !

Merci aux thésards et post-doc de chez PIV que j'ai côtoyé, en particulier Aya, Etienne, Alexis et Seb l'ancien pour leurs bonnes humeurs. Bonnes continuations les amis, j'espère que l'on ne s'oubliera pas.

Merci aux gars du 6ème, Pavlo, Jo et Flo pour les soirées et le foot. On reste en contact les frérots !

Un énorme merci aux chimistes, Fred, Gab, Simon, Lucien, Sanjana, Yifan et Tereza. Merci pour les repas partagés, les soirées, etc. Je n'oublierai pas les bons moments passés avec vous bande de grand fou !

Pour finir, je voudrais remercier ma famille et mes amis pour leurs soutiens. Vous avez toujours été là dans les moments les plus difficiles. Force à nous !

List of acronyms:

AAPH : 2,2'-Azobis(2-amidinopropane) dihydrochloride
AAS : Atomic absorption spectroscopy
AFM : Atomic Force Microscopy
ATR-FTIR : Attenuated Total Reflectance Fourier Transform Infrared Spectroscopy
CH_3CN : Acetonitrile
DCM : Dichloromethane
DCOH : Glycerol lipids
DCOH-R : Reticulated glycerol lipids
DCOMTS : Double Reticulated Methyl Functionalized Lipids
DCPC : 1,2-bis-(10,12-tricosadiynoyl)-sn-glycero-3-phosphocoline
DCTSs : Docosyltrichlorosilanes
DH6T : α,ω-Dihexylsexithiophene
DMF : Dimethylformamide
DOPC : 1,2-dioleoyl-sn-glycero-3-phosphocholine
EDL : Electrical Double Layer
EG-OFET : Electrolyte-Gated Organic Field-Effect Transistor
FET : Field Effect Transistor
HRMS : High Resolution Mass Spectroscopy
ICP-MS: Inductively Coupled Plasma Mass Spectrometry
ISFETs : Ion Sensitive Field Effect Transistors
OFET : Ion Sensitive Organic Field Effect Transistor
LB : Langmuir-Blodgett
MeOH : Methanol
MOSFET : Metal Oxide Semiconductor Field Effect Transistor
MTS : Methyltriethoxysilane
NIMS : National Institute of Material Science
NMR : Nuclear Magnetic Resonance
ODL : Organic Dielectric Layer
ODTS : Octadecyltrichlorosilane
OECT : Organic Electrochemical Transistor
OFET : Organic Field Effect Transistor
OSL : Organic Semiconductor Layer
P3HT : poly(3-hexylthiophene)
PB : Prussian Blue
PBS : Phosphate Buffer Solution
PDMS : Polydimethylsiloxane
PECVD : Plasma-Enhanced Chemical Vapor Deposition
PL : phosphatidylethanolamine
PTFE : Polytetrafluoroethylene
SLM : Supported Lipids Monolayer
SAM : Self Assembled Monolayer
THF : Tetrahydrofuran
TMS : Tetramethylsilane
TsCl : p-toluenesulfonyl chloride
WG-OFET : Water-Gated Organic Field-Effect Transistor
XPS : X-ray Photoelectron Spectroscopy

Overview

Cesium, discovered by Fustov Kirchhoff and Robert Bunsen in 1860, is the most alkaline and electropositive element. Such unique chemical properties made it to be widely employed in the chemical reactions as a catalyst promoter, boosting the performance of other metal oxides and for the hydrogenation of organic compounds. Besides, cesium is being used in different forms in food and drug sterilization processes; in medicine therapies[1] and many industrial applications. For illustration, cesium nitrate is used to make optical glasses, cesium chloride to make photoelectric cells[2], cesium formate for petroleum exploration[3]. Cesium was also exploited as a propellant in the first design of ion thruster for spacecraft made by NASA before being replaced by Xenon. Moreover, the unperturbed ground-state hyperfine transition frequency of the cesium 133 is used as a standard in the atomic clocks[4] which are still regulating the timing of cell phone and internet network.

Despite all of the usefulness procured by the cesium 133, cesium possesses hazardous anthropogenic radioactive isotopes produced by the fission of uranium. We can quote the cesium 134 with a half-life of 2 years, the cesium 135 with a half-life of 2.3 million years and the most common cesium 137 with a half-life of around 30 years[5]. These radioactive isotopes, gamma emitters, are particularly toxic elements that can be found in the flora and fauna[6,7]. Indeed, their high water solubility facilitates their spreadings in nature, leading to detrimental effects both on the environment and human health[8,9]. In addition to the natural cesium, the origin of these contaminations comes from the recent accidental events in nuclear power plants, the routinely discharges from the nuclear reactors either or its uses in nuclear weapons testing. The accident at Tokyo Electric Power Company (TEPCO)'s Fukushima Daiichi NPS followed by a high discharge of radioactive cesium in the seawater is a good example to put forward the necessity to detect and quantify cesium in natural waters but also in drinking water and consumable products. The **Table 1** is showing the decrease of the standard limits of radioactive substances tolerated in food in Japan after the accident. For example, the new authorized low limit of radioactivity for drinking water is 10 bq/kg, i.e 3.10^{-3} ng/l of radiocesium, a concentration out of the low limit range of the actual detection methods.

Table 1 *Standard limits of radioactive substances for food in Japan (Food Sanitation Act, Ministry of Health, Labour and Welfare)*

Foods	General (vegetable, meat, fish, etc.)	Foods for infants	Milk and dairy product	Drinking water
Before 2011 (bq/kg)	500	n/a	200	200
After 2011 (bq/kg)	100	50	50	10

Indeed, the commonly used detection method for cesium is the Inductively Coupled Plasma Mass Spectrometry (ICP-MS). This technique, based on the measure of mass-to-charge ratio of ions after ionization of the sample, possesses several advantages such as selectivity and speciation (can detect different isotopes of the same element), speed and sensitivity. Despite having a low limit of

[1] (Pasternack & Howell, 2013)
[2] (Yuan, Chen, Li, Zhong, & Xu, 2018)
[3] (Downs, 2006)
[4] (Markowitz, Glenn Hall, Essen, & Parry, 1958)
[5] (Unterweger, Hoppes, Schima, & Coursey, 2009)
[6] (Burger & Lichtscheidl, 2018)
[7] (Murakami, et al., 2014)
[8] (Melnikov & Zanoni, 2009)
[9] (Guy, Hostynek, Hinz, & Lorence Marcel Dekker, 2000)

detection level for many elements, for the cesium it is out of the limit (5. 10^{-1} ng/l)[10]. The concentration of the samples is therefore required. Furthermore, ICP-MS is a large costly piece of equipment that requires trained users and it cannot be utilized for on-site analysis.

For these reasons, it appears crucial to develop fast cesium trace quantification for on-site analysis. The sensor shall have a limit of detection sufficiently low to detect cesium in drinking water or in natural waters, it shall be highly selective even in complex analytes medium, transportable, low cost and easy to use. To this end, the use of field-effect transistors (FET) emerges as a promising and reliable technology, which is worth and valuable for such purpose allowing miniaturization and wearable sensing systems. Additionally, FETs are very sensitive to the charges and can be very selective to a targeted ion after some chemical engineering work. Thus, FETs are suited for the detection of ions and are the perfect candidate for the main challenge of this project: the detection of cesium in high concentration interfering saline medium.

In this thesis, I would like to present a new sensing interface for FET devoted to the detection of cesium at a low molar range and composed of two ultra-thin organic layers : a 20 nm thick poly(3-hexylthiophene) (P3HT) as semiconducting layer and a 2.5 nm thick of engineered lipids as dielectric layer. Such assembly presents a certain number of advantages that I will explain in this thesis. After presenting the state of the art in the first chapter, I will focus the discussion of the second chapter on the lipids based nanodielectric. The auto assembly of the lipids on the P3HT layer will be studied. The third chapter will be about the synthesis and characterization of the selective probe for cesium based on calixarene and its grafting on the nanodielectric layer. To finish, in the last chapter I will show the fabrication of the FET based on the developed full organic interface. The performance of the developed FET for the detection of cesium will also be studied in the last part as a proof of concept (**Figure 1**).

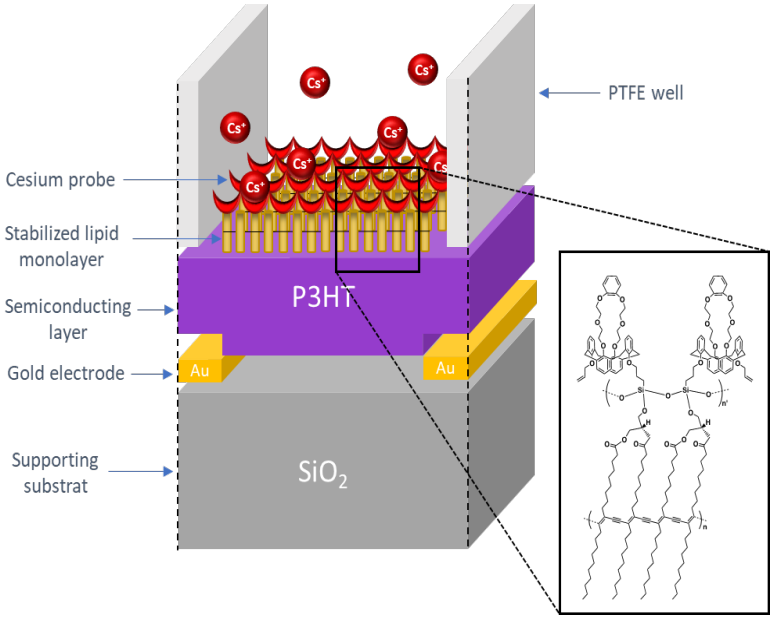

Figure 1 *Prototype of the developed FET for cesium detection*

[10] (Evans Analytical Group)

I. CHAPTER : State of the Art of Cs+ detection

I. CHAPTER : State of the Art of Cs^+ detection

I.1. Actual Cs^+ detection methods

Cesium can be found in very low concentrations in the environment. The cesium-133, the only stable isotope of cesium, occurs naturally in seawater at an average concentration ranging from 0.03 to 0.05 ppb (0.03-0.05 ng/l)[11]. For the radiocesium, soon after the Fukushima nuclear incident, samples collected approximately 330 m from the Fukushima Daiichi Nuclear Power Station's discharge canal contained 32,000 becquerels per liter (9.95 ppb, 9.95 ng/l) of cesium-137 and 31,000 becquerels per liter (0.70 ppb, 0.7 ng/l) of cesium-134[12]. In 2020, the level of radioactive cesium is present in equal concentration as the natural cesium. Several methods are existing or in development for detecting such a low concentration of cesium in complex environments.

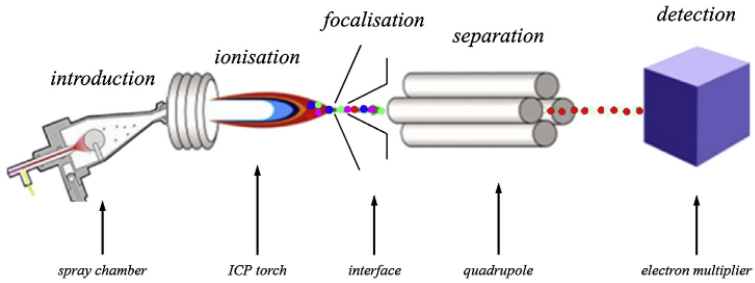

Figure 2 *Scheme of an ICP-MS system*

A rapid survey reveals that the main used method for such purpose is based on the conventional ICP-MS[13,14,15,16,17] (**Figure 2**). Although accurate and sensitive with a low limit of detection for the case of cesium (0.5 ng/l)[10], this technique is not suitable to achieve on-site and real-time detection of pollutants. It requires expensive and sophisticated instrumentation and expert manpower. Nevertheless, the distinction of the different isotopes of the same element constitutes the key advantage of using ICP-MS. Mobile gamma-ray spectrometry through a backpack survey based on a LaBr3(Ce) detector has also been developed recently. They were able to measure diverse dose rate levels of radioactive cesium on-site and they compared the results with non-radioactive area[18]. As a cheaper alternative to ICP-MS, Atomic Absorption Spectroscopy (AAS) can be used in flame atomic absorption or in electrothermal atomic absorption mode to have better sensitivity. It has been shown that a detection limit of 0.18 µg/l can be reached[19]. By amplifying the laser-enhanced ionization signal of Cs atoms in a flame, a high signal-to-noise ratio and a low limit of detection (30 pg/l) was obtained[20]. Recently, it has been demonstrated that THz-spectroscopy can be used (**Figure 3**) to measure the vibration mode (phonon mode) of a cesium ion in a cage of a cyanide-bridged metal framework[21].

[11] (Povinec & Sanchez-Cabeza, 2006)
[12] (TEPCO, 2011)
[13] (Liezers, Farmer, & Thomas, 2009)
[14] (Ohno & Muramatsu, 2014)
[15] (Zheng, Tagami, Bu, Uchida, Watanabe, Kubo-ta, Fuma, Ihara, 2014)
[16] (Zheng, Bu, Tagami, Shikamori, Nakano, Uchida, Ishii, 2014)
[17] (Russell, Warwick, & Croudace, 2014)
[18] (Ji, Lim, Hitomi, & Yajima, 2020)
[19] (Miura, Yamamoto, Yonetani, & Shirasaki, 2013)
[20] (Temirov, Matveev, Smith, & Winefordner, 2003)
[21] (Ohkoshi, et al., 2017)

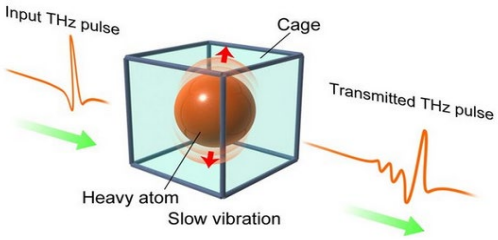

Figure 3 *Concept of detecting the slow vibration of a heavy atom in a cage using THz-light (Ref. 21)*

Another illustration of recent research in this field is focused on microplasmas for the detection of radioactive cesium contamination in seawater (**Figure 4**). By exciting a liquid sample with a high energy micro discharge and recording the spectral wavelengths emitted, it has been showed that the individual elements in the liquid can be distinguishable. The presence of cesium can be determined at concentrations as low as 10 ppb (10 ng/l)[22].

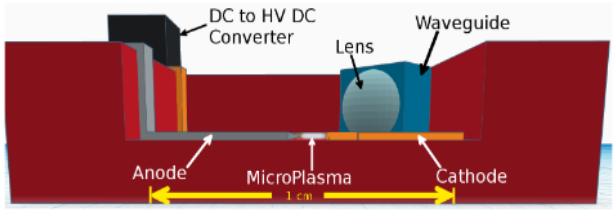

Figure 4 *Scheme of device based on microplasma for cesium detection (Ref.22)*

An Alternative original method based on inorganic material modification was reported[23]. The process of sensing was performed via the selective transformation of $Na_3MnH(P_{0.9}O_4)_2$to a new type of struvite-like cesium-containing solid $CsMn(PO_4).6H_2O$ observed by XRD (**Figure 5**). The inclusion of the cesium in the structure is stable and no reverse exchange is possible. Despite working in a competitive ionic medium, the structure change is triggered at a minimum of 0.01M of cesium.

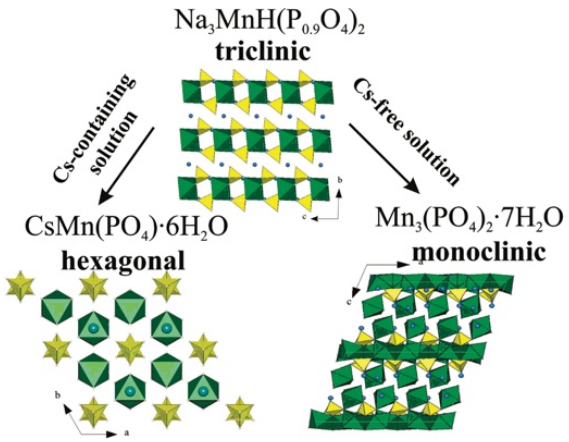

Figure 5 *Schematic presentation of the way of detection of cesium ions via selective phase transformation of $Na_3MnH(P_{0.9}O_4)_2$ to $Mn_3(PO_4)^2.7H2O$ or $CsMn(PO_4).6H_2O$ (Ref.23)*

Colorimetric probe using gold nanoparticles and Prussian blue (PB) have been studied by UV-vis spectroscopy. When a PB precursor solution was added into an Au NP solution, Fe^{3+} was reduced to Fe^{2+} by the citric acid in the gold nanoparticles solution, while the PB coated the surface of the gold

[22] (Joffrion, Mills, & Clower, 2017)
[23] (Ferdov & Lin, 2010)

nanoparticles, causing a change in color and surface plasmon resonance absorption of the gold nanoparticles (Figure 6). The developed probe shows excellent selectivity and anti-interference for Cs+. The naked eye detection limit was 30 µM and the limit of detection by UV-vis spectroscopy was 19 µM[24].

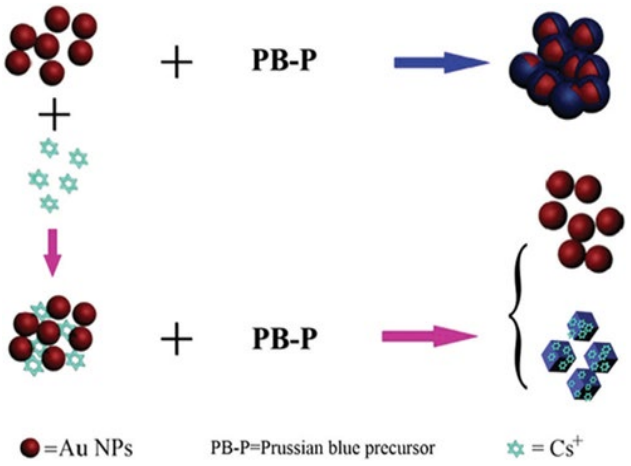

Figure 6 *Mechanism of Cs+ colorimetric detection based on gold nanoparticles and PB (Ref.24)*

We can also mention fluorescence-based methods which have advantage of being both cheap and non-destructive[25,26]. In one example, researchers synthesized a near-infrared emitting squaraine fluorophore that bound cesium with high affinities, resulting in a significant fluorescence enhancement and a 13 µg/l detection limit[27].Fluorescent polymer were also used[28]. A (PB)-embedded coordination polymer (COP) was prepared by simple incorporation of PB into a polymer composed of 1,1,2,2-tetrakis(4-carboxyphenyl)ethane and the Zn ion. As the PB in PB-COP efficiently adsorbed Cs ions, the microstructure of PB-COP was degraded to smaller particles, along with a concomitant decrease in the green fluorescence of the PB-COP. Such a decrease in the green emission of PB-COP was used as a signal for the presence of cesium, and the limit of detection was found to be 73.8 ppb (73.8 ng/l) (Figure 7).

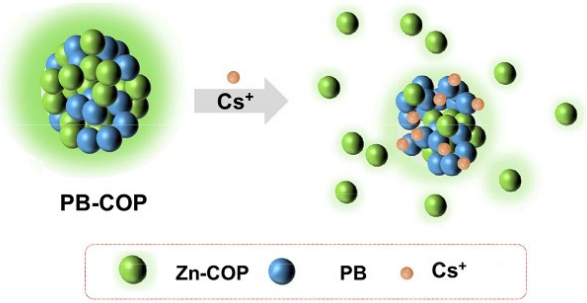

Figure 7 *Illustration of cesium detection by using fluorescent polymer (Ref.28)*

A paper-based colorimetric device impregnated with a chrysoidine G (CG) as chemo-indicator was used as naked-eye quantification technique in environmental analysis. This chemo-indicator is designed to exhibit a powerful detection capability featuring high selectivity and sensitivity to inactive Cs^+, by

[24] (Qiu, Fu, Wang, Zou, Zhang, Li, Wu, 2020)
[25] (Li & Shi, 2013)
[26] (Thomas, Joly, & Swager, 2007)
[27] (Radaram, Mako, & Levine, 2013)
[28] (Namgung, Gwon, Kim, Jang, Pepper, Ogden, Whittle, Harwood, Lee, 2018)

means of color discrimination from light yellow to red orange (Figure 8). The observed detection limit was 100 µg/l[29].

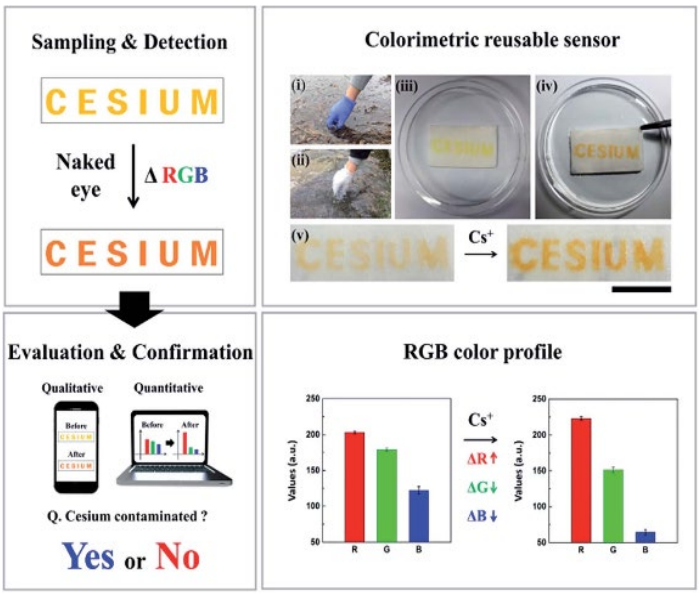

Figure 8 *Example of paper-based naked-eye cesium detection (Ref.29)*

Researchers at the Tokyo University of Science have developed an optode (optical electrode) based on ion-exchange membrane that provides a visual response to the presence of cesium in water in the form of color change (Figure 9). Their optode membrane is fabricated using nanoparticles and can reach a low limit detection of up to 100 µM in sea-water[30]. Optical modification induced by cesium detection appears to be one of the favorite strategies. For further information about the optical sensor, I recommend these reviews[31, 32].

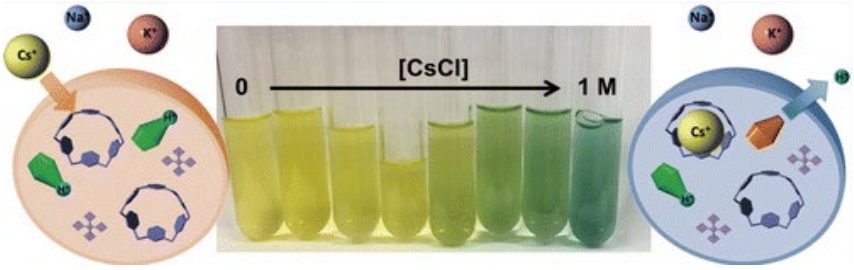

Figure 9 *Cs+ detection based on the concept of optical electrode modification (Ref.30)*

Besides colorimetric methods, the electrochemical method has been widely used for the Cs^+ detection. Clinoptilolite nanoparticles (NClin) modified with hexadecyltrimethyl ammonium bromide surfactant (HDTMABr) and Arsenazo III (ARS) was used for the modification of carbon paste electrode for voltammetric determination. A limit of detection of 3.10^{-9} M was obtained[33]. A self-assembled thiacalix[4]arene containing two sulfur groups in the lower rim on gold surfaces was investigated by cyclic voltammetry (CV) and electrochemistry Impedance spectroscopy (EIS). It was found that

[29] (Kang, Jang, Haldorai, Vilian, Rethinasabapathy, Roh, Han, Huh, 2017)
[30] (Akamatsu, Komatsu, Matsuda, Mori, Nakanishi, Sakai, Hill, Ariga, 2017)
[31] (Kumar, Leray, & Depauw, 2016)
[32] (Leray & Valeur, 2009)
[33] (Saadat & Nezamzadeh-Ejhieh, 2016)

thiacalix[4]arene self-assembled gold electrodes can compel cesium ions. The results show good selectivity for cesium ions and a decrease in its detection limit (1.15×10^{-9} M)[34].

Electronic measurement based on the transistor is another promising method for cesium detection. A water-gated thin film transistor (WGTFT) that allows the detection of Cs^+ in drinking water at very low concentrations was reported (Figure 10). The transistor channel is formed from spray-pyrolyzed tin dioxide SnO_2 with a plasticized PVC membrane containing the Cs^+-selective zeolite "mordenite". It displays a threshold shift when exposed to drinking water samples carrying traces of Cs+. A low limit of detection of 33 pM was observed[35].

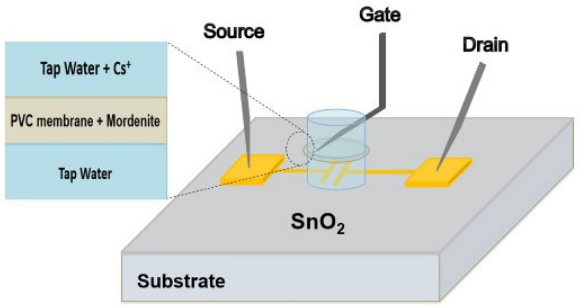

Figure 10 *Design of WGTFT for Cs+ detection (Ref.35)*

In all the presented examples, either a lack of sensitivity, selectivity toward cesium, miniaturization possibility or a high cost are existing. None of them include all of the desired characteristics (Table 2).

Table 2 *Comparison of the different cesium detection method*

Method	Cs^+ detection limit	Selectivity	Miniaturization	Ref.
ICP-MS	10^{-12} M	Very High	no	[10]
AAS	10^{-9} - 10^{-15} M	Medium	no	[19, 20]
Plasma spectroscopy	10^{-10} M	High	yes	[22]
UV-vis spectroscopy	10^{-5} M	High	no	[24]
Fluorescence spectrophotometer	10^{-7} M - 10^{-9} M	High	no	[27, 28]
Colorimetry	10^{-4} M - 10^{-6} M	High	yes	[29, 30]
XRD	10^{-2}M	High	no	[23]
Electrochemical	10^{-9} M	High	yes	[33, 34]
Electronic	10^{-11} M	High	yes	[35]

[34] (Shamsipur, Asgari, Maragheh, & Matt, 2015)
[35] (Alghamdi, Alqahtani, & Grell, 2019)

Nevertheless, only one mentioned research field appears to be promising for the development of a sensor which includes high sensitivity, low level of detection, selectivity, low cost and portability characteristics: Field-Effect Transistors (FETs). Thus, based on this bibliographic analysis, it turns to be natural to focus our research inspiration on the development of FETs based sensors to fulfill the attribute requirements for the development of highly sensitive and selective detection of cesium in seawater.

I.2. Field-Effect Transistors (FET) sensors

I.2.1. FET sensors in general

The development of sensors with attractive qualities including quick response, low cost, miniaturization, high sensitivity and selectivity, and appropriate detection limits is still a challenge in the field of sensors. However, in the last decades, researches and innovations emerging in the large field of FETs that appear to be promising in developing sensors bearing extraordinary characteristics.

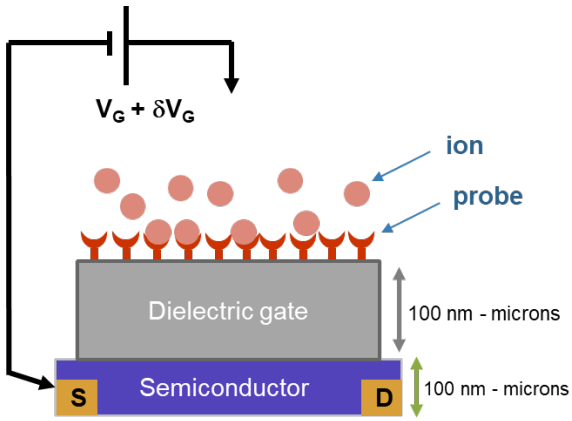

Figure 11 *Basic configured FET scheme*

Most FET sensors are based on the Metal-Oxide-Semiconductor FET (MOS-FET) technology. FET sensor are basically composed (**Figure 11**) of three electrodes (source, drain and gate), a semiconducting layer (often doped silicon) and an insulating layer called dielectric gate (often inorganic oxide). Parameters such as material compositions, the thickness of the layers, geometrical configuration and the targeted analytes will determine the denotation of the FET sensors (i.e ISFET, EGOFET, Chem-FET, Bio-FET, etc.). Independently of the quoted parameters, the working principle of FET sensors are all similar and will be detailed later in the thesis (Chapter 4). However, to understand the strategy of this work it is important to understand the basics of FET sensors principles.

Briefly, a voltage applied to the gate V_{GS} modifies the electric field across the dielectric layer and consequently the charge carrier density in the semiconductor between source and drain, hence leading to a modulation of the source-drain current I_{DS} (**eq. 1**). When the target species react with the receptors immobilized on the insulating layer a surface potential builds up (δV_{GS}) due to the charge carried by the target species, shifting the threshold voltage V_{TH} (the voltage required to have current in the semiconductor) of the transistor. The change in V_{TH} and I_{DS} is proportional to the density of captured targets. The relation between I_{DS}, V_{GS}, δV_{GS} and V_{TH} is given by **eq. 1**.

$$I_{DS} = \frac{W}{2L}\mu C_i (V_{GS} - V_{TH} + \delta V_{GS})^2 \qquad \textbf{eq. 1}$$

W and L are respectively the width and length of the channel in the semiconductor (active area), μ is the charge carrier mobility, C_i is the capacitance of the insulating layer. By interpreting the **eq.1**, it can be noticed that four parameters of the FETs can be modified in order to increase the output electrical signal: the morphology of the FETs, the applied gate voltage, the charge carrier mobility of the semiconductor and the capacitance of the dielectric gate.

For a long time, FET sensors were based on inorganic materials such as silicon for the semiconducting channel and various inorganic oxides for the gate dielectric. An advantage of silicon over other semiconductors, is its low cost and high electron mobility of 1400 $cm^2V^{-1}s^{-1}$ [36]. In late the 1970s, P. Bergveld[37] introduced the first Ion-Sensitive Field Effect Transistor (ISFET) that emerged with dimension below millimeter square. Based on the semiconducting Si layer with SiO_2 as a dielectric gate, the first ISFETs were applied as a pH sensor. In fact, the OH groups present on the oxide surface of the dielectric gate were used as H^+ sensitive receptors in aqueous solution. Based on Bergveld work, lots of studies have been dedicated to improving the sensitivity of the sensor by increasing the capacitance of the dielectric layer (C_i) (See **eq. 1**). This can be achieved by increasing the dielectric constant (k) and/or decreasing the thickness (d) of the insulating layer (**eq. 2**, ε_0 is the vacuum permittivity). The latest is usually limited due to leakage current, lots of work has been focussed on using thicker dielectric materials with high dielectric constant such as tantalum pentaoxide (Ta_2O_5)[38], silicon nitride (Si_3N_4)[38], aluminum oxide (Al_2O_3)[38], or diamond-like carbon insulator[39].

$$C_i = \frac{k\varepsilon_0}{d} \qquad \textbf{eq. 2}$$

It is also important to notice that high sensitivity of the sensor towards the captured targets implies that the ratio $\frac{\delta V_{GS}}{V_{GS}}$ must be as high as possible. Since δV_{GS} depends on the density of captured targets and is of the order of a few tens or hundreds of millivolts, V_{GS} must be be as small as possible. By expressing the electric field across the dielectric as $E = \frac{V_{GS}}{d}$, it is clear that a higher sensitivity will then be obtained with a thin dielectric layer.

I.2.2. Organic Field-Effect Transistor (OFET) sensors

The development of Organic Field-Effect Transistors motivated by the fabrication of low cost, high throughput and flexible electronics has emerged as a major field of research. Like in inorganic FETs, the performances of OFETS are directly linked to the quality of both the semiconducting layer (OSL), and the dielectric layer (ODL) and can be greatly affected by the properties of the dielectric gate/semiconductor interface (**Figure 12**). The carrier mobility in OSL is strongly dependent on the molecular or polymeric organization within the layer; the composition and the molecular organization of the ODL will determine its insulating properties[40,41]. The presence of interfacial charge trapping sites leads to the decrease of the transistor performances[40,41]. Lots of work and strategies have then been set-up to optimize each layer of the transistors to increase carrier mobility in the semiconductor and to decrease the density of interfacial traps[40,41]. Self-Assembled Monolayers (SAMs) on the organic device are the perfect candidate to avoid such drawbacks.

[36] (Canali, Jacoboni, Nava, Ottaviani, & Quaranta, 1975)
[37] (Bergveld, 1970)
[38] (Chiang, Chou, & Chen, 2001)
[39] (Voigt, Schitthelm, Lange, Kullick, & Ferretti, 1997)
[40] (Lee, Kim, Rivnay, Matsuhisa, Lonjaret, Yokota, Yawo, Sekino, Malliaras, Someya, 2016)
[41] (Henning, Matt, & Ni, 2010)

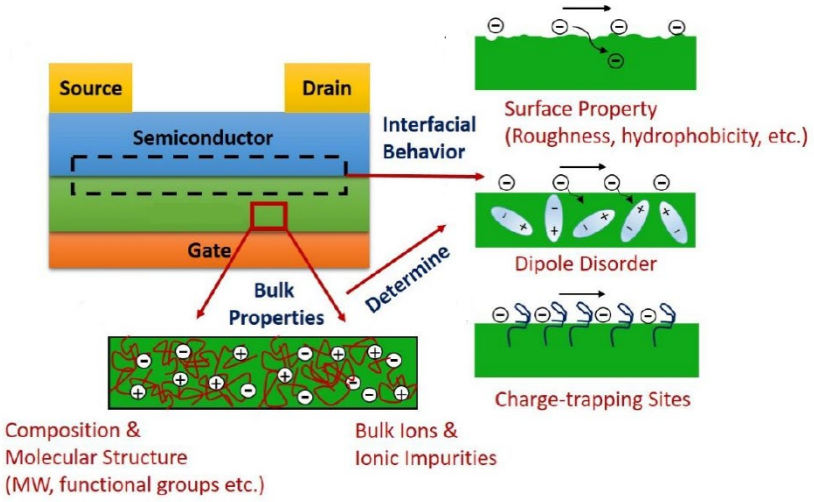

Figure 12 *OFET performance impacted by the interfacial quality of the OSL/ODL (Ref.49)*

One way to reduce the operating voltage and increase the sensitivity of the OFET is to reduce the thickness of the dielectric layer while keeping a low leakage current. Alkyltrichlorosilane SAMs were exploited, formed on a 1 nm thin native oxide SiO_2 layer, as gate dielectrics, on a silicon FET[42] . Independent of the choice of the terminal group, low leakage current densities were achieved. They applied a similar derivatization procedure to build a 2 nm thick alkyl chain SAM as a gate insulating film, this time in a α-sexithiophene (α-6T)-based FET[43]. The OFETs were operated at a voltage as low as 2V, with a good field-effect mobility and despite the molecular thin SAM, they could measure relatively low gate leakage current. These were the first examples of the strategy of the SAM being used as a dielectric, and not just being deposited on top of the dielectric oxide. This approach was further elaborated by Halik *et al.*[44] : they characterized oligothiophene-based OFETs, with the semiconductor being deposited on a 2.5 nm thin ODTS gate dielectric. They found that the length of the π-conjugated core of the semiconductor did not affect the device performances, while the length of the substituted alkyl chain plays an important role. Several SAM/OSC combinations were tested in the following years. Park *et al.* have grafted a 2.6 nm thick densely packed SAM of docosyltrichlorosilanes (DCTSs) in combination with a polymeric organic semiconductor, namely P3HT (**Figure 13**), with a significant reduction of both the operating voltage and the power dissipation[45].

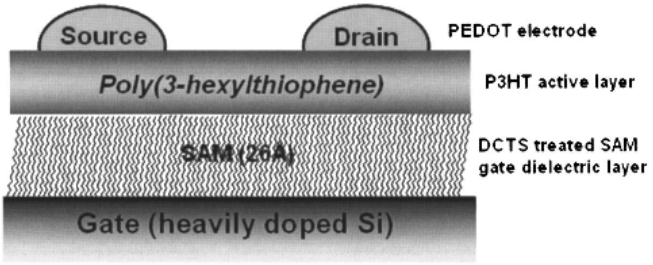

Figure 13 *OFET with DCTS SAM as dielectric gate (Ref.45)*

[42] (Collet & Vuillaume, 1998)
[43] (Collet, Tharaud, Chapoton, & Vuillaume, 2000)
[44] (Halik, Klauk, Zschieschang, Schmid, Ponomarenko, Kirchmeyer, Weber, 2003)
[45] (Park, Kim, Jang, Hwang, Lim, Cho, 2005)

Phosphonic-based monolayers have also been investigated[46] on pentacene OFETs. Besides these promising performances, the advantage of this strategy laid in the choice of uncomplicated functionalization steps, which would not require either specific synthesis of the SAM-forming molecule or vacuum deposition of the semiconductor. Within this respect, Salinas *et al.* have demonstrated a α,ω-Dihexylsexithiophene (DH6T) OFET where they incorporated fullerene photoactive derivatives (**Figure 14**) into a tetradecyl phosphonic acid SAM, endowing the device with photo-switchability properties[47]. Recent reviews[48,49] about the implementation of thin dielectric gate in organic electronics are worth to read to have further knowledge.

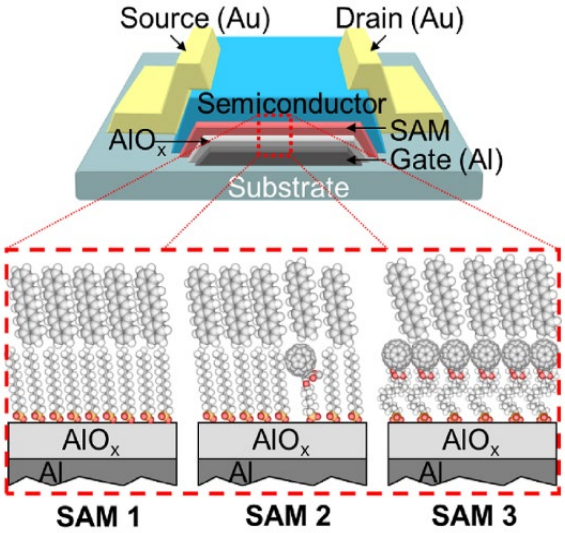

Figure 14 *OFET performance investigated with different ratio of tetradecyl phosphonic acid/fullerenes (Ref.47)*

Since the first OFET made by Tsumura *et al.*[50] in 1986, based on polythiophene semiconductor/thin silicon oxide (300 nm) interface with a charge carrier mobility of 10^{-5} $cm^2V^{-1}s^{-1}$ and a V_{TH} of -13V, lot of progress has been made notably in the biological field[51]. Detection of a variety of biological events such as DNA immobilization and hybridization[52] recognition of odorant protein binding[53] dopamine detection[54] and antibody-antigen interactions[55] have been reported. Apart from the biosensing applications, OFETs have been explored as basic components in logic architectures[56,57,58]. In the field of ion detection also progress was achieved. Usually, polymer mixed with selective molecules towards the targeted ion is cast on the semiconductive layer to form the insulating and selective layer of the OFET. As an example, the detection of Na^+ down to 1 µM was

[46] (Fukuda, Hamamoto, Yokota, Sekitani, Zschieschang, Klauk, Someya, 2009)
[47] (Salinas & Halik, 2013)
[48] (Casalini, Bortolotti, Leonardi, & Biscarini, 2017)
[49] (Wang, Huang, Li, Li, Guo, Jiang, 2019)
[50] (Tsumura, Koezuka, & Ando, 1986)
[51] (Lin & Yan, 2012)
[52] (Kergoat, Piro, Berggren, Pham, Yassar, Horowitz, 2012)
[53] (Mulla, Tuccori, Magliulo, Lattanzi, Palazzo, Persaud, Torsi, 2015)
[54] (Casalini, Leonardi, Cramer, & Biscarini, 2013)
[55] (Berto, Diacci, D'Agata, Pinti, Bianchini, Di Lauro, Casalini, Cossarizza, Berggren, Simon, Spoto, Biscarini, Bortolotti, 2017)
[56] (Yaman, Terkesli, Turksoy, Sanyal, & Mutlu, 2014)
[57] (Porrazzo, Luzio, Bellani, Bonacchini, Noh,Kim, Lanzani, Antognazza, Caironi, 2017)
[58] (Parkula, Maglione, Casalini, Zhang, Greco, Bortolotti, Rovira, Mas-Torrent, Biscarini, 2019)

achieved using a polymer-based OFET[59]. We can also quote the example of K^+/Ca^{2+} detection down to µM range[60] or lead detection down to 0.1 nM[61] based both on polymeric layers. Surprisingly, not so much OFET was developed for the ion detection application. We can also notice that advanced researches in the field of nanodielectrics for OFETs applications are reaching a level of maturity followed by the emergence of new start-ups such as NeuDrive®, Flexterra® or Priways Co., Ltd®

All the presented examples illustrate the potential advantages procured by OFETs based sensor development. The easy processability of the materials allow to trespass the technological difficulties found in inorganic FETs. By engineering thin SAM as ODL on semiconductor, the sensitivity and the limit of detection shall significantly increase. Moreover, besides the low cost, the low voltage consumption to operate the device hence raising interest in further industrial applications. Thus, developing a sensor based on OFETs for cesium detection in seawater appears to be the right strategy.

I.2.3. Electrolyte-Gated Organic Field-Effect Transistors (EGOFETs)

With the aim of detecting cesium in seawater, a competitive ionic medium, a sub-class of OFETs has naturally drawn our attention: the Electrolyte-Gated Organic Field-Effect Transistors (EGOFETs).

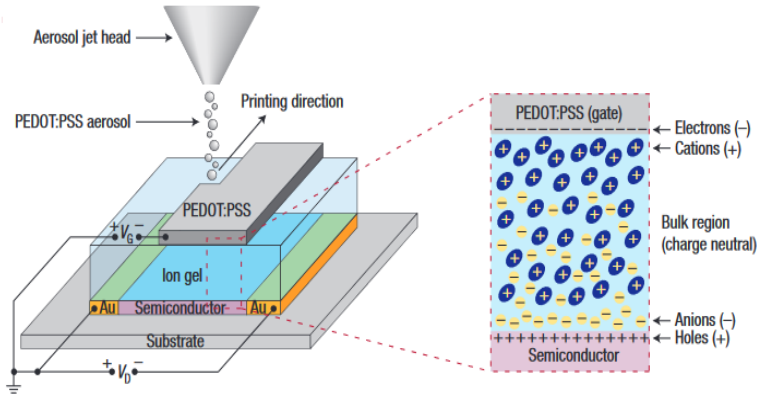

Figure 15 *EG-OFET example by using ionic gel as dielectric gate (Ref. 68)*

In EGOFETs, the solid dielectric gate is substituted by an electrolyte which can be constituted of polymers[62,63] , ionic liquids[64,65] or ionic gels[66,67,68] (**Figure 15**). The gate electrode is immersed in the electrolyte. Source and drain electrodes, isolated from the electrolyte, provide electrical contact to the channel. The function principle relies on the accumulation of charges at the gate/dielectric and dielectric/semiconductor interfaces. The detection principles in EGOFETs are based on changes of these surface capacitances induced by the recognition between probe and target molecules. Compared to other types of OFETs, EGOFETs display higher gate capacitance (up to ~1000 higher). As a consequence, the applied gate voltage V_G for EGOFETs is typically much smaller than those necessary for OFETs (<1 V, versus >10 V or even higher).

[59] (Schmoltner, Kofler, Klug, & List-Kratochvil, 2013)
[60] (Melzera, Münzera, Jaworska, Maksymiuk, Michalska, Scarpa, 2014)
[61] (Chen, Sarangadharan, Sukesan, Hseih, Lee, Chyi, Wang, 2018)
[62] (Liao & Yan, 2013)
[63] (Herlogsson, Crispin, Robinson, Sandberg, Hagel, Gustafsson, Berggren, 2007)
[64] (Ono, Miwa, Seki, & Takeya, 2009)
[65] (Xia, Cho, Lee, Ruden, & Frisbie, 2009)
[66] (Lee, Panzer, He, Lodge, & Frisbie, 2007)
[67] (Cho, Lee, Xia, Kim, He, Renn, Lodge, Frisbie, 2008)
[68] (Facchetti, 2008)

Besides these great advantages, stills a lot of work to improve the EGOFET-based sensors are required. One of the most challenging is certainly the stability of the semiconductors in water or neutral buffers. In fact, electrochemical doping (i.e., insertion into the semiconductor of ions from the electrolyte) may occur, which decreases the capacitance and the field-effect and therefore degrades the semiconductor electrical properties. This is the main reason why the performances of EGOFET often decrease dramatically upon use[69,54]. The second big challenge is about the immobilization of the bioprobes whether onto the gate or the semiconductor surface by avoiding tedious chemical derivatization, which generally impedes the electrical performances of the OSC.

I.3. Achieved fellowship works

The realized bibliographic analysis showed that EGOFETs based sensor constitute the most promising technology for the sensitive detection of cesium in an interfering medium such as seawater. However, as described previously, many challenging drawbacks exist in the development of such kind of transistor. Notably the stability of the OSL in the electrolyte and the immobilization of the selective probe.

Since 2010, Charrier *et al.* have been working on the improvement of field-effect transistor performance by carrying out chemical engineering on insulating layers. They first developed a method for the deposition and stabilization of phospholipids on hydrogenated silicon surface[70,71,72] with unprecedented mechanical and dielectric properties[73]. It has been demonstrated that engineered supported lipids monolayers (SLM) can be used as ultrathin dielectric in FETs leading to sensing properties of iron ions with limits of detection down to the femtomolar (Figure 16) in Chem-field effect transistor sensors[74,75,76]

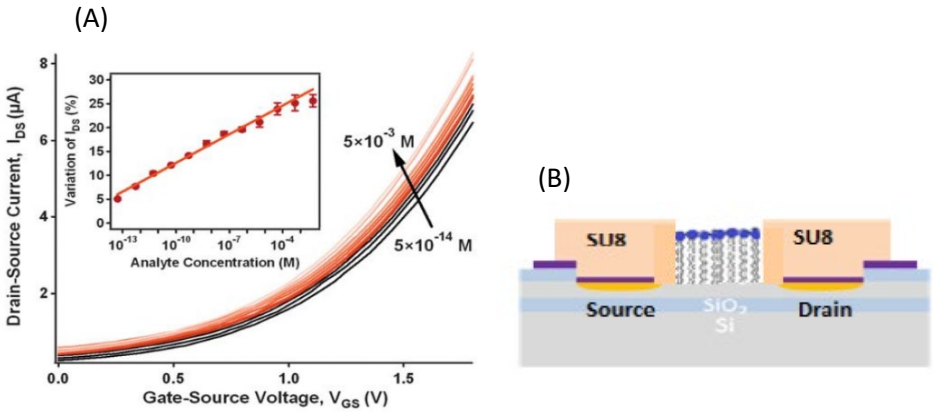

Figure 16 *(A) Transfer curve of SiH FET based on engineered monolayer lipids as dielectric gate for iron detection application (B) Schematic representation of the designed FET (Ref. 74)*

[69] (Belkhir, 2009)
[70] (Charrier, Mischki, & Lopinski, 2010)
[71] (Dumas, El Zein, Dallaporta, & Charrier, 2011)
[72] (El Zein, Dallaporta, & Charrier, 2012)
[73] (Kenaan, El Zein, Kilinc, Lamant, Raimundo, Charrier, 2018)
[74] (Nguyen, El Zein, Raimundo, Dallaporta, & Charrier, 2013)
[75] (Nguyen, Labed, El Zein, Lavandier, Bedu, Ozerov, Dallaporta, Raimundo, Charrier, 2014)
[76] (Kenaan, Nguyen, Dallaporta, Raimundo, & Charrier, 2016)

I. CHAPTER : State of the Art of Cs+ detection

Implementation of the engineered lipids monolayer on EGOFET appears to be a good solution to encompass the electrochemical doping of the semiconductor and the immobilization problems of the probe. By chemically modifying the headgroup of the lipids it could be therefore possible to reach the aim of selective ion detection. I will present herein the synthesis of a novel 1,3-alternate calix[4]arene host exhibiting high selectivity toward the foreseen Cs^+ analyte that can be integrated as probe into lipids monolayer coated poly(3-hexylthiophene) (P3HT) organic semi-conductor substrate generating an innovative sensing interface. The grafting process of the chelator, the structure of the novel full organic lipids/P3HT interface and it impacts on the transistor performance will be investigated here. As a proof of concept, detection measurements of cesium with the developed full-organic ion-sensitive field effect transistor will be performed.

I. CHAPTER : State of the Art of Cs+ detection

II.CHAPTER : Original dielectric gate for OFET application

II.1. The lipid monolayers based dielectric gate

Researches on the self-asssembled layers for application as a dielectric gate for OFET is in expansion as shown in the previous chapter. In my thesis, I will present an original SAM constituted of an engineered lipid monolayer of 2.5 nm which is used as the active sensing layer and as an ultra-thin gate dielectric in field-effect transistor sensors.

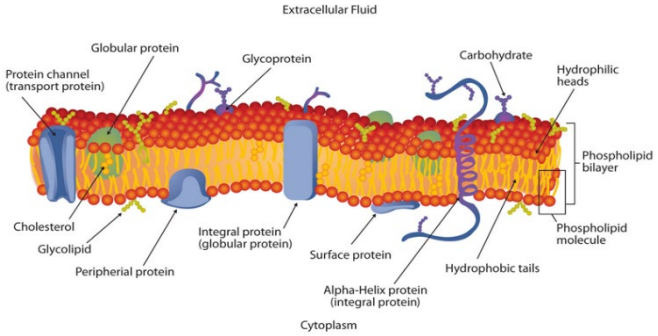

Figure 17 *Composition of cell membrane in human body (Lipid Bilayer Membranes, chem.libretexts.org)*

In the living system, the role of the lipid membrane is to compartmentalize the inner and outer parts of the cells .The membrane is a natural insulator (**Figure 17**) which plays an efficient role as a barrier to both ionic and electronic transport across the membrane, associated with an electrical resistance of the order of several giga-Ohms in magnitude[77]. Among the lipids, phospholipids constitute the larger family of lipids. The most abundant class of lipids in nature[78] is including phosphatidyl choline, phosphatidyl ethanolamine, phosphatidyl serine, phosphatidyl inositol and phosphatidyl glycerol. The tunability of parameters such as the headgroup, chain length and degree of saturation of the aliphatic chain is offering a structural diversity within each type of phospholipids. Because of their amphiphilic nature, i.e hydrophilic headgroup and hydrophobic tails (one or two), lipids spontaneously self-organize in aqueous medium into bilayers under the form of vesicles. In vesicles, lipids headgroups are in contact with the aqueous medium whereas the hydrophobic chains orient themselves towards the inside of the vesicles.

Lipids can also be used to form supported layers on substrates, under the form of monolayers, bilayers or multilayers. The type of layer and the orientation of molecules on the surface (heads up or down) are directly correlated to the hydrophobic properties of the substrate. There are two general methods for the formation of supported phospholipid layers on planar supports. The first method involves the transfer of a lower leaflet of lipids from the air–water interface by Langmuir–Blodgett technique[79]. The second method is the adsorption and fusion of vesicles from an aqueous suspension to the substrate surface[80,81]. Varieties of substrates capable of supporting phospholipid bilayers have been used : fused silica, borosilicate glass, and silicon oxyde[82]. Attempts have been made to deposit supported bilayers on single crystals of TiO_2 and $SrTiO_2$ as well as on thin films of SiO_2 on $LiNbO_3$

[77] (Jung, Choi, Kim, & Jeon, 2012)
[78] (Berg, Tymoczko, & Stryer, 2002)
[79] (Langmuir & Schaefer, 1938)
[80] (Brian & McConnell, 1984)
[81] (McConnell, Watts, Weis, & Brian, 1986)
[82] (Tamm & McConnell, 1985)

crystals[83]. Thin films can be used as solid supports as observed with TiO_2[84], indium-tin-oxide[85], gold[86] , silver[87], and platinum[88]. The only requirements are to have an hydrophilic, smooth and clean surface. Supporting lipids monolayer on the substrate has also been investigated in sensing applications. Compared to bilayers formation, an hydrophic surface is required. Several strategies have been employed since. This includes the use of alkanethiols to covalently functionalize a gold substrate, for example, to form self-assembled monolayers (SAMs) on it[89,90]. Methyl-terminated alkanethiols on gold (Figure 18) provide a well-defined hydrophobic surface to facilitate the formation of a lipid monolayer membrane[91,92]

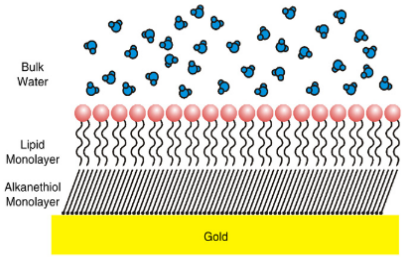

Figure 18 *Lipids monolayer on alkanethiol modified gold substrate (Ref.89)*

An interesting property of lipid layers is their fluidity dependency towards temperature. For each type of lipids, a gel to fluid transition occurs at a given temperature[93]. It is determined mostly by the length of the aliphatic chains, the number of unsaturated bonds within and the headgroup[94]. This fluidity is the limiting factor in the formation of stable layers on the substrate.

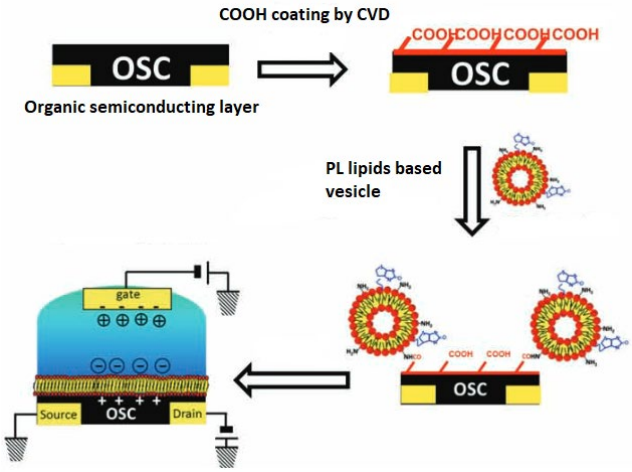

Figure 19 *Lipids bilayer deposition strategy applied in OFETs (Ref.95)*

[83] (Rossetti, Bally, Michel, Textor, & Reviakine, 2005)
[84] (Reimhult, Hook, & Kasemo, 2003)
[85] (Yang & Kleijn, 1999)
[86] (Lahiri, Kalal, Frutos, Jonas, & Schaeffler, 2000)
[87] (Salamon, Wang, Tollin, & Macleod, 1994)
[88] (Puu & Gustafson, 1997)
[89] (Castellana & Cremer, 2006)
[90] (Nuzzo & Allara, 1983)
[91] (Plant, Brighamburke, Petrella, & Oshannessy, 1995)
[92] (Rao, Plant, Silin, Wight, & Hui, 1997)
[93] (Hardy, Nayak, & Zauscher, 2013)
[94] (Lodish, Berk, & Zipursky, 2000)

Their inherent instability in the air, when exposed to solvent or under application of mechanic or electric force is the reason why it has been poorly exploited in the development of advanced devices.

The lipid layers lack of stability on substrates can be encompassed by immobilizing them on functionalized substrate of a transistor device. An example is to perform chemical vapor deposition of molecules rich in -COOH for coating the substrate (Figure 19). Afterward, adding phosphatidylethanolamine (PL) lipids lead to the formation of amide bonds between the -COOH surface groups and the NH_2 moieties on the polar heads of PL resulting in stably anchored phospholipid[95]. Another strategy is to use electrostatic interaction between the substrate modified layer and the lipids (Figure 20). For instance, Misra *et al.* performed deposition of 1,2-dioleoyl-sn-glycero-3-phosphocholine (DOPC) bilayers on the hydrophilic negatively charged native oxide present on the silicon nanowire surface (SiNW)[96]. The advantage of this strategy is to keep the fluidity in the lipids which is essential for the investigation of ion transport for example.

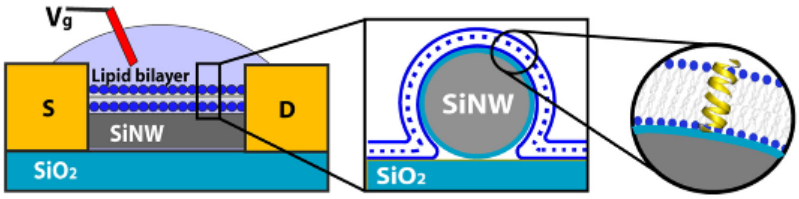

Figure 20 *Lipids bilayer deposition strategy applied in SiNW based FETs (Ref.96)*

Beside these strategies, an alternative way of lipids immobilization and stabilization was proposed by Charrier *et al.* Using the radical polymerization of the acetylene groups present in aliphatic tail of 1,2-bis-(10,12-tricosadiynoyl)-sn-glycero-3-phosphocoline (DCPC) lipids, it has been possible to obtain high mechanical, chemical and dielectric supported reticulated lipids on hydrogenated silicon substrate (SiH) with a thickness of 2.2 nm (+/-0.2)[73]. Such layers where the lipids are reticulated have been used as an ultrathin dielectric layer in silicon-based field-effect transistors and as a capacitive platform for metal ions detection (Figure 21).

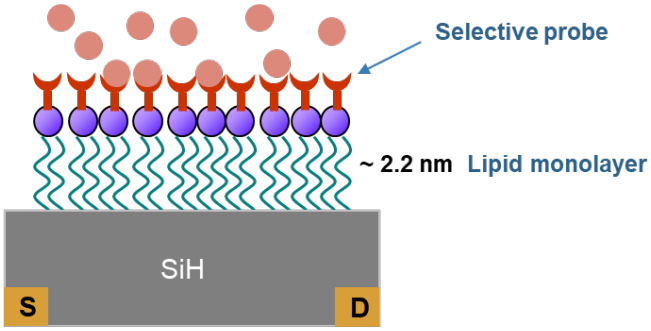

Figure 21 *Schematic representation of the lipids as dielectric gate*

They hence constitute perfect candidates for low operating voltage OFET. The success of such lipid layer as an efficient molecular dielectric depends on several parameters: first, the layer must be dense enough to be a good insulator. Second, the layer must be mechanically robust to be used in devices. Third, the lipid monolayer/semiconducting layer interface shall present a low interfacial charge trapping. All these requirements strongly depend on the quality of the lipid layer in terms of organization, density, reticulation rate which all ultimately depend on the interaction between lipids

[95] (Magliulo, Mallardi, Mulla, Cotrone, Pistillo, Favia, Vikholm-Lundin, Palazzo, Torsi, 2013)
[96] (Misra, Martinez, Huang, Wang, Stroeve, Grigoropoulos, Noy, 2009)

and the semiconducting layer. In particular, it was shown that to obtain efficient reticulation, the arrangement of the diacetylene groups within the monolayer assembly should meet the same spatial conformation found in crystals[97]. An example of dense and loose lipid monolayers are shown in the Figure 22.

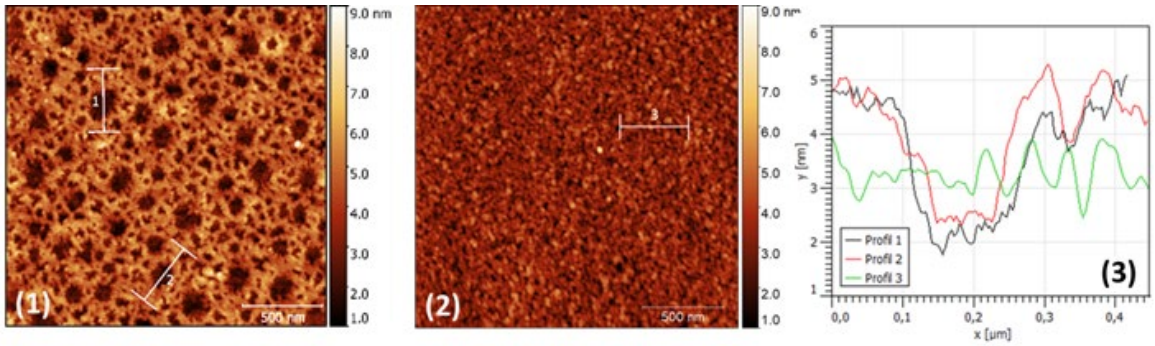

Figure 22 *AFM topographic images of DCOH lipid monolayers on P3HT (1) loose packed (2) dense packed. (3) Profile of the holes present in (1) and surface of the (2)*

This chapter will focus on the formation of the reticulated lipids used as a dielectric gate on the surface of P3HT semiconducting polymer in the FET device. The phosphatidylcholine head-groups of DCPC were cleaved to obtain glycerol lipids (DCOH) which was assembled onto the P3HT layer using a derivative version of the vesicle fusion method. The density, structure and organization of the lipids assembly were investigated using different methods including in-situ attenuated total reflectance mode Fourier-transform infrared spectroscopy (ATR FTIR), X-ray photoelectron spectroscopy (XPS), and atomic force microscopy (AFM). The mechanical stability of the lipid layer on free-standing P3HT layers was investigated by indentation measurements using AFM.

II.1.1. DCPC lipids head-group cleavage

The dielectric layer composing our field-effect transistor is based on lipids and particularly a modified version of the commercially available (Avanti Polar Lipid,Inc.) 1,2-bis-(10,12-tricosadiynoyl)-sn-glycero-3-phosphocoline (DCPC) lipids which are bearing two diacetylene moieties. Prior to the deposition on the semiconducting layer, the modification of the DCPC is crucial. Removing the initial phosphatidylcholine headgroup present on the DCPC leaves to the lipid head-group a hydroxyl (OH) function that will be used later to graft the cesium probe and further stabilize the layer. Description of the probe and its grafting on the dielectric layer will be discussed in detail in the next chapter. At this stage, it is worth understanding that a lipid containing a hydroxyl head group is necessary for the future steps of the dielectric layer functionalization and stabilization.

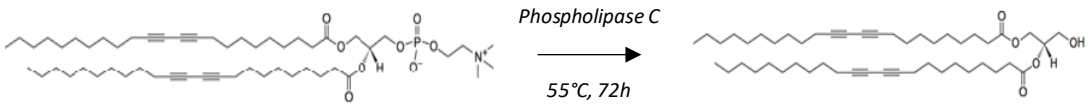

Figure 23 *Enzymatic cleavage reaction of DCPC*

Modification of DCPC by cleaving the phosphatidylcholine headgroup to obtain glycerol lipid (DCOH) was achieved by using an enzymatic reaction (Figure 23). The actual protocol based on previous work by Charrier *et al.*[70,71,72] was optimized to increase the yield (*Exp.Tech. part VI.4.1.*). The

[97] (Hu, Hsiao, Mao, Chen, Chang, Chao, 2013)

success of lipid cleavage to get DCOH was verified by Nuclear Magnetic Resonance (NMR) of ^{1}H and XPS. NMR ^{1}H of the DCPC during the enzymatic reaction was recorded on a JEOL ECS spectrometer at 400 MHz. Proton NMR of lipids is known to be quite complex to analyze. However, by focusing on the $–N^{+}(CH_3)_3$ group at 3.2 ppm located at the head group at different intervals of time of the enzymatic reaction it is possible to obtain kinetic information about the cleaving process (**Figure 24**). The calculated area of this peak at 3.2 ppm normalized by the tetramethylsilane (TMS) present in the used solvent $CDCl_3$ shows the evolution of the percentage of cleaved DCPC, i.e of DCOH (**Figure 25**). 42h is required to attain an almost 85% yield of conversion. The enzymatic cleavage can also lead to sub-product such as phosphoric acid which adds more difficulty in the data analysis. Another technique is therefore required to confirm the cleavage of the lipids.

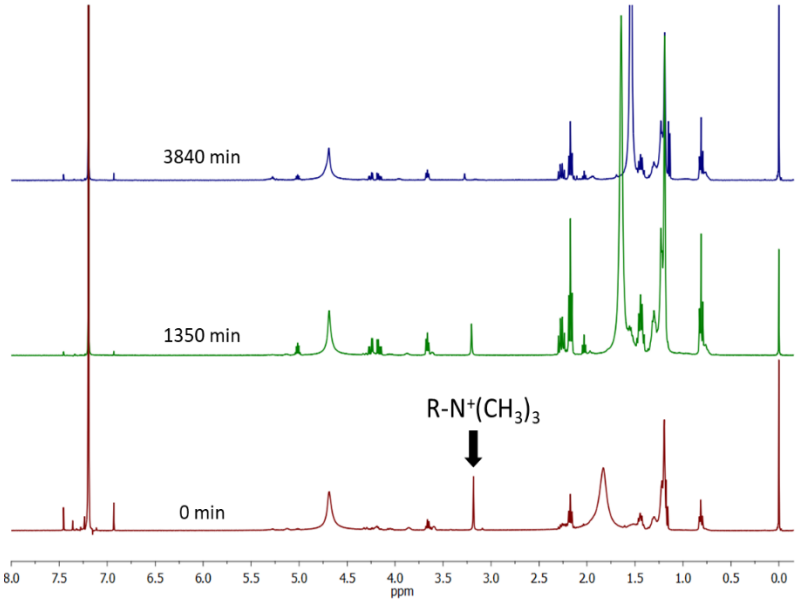

Figure 24 *NMR ^{1}H of the enzymatic cleavage reaction recorded at different time*

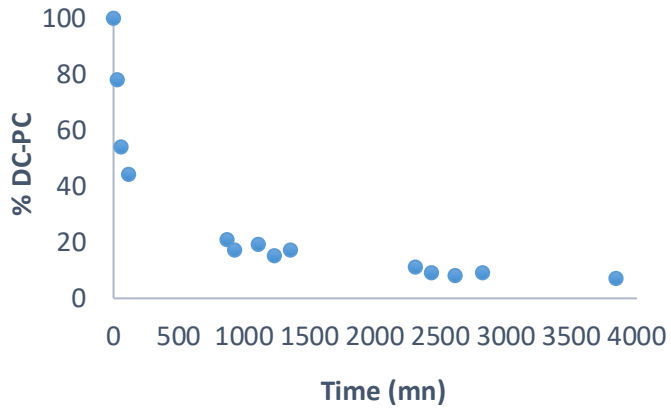

Figure 25 *Evolution overtime of the DCPC cleaving process*

X-ray photoelectron spectroscopy (XPS) is a well-known technique to analyze the chemical composition of materials and especially the surface chemical composition (*Exp.Tech. part VI.6.2*). In order to confirm the phosphatidylcholine head-group cleaveage, two samples were prepared using DCPC and DCOH lipid monolayers both deposited on P3HT layer. The formation of the lipid monolayers on P3HT will be described in the next section of this chapter. Phosphorus 2p (P2p) area was scanned by XPS (**Figure 26**). For the DCPC sample, a peak is observed at 134 e.V. corresponding to the phosphorous atom present on the phosphatidylcholine head groups. After cleavage, the

disappearance of this peak is noticed. Indirectly, it is possible to claim the good cleavage of the phosphatidylcholine head group from the DCPC lipids and the successful deposition of both kind of lipids on P3HT. These results from XPS, where produced sub-product of the reaction are not interfering thanks the the rinsing steps, can therefore be correlated with the observation made by NMR ^{1}H analysis during the cleavage process.

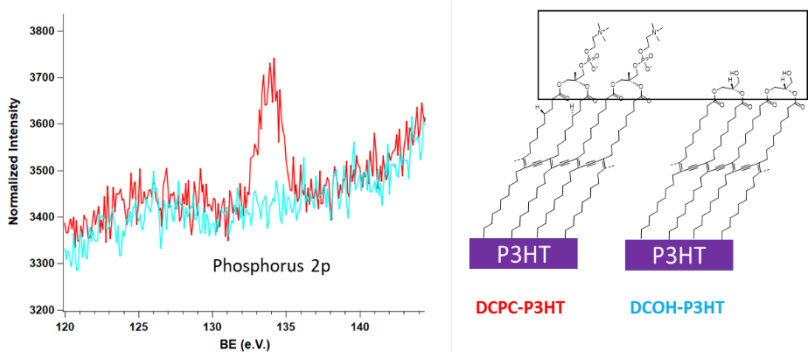

Figure 26 *Phosphorus 2p eV range scanned by XPS. Two sample was compared: DCPC on P3HT and DCOH on P3HT*

In this part, we showed the obtention of the DCOH lipids by enzymatic cleavage. The cleavage process was confirmed by NMR ^{1}H and XPS.

II.1.2. Deposition & stabilization of the DCOH lipid monolayers

As presented in the introduction of this chapter, stability is the main issue for the application of SAM lipid monolayers as a dielectric layer in the electronic devices. First, such layers are very unstable in the air or when rinsed with solvents; second, they do not handle mechanical or electrical forces. The application of an electric field leads to electroporation even at a low field leading to the degradation of its dielectric properties[98].

After comparing the two main methods for the lipids deposition on a solid substrate, I will present in this section a method to obtain a highly stable lipid layer on organic semiconductor.

II.1.2.a. Comparison of the lipid layers deposition methods

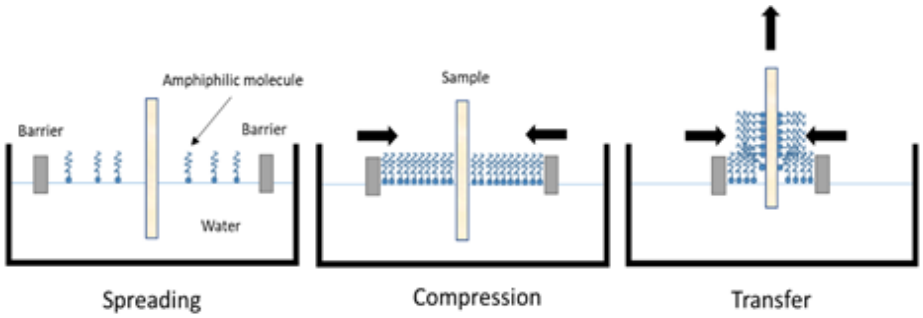

Figure 27 *Langmuir-Blodgett monolayer fabrication technique*

When deposition of a nanometric scaled layers such as lipid monolayers are evoked, the Langmuir-Blodgett (LB) is obviously called to mind. This technique enables the fabrication and characterization of single-molecule thick films with control over the packing density of molecules (**Figure 27**). The amphiphilic solution is deposited on the water surface with a microsyringe, the

[98] (Heurtault, Saulnier, Pech, Proust, & Benoit, 2003)

solution spreads rapidly to cover the available area. As the solvent of the amphiphilic molecules evaporates, a monolayer forms at the air-water interface and a Langmuir film is created. The software-controlled barriers located at the interface then compress the monolayer until the surface pressure sensor indicates the desired packing density. Langmuir-Blodgett transfer is considered as the perfect technique to obtain lipid monolayer with high packing density. Nevertheless, this technique requires specific equipment and is not suitable for deposition on devices.

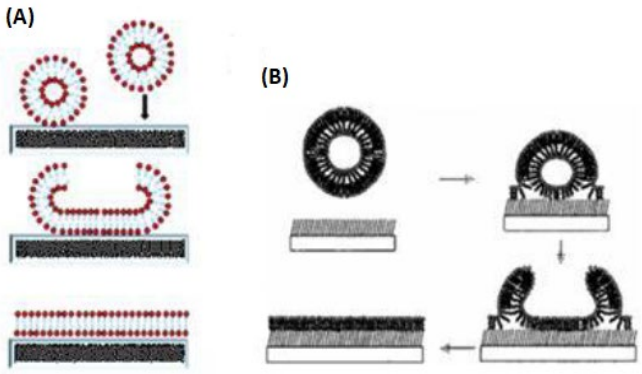

Figure 28 *Vesicle fusion technique for lipid layers fabrication (A) on hydrophilic substrate (B) on hydrophobic substrate*

An alternative to LB technique is the vesicle fusion process which is simple, much faster and can be applied to the devices (**Figure 28**). This process is based on the adsorption and fusion of small unilamellar vesicles on a substrate from their aqueous dispersion[80,99]. Depending on the hydrophobicity of the substrate, vesicle fusion will give rise to a bilayer or a monolayer. The formation of a bilayer on a hydrophilic surface is quite spontaneous. The vesicle contacts the surface, adheres due to hydrophilic interactions, ruptures and spreads to form a domain of lipid bilayer with a thickness between 4 to 6 nm depending on the lipids. The formation of a monolayer on a hydrophobic surface is more complicated. The initial contact of the vesicles over the substrate is crucial in the formation of the lipid monolayer. It is controlled by the competition between the favorable adhesion energy and unfavorable bending energy of the deformed vesicles after adhesion on the surface. The hydrophilic nature of the polar head-groups of the vesicles impedes the adhesion of these vesicles on hydrophobic surfaces[100,101]. Then in order to form a lipid monolayer, adhesion of the vesicle and splitting into two monomolecular layers must occur simultaneously followed by unrolling and spreading process[70]. Resulting monolayer thickness varies between 2-3 nm[71]. For the fabrication of the ODL for OFET, this method will be selected.

II.1.2.b. Deposition and stabilization of DCOH lipid monolayer on organic substrate

The formation of stable DCOH lipid monolayer on P3HT was hence obtained using a protocol derived from the vesicle fusion method. A compacted version of the protocol is added to the *Exp. Tech. part VI.4.2*. As this technique is crucial for the project, it will be detailed here.

The DCOH lipids are stored in chloroform at -20°C to avoid any alteration. The first step is to evaporate the solvent slowly at 45°C to avoid damage to lipids. Once most of the solvent is evaporated,

[99] (Tero, Takizawa, Li, Yamazaki, & Urisu, 2004)
[100] (Khan, Dosoky, & Williams, 2013)
[101] (McColl, Yakubov, & Ramsden, 2007)

deionized water is added to obtain a DCOH solution at 0.27 mM. At this stage, multilamellar lipids vesicles form spontaneously (Figure 29). Unilamellar vesicles are then obtained by sonication of the lipid solution for 30 min. Afterward, vesicles are filtrated several times with 0.1 µm pore sized polycarbonate membranes in order to reduce their size. These steps are important to do just prior to the deposition. In fact, after this process, vesicles have high curvature which makes them unstable and easier to break. The DCOH lipids vesicles are then injected in a PTFE well on a clean surface of P3HT at 25°C. The configuration of the setup is shown (Figure 30). Under manual stirring, the temperature is reduced abruptly to 10°C inducing vesicle condensation and the fusion of lipids on the P3HT. Such low-temperature lipid deposition is expected to produce high-density layers[102,103].

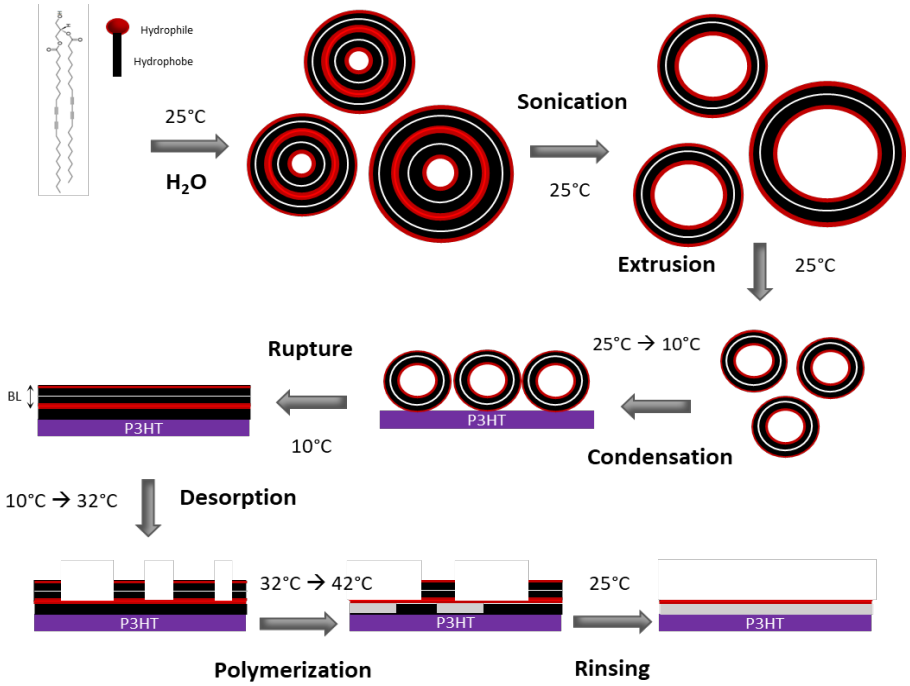

Figure 29 *Schematic representation of the derivated lipids vesicle fusion method for the fabrication of the insulating layer used in OFET*

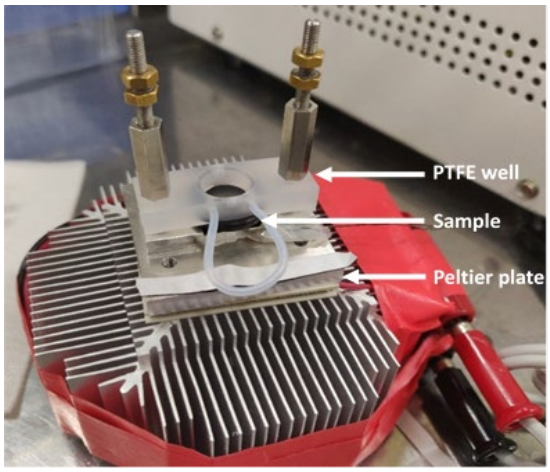

Figure 30 *Setup of the lipid deposition process*

[102] (Almeida, Vaz, & Thompson, 1992)
[103] (Sun, Tristram-Nagle, Suter, & Nagles, 1996)

At this step, a monolayer with additional patches of bilayers on top with 5 nm heights is formed. As shown on the AFM images (Figure 31).

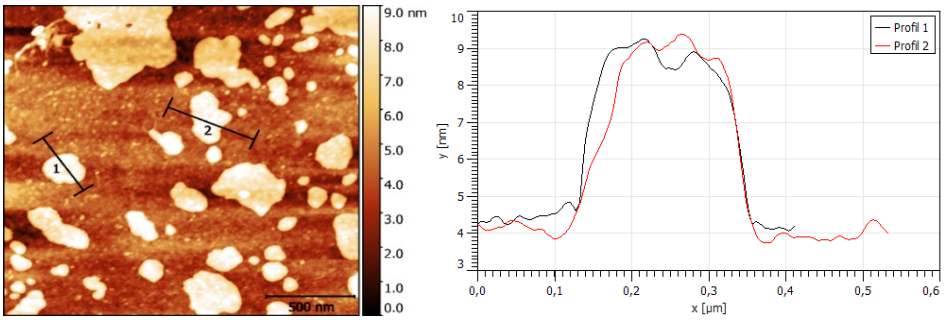

Figure 31 *AFM topographic images and profiles of DCOH bilayers patch on top of monolayer*

After staying 10 min at this temperature, the surface was heated 1°C/min until 32°C, the temperature at which the over-layers desorb from the surface, leaving a homogeneous DCOH monolayer on top of the P3HT. The stabilization of the monolayer was obtained by radical polymerization of the lipids. It occurs in the aliphatic chains where the diacetylene groups are located. The initiator of the radical polymerization is the 2,2'-Azobis(2-amidinopropane) dihydrochloride (AAPH) added at 0.5 % in the liquid cell. The temperature was then slowly raised to 35°C for 10 min then 42°C for 60 min. The sample was then rinsed with DI water at 25°C under stirring. At this stage, the reticulated layer DCOH-R is sufficiently stable on P3HT to be rinsed and dried. AFM topographic images of the P3HT surface before and after the formation of a stable DCOH-R layer were obtained (Figure 32).

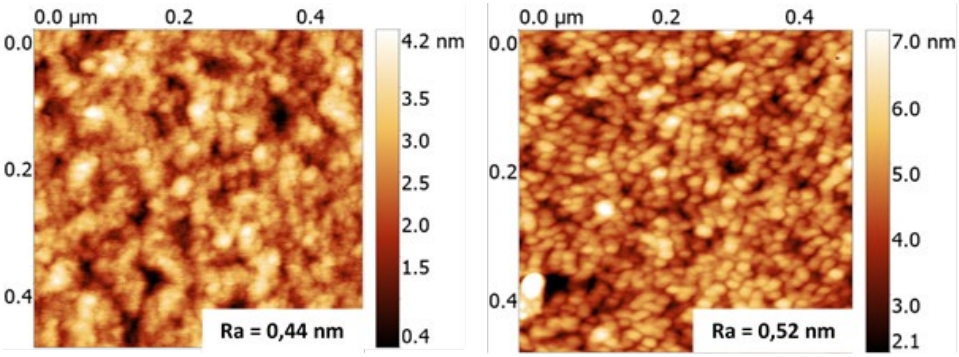

Figure 32 *AFM topographic images of bare P3HT (left) and DCOH-R (right) in air*

The average roughness was increased slightly from 0,44 nm to 0,52 nm before and after lipid layers formation respectively. But the main change has occurred on the structure. Small roundly shaped domains of around 20 nm of diameter are observable after DCOH-R formation. The contact angle before and after DCOH deposition was also investigated (Figure 33).

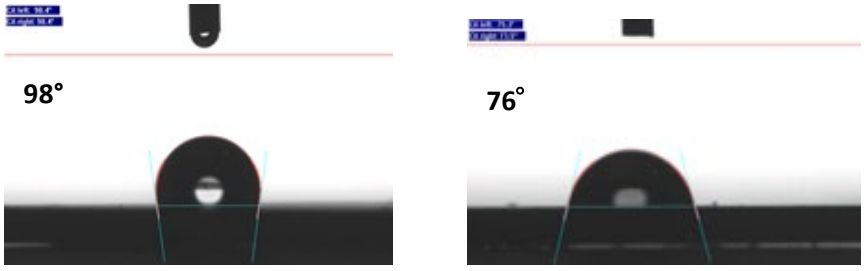

Figure 33 *Contact angle of water drop on bare P3HT (left) and DCOH-R (right) measured by a goniometer*

The surface of the bare P3HT has a high contact angle of 98° which means a hydrophobic material. After DCOH-R formation, a decrease of the contact angle to 76° is observed due to the very polar properties of the DCOH headgroups.

These results, obtained both by AFM topographic measurements and contact angle measurements, are confirming the good deposition of the DCOH-R on P3HT by using the modified vesicle fusion technique *(Figure 34)*. Nevertheless, with these common methods, reaching quantitative information about lipids density, organization and polymerization efficiency is not possible. Another method must be used.

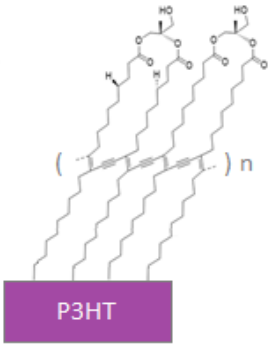

Figure 34 *Schematic representation of DCOH-R on P3HT.*

II.2. Structural characterization of the dielectric gate

In the first part of this chapter, the protocol of the lipids layer deposition, designated as a dielectric gate for FET application, based on vesicle fusion technique was presented. The success of the deposition was observed by AFM and contact angle measurement. At this stage, the reticulation of lipids by polymerizing the acetylene groups in the aliphatic group during the deposition process guaranteed their stability on the hydrophobic substrate. In order to obtain further quantitative and qualitative information about the reticulation, density and organization of the lipids, Attenuated Total Reflectance Fourier – Fourier Transform Infrared Spectroscopy (ATR-FTIR) was used. Indeed, FT-IR in ATR mode is a well-known technique for characterizing thin layers: it relies on the presence of an evanescent wave at the reflecting interface (**Figure 35**).

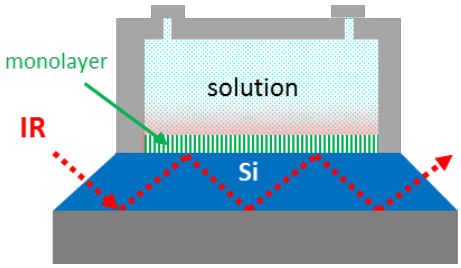

Figure 35 *Evanescent waves apparition (light red) at the surface in ATR configuration of FT-IR*

In ATR-FTIR, the infrared beam is directed into a high refractive index medium which is transparent for the IR radiation of interest, here a silicon prism. Below a critical angle, the beam is completely reflected when it impinges on the surface of the internal reflective element. Several internal total reflections can occur within the internal reflective element until the beam reaches the end of the medium. It can be shown from Maxwell's equations that superimposition of incoming and reflected waves yields a standing wave within the internal reflection element and an electromagnetic

disturbance exists in the rarer medium beyond the reflecting interface. This so-called evanescent wave, whose energy is spatially concentrated in the vicinity of the interface, is characterized by its amplitude which falls off exponentially with the distance from the interface[104]. Any molecule present in the evanescent wave will contribute to the spectrum: the molecular species nearby the surface will absorb the evanescent waves giving rise to a diminution of the IR intensity. The penetration depth into the sample is typically between 0.5 and 2 micrometers, with the exact value being determined by the wavelength of light, the angle of incidence and the indices of refraction for the ATR crystal and the medium being probed[105]. The number of reflections may be varied by varying the angle of incidence and the length of the prism. The beam is then collected by a detector as it exits the crystal.

To our knowledge, the process of vesicle fusion on surfaces has been only investigated by surface plasmon resonance[106], cyclic voltammetry, and impedance spectroscopy[107]. FT-IR in ATR mode was never used to study a dynamic process occurring at the nanometer scale. By applying a few modifications in the experimental system, ATR-FTIR could be used for the purpose of studying lipids vesicle fusion on organic substrates.

II.2.1. ATR-FTIR *in-situ* measurements: setup & records

In order to follow the formation of the lipid monolayer, a new *in-situ* cell was built for the purpose of this study. It contains a heating/cooling system, a fluidic system, and a stirring system to mix the solutions.

II.2.1.a. Setup of the device

The FTIR ATR experiments were performed at LPMC (Laboratoire de Physique et Matière Condensée) at Ecole Polytechnique, in collaboration with Dr. C. Henry-de-Villeneuve. A customized EQUINOX 55 spectrophotometer (Brucker, Germany) equipped with a liquid nitrogen-cooled Mercury-Cadmium Telluride photovoltaic detector was used. The ATR samples (FZ-purified Si(111) wafer, thickness 500 µm) were shaped as prisms with two opposite sides beveled at ~ 45° to guide the IR beam into the silicon such to have a total reflection at the silicon/air (or solution) interface. Their length (~15 mm, for ~ 25 internal reflections) was chosen to obtain intense signals of the sample in wide-range FTIR spectra (1000-4000 cm^{-1}). Measurements were carried out in an N_2 purged chamber in order to minimize H_2O vapor and CO_2 absorption. Spectra were averaged over 150 scans (4 cm^{-1} resolution). For the experiment, a close cell made of Teflon with a circular aperture (PTFE coated O-Ring diameter of 10 mm, exposed area 0.8 cm^2) was pressed against the silicon prism and filled with the solution of interest. Heating and cooling of the sample were achieved using a Peltier system installed under the sample. A magnet was also added in the cell in order to add enough mechanical energy during the condensation step of the lipids (**Figure 36**).

[104] (Goormaghtigh, Raussens, & Ruysschaert, 1999)
[105] (Mirabella, 1993)
[106] (Hubbard, Silin, & Plant, 1998)
[107] (Peng, Tang, Han, Wang, & Dong, 2002)

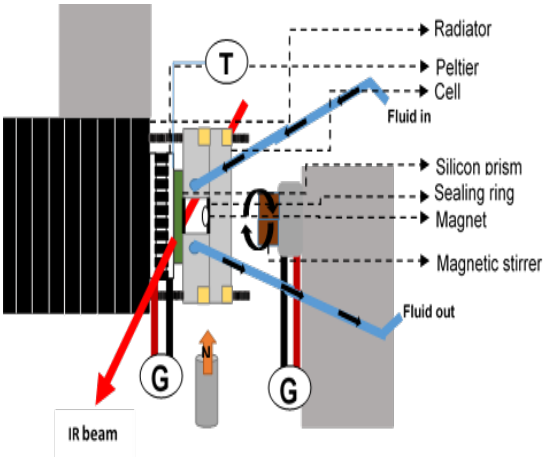

Figure 36 *Schematic representation of the setup designed for in-situ ATR FT-IR measurements*

Such cell implanted in an ATR FT-IR experimental setup presents several benefits besides the advantage brought by the ATR mode:

- Making *in-situ* experiments and chemical reactions allows signal subtraction of reference sample without having the problem of baseline change.
- The Peltier plate, the fluidic system and the magnetic stirrer allowed to play on different parameters such as temperature, concentration and stirring of the injected solution.
- Spectra recording can be achieved over time which allows following kinetics evolution of reactions occurring in the surface of the substrate.
- The inert Teflon based cell and fluidic tubings avoid parasite reactions.

II.2.1.b. Spectra records and in-situ DCOH-R lipid monolayers formation process on P3HT

The protocol for the formation of DCOH-R on P3HT was adapted to be used in the *in-situ* cell of the FTIR-ATR. First, the semiconducting polymer P3HT film was formed on SiO_2 based ATR prism (Si(111)) by spin-coating to obtain a 20 nm thick layer. The preparation of the P3HT layer will be discussed in detail in the Chapter 4. The P3HT coated prism is then fixed in the cell in the FTIR chamber and the air was purged with N_2 to remove parasite H_2O and CO_2 signals from the spectra. Prior to the lipids deposition, a series of spectra were acquired at a whole range of temperatures between 10°C and 45°C to be used later as reference spectra (in organic layers especially, FTIR spectra may change with temperature due to molecular reorganization). The P3HT substrate and the lipids solution in H_2O at 0.27 mM were pre-heated at 45°C C to facilitate lipid vesicle fusion on the substrate. Lipids solution was then injected through the fluidic system in the 0,4 ml capacity Teflon cell with the sample under stirring. The temperature of the surface in contact with the lipid solution was quickly cooled down to condensate the lipids and form layers and then progressively warmed up and polymerized with AAPH to form a dense, stable and close-packed lipid monolayer according to the procedure described previously. FT-IR spectra were acquired at each step of the lipid layer formation process. To extract information provided only by the lipids, all spectra were normalized by a corresponding reference spectrum (same temperature) measured on the initial P3HT layer as mentioned previously.

The condensation phase is primordial in the deposition process. Compared to the lipids deposition method in open-cell, bringing enough energy to break lipids vesicles is challenging in close space. In the **Figure 37** we can see the important role of stirring. Lipids vesicles were introduced at several concentrations (0.05 mM to 1 mM) in the liquid cell at 45°C and condensation at 10°C with and

without mechanical stirring was applied. When stirring is not applied the intensity of the peaks corresponding to the aliphatic chains (CH_2 stretching symmetric 2850 cm^{-1} and CH_2 stretching asymmetric 2920 cm^{-1}) is very low even with high concentration of lipids. Moreover, the low frequencies of these peaks and the absence of the CH_3 peak normally located at around 2960 cm^{-1}, are the evidence that the lipids vesicles did not break to form layers. In fact, in vesicle structure, the CH_3 groups of the DCOH lipids, which are located at the extremity of the aliphatic tail (**Figure 34**), are not facing-up to the surface. As a consequence, the density of CH_3 groups is reduced nearby the surface. When mechanical energy is induced by stirring, the intensity of the quoted peaks increases versus the DCOH concentration and the CH_3 peak appears which means the successful formation of the lipid layers.

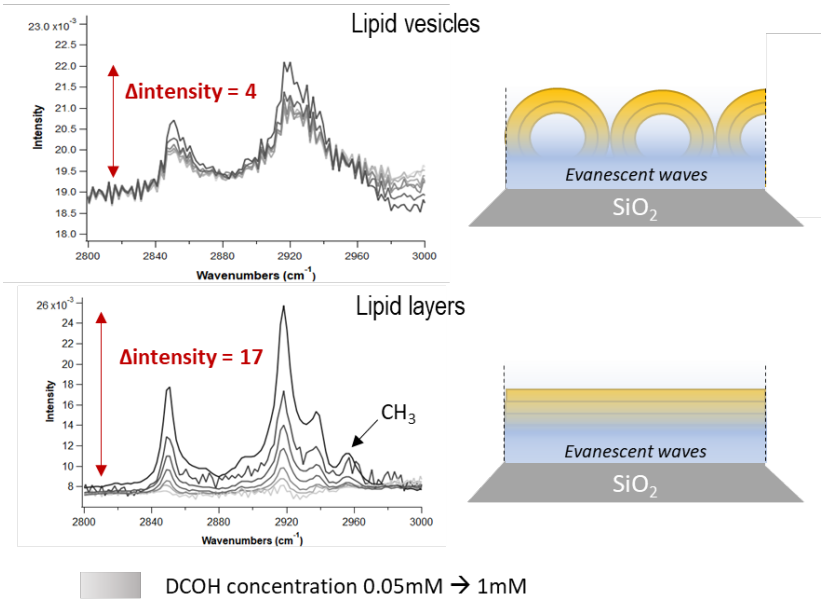

Figure 37 *IR signal difference in the range of aliphatic chains (2800-3000 cm^{-1}) in case of vesicles or layers adsorption on substrate. Stirring was applied in the second case.*

In the following, all spectra were recorded (**Figure 38**) in the range of 1000-3200 cm^{-1} wavenumbers with p and s polarization of the IR beam. The necessity of recording in p and s polarization will be explained in the density calculation part. Several peaks associated with the signature of the DCOH are visible. Signal of the ester group of DCOH is observable (1154 cm^{-1}; 1217 cm^{-1}; 1241 cm^{-1}; 1735 cm^{-1}). As well as the signal of the aliphatic chain of DCOH (2849 cm^{-1}; 2917 cm^{-1}; 2958 cm^{-1}). As the spectra are normalized with references in water, a negative peak corresponding to the loss of water volume after lipids deposition is apparent at 1640 cm^{-1}. Absence of the peak related to the medial acetylene group (stretching occurring in the range 2260–2100 cm^{-1})[108] before polymerization can be surprising. However, it has been showed that in some cases, such as in highly symmetrical substituted alkynes, it may not show at all due to the low polarity of the triple bond associated with those alkynes[109].

[108] (Coates, 2006)
[109] (Smith B. , 1999)

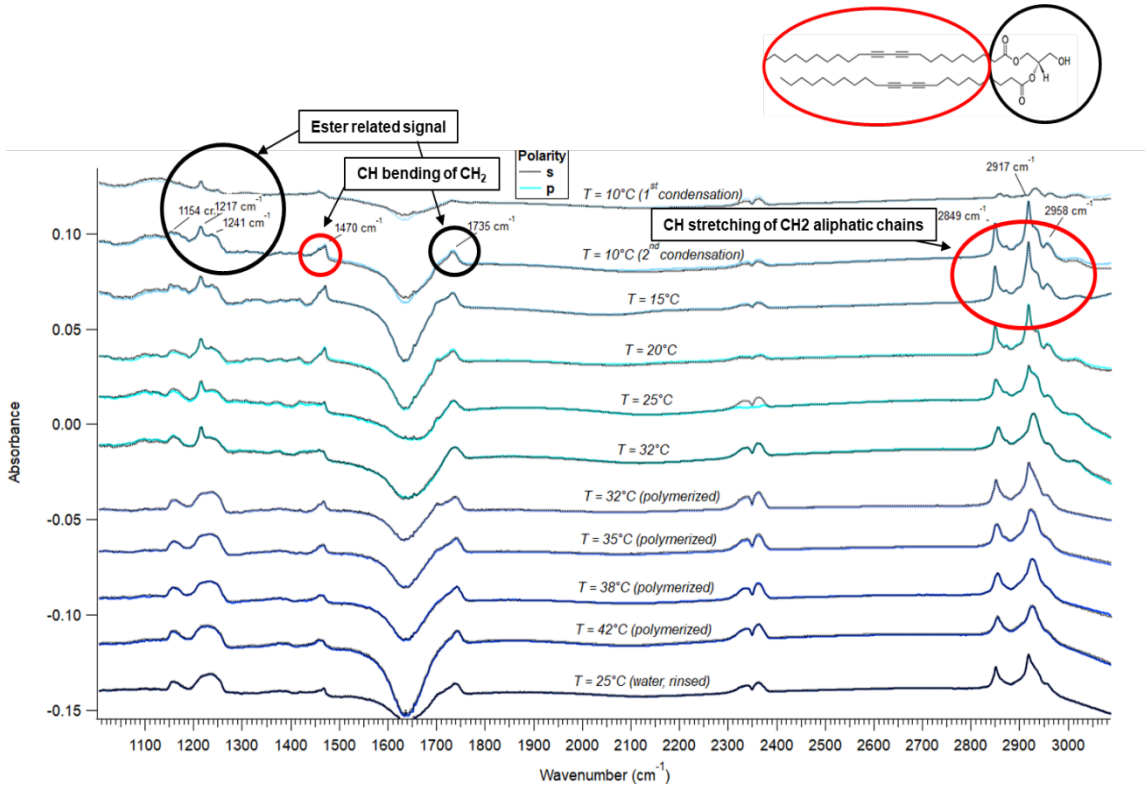

Figure 38 *Full IR spectra recorded in ATR in-situ mode with p & s polarization of the beam at different step of the DCOH-R formation process on P3HT. Spectra were normalized with P3HT in water reference to keep only signal of the DCOH lipids in water.*

From these spectra, it is possible to obtain qualitative and quantitative information about the polymerization, density, organization and inclination of the lipids on P3HT.

II.2.2. Density, organization and orientation of the DCOH monolayer on P3HT during the stabiliation process

II.2.2.a. Fitting method of the peaks

To extract quantitative information from the deposition process, we focussed on the aliphatic region in the wavenumber range 2800-3000 cm^{-1}. Each spectrum was then fitted using a combination of Lorentzian and Gaussians profiles. 9 peaks assigned to the different vibrational modes of the CH bond in the aliphatic chains of the lipids were used for the fitting (**Figure 39**). Assignments and positions are reported in **Table 3**. Supported by previous studies from the literature[110,111,112,113,114], we found that the SLM organization can be decomposed into two phases, a crystal-like structure and a liquid-like structure.

[110] (Parikh, Beers, Shreve, & Swanson, 1999)
[111] (Batchelder, Evans, Freeman, Haussling, Ringsdorf, Wolf, 1994)
[112] (Porter, Bright, Allara, & Chidsey, 1987)
[113] (Golden, Snyder, & Smith, 1982)
[114] (Nuzzo, Dubois, & Allara, 1990)

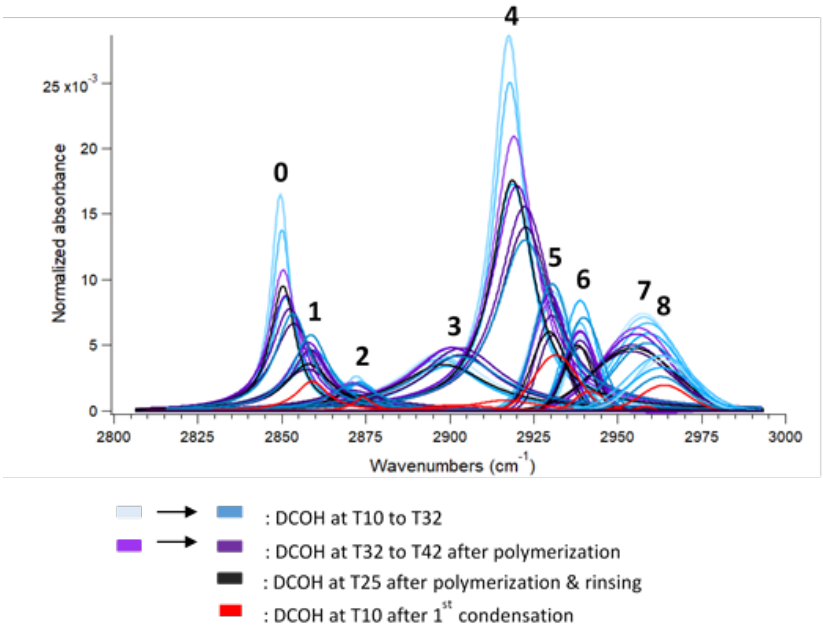

Figure 39 *Aliphatic area (2800-3000 cm^{-1}) of DCOH-R. IR spectra fitted with 9 peaks (0 to 8) at different step of the deposition process*

Table 3 *Assignments and position of peaks used for fitting*

PEAK ASSIGNEMENT	POSITION (CM^{-1})	POSITION FROM LIT. (CM^{-1})
0 vCH_2 sym. stretch. (cryst.)	2849	2843-2863, CH sym of CH_2 in aliphatic chains
1 vCH_2 sym. stretch. (liq.)	2858	2843-2863, CH sym of CH_2 in aliphatic chains
2 vCH_3 sym. stretch.	2872	2878, CH sym of CH_3
3 vCH FR	2898	2898 CH_2 Fermi Resonance
4 vCH_2 asym. stretch. (cryst.)	2917	2916-2936, CH asym of CH_2 in aliphatic chains
5 vCH_2 asym. stretch. (liq.)	2929	2916-2936, CH asym of CH_2 in aliphatic chains
6 vCH FR	2938	2935 CH_3 FR
7 vCH_3 asym. stretch. (ip)	2955	2956, CH asym of CH_3 (in plane)
8 vCH_3 asym. stretch. (op)	2964	2965, CH asym of CH_3 (out of plane)

The more intense peaks located at 2849 cm^{-1} and 2917 cm^{-1} (0 and 4 in **Figure 39**) are attributed to the symmetric and asymmetric stretching vibrational mode of CH_2 respectively of the crystal-like phase; the less intense ones at 2858 cm^{-1} and 2929 cm^{-1} (1 and 5 in **Figure 39**) to the symmetric and asymmetric stretching mode of CH_2 in the liquid-like phase. CH_3 symmetric stretching mode is located at 2872 cm^{-1} (2 in **Figure 39**). For the asymmetric counterpart, in-plane CH_3 and out-of-plane CH_3 peaks are located at 2955 cm^{-1} and 2964 cm^{-1} respectively (7 and 8 in **Figure 39**). Finally, two other peaks positioned at 2898 cm^{-1} and 2938 cm^{-1} have been attributed to C-H bonds Fermi resonances. (3 and 6 in **Figure 39**). Experimental results about the evolution of the IR absorbance of the lipids during the different steps of the process showed in **Figure 38** are also correlated with the hypothesis of the coexistence of two phases as reported in the literature. The first spectrum, 10°C (1) in **Fig. 38** , reflects

the IR response of a sample with small amounts of deposited lipids. In this spectrum only peaks resulting from the CH_2 in liquid-like phase are present. In contrast, the spectrum obtained for a dense layer, 10°C (2) in Fig. 38, indicates the presence of both liquid and crystalline phases with a dominance of the crystal-like phase. With this experiment, we could identify the positions of disordered lipids and of crystal-like phases at 2858 cm^{-1} & 2929 cm^{-1} and 2849 cm^{-1} & 2917 cm^{-1} respectively for CH_2 symmetric and asymmetric stretching (Table 3).

II.2.2.a. DCOH lipids organization

The position of the vibrational bonds in the waverange extracted by fitting the aliphatic area of the FT-IR spectra is giving information about the organization of the DCOH lipids on P3HT. Aliphatic chain organization is a major condition for making dense layers, and to allow reticulation between the different chains, i.e. requiring spatial proximity of the neighboring acetylenic units[115]. It is known from the literature, that the organization of such chains is mainly governs by Van der Waals interaction between the aliphatic chains[114]. It was also shown that close-packed structures of π-systems such as electron-rich diacetylene units laterally associate within the monolayer resulting in a non-covalent molecular scaffolding[116], making the system highly favorable for reticulation.

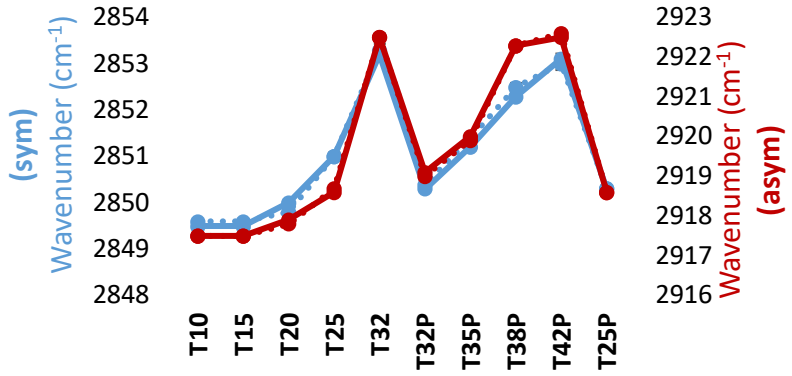

Figure 40 *Organization of DCOH on P3HT. Position of the crystal-like structure related peaks were reported at different temperature step of the deposition process*

The crystallinity of the lipid monolayer was followed along its fabrication process by extracting the positions of $\nu CH_{2}{}^{s,c}_{str}$, (CH_2 stretching symmetric) and $\nu CH_{2}{}^{as,c}_{str}$ (CH_2 stretching antisymmetric) vibrations (peaks 0 and 4 in Figure 39 respectively). These modes are highly sensitive to the structural environment of the alkyl chains and provide good information on the crystallinity of the layer. The extracted positions at the different stages of the fabrication are reported in Figure 40. Both vibrations show the same behavior : right after monolayer formation at 10°C, the low frequencies at 2849.5 and 2917.5 cm^{-1} are the signature of a highly crystalline phase; these frequencies systematically shift towards higher values with increasing temperature as the chains become more disordered and reach values of 2853.5 and 2922.5 cm^{-1} at 32°C before the polymerization. Right shifting of the peak position to highest values of wavenumber versus the temperature means that higher energy is required to obtain vibration of the CH_2 bonds and indirectly in our case that the aliphatic chain is less organized and packed. After the addition of free radical AAPH at 32°C, both these frequencies decrease certainly due to the reticulation of the layer which must be generating order. At the end of the process, the final $\nu CH_{2}{}^{s}_{str}$, and $\nu CH_{2}{}^{as}_{str}$ frequencies are 2950.2 and 2918.5 cm^{-1} at 25°C, hence indicating a crystal-like organization of the layer even at room temperature.

[115] (Baughman & Yee, 1978)
[116] (Menzel, Mowery, Cai, & Evans, 1999)

II.2.2.b. DCOH lipids surface concentration

The density of lipids adsorbed on the surface at different step of the deposition process (**Figure 41**) was calculated according to a quantification method based on IR measurements in ATR mode of the lipid layer using p and s polarized IR beam and a calibration of a characteristic absorbing dipoles (vCH_2 in this case) with similar absorption cross-section than the measured sample[117,118,104]. Please refer to the *Exp. Tech. part VI.5.4* for further information.

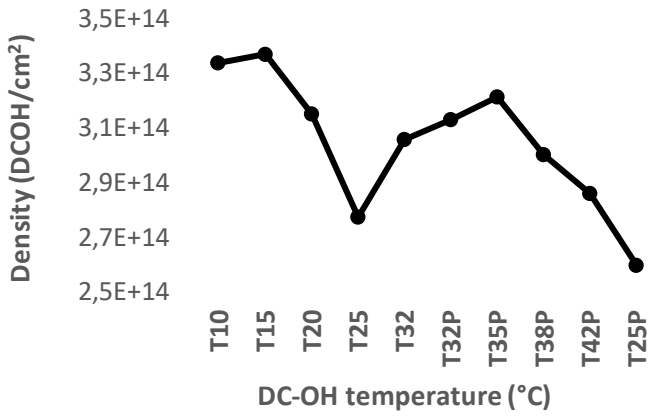

Figure 41 *Evolution of the DCOH density on P3HT over different temperature step of the deposition process*

At 10°C, a very high density of 3.3 10^{-14} lipid/cm² is in agreement with the formation of a monolayer with additional patches of multi-layers. This density evolves along the process showing at the exception of the 32°C point, a continuous decrease of density that we have attributed to the desorption of the over-layers due to temperature rise. At 32°C, the large increase of density following the addition of free radical AAPH suggests the re-deposition on the surface of polymerized lipid aggregates from the solution. After the first reticulation and rinsing at 25°C, the final lipid monolayer with no upper layers remaining, as confirmed by AFM measurements, presents an estimated extremely high density of 2.6 10^{14} lipid/cm², i.e. of 5.1 10^{14} aliphatic chains/cm². It corresponds to a lipid molecular area of 38.5 Å² and an aliphatic chain area of 19.25 Å² by projection in the plane perpendicular to the chains. In the literature[103] the obtained area is similar to the area of lecithin lipids bilayer vesicles in the gel phase (19.6 Å). By comparing this molecular area to those obtained in surface/pressure isotherm experiments for DC8,9PC[119] or for amine-based diacetylene chains[120] the surface tension can be estimated to be ~50 mN/m at room temperature with a lipid layer in the solid-state hence supporting our conclusion on the crystallinity of the monolayer at room temperature. Note that this value of the surface tension is certainly slightly over-estimated as the head-group of DCOH lipids is much smaller than of DC8,9PC.

II.2.2.c. Evolution of the liquid-like phase of the DCOH lipids

[117] (Faucheux, Gouget-Laemmel, Henry de Villeneuve, Boukherroub, Ozanam, Allongue, Chazalviel, 2006)
[118] (Faucheux, 2005)
[119] (Baek, Phan, Lee, & Shin, 2016)
[120] (Walsh & Lando, 1994)

Obtaining a crystal-like structured lipid layers is very important to have high polymerization rate and therefore better stability. The calculated density in the previous part is showing a highly packed lipid layers with good crystallinity. In order to understand what is occurring during the vesicle fusion deposition process, it is interesting to study the liquid-like phase of the lipids. From the literature[110-114] and the data of the first incomplete condensation at 10°C where totally disorganized lipids were observed (Fig. 39), it is relatively easy to attribute the peaks related to the liquid-like phase of the lipids from the fit. The absorbance of the peak 1 & 5 (respectively vCH_2 symmetric stretching at 2858 cm^{-1} and vCH_2 asymmetric stretching at 2929 cm^{-1}) during the deposition process were displayed in the Fig. 42.

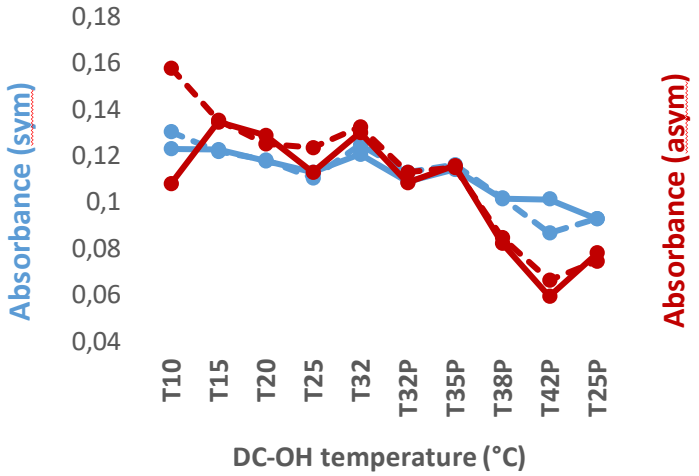

Figure 42 *Absorbance evolution of the CH_2 stretching (asym. and sym.) from the liquid-like phase of DCOH lipid layers. Dashed lines are related to the s polarization.*

A small difference is observed in p and s polarization but the overall trend is showing a decrease of the liquid-phase absorbance probably due to the desorption of the disorganized lipids patch on the top of the monolayer and the reorganization of the lipids with the polymerization started at 32°C. Studying the liquid-phase lipids absorbance in the layer brought more information about the lipids patches desorption of the additional layers occurring up to 32°C.

II.2.2.d. Orientation of the DCOH lipids

Along with the crystallinity and density characteristic of the lipids on P3HT, ATR spectroscopy also provides insight into the orientation of the lipid molecules. The tilt angle of DCOH on P3HT has been calculated using a derivate method from the literature[121,122]. The method uses the dichroic ratio, R_{exp}, for symmetric and asymmetric stretching vibrations of CH_2 bonds, $R_{Exp} = A_s^{CH_2}/A_p^{CH_2}$ with $A_p^{CH_2}$ and $A_s^{CH_2}$ the integrated absorbances for parallel (***s***) and perpendicular (***p***) polarized light respectively. The dichroic ratio is related to an orientational order parameter ***S*** according to eq.3 :

$$S = \frac{2(E_x^2 - R_{exp}E_y^2 + E_z^2)}{(3cos^2\alpha - 1)(E_x^2 - R_{exp}E_y^2 - 2E_z^2)} \qquad \text{eq. 3}$$

[121] (Tamm, 1997)
[122] (Scheibe, 2018)

E_x, E_y and E_z are the amplitudes of the evanescent wave in the film at the ATR prism/organic film interface. (eq. 4-6).

$$E_x = \frac{2cos\gamma\sqrt{(sin^2\gamma - {n_{31}}^2)}}{\sqrt{(1-{n_{31}}^2)}\sqrt{[(1+{n_{31}}^2)sin^2\gamma - {n_{31}}^2]}} \qquad \text{eq. 4}$$

$$E_y = \frac{2cos\gamma}{\sqrt{(1-{n_{31}}^2)}} \qquad \text{eq. 5}$$

$$E_z = \frac{2cos\gamma {n_{32}}^2 sin\gamma}{\sqrt{(1-{n_{31}}^2)}\sqrt{[(1+{n_{31}}^2)sin^2\gamma - {n_{31}}^2]}} \qquad \text{eq. 6}$$

These expressions have been described previously[123] ; they depend on γ, the angle of incidence of the IR beam at the solid/liquid interface, and n_1, n_2, and n_3 the refractive index of the silicon prism, the organic film and the water medium respectively (where $n_{31} = n_3/n_1$ and $n_{32} = n_3/n_2$). In our case γ= 43°, n_1 = 3.42, n_2 = 1.47, and n_3 = 1.33. We assume the refractive index of P3HT and lipid monolayer are similar. α is the angle between the transition dipole moment of $\nu CH_{2_{str}}$ and the long axis of the lipid alkyl chain in eq.3. Assuming an extended all-trans conformation of the alkyl chain, the transition dipole moments of both methylene stretching modes are approximately perpendicular to the alkyl chain, i.e., $\alpha \approx 90°$. For an axially symmetric distribution of transition dipole moments around the molecular main axis (Fig.43), the order parameter is related to β, the angle between the main axis of symmetry of the lipids and the substrate normal as represented is the eq.7

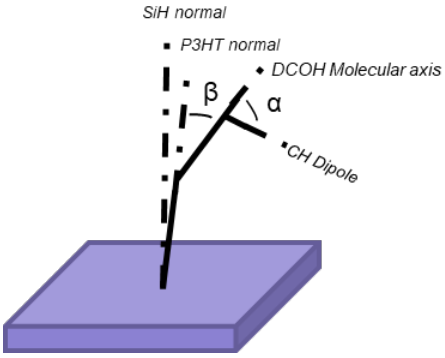

Figure 43 *Orientational parameter representation of DCOH on P3HT*

$$S = \frac{3cos^2\beta - 1}{2} \qquad \text{eq. 7}$$

Resulting average tilt angle of 26° *(Fig.44)* does not seem to vary along the lipid monolayer fabrication process and with increasing temperature. Such behavior confirms the previous results

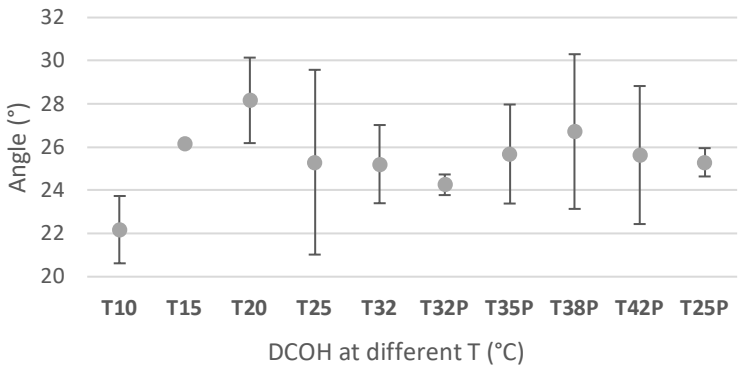

Figure 44 *Determined tilt angle of DCOH on P3HT at different temperature step of the deposition process*

[123] (Fringeli, 1992)

suggesting that the lipids organize very effectively on the substrate at 10°C and that this organization remains. This also suggests that the layer must be well reticulated otherwise an increase of β tilt angle would be expected at 42°C, corresponding to the lipid layer phase transition from a gel state to fluid phase[124]. Such behavior is in agreement with data previously reported for assemblies of alkyl chains bearing diacetylene groups in which these groups associate to form close-packed structures of π-systems[116] and govern the molecular orientation. The tilt angle of 26° is also matching with the previous results reported in the literature for crystal-like densely packed organic monolayers[125,126] Such results are quite striking: it first shows that our deposition procedure is very effective in forming dense layers and second the layer remains undamaged along the heating and reticulation process. A hypothesis to explain the high density of the lipids on P3HT is the presence of the underlying alkyls from the P3HT. Indeed, in well-organized P3HT layers, the distance between two carbonyl chains popping out of the surface was reported to be ~7.5 Å[127]. These alkyls chains, with a tilt of 50° regarding the thiophene backbone normal[128] are expected to interact strongly to interdigitate with the lipid chains and may influence the lipid distribution. Such hypothesis was already presented[107] for the alkanethiol-coated surface and lipids.

Based on this hypothesis and using the molecular area extracted below (A_{lipid} = 38.5 Å^2), one can estimate the distance between two lipid chains d by using **eq.8** to be ~4.8 Å (theoretically, it is 4,7-5,2 Å[129])(**Fig. 45**).

$$d = \frac{2\sqrt{A_{lipid}}}{\pi} - 2d_{C-H} \qquad \textbf{eq. 8}$$

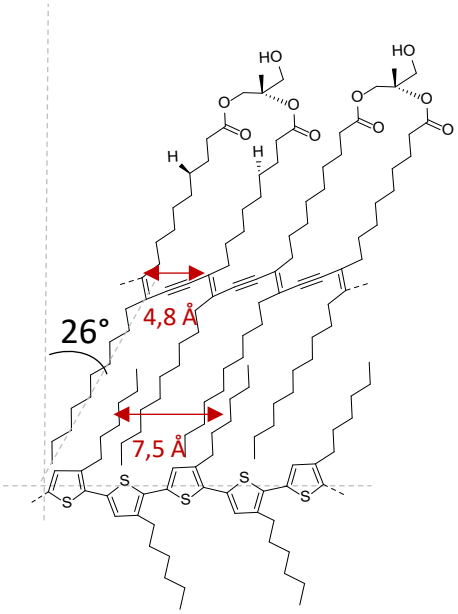

Figure 45 *Molecular representation of tangled DCOH-R on P3HT*

[124] (Johnston, Sanghera, Pons, Chapman, 1980)
[125] (Nuzzo, Fusco, & Allara, 1987)
[126] (Strong & Whitesides, 1988)
[127] (Verploegen, Miller, Schmidt, Bao, & Toney, 2012)
[128] (Yamamoto, Komarudin, Ara, Lee, Suganuma, Asakawa,Inoue,Kubota, Sasaki, Fukuda, Matsuda, 1998)
[129] (Menzel, Horstmann, Mowery, Cai, & Evans, 2000)

II.2.3. DCOH lipids polymerization

Lipids containing diacetylene fatty acids are known to be used in synthetic biomembrane for drug release experiments[130,131]. These lipids can be either photopolymerized or chemically polymerized. Here only the chemical polymerization approach will be discussed.

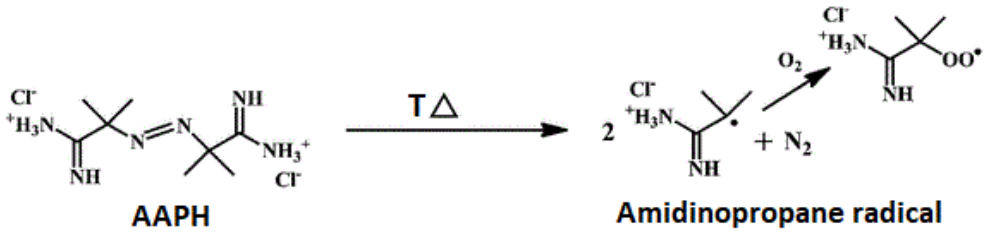

Figure 46 *Thermal decomposition reaction of AAPH*

The stabilization of the DCOH on P3HT surface is achieved by radical polymerization of the acetylene moieties present in the middle of the aliphatic chains. The radical is supplied by the AAPH polymerization initiator (Figure 46). By applying temperature (30-40°C), AAPH can be decomposed to give amidinopropane radical. These radicals will react with the acetylene groups of the DCOH to initiate the polymerization.

In order to put forward the effect and the evidence of the DCOH lipids polymerization, FT-IR spectra obtained after polymerization at 25°C was subtracted with the spectra before polymerization at 25°C in p and s polarization (Figure 47).

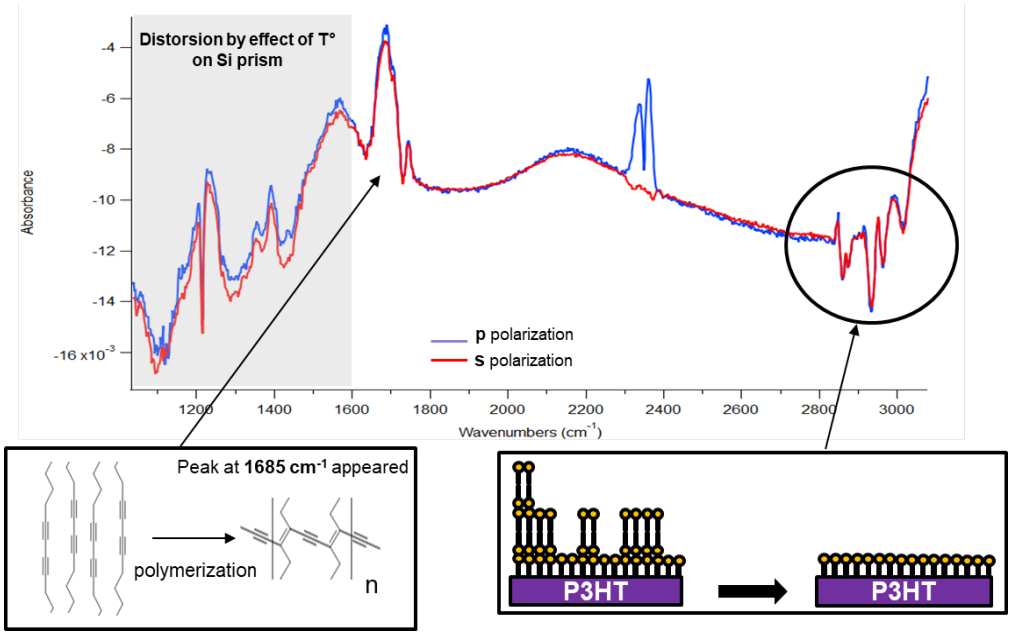

Figure 47 *Effect of the polymerization observed after subtracting the spectra after and before polymerization at 25°C in p & s polarization*

Unfortunately, this operation caused baseline modification and peaks of the Si substrate are visible below 1600 cm^{-1}. The reason is that the temperature was not exactly 25°C during the recording of the two spectra. Despite this problem, qualitative analysis can be achieved : the first observation is the

[130] (Yavlovich, 2011)
[131] (Punnamaraju, You, & Steckl, 2012)

broad peak located in the range of 1630 cm^{-1} - 1730 cm^{-1} . In the literature, the alkenyl C=C stretching bonds created here after polymerization[129] appear in the range of 1620 cm^{-1} - 1680 cm^{-1} [108,132] which might match with the signal observed here. As the signal is broad, the small shoulder also indicates that the polymerization has affected the C=O bonds present in the range of 1700 cm^{-1} - 1730 cm^{-1} [108,132]. The second observation is the negative peaks at 2860 cm^{-1} and 2930 cm^{-1} corresponding to the unorganized liquid phase lipids present in the upper layer while the peaks at 2850 cm^{-1} and 2918 cm^{-1} are related to the organized crystal phase lipids. This observation point out the desorption of the lipids in the upper layer during the desorption step between 10°C to 32°C of the described protocol.

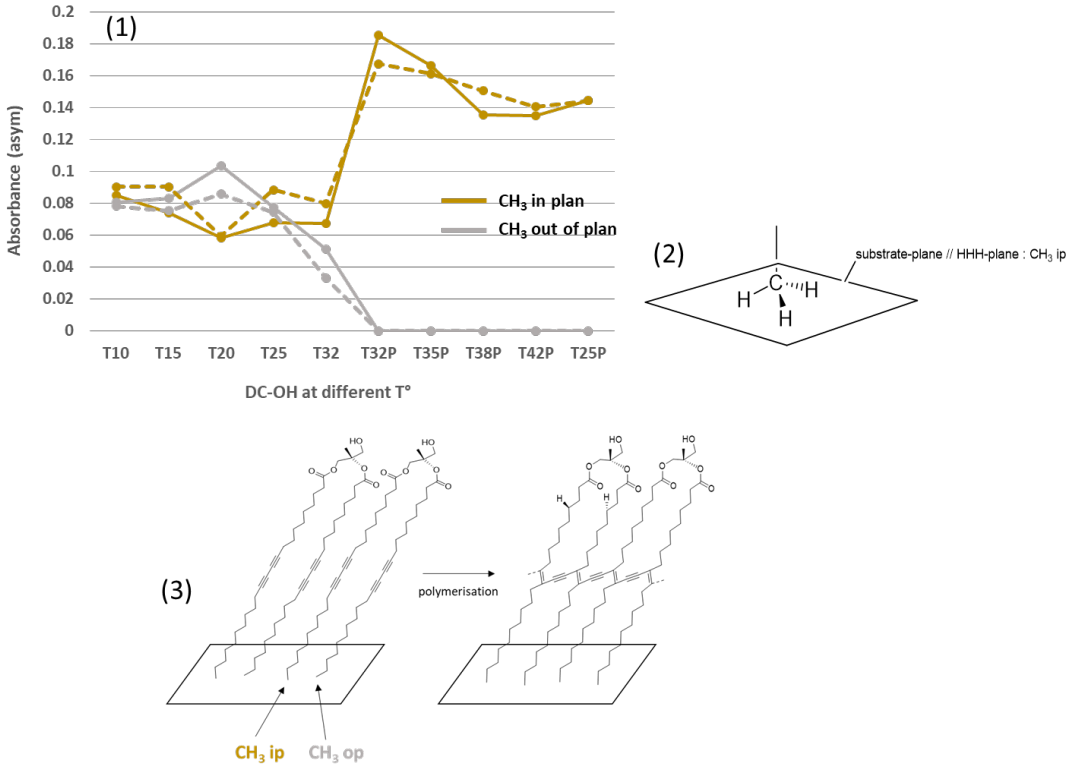

Figure 48 *(1) Absorbance evolution of the CH_3 stretching asym. in plan and out of the substrate plan. Dashed lines are related to the s polarization. (2) Schematic representation of the CH_3 ip (3) Molecular structure evolution of the lipids after polymerization*

Besides these observations, interesting peaks to confirm the polymerization are the ones corresponding to the CH_3 modes. The lipids are bearing one CH_3 group at each extremity of the aliphatic chains. In the literature[133,116], it was reported that two positions can be observed for the CH_3 bonds: CH_3 asymmetric stretching at 2955 cm^{-1} for the CH_3 in the substrate plan and the CH_3 asymmetric stretching at 2964 cm^{-1} for the CH_3 out of the substrate plan **Fig 48 (2)**. We observed that the CH_3 present on the two chains of the lipids are indeed not similar. Because of some gauche defects[116], the CH_3 of one alkyl chain might not be oriented in the plane of the substrate before polymerization (**Fig.48(3)**). Moreover, as one of the aliphatic chain is slightly longer than the other one, the CH_3 groups could have a different chemical environments (in contact with P3HT or not). In the **Fig.48(1)**, the absorbance evolution of the CH_3 asymmetric stretching during the deposition process is plotted. An absorbance decreasing related to the signal of CH_3 out of plan is observed just after polymerization at

[132] (Bower, 1989)
[133] (Porter, Bright, Allara, & Chidsey, 1987)

32°C meanwhile the signal of the CH_3 in plan appears to be doubled. Actually, this may suggest that the CH_3 out of plan switch conformation by a strain effect on the backbone of the lipids applied by polymerization. This signature might be an indirect way to prove the reticulation occurrence.

II.3. Mechanical characterization of the dielectric gate

For the purpose of exploiting such lipid monolayer/P3HT interface in the development of devices that could be used on-site, high mechanical robustness of the lipid monolayer on P3HT is essential. Lipid layers are well known to be very unstable on substrates in particular when they undergo chemical treatments, when drying or when exposed to an electric field or mechanical stress. They can be washed off of their support or undergo unwanted electrical or mechano-poration. It has been shown in the previous part that the diacetylene groups present in the aliphatic chain of the DCOH lipids can be polymerized by introducing the AAPH polymerizing agent at 30°C on well-organized DCOH lipids monolayer on P3HT. After maintaining at least 1h at 42°C, reticulated lipids with enough mechanical resistance toward water washing can be acquired. However, the layer stability obtained after this process may not be enough for further harsh chemical engineering.

In this part, the mechanical stability of the DCOH-R SAM lipids based dielectric gate will be investigated. An extra stabilization pathway will be presented and studied.

II.3.1. Additional reticulation step for higher stability

We have seen earlier that DCOH-R bears active OH chemical moieties on their head-groups. The head group of the lipids can therefore be used for an additional reticulation step to improve the stability of the layer: it was subsequently obtained by reacting the active hydroxyl group of the DCOH –R lipids with siloxane based molecules (Fig. 49).

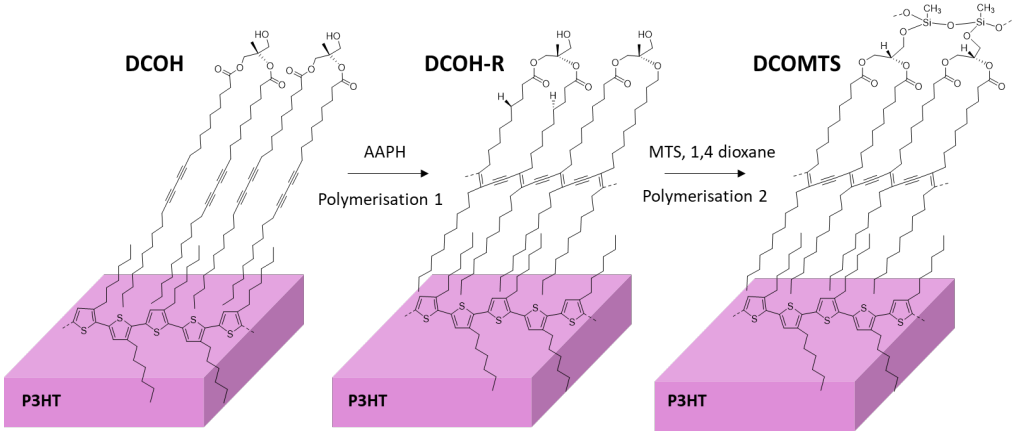

Figure 49 *Molecular reaction steps to obtain double reticulated lipids monolayer (DCOMTS)*

Methyltriethoxysilane (MTS) at 0.25 mM in anhydrous 1,4-dioxane was poured on the layer. After 60 min, the sample was abundantly rinsed with 1,4-dioxane first then with methanol and DI water. The process leads to the surface roughness increases from 0.5±0.1 nm for the DCOH-R on P3HT substrate to 1.1±0.1 nm for DCOH-R grafted with MTS (DCOMTS). The final so-called DCOMTS monolayer was perfectly homogeneous over the whole sample area as shown on the AFM image (Fig. 50, A2). Grafting of the MTS could be verified by (XPS) by measuring the binding energy in the range corresponding to the Si_{2p} signal. The spectra (Fig. 50, B) were acquired on three different samples: a neat P3HT layer

spin-coated on SiO_2 substrate (grey), after the formation of DCOH layer and reticulation of the aliphatic chains (purple) and after the reticulation of the head groups with MTS (green).

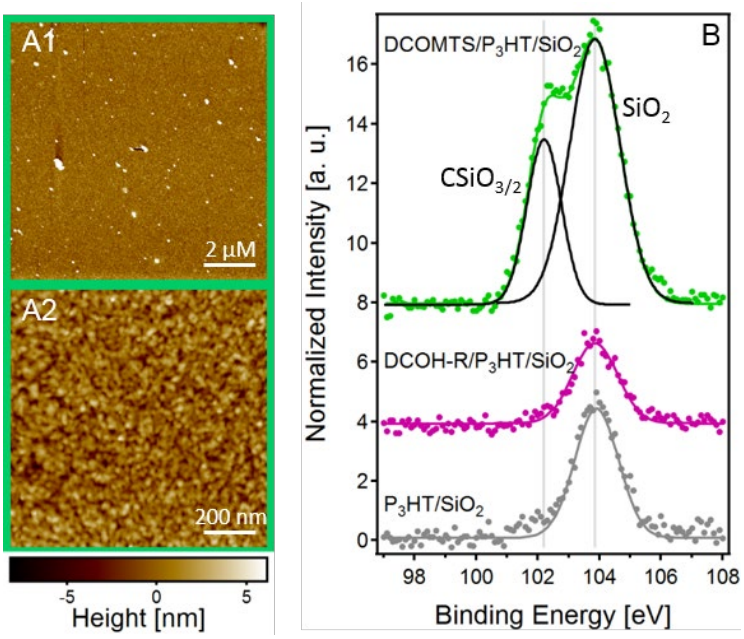

Figure 50 *(A1) AFM topographic image of DCOH (A2) AFM topographic image of DCOMTS (B) XPS measurements of P3HT (grey), DCOH (pink) and DCOMTS (green) in the eV range of Si2p3/2*

In all spectra, the peak observed at 103.9 eV is a reminiscence of the SiO_2 substrate below the P3HT layer (the change in intensity of this peak from one spectrum to another is attributed to the fact that the thickness of the P3HT layer varies a little from one sample to another). After head-groups reticulation, an additional peak appearing at 102.2 eV is in agreement with the grafting of MTS and confirming the head-groups reticulation of the lipids.

II.3.2. AFM force measurements

The effect of the two successive reticulations described above on the mechanical stability of the lipids monolayer supported on P3HT was investigated using indentation measurements by AFM[134]. The sample (or the tip) is moved forward and backward to the tip (or sample) in the z-direction. The strong interaction between the tip and the sample surface will cause the deflection of the cantilever. Thus, the deflection acquired along the cantilever displacement can be converted to a force. Further information is given in the *Exp.Tech. part VI.6.1.b*.

In this experiment, a normal force is exerted to the lipid layer through an AFM tip until the lipid layer ruptures (**Fig. 51, A**). The rupture forces obtained on non-reticulated layers formed on P3HT (DCOH), after the aliphatic chains reticulation (DCOH-R) and after head-groups reticulation (DCOMTS) are reported (**Fig. 51, B**). For each type of lipid layer, about 300 measurements were performed. The very low average rupture force of ~0.1 nN obtained with the DCOH layer increases with the reticulations to 0.6 nN for DCOH-R and up to 1.8 nN for DCOMTS showing a drastic benefit of reticulations. This is emphasized by a statistical analysis of the data that shows a significant difference between the three types of samples.

[134] (Florin, Moy, & Gaub, 1994)

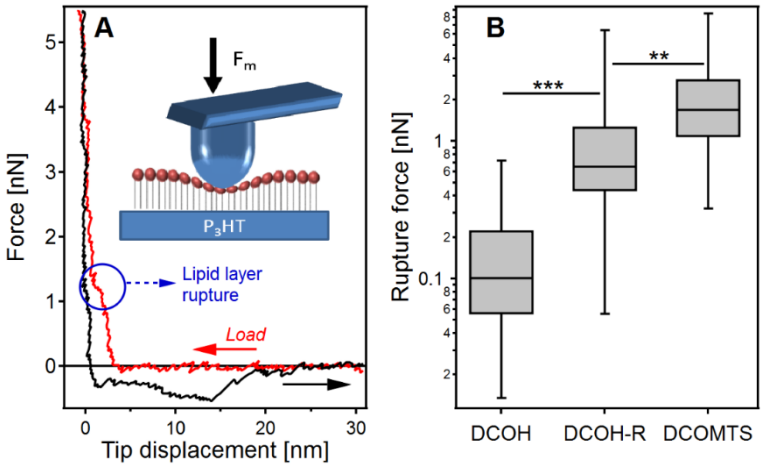

Figure 51 *(A) Experimental example of force vs tip displacement curve obtained on DCOH-R/P3HT force measurements (B) Comparison of the layer breakthrough force for DCOH/P3HT, DCOH-R/P3HT and DCOMTS/P3HT*

This improved stability is also marked by the fact that the double reticulated lipid on P3HT substrate can then be rinsed with solvents, dried and kept for several weeks without any evidence of damages.

II.4. Conclusion

In this chapter, we showed the formation and the characterization of the insulating gate based on lipids that will be used for the OFET sensor development. By using the homemade fluidic cell for in-situ ATR-FTIR measurements, we have been able to follow the formation of an interface based on the assembly of a 2.5 nm lipid monolayer and a P3HT semiconducting polymer. We showed that the lipids at first deposited on the very flat P3HT surface at 10°C, i.e. far below the gel/liquid phase transition temperature of the lipid, organize into a super-dense monolayer allowing an efficient reticulation of the diacetylene groups in the aliphatic chains and a stabilization of the layer. We showed that further reticulation at the head-groups using silanization increases, even more, the layer mechanical stability. The final layer has a striking high density of ~2.6 x 10^{14} lipids/cm², i.e. corresponding to a molecular area of 38.5 Å², in which the lipids are tilted by an angle of 26° with respect to the surface normal. We believe that such high packing of the lipids is favored by their interaction with the aliphatic chains of P3HT which may control the lipid distribution. We believe that this interface is very promising for further integration into electronic devices such as field-effect transistors.

III. CHAPTER : Synthesis and characterizations of a specific Cesium calix[4]arene-based probe

The seminal importance of detecting ions and molecules for point-of-care tests has driven the research for more sensitive, specific, and robust sensors. The sensor specificity comes mostly from the design and synthesis of effective complexing agents (chelator) for the sensing of the targeted analyte. Furthermore, the selected chelator must present intrinsic characteristics that allow it to be efficiently used in sensing devices. Those include among others (*i*) easy of synthesis, (*ii*) low cost, (*iii*) easy chemical functionalization, (*iv*) chemical stability, (*v*) high specificity toward the targeted analyte, (*vi*) easy read-out of the specific probe-analyte interaction.

Thus, during the last decades, cesium sensing has led to the development of a variety of materials including molecular probes, absorbent materials (inorganic, polymers), organic/inorganic composites, carbon nanomaterials, semiconductors and so on, based on various sensing techniques and principles. Sensing properties are strongly affected both by the specific surface area and nature of the interaction between the analyte and the sensing materials. As a prologue of this chapter a literature survey will give a brief and concise overview of the main materials that have been used for either the detection or selective separation of cesium.

Selective separation and extraction of cesium (radioactive or not), or even for other ions, can be viewed as the first step before analysis or diagnostic by specific analytical equipment such as mass spectrometry (MS), gamma spectrometry, spectrophotometry, atomic absorption spectroscopy (AAS) and so on. Although known to be accurate techniques, these methods are somewhat tricky as usually require expensive and sophisticated instrumentation, expert manpower and are time-consuming. In addition, they oftenly need a pre-concentration or a filtering step acting as a drag in real-time detection or systematic analysis at the point-of-need. However, they continue to arouse some interest notably in the case of differentiation of radioactive from the non-radioactive species.

In this context, Elahi *et al.* have recently developed an original method based on an engineered proteoliposome for the cesium extraction (**Figure 52**).[135]

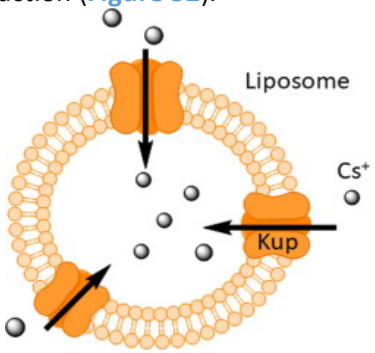

Figure 52 *Engineered proteoliposome for the selective extraction of Cs^+ (Ref. 135)*

The proteoliposome is composed of a vesicle in which a membrane protein, namely Kup (membrane-bound potassium uptake), extracted from *Escherichia Coli* strain was inserted. Placed in an aqueous solution containing Cs^+ (10-100 mg/l), the proteoliposome can uptake the free cesium inside the vesicle. Subsequent ultracentrifugation allows recovering the charged proteoliposomes that are analyzed by inductively coupled plasma mass spectrometry (ICP-MS). Gradual increases of the proteoliposome concentration (*i.e* 0.015-1.2 mg of Kup protein) in a 100 mg/l cesium solution results in a linear removal by 0.29-12.7%.

Besides, porous materials like zeolites (such as Chabazite, Mordenite) have been envisioned as effective cesium absorbent materials. Those materials can be used either as materials in ion-exchange

[135] (Hakim Elahi, Abbaszadegan, & Conroy-Ben, 2019)

chromatographies or in selective membranes.[136,137] To this aim, Miyake *et al.* have recently demonstrated the effectiveness of the zeolite RHO, as pristine, (Figure 53) for the removal of cesium in water and artificial seawater. [138] From this zeolite RHO containing a low Si/Al ratio they have succeed in removing 60% of cesium from seawater successfully determined by atomic absorption spectroscopy.

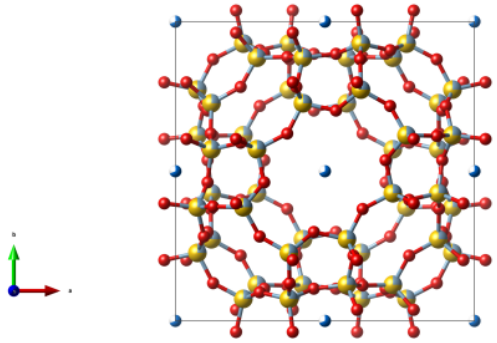

Figure 53 *Structure of the zeolite RHO (Ref. 138)*

In the line of this direction, metal organic frameworks (MOFs) have been also used as an active components in absorbent composite-based materials. MOFs are organic/inorganic hybrid materials possessing similarities to zeolites related notably to the porosity. The latter can be easily tuned by tailoring the organic part allowing the possibility to adjust the cavity size to the analyte. Recently Cheng and co-workers have fabricated a self-assembled membrane consisting of 2D-MOF and graphene oxide (GO) for cesium extraction from aqueous solutions (Figure 54).[139] Thanks to the properties of the composite the authors have demonstrated that the membrane can efficiently extract 88% of the cesium from the aqueous solutions by absorption.

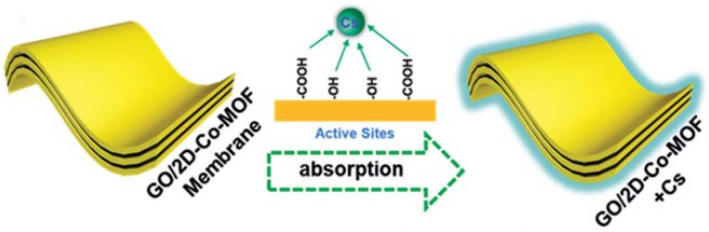

Figure 54 *Absorbent composite-based materials made from GO and a MOF (Ref. 139)*

Among other materials, polymeric organic structures have been shown to be useful for such purpose. They present several advantages compared to their inorganic counterpart in which for instance the sensed ions can replace others in the inorganic scaffold hence releasing other substances in the medium. Recently an example developed by Yu and co-workers based on a hydrogel demonstrated a synergistic effect of the hydrogel structure and the embedded chelator leading to efficient extraction of 60% of cesium from aqueous solutions. [140] The hydrogel backbone is composed of polyacrylic acid (AAc) and acrylamide functionalized with benzo-18-crown-6-ether used as a sensing element (poly(AAc-co-B18C6Am)). Carboxylate groups play the role of the electrostatic trap while the benzo-18-crown-6-ether entrap and stabilize the cesium by forming a 2:1 sandwiched complex (Figure 55).

[136] (Song, Lee, Moon, & Lee, 1997)
[137] (Miura, Yamagishi, & Akiba, 1989)
[138] (Miyake, Miyake, & Sano, 2019)
[139] (Cheng, Liang, Dong, Chai, Zhao, Ullah, Wang, Zhang, Imtiaz, Shan, Zheng, 2018)
[140] (Yu, Hu, Liu, Ju, Xie, Wang, Chu, 2017)

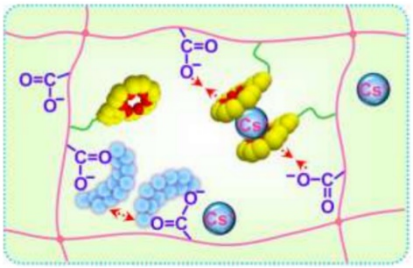

Figure 55 *Hydrogel as selective cesium membrane (Ref. 140)*

Molecular probes are certainly the most representative and developed class of chelators used in ions sensing. They are easy to synthesize and customize in order to tailor the recognition properties to the targeted analyte. Furthermore, they can be pre- or post-functionalized facilitating their implementation and integration on various substrates and devices. In molecular probes, there is two level of recognition taking into account both the shape (form, geometry, etc.) and the chemical interaction (hydrogen bonds, electrostatic, π-π interactions, etc.) and a synergistic effect is commonly found. Thus, the specific molecular design usually considers these levels of recognition to ensure the highest constant of affinity.

An elegant molecular tweezer has been recently designed and synthesized by Kasprzak *et al.* based on the sumanene scaffold (**Figure 56**).[141] The bowl shape of the sumanene is used to form a stable sandwiched complex (intramolecularly or intermolecularly) with the cesium and in which the ion is retained by π -cation interactions. High-affinity constant was found (10^4 - 10^5 M^{-1}, Stern-Volmer method) associated with low limit of detection (1.8 - 7.0 × 10^{-5} M) for this complex. In addition, oxidation of the molecular scaffold can be used to release the entrapped ion ensuring perfect reversibility of the probe.

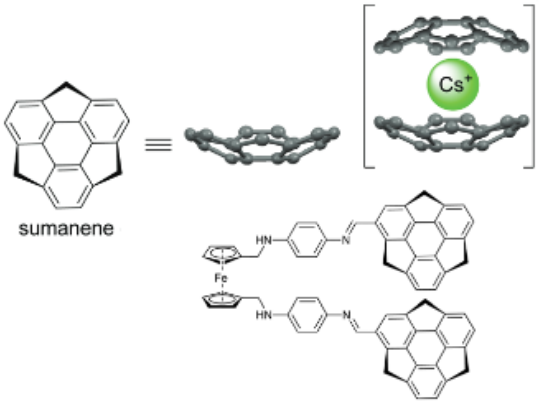

Figure 56 *Sumanene-based probe of cesium (Ref. 141)*

Preorganized or constrained molecules exhibiting cavities are also of great interest in molecular chelators as they can be viewed as a unique pore found in mesoporous materials such as zeolite or MOF-like materials. Thus, chemists have striven to develop molecular structures in which a cavity can be formed. Several known scaffolds can be used for this purpose including cyclophanes, calixarenes, pillararenes, curcubiturils for instance and so on.

[141] (Kasprzak & Sakurai, 2019)

In 2017, Makrlik *et al.* have used a [2,2,2]-paracyclophane[142] to entrap specifically the cesium as its cavity fit perfectly with the ion size (**Figure 57**). The elucidation and characterization of the formed complex were done spectroscopically (fluorescence) and by mass spectrometry (ESI-MS).

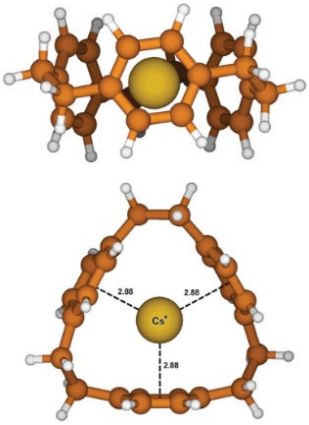

Figure 57 *A [2,2,2]-paracyclophane used as cesium chelator (Ref. 142)*

Host-guest inclusion complexes based on fluorescent cucurbituril derivatives have been recently developed by *Deng et al.* for the detection cesium.[143] The detection of the cations is associated to a quenching of the fluorescence by displacement of the dye (DSMI, 4-[4-(dimethylamino)styryl]-1-pyridinium iodide) out of the cucurbituril cavity by the analyte (**Figure 58**). The experimental results revealed that the probe responded to Cs^+ cations in alkali metal systems via fluorescence quenching with a $K_a = 0.63 \times 10^5\ M^{-1}$ and a low limit of detection of 8.24×10^{-7} M.

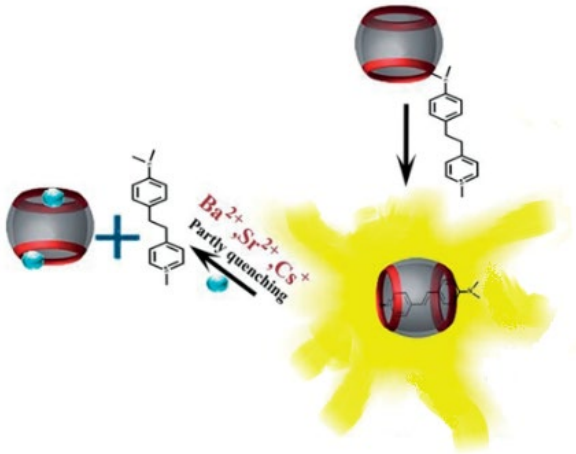

Figure 58 *A cucurbit[6]uril used as cesium chelator (Ref. 143)*

Aforementioned in Chapter 1 and *Figure 58*, fluorescence constitutes a widely used method in chemosensors. A myriad of fluorophores has been designed and synthesized for the detection of various analytes. Recently, Jung *et al.* have synthesized a bis-(trihydroxyphenyl)-based fluorescent ligand (**Figure 59**) which is able to detect specifically Cs^+ among other cations. [144]. The recognition of cesium in aqueous leads to a modification of the structure morphology as in water the ligand forms non-fluorescent nanofibers that turn into fluorescent spherical structure upon the addition of cesium.

[142] (Makrlik, Sykora, Bohm, & Vanura, 2017)
[143] (Deng, Chen, Chen, Lue, & Tao, 2019)
[144] (Jung, Hyun, et al. 2015)

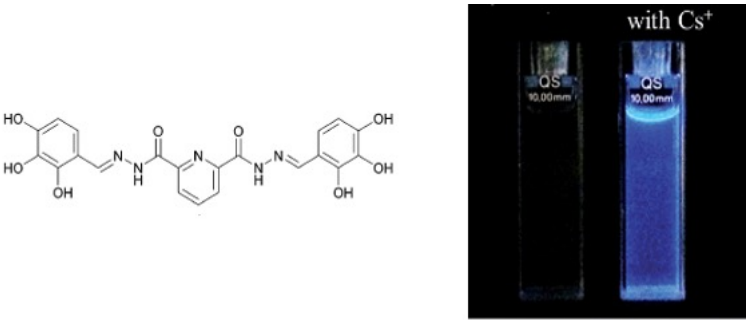

Figure 59 *Bis(trihydroxyphenyl)-fluorescent ligand used as cesium chelator (Ref. 144)*

Another turn-on fluorescence chemosensor (named Cesium Green) has been developed by Akamatsu *et al.* for cesium detection.[145] The optical process is based on a Förster resonance energy transfer between the terphenyl moiety (donor) and the nitrophenyl part (acceptor) rendered possible when the cesium is recognized by the ethylene glycol linker (**Figure 60**). Upon complexation, the donor and acceptor moieties are brought close each to other favoring the charge transfer. Interestingly cesium green has been efficiently used in the plant for cellular imaging.

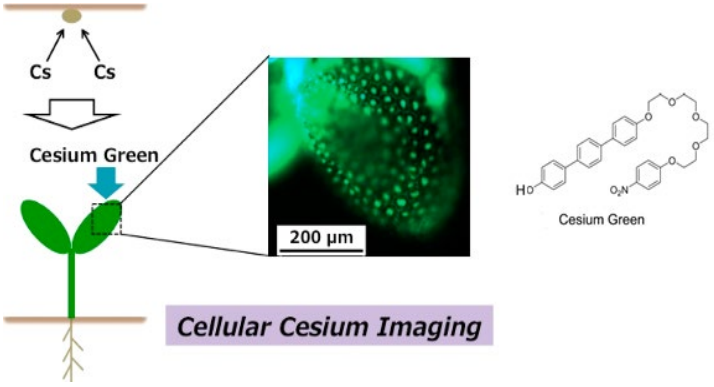

Figure 60 *Green cesium fluorophore for Cs+ sensing in plant (Ref. 145)*

It is known that biological molecules or units can specifically bind cations due to their importance in many physiological, biological events or processes. Thus, such structures can be used for the development of sensing devices. Luo *et al.* have been shown that ribose-protected thioguanosine (**Figure 61**) can interact more specifically with cesium compared to alkali metal (Na^+, K^+ and Rb^+) and alkaline earth metal ions (Mg^{2+}, Ca^{2+}, Sr^{2+} and Ba^{2+}).[146] NMR measurements conducted in CD_3CN have been performed in order to follow the observed specificity.

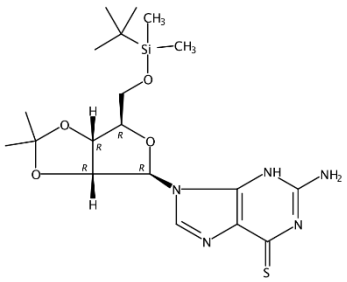

Figure 61 *Ribose-protected thioguanosine as biological unit for specific Cs^+ sensing (Ref. 146)*

[145] (Akamatsu, Komatsu, Mori, Adams, Shin, Sakai, Abe, Hill, Ariga, 2014)
[146] (Luo, Tang, & Wu, 2008)

Among other important biological structure, one can cite the DNA which is a negatively charged entity and can bind cations. In this context, Lin *et al.* have designed and synthesized a G-pentaplex incorporating iso-guanine units (DNA1, 5'-T(iG)4T-3', where iG = isoguanine) existing as single DNA strand and capable to interact with cesium. Upon addition of cesium the G-pentaplex leads to a supramolecular structure which is can be visualized by the fluorescence of Ir(III) after complexation with the G-pentaplex superstructure (**Figure 62**).[147]

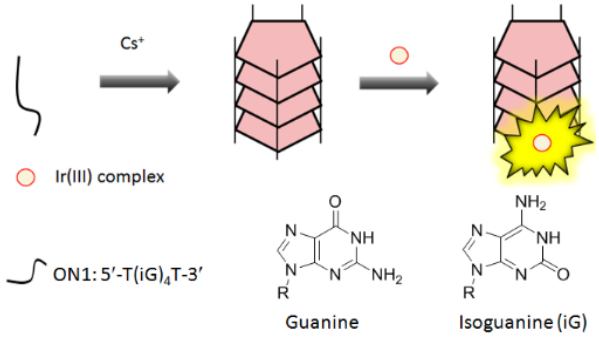

Figure 62 *G-pentaplex for specific Cs+ sensing (Ref. 147)*

Ether-crowns are another sub-class of molecules that have high binding ability with cesium ions. Cesium-133 nuclear magnetic resonance spectroscopy was used as a sensitive probe to investigate the stoichiometry and stability of Cs^+ ion complexes with aza-18-crown-6 (A18C6), diaza-18-crown-6 (DA18C6) and dibenzylediaza-18-crown-6(DBzDA18C6) (**Figure 63**) in different binary acetonitrile–nitromethane mixtures[148].

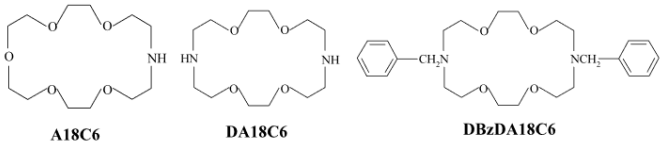

Figure 63 *Structure of the different ether-crown Cs+ chelator studied by 133Cs NMR (Ref. 148)*

The crown-ether structures were successfully used in the radiocesium removal from wastewater[149]. The ether crown cesium complexing structure was also been implemented in calix[n]arene.

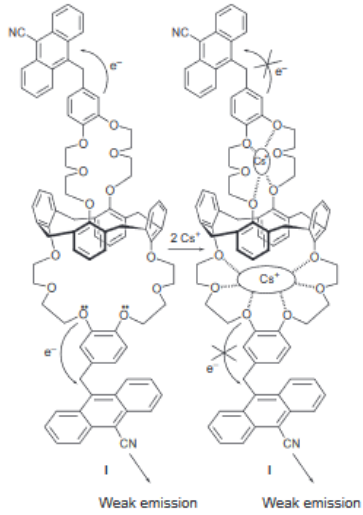

Figure 64 *Structure of Cs+ selective bis-calix[4]arene (Ref.150)*

[147] (Lin, Yang, Mao, He, Wang, Leung, Ma, 2016)
[148] (Shamsipur, Gilani, & Rofouei, 2011)
[149] (Rabiul Awuala, Yaita, Taguchi, Shiwaku, Suzuki, Okamoto, 2014)

1,3-Calix[4]bis(9-cyano-10-anthrylmethyl)-o-benzocrown-6 has been synthesized by Ji *et al.*(**Figure 64**) as a first-generation cesium selective fluorescent probe, and its emission behavior in the presence of Li_+, Na_+, K_+ and Cs_+ ions has been examined[150].

III.1. Calix[n]arene based probe

Among the presented molecular structures, the cesium is immobilized by either a cation-π interaction or chelating coordinate bonds in a well-defined cavity. Thus, to be very selective toward cesium, the designed probe must bear at least one of these functions. Moreover, an anchor function might be possible to add in order to graft it on the lipids monolayer surface.

A mentioned class of molecules appears to be perfect for the desired cesium probe: the calix[n]arenes. The interest for this class of solid-state molecular materials is based on their multiple potential applications, resulting from structure/properties relationships, in catalysis, separation and storage for example and from the collective physical properties that some of these solids may exhibit: electronic, optic, magnetism, conduction, etc[151,152]. The key to success lies in the design of molecular building blocks that display the appropriate geometry, structure, chemical and physical properties, like organo-metallic systems, as well as in the control of the molecular self-assembly. The exploiting of calix[n]arenes (especially, calix[4]arenes is favoured by their particular ability to adopt different conformations (cone, partial cone, 1,2-Alternate and 1,3-Alternate), by the possibility of anchoring up to eight or more coordinating sites by functionalization of the lower and/or upper rims and also by varying the nature of the connecting groups between the phenolic units (–CH_2– or –S bridges). During the last decades, a huge variety of architectures using the calixarene backbone have been provided for the creation of new supramolecular systems, based on the principles of molecular recognition and host–guest chemistry[153, 154, 155, 156]. As already explained, extended structures containing calix[4] arenes have started to attract attention, because of their huge versatility. Among the four possible conformers, the one blocked in the 1,3-Alternate conformation, bearing peripheral binding sites, is of particular interest for the formation of extended coordination networks.

Therefore, 1,3-alternate calix[4]arenes based scaffolds topped with a crown ether have paid our interest due to their well-defined structures exhibiting a cavity that fits perfectly with the cesium ionic radius[157,158,159]. Additionally they are easily functionalizable with fluorophores such as naphthalene or anthracene[160] indanone[161] or coumarin[162,163] providing additional benefits in the optical properties modulation.

[150] (Ji, Brown, & Dabestani, 1999)
[151] (Blake, Champness, Hubberstey, Li, Withersby, Schröder, 1999)
[152] (Long & Yaghi, 2009)
[153] (Shinkai, 1993)
[154] (Gutsche, 1998)
[155] (Asfari, Böhmer, Harrowfield, & Vicens, 2001)
[156] (Neri, Sessler, & Wang, 2016)
[157] (Ungaro, Casnati, Ugozzoli, Pochini, Dozol, Hill, Rouquette, 1994)
[158] (Lamare, Dozol, Fuangswasdi, Arnaud-Neu, Thuéry, Nierlich, Asfari, Vicens, 1999)
[159] (Kim, Vargas-Zunica, Hay, Young, Delmau, Masselin, Lee, Kim, Lynch, Moyer, Sessler, 2012)
[160] (Roper, Talanov, Gorbunova, Bartsch, & Talanova, 2007)
[161] (Yeon, Leem, Wagen, Lynch, Kim, Sessler, 2016)
[162] (Kumar, Pham-Xuan, Depauw, Hemadi, Ha-Duong, Lefevre, Ha-Thi, Leray, 2017)
[163] (Pham-Xuan, Jonusauskaite, Depauw, Kumar, Lefevre, Perrier, Ha-Thi, Leray, 2018)

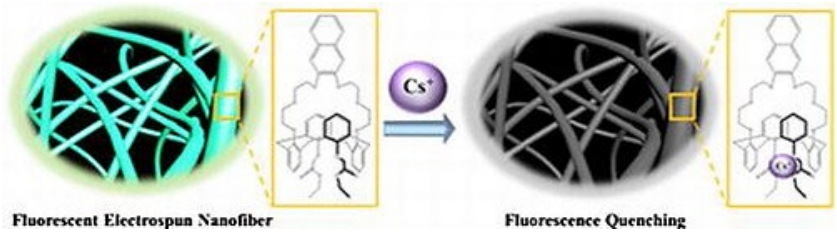

Figure 65 *Nanofibrous embedded with fluorescent sensible calix[4]arene cesium probe (Ref. 164)*

Calix[n]arene can also be implemented in functional devices. A few examples are reported in the literature. The fluorescence properties of calix[4]arene based probe upon the addition of various metal ions were investigated by fluorescence spectroscopy (**Figure 65**). As a result, Jung *et al.* have revealed that the synthesized calix[4]arene based probe displayed dramatic quenching effect upon the exposure to Cs^+. Afterward, the probe was embedded in electrospun nanofibrous film as a cesium adsorbent. The calix[4]arene embedded nanofibrous proved to adsorb cesium effectively from an aqueous solution, indicating that it would be usefully utilized as an adsorbent to remove Cs^+[164]. A highly selective membrane electrode based on p-isopropylcalix-[6]arene for accurate determination of trace amounts of cesium cations was reported[165]. The membrane was constituted of the cesium ionophore (**Figure 66**), PVC, dioctyl phthalate as a plasticizer and potassium tetrakis(4-chlorophenyl)borate as an ionic additive. The value of 10^{-6} M was obtained as a lower detection limit for the fabricated cesium-selective electrode.

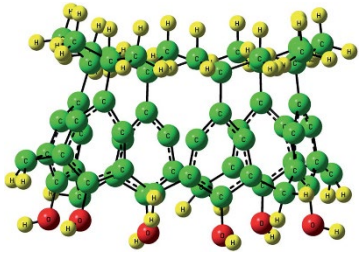

Figure 66 *Cesium ionophore based on p-isopropylcalix[6]arene (Ref. 165)*

Besides these applications, a sensor concept based on an ion-selective SAM modified micro cantilever which can detect cesium ion concentration in the range of 10^{-11}-10^{-7} M was reported[166,167]. This sensor concept is based on chemical modifying micro cantilevers with ion-selective SAMs.

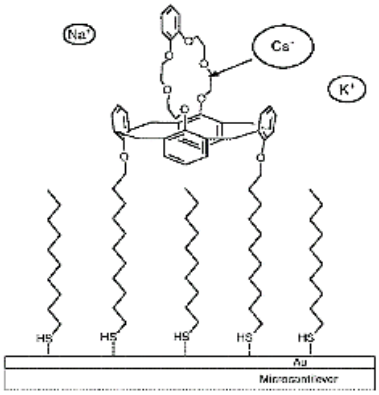

Figure 67 *Cesium sensor based on SAM and calix[4]arene (Ref.166)*

[164] (Jung, Park, Choi, Kim, & Jung, 2017)
[165] (Ahmadzadeh, Rezayi, Kassim, & Aghasi, 2015)
[166] (Ji, Finot, Dabestani, Thundat, Brown, Britt, 2000)
[167] (Thundat, Finot, Ji, Dabestani, Britt, Bonnesen, Brown, Warmack, 1999)

Micro cantilevers undergo bending due to a differential surface stress caused by the forces involved in the adsorption process. Chemical modification of the cantilevers was achieved by a SAM consisting of 1,3-alternate calix[4]-crown-6 (receptor) and two alkyl thiol side chains (Figure 67).

The obvious cesium selective properties of the calix[4]arene and it is possible integration in solid material leads us to be focused on the similar structures for the synthesis of the cesium probe applied in lipids coated organic transistors. In this sub-part, we will present hereby the synthesis and characterization of an 1,3-alternate calix[4]arenes based host molecule for cesium cation guest.

III.1.1. Synthesis

The synthesis of the target chelator **6** is outlined in Scheme 1.Compound **6** was readily obtained from the cross-coupling of the ditosylate **5** and the calix[4]arene **2**[168,169] in CH_3CN at 80°C in presence of Cs_2CO_3 in 61% yield[170]. The ditosylate **5** was prepared according to reported literature procedures[171,172] from commercially available catechol **3**, which first was alkylated with 2-(2 chloroethoxy)-ethanol in the presence of K_2CO_3 in DMF to form a diol intermediate **4** in 47% yield. The latter was subsequently treated with p-toluenesulfonyl chloride in pyridine affording the ditosylate **5** in 62% yield.[173,174].

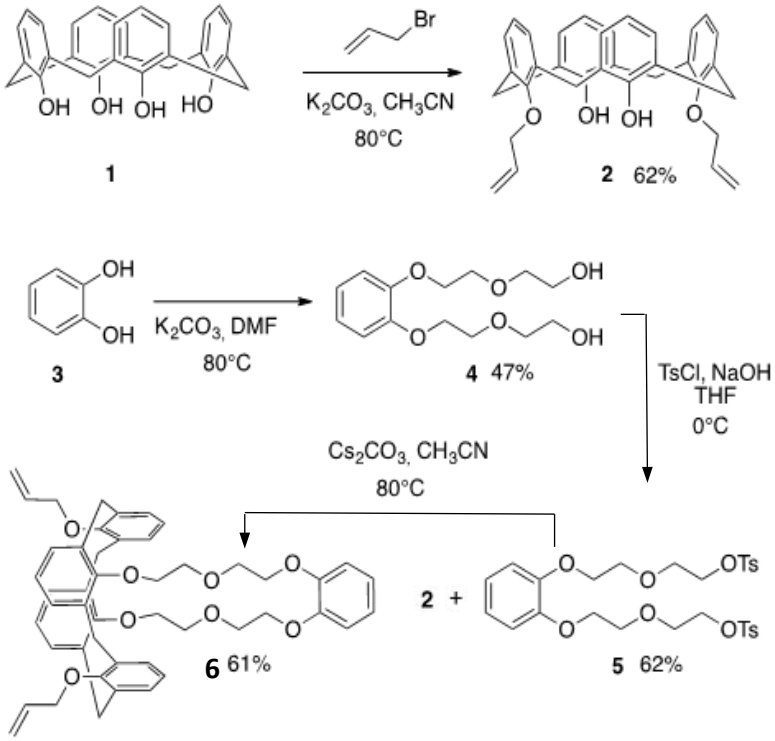

Scheme 1 *Chemical reaction pathway to synthesis the cesium probe*

III.1.2. Characterization

[168] (Kim, Cho, Yu, Pang, Kim, Suh, Oh, Ra, Cho, 1997)
[169] (Kim, Yu, Pang, Kim, Lee, Lee, Oh, 1998)
[170] (Ji, Dabestani, Brown, & Hettich, 2001)
[171] (Wright, Melandri, Cannizzo, Wakselman, & Mazaleyrat, 2002)
[172] (Deutman, Smits, de Gelder, Elemans, Nolte, Rowan, 2014)
[173] (Weber, 1983)
[174] (Surowiec, Custelcean, Surowiec, & Bartsch, 2009)

Obtained cesium chelator **6** was then characterized by classical analytical chemistry method (NMR ^{1}H & ^{13}C, HRMS, elementary analysis and RX crystal analysis).

III.1.2.a. Chemical characterization

^{1}H NMR, ^{13}C NMR, HRMS and the elemental analysis are confirming the molecular formula $C_{48}H_{50}O_8$ of the synthesized compound **6**. Please refer to *Annexe VII.1* and *VII.3* for further details.

III.1.2.b. Structural characterization by XRD

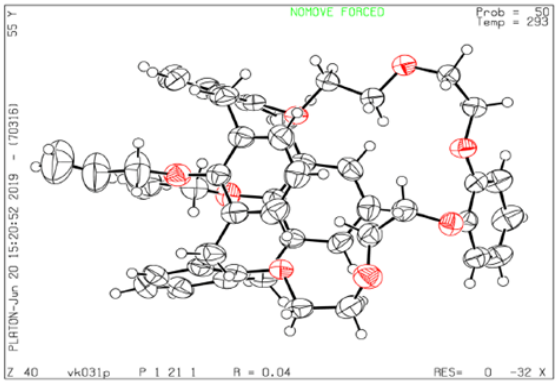

Figure 68 *Crystallographic structure of **6** obtained by X-ray diffraction*

Colorless crystals of **6** were obtained by slow diffusion of a CH_2Cl_2 solution into MeOH solvent. X-Ray diffraction of the crystal **6** was then performed. The crystallographic observations obtained from X-ray structure of **6** *(Fig. 68)* is showing a monoclinic space group P21 with a = 11.3911 (2) Å, b = 10.4981 (2) Å, c = 17.4878 (3) Å, $\alpha = 90°$, $\beta = 106.375\ (2)°$, $\gamma = 90°$ at 293 K, with Z=2 and V= 2006.45 $Å^3$ *(Annexe VI.4)*. Further examination of the cavity size from the X-ray structure revealed that the measured distances Cs^+-O (3.31Å) and Cs^+-Ar_{calix} (3.44 Å) are in accordance with similar reported systems indicating that the cavity of **6** is more suitable for the Cs^+ compared to the other cations. [175]

III.2. Specificity toward cations

Table 4 *ASTM D665 seawater standard composition*

Ion	Concentration (g/L)
NaCl	24.54
$MgCl_2 . 6H_2O$	11.10
Na_2SO_4	4.09
$CaCl_2 . 2H_2O$	1.54
KCl	0.69
$NaHCO_3$	0.20
KBr	0.10
H_3BO_3	0.03
$SrCl_2.6H_2O$	0.04
NaF	0.003

[175] (Sessler, Kim, Gross, Lee, Kim, Lynch, 2008)

As the detection will be performed in seawater, the synthesized probe must have the highest selectivity toward the cesium ion. In fact, the seawater is composed of many cations and anions (*Table 4*). In this section, the selectivity of the designed chelator **6** will be checked and tested. The affinity constant, stoichiometric parameter and competition between ions will be studied both by UV-visible spectroscopy and ^{1}H NMR.

III.2.1. UV-vis optical observation with potential competitive cations

The absorption properties of the chelator **6** have been investigated in a solvent mixture MeOH: DCM (v/v, 1:1). The UV-visible absorption spectrum of the receptor **6** presents several absorption bands in the region 240-300 nm ascribed to the absorption of the benzene rings of both the calix[4]arene scaffold and the benzocrown ether. The cation binding properties of the chelator **6** were screened by UV-visible spectroscopy with 1 equivalent of several putative competitive monovalent cations (Li^+, Na^+, K^+, Rb^+, Cs^+) and also with a divalent cation (Mg^{2+}) (**Figure 69**).

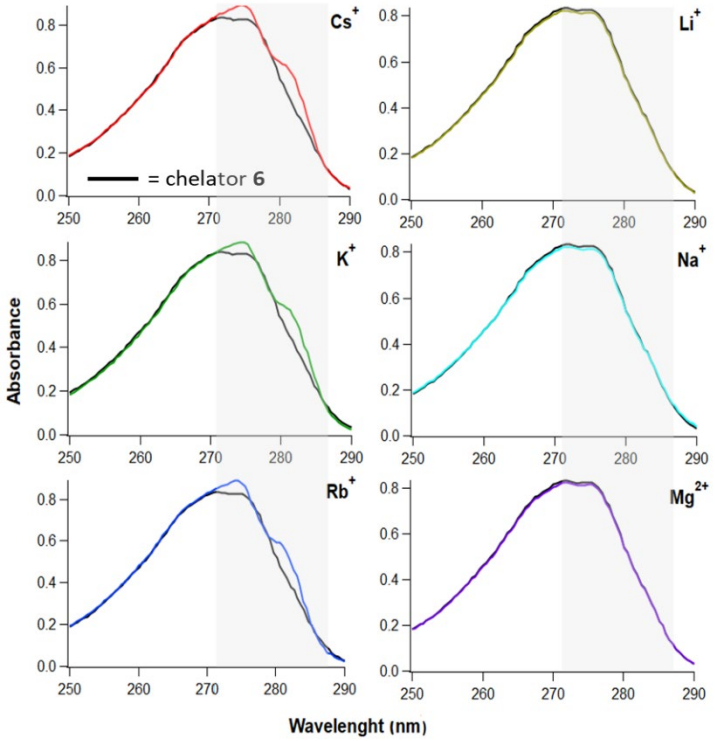

Figure 69 *Optical properties of the receptor **6** after addition of 1 equiv of Li^+(yellow), Na^+(turquoise), K^+(green), Rb^+(blue), Cs^+(red) and Mg^{2+}(purple) cations*

The greater optical changes were observed for Cs^+, K^+ and Rb^+ while for the other cations (Na^+, Li^+ and Mg^{2+}) much smaller variations are observed as the spectra remain almost unchanged. Upon addition of Cs^+, K^+ or Rb^+ an enhancement of the absorption bands centered at 275 nm and 281 nm was observed, highlighting the formation of the 6.X^+ complexes. It was anticipated that the presence of the benzene ring in the crown ether part could impart a reduction of the flexibility of the cavity preventing the complexation of smaller cations such as Na^+, Li^+ and Mg^{2+}. Indeed, the ionic radius of Cs^+, K^+ or Rb^+ in 6 coordinated structure are respectively 1.67 Å, 1.38 Å and 1.52 Å whereas for Na^+ and Li^+ it is respectively 0.76 Å and 1.02 Å[176]. The resulting structure of **6** showed that the distance Cs^+-O (3.31Å) and Cs^+-Ar_{calix} (3.44 Å) of the ether crown cavity characterize well the cation-π interaction for the Cs^+, K^+ and Rb^+ cations.

[176] (Database of Ionic Radii, Imperial College of London, s.d.)

Based on these results further studies will be conducted only on the most competitive cations: Cs^+, Rb^+ and K^+.

III.2.2. Affinity concerning the targeted and the competitive cations

III.2.2.a. Fitting method

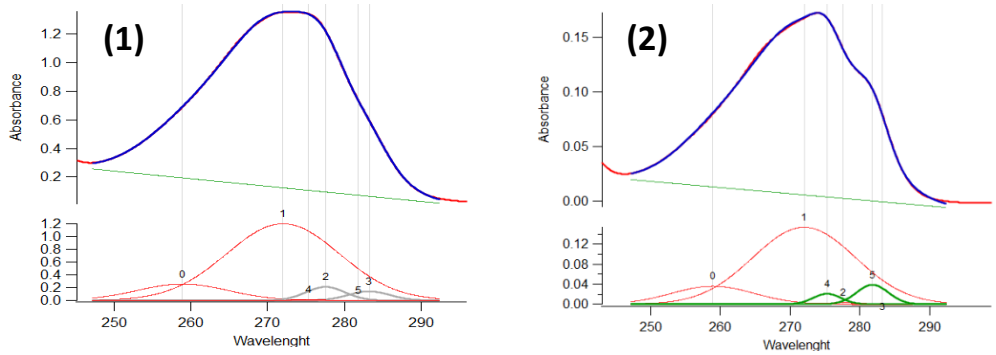

Figure 70 *Fitting method with 6 gaussians peaks of the UV spectra of (1) chelator alone (2) and chelator with addition of competitive cations. Peaks 2&3 are shifted to peaks 4&5 after complexation of the chelator with a competitive cation (Cs^+, Rb^+ or K^+)*

Although it is easy to differentiate between the ions interacting with the crown ether from those that cannot, due to the emergence of new peaks on the absorption spectra, it appears less obvious for Cs^+, K^+ and Rb^+ because they displayed similar behaviors. Thus, in order to have a more pronounced difference between these three cations, giving a positive signal, it is necessary to apply a fitting mathematical function taking into account the spectral modifications. All the spectra were fitted using a set of 6 Gaussians after removal of the background (**Figure 70**). The width of all the peaks and the position of the peaks 0 & 1 (at 258.23 and 271.29 nm) are kept fixed. The variation occurred on the position and absorbance intensity of the peaks 2, 3, 4, 5 after the addition of the competitive cations in a chelator solution (**Table 5**).

Table 5 *The position of the peaks after fitting was reported here. In red, the peaks are fixed. The position of the peaks in grey are shifted to the position of the peaks in green.*

Peaks	Peaks position chelator 6	Peaks position 6.Cs+	Peaks position 6.K+	Peaks position 6.Rb+
0	258.23	258.23	258.23	258.23
1	271.29	271.29	271.29	271.29
2	277.54	n/a	n/a	n/a
3	283.23	n/a	n/a	n/a
4	n/a	275.39	275.39	275.39
5	n/a	281.35	281.06	281.13

These peaks are therefore directly related to the complexation phenomenon. For the example of Cs^+ addition, it was observed that the peaks 2 and 3 at respectively 277.54 nm and 283.23 nm are shifted to lower wavelength (peaks 4 and 5 at respectively 275.39 nm and 281.35 nm). The small variation of the position related to the type of cation cannot be exploited due to the resolution limit of the spectrometer. By taking into consideration the absorbance of the peak appearing after complexation at around 281 nm, it is possible to obtain the affinity constant between the chelator and the competitive cation and furthermore, it is stoichiometric parameter toward the guest cation.

III.2.2.b. Cs^+, K^+, and Rb^+ affinity constant K_a determination

Absorption signal related to the complexation is required to calculate the affinity constant. The measurements were done as follows : 30 µL of 40 mM chelator **6** was diluted in 2940 µL of (DCM:MeOH) mixture. The concentration of the chelator was kept stable while [X^+] was added up to 1.5 equiv. of chelator **6**. For instance, upon the gradual addition of the [X^+] cation the variations of the absorption properties of **6** are associated with hyperchromic (at 275 nm and 281 nm) and hypsochromic effects respectively (shift from 277 to 275 nm and from 283 to 281 nm) (**Figure 71**). These optical changes and the appearance of isobestic points attest undoubtedly of the ability of **6** to bind these cations.

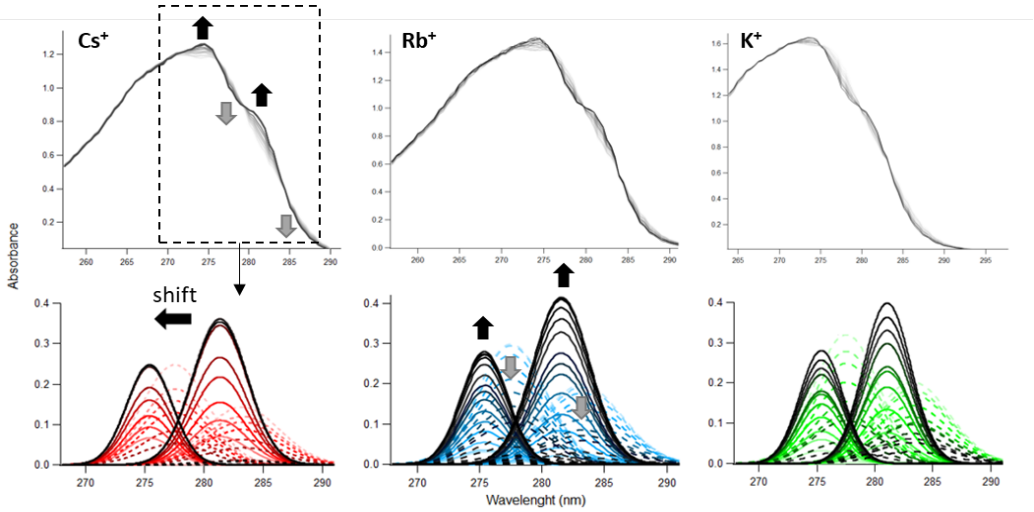

Figure 71 *UV spectra of the chelator **6** with gradually increased concentration of different competitive ions (Cs^+, Rb^+, K^+). Gaussian fit was applied (Figures at the bottom) to highlight the difference occurred after cationic complexation.*

The complexation of the chelator **6** with a competitive cation X^+ (Cs^+, K^+ or Rb^+) lead to the formation of a binary complex as stated below (**eq. 9**).

$$Chelator\ \mathbf{6} + X^+ \underset{K_a\ or\ K_d}{\Longleftrightarrow} Complex\ \mathbf{6}.X^+ \qquad \textbf{eq. 9}$$

The association constant K_a between the chelator **6** and the studied cation $X^+$was calculated by using the Benesi-Hildebrand[177,178] equation (**eq. 10**) from the UV-vis spectroscopic data.

$$\frac{1}{A_{obs} - A_0} = \frac{1}{\{K_a(A_{max} - A_0)[X^+]\}} + \frac{1}{A_{max} - A_0} \qquad \textbf{eq. 10}$$

where A_0 is the absorbance of the signal related to the complex **6**.X^+ (at 281 nm) without X^+, A_{obs} the absorbance of the mentioned signal with x concentration of X^+ and A_{max} the absorbance of the mentioned signal with a saturated concentration of X^+. The association constant (K_a) for each cation could be then obtained from the slope of the straight line of the plot of ($A_{max} - A_0$) / ($A_{obs} - A_0$) against 1 / [X^+]. Results evidence that **6** presents the higher selectivity toward Cs^+ with a K_a = 6.024 x 10^3 M^{-1} which is three or two-fold magnitude higher than the ones of K^+ (2.825 x 10^3 M^{-1}) and Rb^+ (2.288 x 10^3

[177] (Benesi & Hildebrand, 1949)
[178] (Ravikumar & Ghosh, 2011)

M^{-1}), respectively. On the basis of these results an approximate Hofmeister series can be settled, which follows approximately the radius of each cation: $Cs^+ > Rb^+ > K^+ > Na^+ > Li^+ \approx Mg^{2+}$ (Figure 72)[179,180].

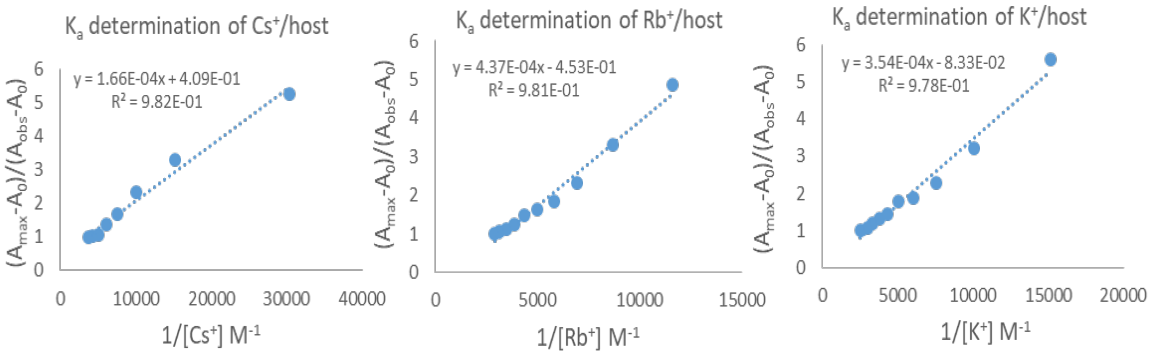

Figure 72 *Affinity constant determination by using Benesi-Hildebrand equation*

III.2.2.c. Stoichiometric parameter of the chelator

Job's plots[181,182] were performed in a solvent mixture of MeOH:DCM with different proportions of chelator/cation (Table 6) to obtain the host/guest ratio. The absorbance spectra of each solution is then obtained in the wavelength range of 240-320 nm. By using mathematical fitting as described in the last part, the signal corresponding to the complexation at 281 nm is extracted. The absorbance versus the molar fraction of each guest (here Cs^+, Rb^+ and K^+ cations) is plotted (Fig. 73).

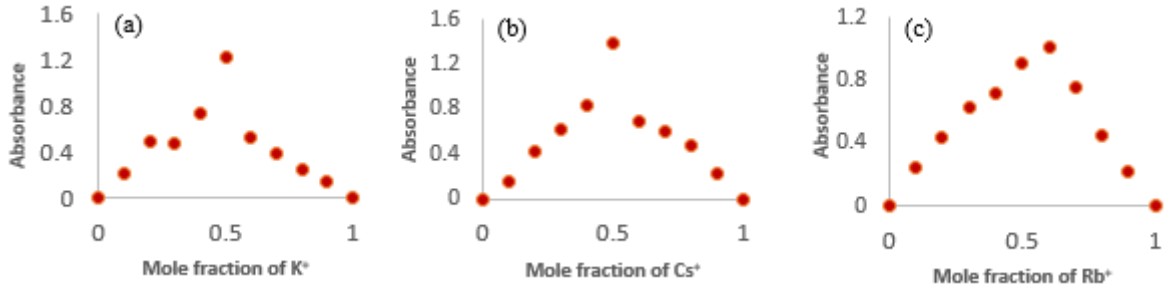

Figure 73 *Job's plot of the chelator **6** with different cations (a) K^+ (b) Cs^+ and (c) Rb^+*

The results are clearly indicating, for the studied cations, a maximum absorption at 0.5 molar fraction. The formation of a [1+1] complex **6**.X+ is confirmed for each cation and is fully in agreement with the results reported on similar scaffolds[157-159]. Moreover, it is important to notice that even in a competitive polar solvent such as MeOH we observed for the cationic guest of interest, Cs^+, some interactions with **6** allowing its detection. Furthermore, the minor optical changes upon the addition of the cationic guests constitute proof that the host-guest interaction occurs predominantly in the crown ether part.

[179] (Hofmeister, 1888)
[180] (Lo Nostro & Ninham, 2012)
[181] (Yoe & Jones, 1944)
[182] (Job, 1971)

Table 6 *Prepared solutions of Job's plot analysis. All volumes are indicated in µL and comes from 40 mM of stock solution for each indicated product.*

Solvant	2980	2980	2980	2980	2980	2980	2980	2980	2980	2980	2980
Chelator	20	18	16	14	12	10	8	6	4	2	0
Cation	0	2	4	6	8	10	12	14	16	18	20

III.2.3. Chelator binding mechanism and guest-displacement experiments : 6.K^+ replacement by 6.Cs^+

As previously demonstrated, the synthesized chelator **6** is presenting a high affinity toward Cs^+ compared to the putative interfering ions such as K^+ and Rb^+. In order to have more insights on that, guest-displacement experiments have been performed both by ^1H NMR. Moreover, the binding mechanism of the chelator toward Cs^+ has been clarified by ^1H NMR.

III.2.3.a. Chelator binding mechanism

In order to get further information on the chelating ability of **6**, ^1H NMR titration experiments were conducted in a mixture of deuterated $CDCl_3$: MeOD (1:1) solutions in presence of traces of D_2O (cations were dissolved in). By varying gradually the number of equivalents of Cs^+, it is clearly evidenced that the complexes **6**.Cs^+ is formed. Indeed, both aromatic and aliphatic regions dramatically change as the number of equivalents of the added cation increases (Figure 74 and *Annexe VII.5*).

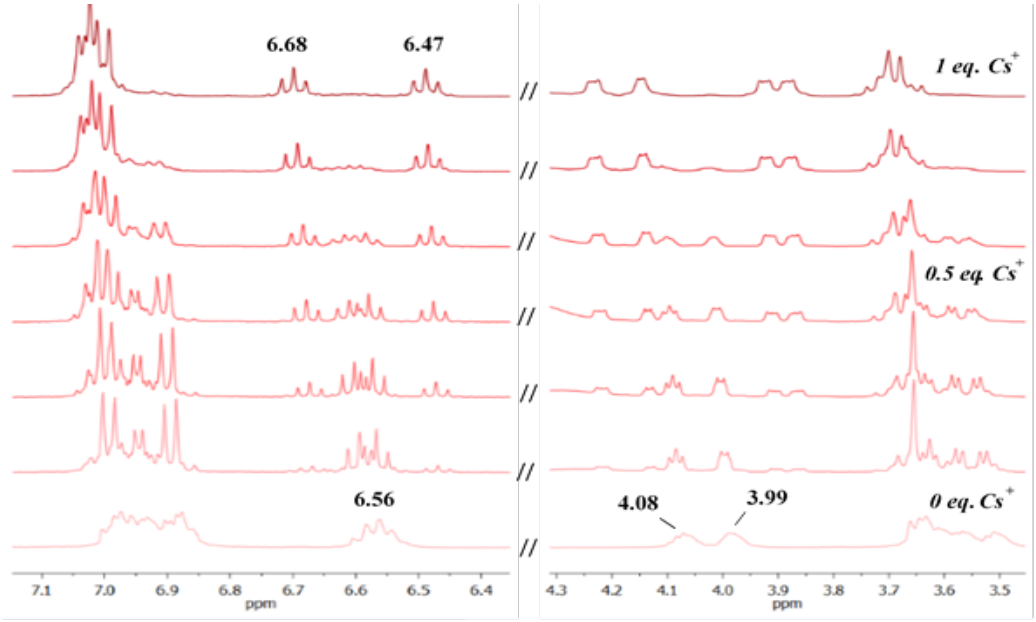

Figure 74 *NMR ^1H of the chelator **6** with gradual addition of Cs^+ up to 1 equiv.*

Most of the protons in these two regions are affected, shifting progressively downfield or upfield, and are preeminent after the addition of 1 equiv of Cs^+. If an excess of cation Cs^+ is added no further chemical shift is noticed in these two regions. Remarkably, in the ^1H aromatic region of the free host **6** the multiplet centered at 6.56 ppm splits into two separated triplet signals (one at downfield and the second one at upfield) after the addition of 1 equiv of Cs^+. Moreover, in the ^1H aliphatic region, the two multiplets centered respectively at 4.08 and 3.99 ppm are more strongly affected upon complexation as four new signals are observed both at downfield and upfield compared to the two original multiplets. These findings indicate that the binding of Cs^+, as well as for the other cations takes

place mostly, in the crown ether part as reported on similar systems. The excellent selectivity toward cesium was found and ascribed to the combined electrostatic and cation-π interactions arising respectively from cesium and oxygens of the crown ether or the aromatic rings of the scaffold[157-159].

III.2.3.b. Guest-displacement experiment by NMR

The developed very selective cesium probe is aimed to be implemented in OFET for detection measurements in seawater. Rubidium interference can be neglect due to his lower affinity with the probe compared to the potassium and also to his very low concentration in seawater: 3580 times lower than potassium[183]. Potassium may therefore be the most interfering cation in detection measurements. A guest-displacement from the host molecule experiment was then achieved by proton NMR.

A mixture of deuterated $CDCl_3$: MeOD (1:1) solution with the chelator **6** saturated with K^+ in the presence of traces of D_2O was prepared. Starting from complex **6**.K^+ the incremental addition of Cs^+ amounts leads to a dramatical change of the ^1H NMR spectrum. In the aliphatic area and more especially in the ether ppm range, some modification occurs. Unfortunately, water trace signal appearing in the same range and the overlapping of the signals make the analysis difficult. Therefore, focusing on the aromatic ppm range seems to be more legit (Figure 75).

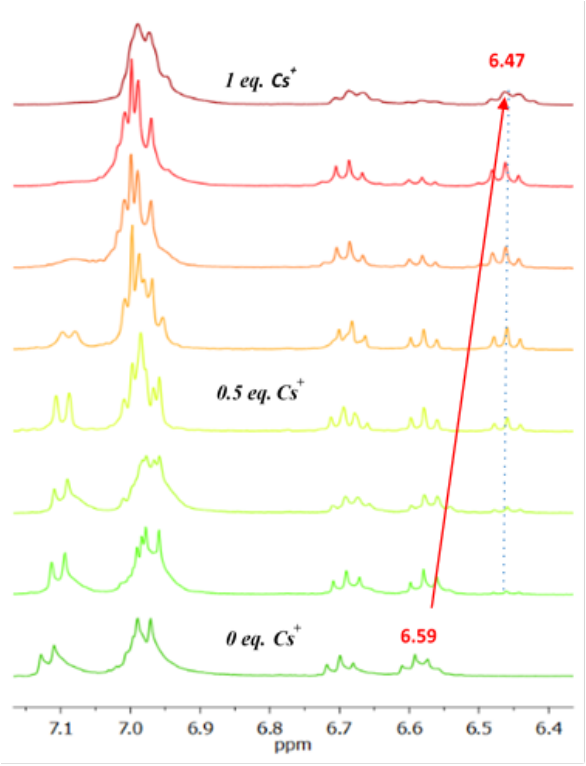

Figure 75 *^1H aromatic regions of **6**.K^+ upon addition of 0 to 1 equiv of Cs^+ as chlorine salts in $CDCl_3$: MeOD (1:1) with traces of D_2O.*

After complete addition of 1 equivalent of Cs^+ the obtained ^1H NMR spectrum appears to be the footprint of the one with the complex **6**.Cs^+ (Figure 74). The triplet signal at 6.59 ppm shifts to 6.47 ppm and the signal at 7.1 ppm overlap with the signal at 7 ppm to form an intense multiplet. This behavior reflects the greater ability of **6** to bind Cs^+ compared to K^+, as Cs^+ can replace K^+ guests.

[183] (Smith, Pillai, Chow, & Folsom, 1965)

Moreover, if an admixture of cations is added to the chelator **6**, the obtained ^{1}H NMR corresponds to the one of **6**.Cs^{+} when Cs^{+} is added alone.

These features constitute clear proof that the host molecule **6** behaves as a specific and selective probe to the cesium cation even if competitive cations are present in the medium.

III.3. Cs^{+} probe grafting on DCOH-R lipids surface

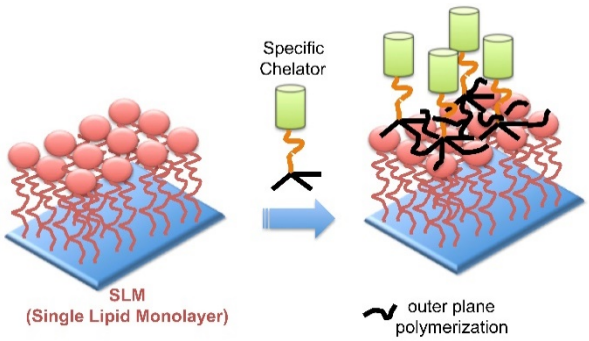

Figure 76 *Illustration of the SLM functionalization with the Cs^{+} probe*

The intrinsic sensing properties of the novel chelator **6** with respect to Cs^{+}, led us to consider its possible use in a sensor device such as a Chem-OFET. Nevertheless, prior to its implementation in a real device, it is required to graft it efficiently on a suitable surface. In this context, we have recently demonstrated that SLM[70-72] can be used as an efficient organic dielectrics in Field Effect Transistors devices. Based on these relevant facts, we decided to functionalize the chelator **6** with an appropriate anchoring group in order to be grafted on the DCOH-R lipid monolayers (**Fig. 76**).

III.3.1. Silane based anchor function

Synthesized probe **6** possesses two allyl functions in the lower rim of the structure which is allowing the possibility to tune it with an anchor function.

III.3.1.a. Synthesis

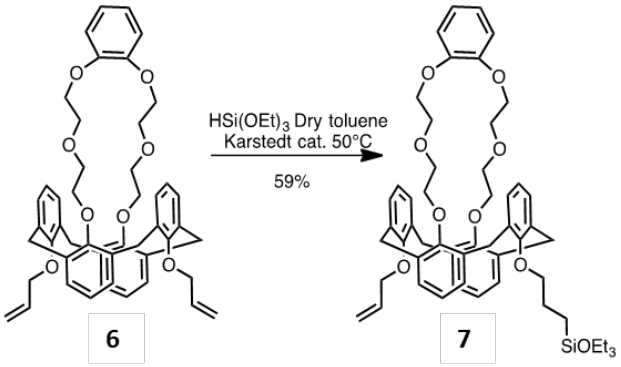

Figure 77 *Anchor group functionalization of the probe*

Owing to our strategy, the triethoxysilane group was selected and used as anchoring group. Indeed, silane groups are well known to be reactive to hydroxyl moieties (present on the DCOH-R surface). From **6**, this functional group can be easily introduced on the allyl part of the lower rim in one

step using the Karstedt catalyst (Figure 77)[184]. The target functionalized compound **7** was obtained in 59% and was used without further purification in the next step (*Exp. Tech. part VI.1.1*.). Indeed, compound **7** might be also contaminated by the bis-silylated derivative but this will not have any consequence on the grafting.

III.3.1.b. NMR ^{1}H & ^{29}Si characterization

The obtained silane functionalized probe was characterized by ^{1}H NMR and ^{29}Si NMR (*Annexe part VII.2*). Results are showing the success of the silanization of the chelator **6**.

III.3.2. Probe grafting on DCOH-R lipids

Firstly, a DCOH-R lipid was assembled on an edge-tailored silicon prism by applying the protocol described in Chapter 2. After full characterization by using the homemade Infrared cell placed in an attenuated total reflectance mode Fourier-transform infrared (ATR-FTIR) spectrophotometer (Chapter 2), the initiation and propagation of the polymerization at the lipids headgroup was initiated and ensured by the polycondensation of triethoxysilane group with the ester group on the top of the DCOH-R (Figure 78). It was performed by exposing the supported DCOH-R lipid monolayers to 0.25 mM solution of the substituted chelators **7** in anhydrous 1,4-dioxane for 1 hour. The surface was afterward rinsed copiously with 1,4-dioxane, methanol and water.

Silane based molecules functionalization is not always straightforward, due to parallel self polymerization that yields a polysiloxane thick film covering the substrate[185]. In fact, the condensation reaction is autocatalytic as water molecules activate the chlorosilane into reactive silanols. Excess of water, in the absence of controlled relative humidity, leads to the competition of poly-condensation of the precursor molecule instead of surface grafting. However, the density of the probe **7** and the rinsing step with the solvents is applied to reduce this unwanted side effect of the grafting process.

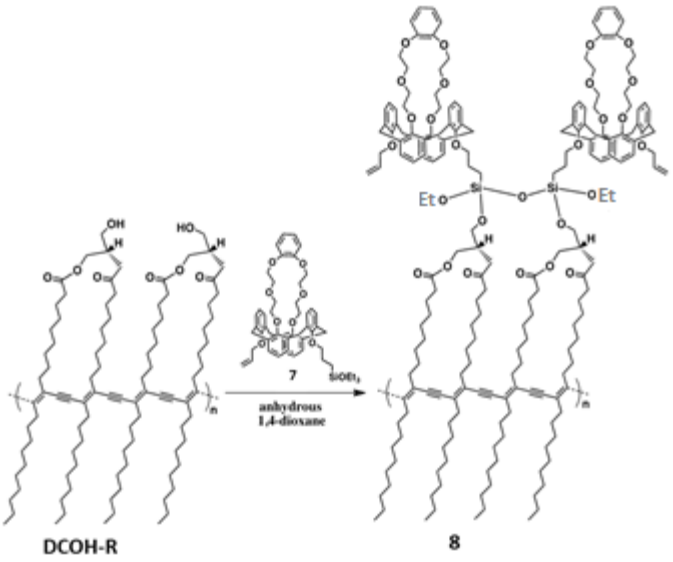

Figure 78 *Grafting chemical reaction of the molecule **7** on the DCOH-R lipid*

III.3.2.a. Confirmation of the grafting process

[184] (Kim, Jung, Lim, Ryu, & Lee, 2016)
[185] (Parikh, et al., 1997)

FTIR spectra obtained in water, confirm the occurrence of the condensation reaction (*Figure 79*). After 1h exposure in the chelator solution and rinsing with dioxane 1,4, MeOH and water, a decrease and a shift of the peak assigned to the carbonyl of the ester head groups ($\nu_{C=O}$ at 1702 cm^{-1}) and the appearance of new bands in the 1000-1300 cm^{-1} assigned to siloxane and/or calixarene

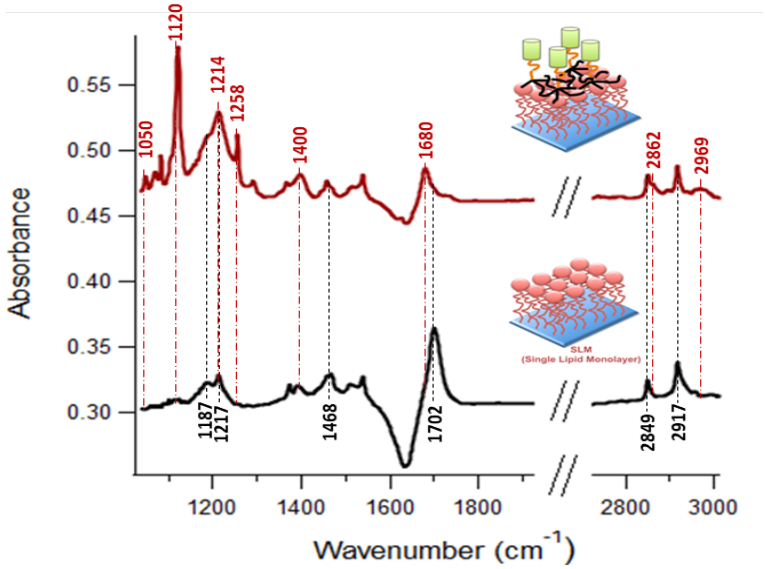

Figure 79 *Probe **7** grafting reaction observed by FTIR ATR. Black line is the DCOH-R lipids and red line is the DCOH-R + probe **7***

bonding (ν_{Si-O}, ν_{C-O}), indicating the successful anchoring of the host molecule **7** on the surface. In addition, the spectra show that the intensity and position of the peaks corresponding to the aliphatic chains of the lipids (sym. ν_{CH2} at 2849 cm^{-1} and asym. ν_{CH2} at 2917 cm^{-1}) remain unchanged indicating that the close-packed structure of the lipid monolayer is preserved. Note that the negative peak at 1640 cm^{-1} is related to the liquid water. As for both spectra the reference is P3HT substrate in water, the addition of an organic layer on P3HT surface leads to the natural decrease of the water amount. All these observations are in favor of a successful anchoring of the host molecule at the surface of the DCOH-R lipids. This unique combination of this novel interface is of great interest to be used as an active layer in a Chem-FET.

III.3.2.b. Density of the grafted probe

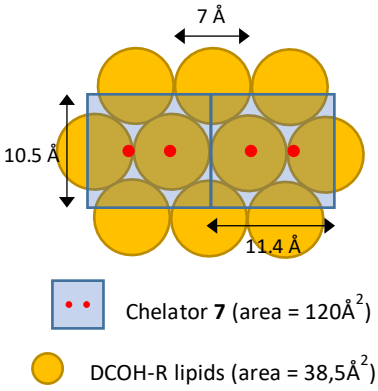

Figure 80 *Simplified molecular architecture of the DCOH-R lipids/chelator **7** interface. (2D top view)*

Direct quantification of the amount of grafted chelator on the DCOH-R lipid monolayers is not trivial. Indeed, despite the presence of one grafting site per lipid, molecular hindrance induced by the big volume of the chelator (showed by the crystallographic data of the chelator presented in this

chapter) makes the grafting ratio 1:1 with the lipids impossible to reach. Nevertheless, this information can be obtained indirectly. It has been demonstrated in the first chapter that the density of lipids is around 2.6 x 10^{14}/cm^2. By fixing two hypotheses, we can estimate the number of grafted chelators per lipids. First, we consider that the volume of the chelator **6** is roughly equivalent to the volume of the chelator **7**. Secondly, we set that the lipids have a hexagonal crystal packing[186]. Consequently, by applying these hypotheses and regarding to the area of the chelator **7** (120 Å^2), a simplified model of the DCOH-R lipids monolayer/chelator **7** interface can be hence drawn (**Figure 80**). Without taking into account the angles of the different molecular architectures, a ratio of DCOH 5:1 chelator **7** is estimated. In case of total grafting, the density of the cesium chelator on SLM surface must then be equal to 5.2 x 10^{13}/cm^2.

III.3.2.c. Kinetic studies of the grafting process

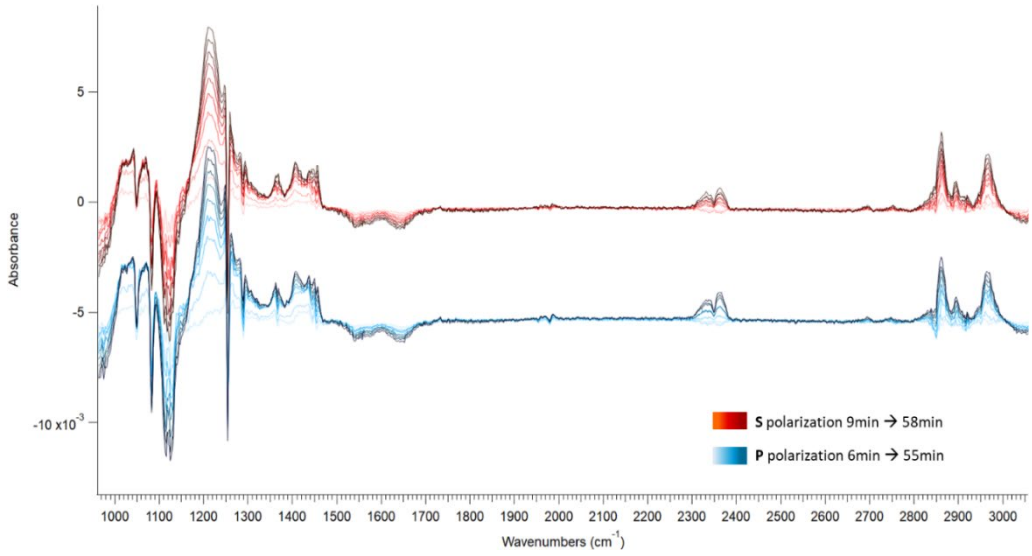

Figure 81 *Evolution of the grafting process recorded by FTIR*

The developed homemade cell for FT-IR ATR measurements (Chapter 2) was used to obtain the kinetic evolution of the grafting reaction. In this experiment 0.25 mM of chelator solution is injected in the liquid cell in one shot and left to diffuse without any stirring. After the grafting reaction started, several spectra were recorded in p and s polarization. The first spectra (starting at 6 min for s and 9 min for p) was used to normalize in each respective polarization mode to follow the evolution of the grafting process over time (**Figure 81**). As expected, the spectra are difficult to analyze due to the complexity of the chelator **7**. However, we can clearly distinguish the aliphatic area at 2800-3000 cm^{-1} (**Figure 82(1)**). The intense peak at 2862 cm^{-1} can be related either to the CH_2-O dipole present in the ether crown and the CH_2-O dipole in the anchor chain. On the other hand, the single peak at 2966 cm^{-1} can only be related to the CH_3 in the anchor chain. Therefore, by following the evolution of this signal over time it is possible to extract kinetic information about the grafting process.

The absorbance related to the probe (**Figure 82(2)**) in general is showing linear dependency over time which indicates that the diffusion governs the chelator motion once injected in the cell. However, the absorbance related to the grafting process (**Figure 82(3)**) is not evolving linearly. Two curves with two slopes can be distinguished. In the case of a reaction, the substitution of the CH_3 group occurs and siloxane bonds are created. The reaction leads to a decrease of the CH_3 group absorbance. Therefore, the first curve (orange) corresponds to the silanization reaction of the probe with the lipids.

[186] (Small, 1984)

By using the theoretical maximum density of chelator (5.2 x 10^{13}/cm^2), the silanization rate is estimated to be 3.47 x 10^{12} grafted chelator/min with full coverage attained in 15 min.

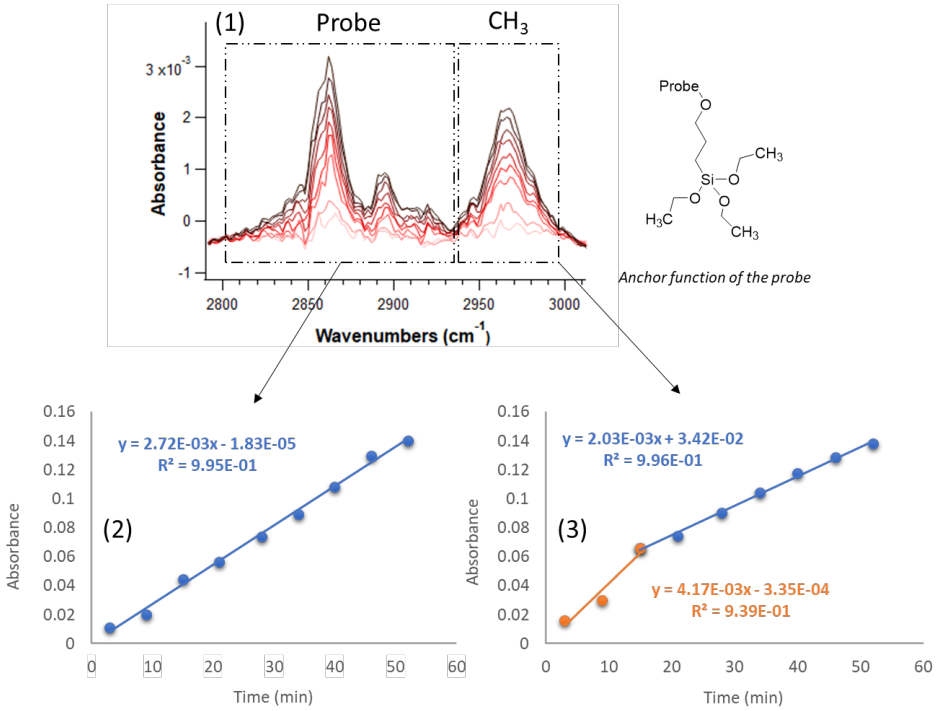

Figure 82 *(1) Evolution of the probe **7** in the aliphatic area in s polarization.(2) Absorbance evolution of the area related to the probe **7** (3) Absorbance evolution of the CH_3 moieties of the anchor function present in the probe **7***

III.4. Conclusion

In this part, we have studied the synthesis and the characterization of a calix[4]arene tethered with a benzocrown ether based cesium probe. We showed the success of his implementation in a solid SLM substrate. The newly appended calix[4]arene possesses remarkable selectivity toward Cs^+, over other interfering cations. From the lipids density calculation achieved in the previous chapter and the crystallographic parameters of the probe, we estimated a ratio of 5 lipids for one chelator. Therefore, the maximum density of the chelator is 5.2 x 10^{13}/cm^2. Moreover, by using the developed FTIR ATR in-situ measurement cell, we managed to obtain the grafting rate of the chelator on the SLM coated P3HT surface.

The synthesized probe has high selectivity toward Cs^+ and we showed the possibility to graft the chelator to the head-groups of the lipids via a silanization reaction. In the next chapter, we will implement this new sensitive and selective interface into an organic field-effect transistor for the selective detection of Cs^+ in seawater.

IV. EGOFET development

In the previous chapters, I introduced a new full-organic interface based on semi-conducting polymer P3HT and self-assembled stable lipids monolayer as a dielectric layer. After full characterization, the interface was activated by grafting a very selective designed cesium probe.

In this chapter, I will focus the discussion on the integration of this promising triple-layered system in electrolyte-gated field effect transistor (EGOFET). Why implementing such an interface in EGOFET ?

With respect to sensor applications in the aqueous environment, liquid electrolytes have been widely used as electrical gates in these transistors[44,187,188,189,190](Figure 83). Of importance is that the electrolyte-gated OFETs (EG-OFETs) effectively work at the millivolt range. This is owing to the high capacitance (1–20 $\mu F.cm^{-2}$)[191,192] of an electrical double layer (EDL) formed at the interface between the electrolyte solution and the organic semiconductor channel. This merit leads to an ultra-low threshold voltage (V_{TH}) under 1 V, which is effective to avoid any electrochemical reaction in the electrolyte solution[191,52] Here, it should be noted that V_{TH} is highly responsive to surface charges provided from analytes such as ions or biomolecules[75,188,193]. Therefore, ultra-low V_{TH} is advantageous to detect even small signals. Because of these features, the EG-OFETs are suitable for sensing ions in the aqueous environment.

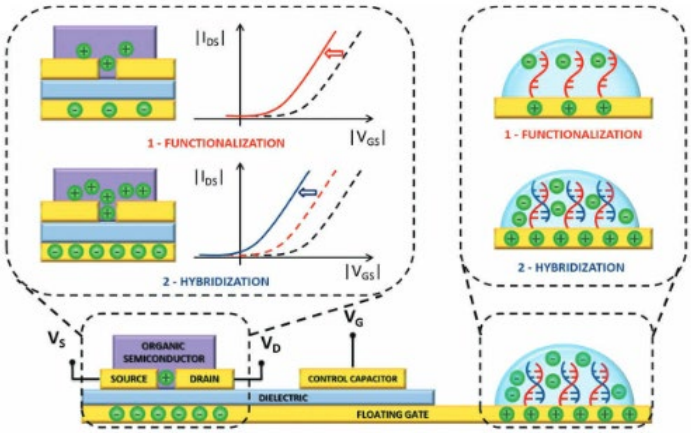

Figure 83 *EGOFET applied for the DNA recognition (Ref.188)*

However, the EG-OFET-based sensors faced the following obstacles. First, the detection of these analytes is typically carried out in the presence of interfering ions, e.g., potassium and sodium. These ions are well known to degrade the transistor performance because they act as electrical traps for OFETs[191,192,194,]. The stable operation of EG-OFETs in such aqueous environment, therefore, still remains a challenge[191,195,196]. Second, specific sensing probes should be attached on the surface of the transistor channels for detecting analytes such as ions and proteins.

[187] (Kergoat, Herlogsson, Braga, Piro, Pham, Crispin, Berggren, Horowitz, 2010)
[188] (Lai, Demelas, Casula, Cosseddu, Barbaro, Bonfiglio, 2013)
[189] (Buth, Donner, Sachsenhauser, Stutzmann, & Garrido, 2012)
[190] (Nguy, Hayakawa, Kilinc, Petit, Raimundo, Charrier, Wakayama, 2019)
[191] (Cotrone, Ambrico, Toss, Angione, Magliulo, Mallardi, Berggren, Palazzo, Horowitz, Ligonzo, Torsi, 2012)
[192] (Buth, Kumar, Stutzmann, & Garrido, 2011)
[193] (Minamiki, Hashima, Sasaki, & Minami, 2018)
[194] (Knopfmacher, Hammock, Appleton, Schwartz, Mei, Lei, Pei, Bao, 2014)
[195] (Porrazzo, Bellani, Luzio, Lanzarini, Caironi, Antognazza, 2014)
[196] (Cramer, Campana, Leonardi, Casalini, Kyndiah, Murgia, Biscarini, 2013)

Fabrication process and effect of the integrated P3HT/lipids interface on transistor properties will be first presented. It is worth to note that this part was essentially carried out by Tin Nguy, PhD student in the group of professor Wakayama at the National Institute of Material Science (NIMS) in Tsukuba, Japan. I found necessary to present the results of our Japanese partner in the framework of the collaborating ANR project SenCei in order to clarify the last part of my thesis. In fact, in the last part of my thesis, I will show the cesium detection results obtained in seawater by using our developed electrolyte-gated organic field effect transistor (EGOFET).

IV.1. Design and fabrication

IV.1.1. EGOFET design

The developed EGOFET presented in this chapter was applied as a cesium sensor. For that, the cesium selective probe based on calixarene was grafted on the DCOH-R lipid monolayer coated on the P3HT semiconducting layer (see Chapter 3 for grafting detail).

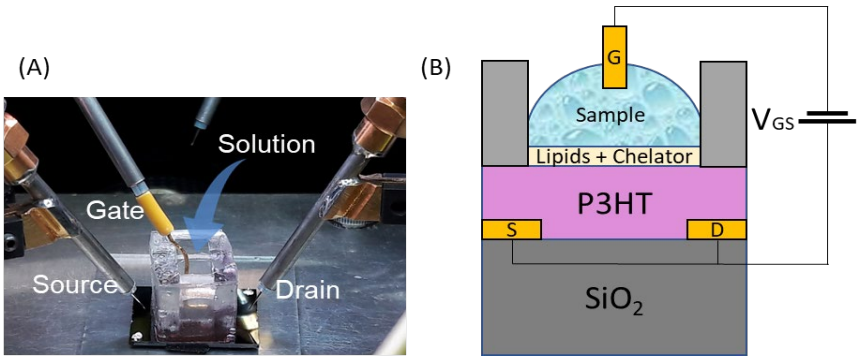

Figure 84 *Setup of the detection measurement with the developed EGOFET. (A) real picture (B) scheme*

Figure 84 is showing the design of the developed EGOFET. The electrodes are gold made. The thickness of the P3HT is 20 nm and it is regioregular at 90%. The thickness of the DCOH-R lipid monolayer grafted with the calixarene based cesium chelator is estimated to be 4.5 nm.

IV.1.2. EGOFET fabrication and configuration

IV.1.2.a. Top gate – bottom contact geometric configuration

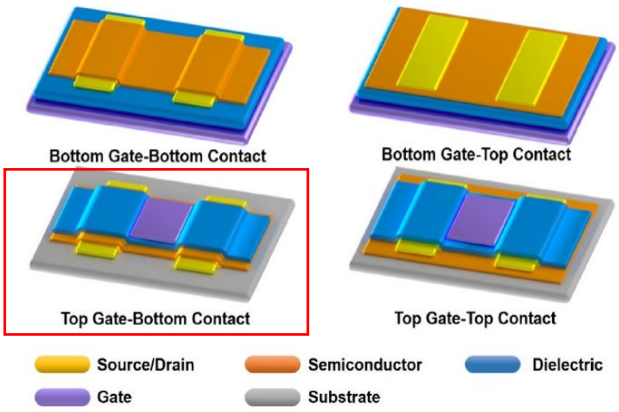

Figure 85 *Main four material configuration of FET (Ref. 49)*

The four main configurations of EGOFET are shown in the Figure 85. Each configuration is viable but we focused our research on the development of EGOFET based on the top gate - bottom contact configuration. Several reasons influenced our decision: first, the very thin lipids dielectric layer (2.5 nm) does not allow working in bottom-gate configuration. In fact, spin-coating the P3HT on top of it would probably damage it. Secondly, the top contact configuration was excluded to minimize the formation of parasitic charging currents under the contacts. Furthermore, bottom-contact structures are more commonly used and more applicable for large-scale production[197,198,199]. These reasons explain our selection to develop a reliable EGOFET based on top gate – bottom contact structure configuration.

IV.1.2.b. EGOFET fabrication

Figure 86 *Microscopic view of the developed transistor chip*

The top-gate and bottom-contact-type EGOFETs were prepared on SiO_2 substrate, where P3HT films were used as the transistor channel. First, source and drain electrodes were patterned on SiO_2/p-Si substrates through a shadow mask by thermal evaporation. Then P3HT semiconducting polymer was deposed by spin coating on the electrode supported SiO_2. Please refer to the Exp. Tech. section for detailed information about the fabrication protocol (*VI.2*). The obtained chip contains two duplicates of 4 transistors with different channel width: 100 µm, 120 µm, 150 µm and 200 µm (Figure 86). The chips were stored in a sealed vacuum bag.

In order to be used in the EGOFETs application, it is necessary to fixup an electrolyte container where dielectric gate deposition and measurements will occur. During my thesis, the design has evolved. First, a PDMS (polydimethylsiloxane) based container was carefully sealed on top of the P3HT film. However, leakage happened sometimes during the 2nd reticulation process with dioxane. Thus, a container made of polytetrafluoroethylene (PTFE) was designed and used (Figure 87).

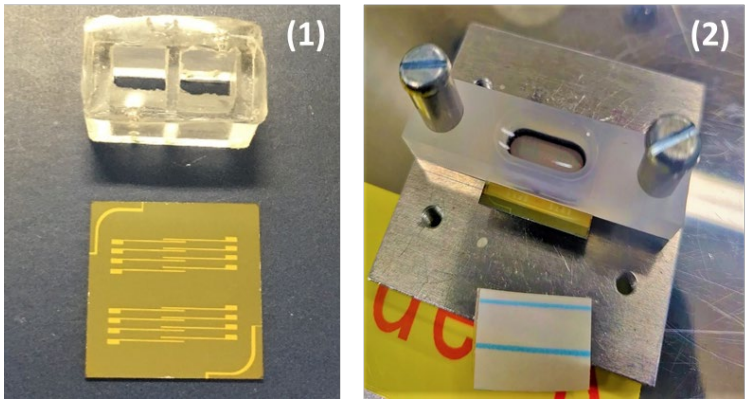

Figure 87 *(1) Image of the first design of the container made of PDMS (2) Image of the setup with the PTFE made container*

[197] (Piliego, Jarzab, Gigli, Chen, Facchetti, Loi, 2009)
[198] (Crone, Dodabalapur, Gelperin, Torsi, Katz, Lovinger, Bao, 2001)
[199] (Facchetti, Yoon, & Marks, 2005)

IV.2. The poly-3-hexylthiophene (P3HT) semiconducting layer

Poly-3-hexylthiophene (P3HT) (Figure 88) is a well-known p-type polymeric semiconductor with reasonable hole mobility (~10-2 $cm^2.v\text{-}1.s\text{-}1$) which presents a great advantage of forming homogeneous flat layers with low surface roughness. Easily processable and commercially accessible, P3HT is the ideal candidate to assume the semiconducting layer function in the developed OFET. Here, the morphology of the deposed P3HT and his effect on the transistor performance will be discussed.

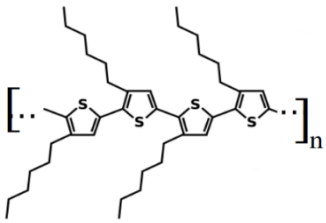

Figure 88 *P3HT molecular structure*

IV.2.1. Structure of the P3HT functionalized substrate

In the previous part, we showed that the EDL plays an important role in the operation of the EGOFETs because it provides a very high gate capacitance enabling millivoltage operation[191,52]. The EDL has sub-nanometer order thickness, and therefore its capacitance depends strongly on the surface morphology of the semiconducting channel[195, 200,201]. The structure of the P3HT is therefore important toward the transistor performance. Two parameters can critically impact the transistor performance: the hole mobility and the roughness of the P3HT semiconducting layer.

IV.2.1.a. Hole mobility of the P3HT

The hole mobility is governed by the crystallinity and molecular weight, resulting from the well-defined molecular architecture of P3HT[202]. For example, 3-hexylthiophene units may polymerize through head-to-tail, head-to-head or tail-to-tail couplings; the percentage of head-to-tail coupling represents the degree of regioregularity of P3HT, which is critical to the electronic properties of the material. Highly regioregular P3HT leads to materials with high performance in terms of hole mobilities. P3HT with regioregularity > 90% is available commercially. Nevertheless, transition metal catalyzed polymerization is mandatory to reach a very high degree of regioregularity[203,204]. It has been

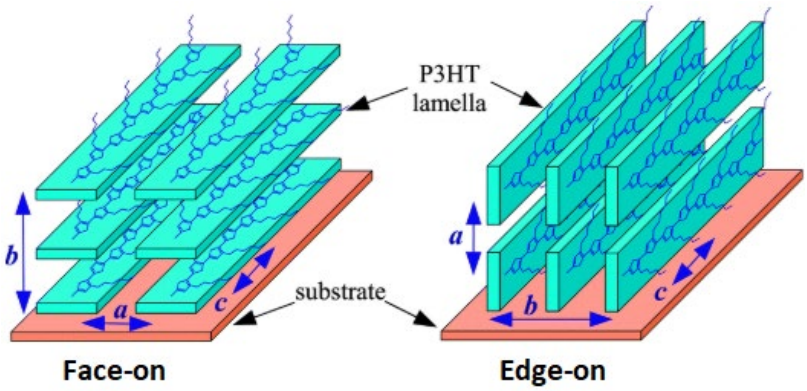

Figure 89 *P3HT layer orientations (Ref. 222)*

[200] (Tsao, Cho, Andreasen, Rouhanipour, Breiby, Pisula, Müllen, 2009)
[201] (Liu, Xu, Li, Scheideler, & Minari, 2013)
[202] (Kline, McGehee, Kadnikova, Liu, & Frechet, 2003)
[203] (McCullough, Lowe, Jayaraman, & Anderson, 1993)
[204] (Chen, Wu, & Rieke, 1995)

also showed that the regioregularity have effect on the orientation of the P3HT microstructure: in samples with high regioregularity (>90%) and low molecular weight the preferential orientation of ordered domains is with the lamella layer structure normal to the substrate and the p–p interchain stacking in the plane of the substrate (Edge-on conformation). In contrast, in samples with low regioregularity and high molecular weight, the crystallites are preferentially oriented with the lamella layer structure in the plane and the p–p interchain stacking normal to the substrate (Face-on conformation) (Figure 89)[205,206]. The orientation of the P3HT lamella has therefore a direct impact on the hole mobility : It was shown that it varies by two orders of magnitude depending on orientation (parallel or normal to the substrate) of the lamellae[206, 207], the normal one giving the highest mobility.

IV.2.1.b. Roughness of the deposited P3HT film

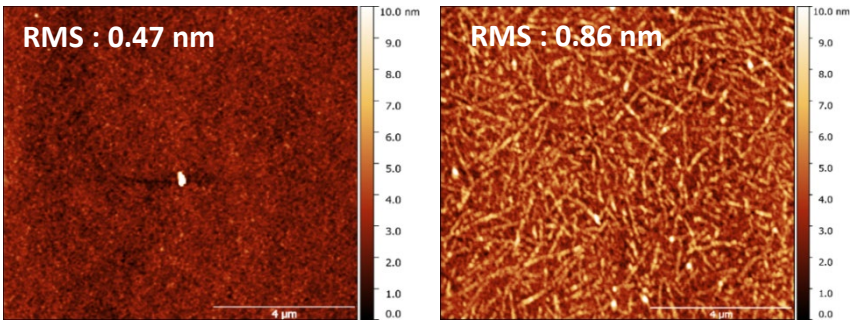

Figure 90 *AFM images of P3HT (left) and P3HT fibrils (right) deposited on SiO_2 substrate*

Besides the regioregularity, the correct dissolution of the polymer in the solvent is also playing a key role in the roughness of the deposited P3HT. Indeed depending on the affinity between the polymer and the solvent, crystallization can occur prior to deposition and results in the structuration of fibrils. In the case of P3HT in chlorobenzene, when the polymer is not fully solubilized in the solvent, recrystallization occurs. After deposition on the substrate, a fibrils-like structure with high roughness is observed.

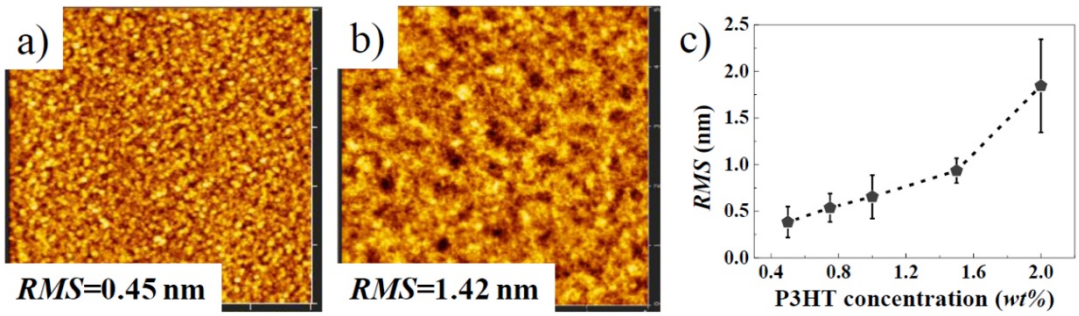

Figure 91 *AFM images of P3HT deposited on SiO_2 with low (0.5 wt%) (a) and high (2 wt%) (b) initial solution concentration. Evolution of the roughness over P3HT initial solution concentration (c) is*

Whereas, when the polymer is fully solubilized by heating-up, a flat surface is obtained (Figure 90). The roughness of the deposited P3HT can also be modulated by the initial concentration of the P3HT solution. By increasing the initial concentration of the P3HT in chlorobenzene solution, it has been showed that the roughness increases highly after around 1wt% of P3HT (Figure 91).

[205] (Fell & Mardalen, 1995)
[206] (Sirringhaus, Brown, Friend, Nielsen, Bechgaard, Langeveld-Voss, Spiering, Janssen, Meijer, Herwig, 1999)
[207] (Alberga, Mangiatordi, Torsi, & Lattanzi, 2014)

All these approaches impose making compromises between the electrical and immobilization properties but procurement of flat surface will be favored for the next steps as it is crucial for the insulating lipid layer deposition.

IV.2.2. Influence of the P3HT film roughness on the electrical properties of the EGOFET without the lipid monolayer coating

The semiconducting polymer P3HT is one of the main compound with the dielectric layer in the elaboration of the EGOFET. The roughness of the P3HT film can have high impact on the EGOFET performance. Indeed, the charge trapping caused by the surface roughness is enhanced in low thickness films (P3HT thickness = 20nm). Hence, in this subpart, we will look at the relationship between the roughness of the P3HT and the performance of the transistor.

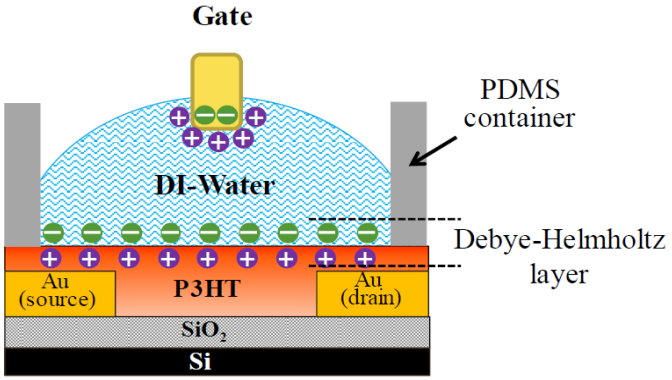

Figure 92 *WG-OFET based on P3HT semiconducting polymer*

For the purpose of this experiment, a water-gated organic field-effect transistor (WG-OFET) was made without the lipid layer. The transfer curves in order to obtain the V_{TH} and the on/off ratio were measured in the range of +0.5 V to -0.5 V gate-source voltage by using a semiconductor parameter analyzer (Agilent B1500A) under ambient conditions with V_{DS} fixed at -0.5V. Coupling between charged elements in the organic semiconductor and ions in water forms an ultra-thin EDL at the interface as shown (Figure 92). This is known as the Debye-Helmholtz layer[187]. As the EDL has a sub-nanometric thickness, the flatness of P3HT films can have a significant impact on WG-OFET operation.

The Figure 93 (a) displays the threshold voltage V_{TH} and the on/off ratio plotted as a function of RMS. The V_{TH} showed no dependence on the flatness and was constant at approximately −400 mV. Meanwhile, the on/off ratio decreased linearly with increasing RMS. The low roughness film showed the highest on/off ratio of 130, which is around three times higher than that obtained from the film with an RMS of 1.8 nm. The low roughness surface had another notable advantage as regards the repeatability of the on/off ratio, as shown in Figure 93 (b). A surface with a small RMS of 0.5 nm maintained a constant on/off ratio of around 130 even after 10 measurement cycles (one cycle corresponds to one transfer curve measured in 10 min). In contrast, a rough surface with an RMS of 1.8 nm results in a significant degradation of the on/off ratio. An AFM observation (Figure 91 (b)) provided a possible reason for these results. The rough surface has many dimples and holes as observed in the AFM image. Ions present in the electrolyte could be trapped or penetrate into the P3HT film through these defective parts. These are the primary causes leading to the degradation of the on/off ratio. Furthermore, a low roughness surface is better for the lipid monolayer formation.

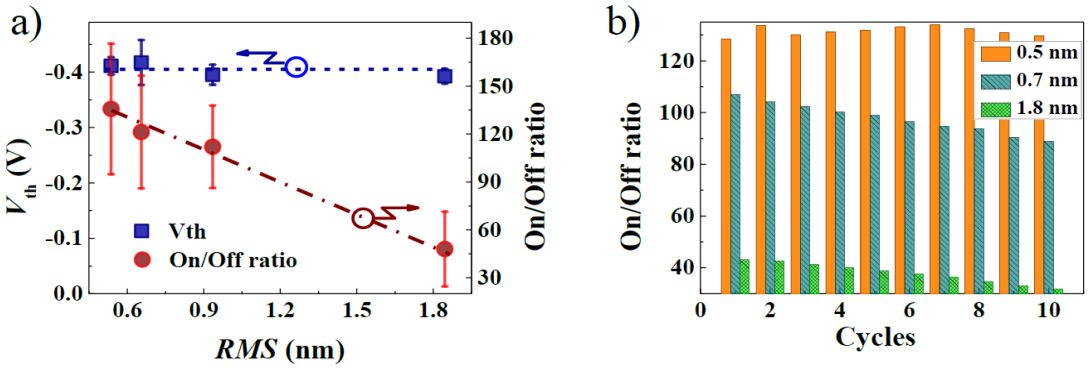

Figure 93 *(a) Effect of the P3HT surface roughness on the V_{TH} and on/off ratio of the WGOFET. (b) Effect of the P3HT surface roughness on the long-term switching performance of the WGOFET*

Consequently, a low roughness surface was found to have advantages in terms of realizing a high on/off ratio with long-term repeatability.

IV.3. P3HT/Lipid interface: effect on the transistor

DCOH-R lipid monolayer was then formed on top of the transistor and the properties of this new OFET were investigated to measure the impact of the presence of the lipid layer on the transistor response.

IV.3.1. Characterization of OFET with a DCOH-R layer as gate dielectric in DI water

The output and transfer curves were recorded using a semiconductor parameter analyzer (Agilent B1500A) under ambient conditions. More than five transistors were undergone electrical characterization to obtain average values. Measurements were performed in DI water.

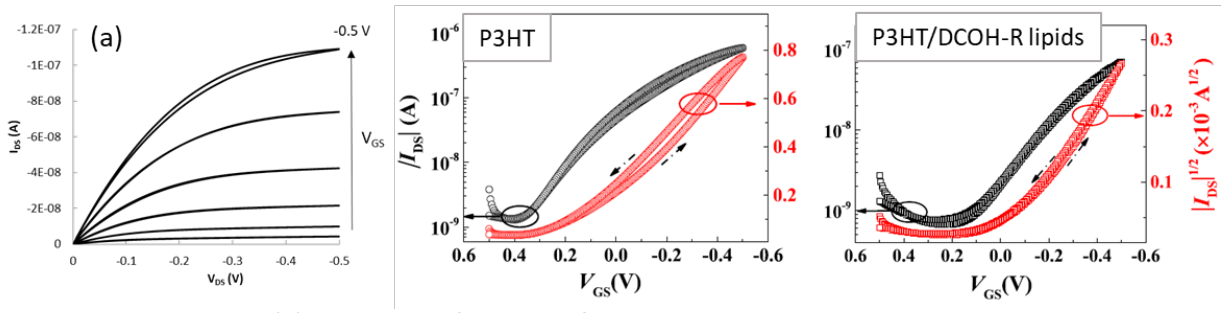

Figure 94 *Output curve (a) and the transfer curves of DCOH-R coated and non-coated P3HT based WG-OFET*

Output curves of the P3HT based transistor functionalized with DCOH-R lipids layer was obtained (Figure 94 (a)) by ranging the V_{GS} from 0 to -0.5V. The cut-off, linear and saturation regions can be distinguished showing that the transistor can be operated at a low working potential. Ideally sensing measurement will be performed in the saturation regime. Hence in the following, we have fixed V_{DS} to -0.5 V.

Transfer curves of the DCOH-R lipids coated and non-coated on P3HT based WG-OFETs are shown in Figure 94. A gold electrode was used for these measurements. The surface coating with the lipid membrane caused clear differences, namely a decrease in the drain current and a narrowing of the hysteresis. The decreased drain current by nearly one order of magnitude can be attributed to the

reduction in the EDL capacitance. This is because the total gate capacitance was reduced by coating with the 2.5 nm thick lipid membrane. Meanwhile, the WG-OFET with the lipid membrane exhibited a negligible hysteresis loop in the transfer curve. The large hysteresis present on non-coated P3HT was probably caused by carrier traps inside or at the surface of the P3HT layer. On the other hand, the lipid membrane prevented the P3HT surface from making direct contact with water to reduce such degradation of the electrical properties[70,80.] It should be noted that the combination of an Au gate electrode and lipid membrane coating resulted in a low threshold voltage of +35 mV.

These results proved that the mechanical stability and electrical durability of the lipid membrane were effective in realizing the stable operation of WG-OFETs. These motivating transistor performance improvements brought by the implementation of the lipids/P3HT interface lead to his application on EG-OFET.

IV.3.2. Characterization of the transistor in high concentration saline analyte

As the final goal of the project aim to the detection of cesium in sea-water, investigating fundamental properties of lipids coated EG-OFET using a high concentration saline analyte seems to be the next logical step.

IV.3.2.a. Transfer curves

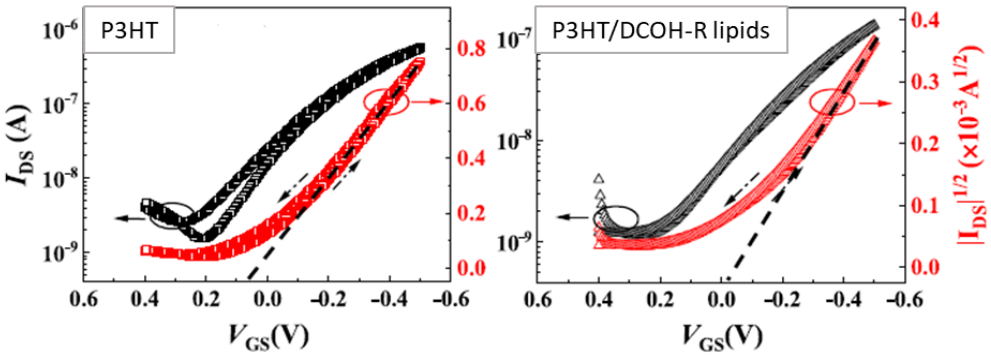

Figure 95 *Transfer curves of DCOH coated (right) and non-coated (left) P3HT*

Pristine P3HT without lipids monolayer and the P3HT with DCOH-R lipids implemented in EGOFET were compared. The I–V curves were measured by using a semiconductor parameter analyzer (Agilent B1500A) under ambient conditions. The phosphate-buffered solution (PBS) with a fixed pH of 6.86 was used as an electrolyte gate to evaluate the performance of EGOFET. **Figure 95** shows the transfer curves of two devices : with and without DCOH-R coating. The gate voltage was swept from +0.4 V to −0.5 V at a fixed drain voltage of −0.5 V. The V_{TH} was calculated with the equation **eq.12**.(*Exp. Part VI.3.2*). The transistor with 100 µm channel width was used for the experiments.

The V_{TH} of the pristine P3HT transistor was estimated to be +70 mV (±27 mV). Meanwhile, the transistor with DCOH-R lipid monolayer was −29 mV (±33 mV). The estimated capacitance of the lipid monolayer on the P3HT film (16.25 µFcm^{-2}) was smaller than that of pristine P3HT film (20.5 µFcm^{-2}) due to the presence of the lipid membrane. The carrier mobilities were calculated to be 7.2 x 10^{-3} cm^{2}V^{-1}s^{-1} for pristine P3HT and 4.3 x 10^{-3} cm^{2}V^{-1}s^{-1} for P3HT with DCOH-R, respectively[208]. The estimated

[208] (Nguy, et al., 2020)

carrier mobilities are comparable to those reported in the P3HT-based EG-OFETs[187,191] suggesting that the lipid monolayers had a moderate impact on the carrier transport in the channel layers.

As shown in the WG-OFET example, the lipids monolayer coating of the P3HT affects also the hysteresis of the transfer curves. Clear differences were observed in the forwards and backwards potential sweeps. The pristine P3HT showed a hysteresis around low gate bias range of +0.4 to 0 V. In contrast, the EG-OFETs covered by the lipids monolayer coating demonstrated negligible hysteresis in the loops (Figure 95). The observed hysteresis in the pristine P3HT can be ascribed to the ion doping from the electrolyte solution into the P3HT channel during the potential sweeps. Meanwhile, the lipids monolayer coating suppressed such electrochemical doping effects.

IV.3.2.b. Long-term stability

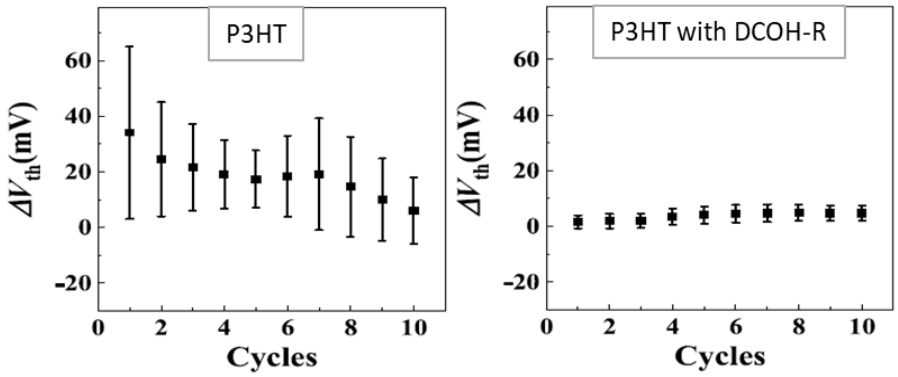

Figure 96 *Stability of the DCOH-R coated (right) and non-coated (left) P3HT EG-OFET over many electrical measurements cycles*

The advantage of the lipids monolayer coated EG-OFET was pronounced in the long-term operation. In fact, the long-term operation stability in the electrolyte solution is strictly required for sensor applications. The operation stability of two devices (DCOH-R coated and non-coated) was evaluated by repeating measurements of ten cycles for 10 min each in PBS electrolyte solution. A gradual decrease of the V_{TH} with significant deviation in the pristine P3HT EG-OFET was observed (Figure 96). The ΔV_{TH} was defined by the difference between the lowest V_{TH} values to other V_{TH} values. The standard deviation is calculated from the ΔV_{TH} mean of the 5 transistors. This result can be explained by the doping from the electrolyte solution into the P3HT channel. In contrast, lipids monolayer coated P3HT film improved the stability of the EG-OFET for the long-term measurement; no shifts in V_{TH} were observed as shown in the Figure 96. The deviations at each cycle were also negligibly small. These results also indicate that the lipids monolayer coating is effective to reduce the ion doping into the P3HT channel. This is a clear advantage for the sustainable operation of EG-OFETs in a electrolyte solution.

IV.3.2.c. pH non-sensitivity

The development of sensors with non-sensitivity to pH variations is also crucial in some cases. This is because the sensors are required to selectively detect only the analytes (ions or proteins) even in electrolyte solutions with different pH levels. For these purposes, DCOH-R lipid monolayer on P3HT was passivated by a silanization reaction to convert the head group from hydroxyl pH-sensitive group to methyltrichlorosilane (MTS) group. Then, the pH sensitivity and operation stability of the EG-OFET was evaluated.

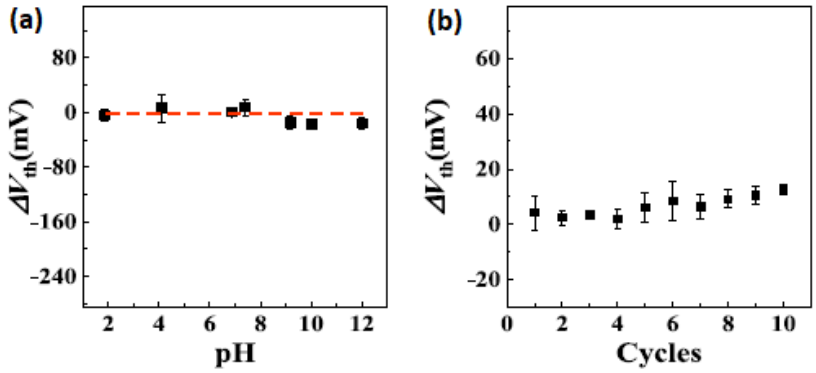

Figure 97 *V_{TH} Stability of the lipids coated P3HT EG-OFET and passivated with MTS over pH (a) and many electrical measurements cycles (b)*

Details of the measurement conditions were the same as those of other EG-OFETs. The low V_{TH} (+120 mV) was confirmed. Importantly, the transistors became non-sensitive to the pH variation, as shown in **Figure 97 (a)**. No variation in V_{TH} (ΔV_{TH} = 0 mV) was observed regardless of pH levels. The deviation of V_{TH} at each pH level was also small enough due to the reduced doping effect in the P3HT film. The results indicate that MTS groups successfully passivated OH-groups. Furthermore, the devices showed a stable operation even after exposure to the organic solvent **Figure 97 (b)**. The V_{TH} showed a negligible change even after repeated measurements for two hours. It should be emphasized that this technique provides the potential benefit for passivating OH terminals as well as for grafting other receptors onto the lipids monolayer. That is, the EG-OFET with DCOH-R monolayer has high potential in further functionalization by specific probes for versatile sensor applications.

Meanwhile, methyltrichlorosilane (MTS)-terminated lipids monolayer showed no sensitivity against pH levels and significantly stable operation even with the presence of high ion concentration in the electrolyte solution (PBS at 10^{-2} M). In this manner, the developed EG-OFETs with engineered lipids monolayer provide an innovative concept for further biosensors or chemical sensors.

IV.4. Detection measurements: EGOFET applied as Cs^+ sensor

In the last part of this chapter, I will show an example of an application of the developed EGOFET presented in this thesis as Cs^+ sensor. The chelator is grated to the reticulated lipid monolayer via the silane function according to the protocol described earlier in Chapter 3. V_{DS} was fixed at -0.3 V and V_{GS} was varied from 0 to -0.3 V to optimize the measurement time. The transfer curves were recorded by using a semiconductor parameter analyzer (Agilent B1500A) under ambient conditions. ΔV_{TH} mean of 5 transistors was obtained by normalizing the obtained V_{TH} with the V_{TH} without added cations (concentration 0). Detection experiments were achieved with several electrolytes and cations.

IV.4.1. Detection of cesium in deionized (DI) water

Intuitively, the detection of cesium in DI water was achieved first. Several concentration of Cesium Chloride from Sigma Aldrich was prepared in DI water. The results (**Figure 98**) are showing a very strange behavior of the transistor. A small decrease of the ΔV_{TH} followed by a sharp increase after 10^{-15} M of cesium chloride concentration was observed.

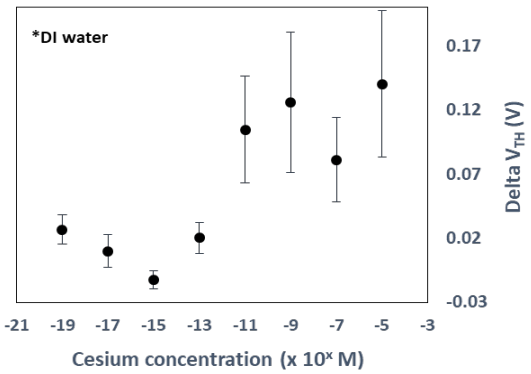

Figure 98 *Evolution of the V_{TH} versus the cesium concentration in DI water*

However, these strange results seem to be correlated to the adjustment of the polymer film in the water environment[209,210]. In fact, a decay that was not respected here is required for the adjustment of the polymer film. Moreover, due to continuous contact with the electrolyte, other effects such as the partial penetration of water in the P3HT film as well as formation of a passivating oxide layer on gold should be also taken into account.

IV.4.2. Detection of cesium in Phosphate Buffer Saline (PBS) solution

The aim of my project is to be able to do cesium detection in seawater. As seawater is composed of multiple ions and notably potassium which is also detected by the synthesized probe, a first detection experiment in an interfering medium was decided to be performed.

We started with a PBS buffer with pH fixed at 7.4 and with 10^{-1} M of NaCl and of 10^{-3} M KCl. The method of detection described below was followed:

- Add 200 µL of PBS in the cell → measurements to get the V_{TH} at concentration 0.
- Take 100 µL and add 100 µL of CsCl at 10^{-19} M. Wait 5 min → measurements to get V_{TH}
- Rinse with DI water
- Add back 100 µL of PBS and 100 µL of CsCl at 10^{-17} M. Wait 5min → measurements to get V_{TH}
- Rinse with DI water
- Etc.

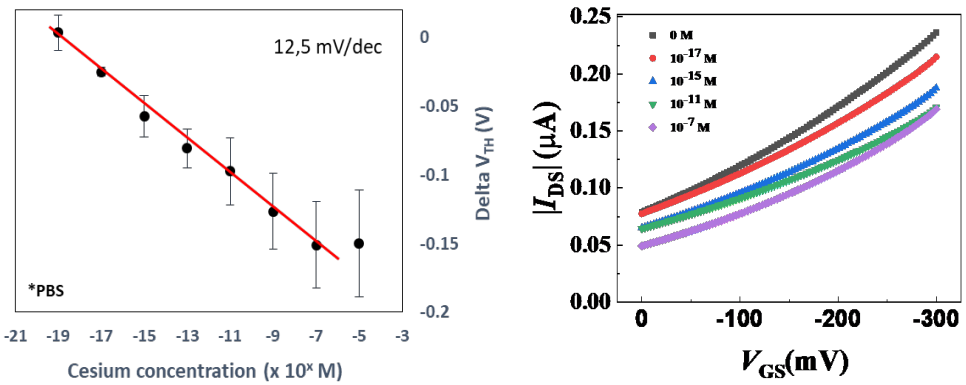

Figure 99 *Evolution of the V_{TH} versus the cesium concentration in PBS (left) Associated transfer*

[209] (Picca, Manoli, Macchia, Tricase, Di Franco, Scamarcio, Cioffi, Torsi, 2019)
[210] (Zhang, Leonardi, Casalini, Temiño, & Mas-Torrent, 2016)

Measured data (Figure 99) show a linear behavior of the ΔV_{TH} in a range of 10^{-19} M to 10^{-7} M of cesium chloride. A low limit detection at 10^{-19} M and a saturation limit of detection at 10^{-7} M can be attributed. The calculated sensitivity is 12.5 mV/decade. Even if the sensitivity is low, the super selectivity of the transistor must be highlighted. In fact, the cesium chelators grafted on the DCOH lipids layer are saturated with potassium K^+ present in PBS solution prior to the detection measurements. What is therefore measured is the surface charge modification provided by the switching from the chelator/K^+ host-guest bindings system to the chelator/Cs^+ host-guest bindings system. Although Cs^+ and K^+ carry the same charge, cesium cation has a larger radius and the screening of Cs^+ charge due to the ions in the electrolyte is expected to be different than for K^+. The effective surface charge is hence expected to be different.

IV.4.2.a. Cesium selective efficiency of the grafted probe

To confirm that the ΔV_{TH} shift comes really from the Cs^+/calixarene probe association, several negative control experiments were achieved:

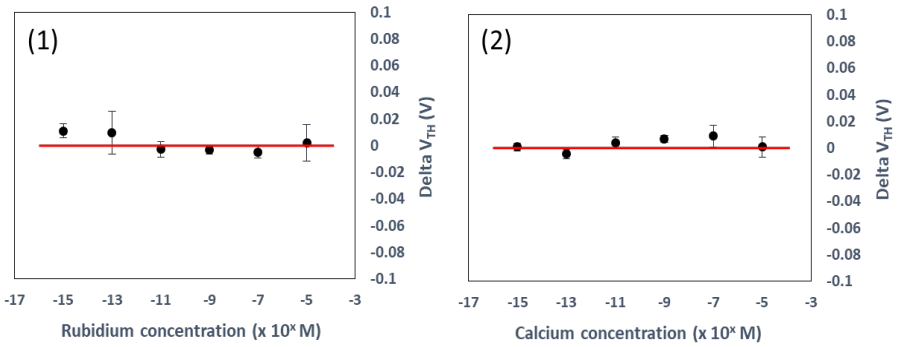

Figure 100 *Evolution of the V_{TH} versus the rubidium (1) and calcium (2) concentration*

First, rubidium cation (which has the third higher association constant with the calixarene probe compared to the potassium and cesium) and calcium cation were used instead of cesium in PBS for detection measurements. No variation of ΔV_{TH} was observed (Figure 100). As potassium present in the PBS has a higher affinity with the probe, this result was expected.

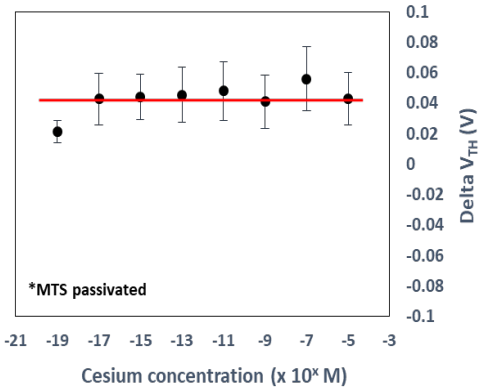

Figure 101 *Evolution of the V_{TH} versus the cesium concentration in PBS on MTS passivated surface (without Cs^+ probe)*

Secondly, the surface was passivated with methyltriethoxysilane and cesium with different concentration in PBS was added. Without the probe, no shift of ΔV_{TH} was observed (Figure 101). The little variation of the ΔV_{TH} and the higher standard deviation compared to the results obtained in the Figure 101 can be associated to the increase of the roughness by MTS grafting. Nevertheless, these

control experiments results confirm the selective impact of the Cs^+/chelator binding couple on the ΔV_{TH} shift.

IV.4.3. Detection of cesium in seawater

Table 7 *ASTM D665 seawater standard composition (I = 908mM)*

Ion	Concentration (g/L)
NaCl	24.54
$MgCl_2 . 6H_2O$	11.10
Na_2SO_4	4.09
$CaCl_2 . 2H_2O$	1.54
KCl	0.69
$NaHCO_3$	0.20
KBr	0.10
H_3BO_3	0.03
$SrCl_2.6H_2O$	0.04
NaF	0.003

After the results obtained in the interfering PBS medium, the cesium detection experiment was achieved in seawater. ASTM D665 standard seawater from Sigma Aldrich was bought. The composition of the seawater is revealed (Table 7). Cesium chloride at different concentrations was diluted in pure seawater. The method of detection described below was followed (PBS was kept to ensure constant pH):

- Add 100 µL of PBS + 100 µL of pure seawater in the cell → measurements to get the V_{TH} at concentration 0.
- Take 100 µL and add 100 µL of Cs^+ in seawater at 10^{-19} M. Wait 5 min → measurements to get V_{TH}
- Rinse with DI water
- Add back 100 µL of PBS and 100 µL of Cs^+ in seawater at 10^{-17} M. Wait 5 min → measurements to get V_{TH}
- Rinse with DI water

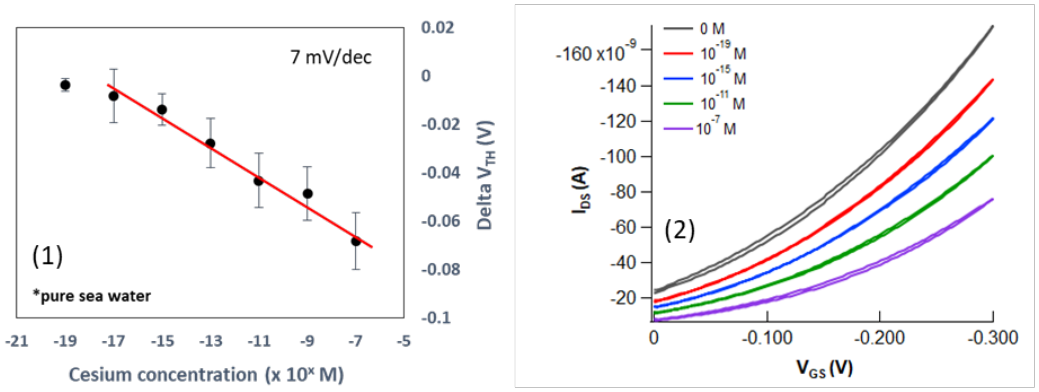

Figure 102 *(1) Evolution of the V_{TH} versus the cesium concentration in pure seawater. (2) Transfer curves at different concentration of CsCl in seawater with the designed EGOFET*

A linear decrease of the ΔV_{TH} is again observed (Figure 102) with a limit of detection of 10 aM. Compared to the experiment in PBS, the sensitivity is reduced. It can be explained by the increase of charge screening in seawater. Indeed, in the FET-based sensing measurements, the solution

environment plays an important role in determining the sensing performance. In solutions containing high-salt concentrations (such as seawater or PBS), the interaction potential (V(r)) between the receptor and analytes that cause the conductance change in the FET sensor could be partially screened by the strong ionic strength of the solution, thus reducing the signals obtained from the electrical measurements. The screening of V(r) in the FET measurements is enhanced exponentially by the distance (r_{bs}) measured from the binding site of receptor - analyte complex to the FET surface and can be represented as $V(r)e^{-r_{bs}/\lambda_d}$ where λ_d is the Debye - Hückel length[198,211] and is given by eq.11.

$$\lambda_d = \sqrt{(\varepsilon_0 \varepsilon_r k_B T / 2 N_A e^2 I)} \qquad \text{eq.11}$$

where ε_0 represents the vacuum permittivity, ε_r is the relative permittivity of the medium, k_B is the Boltzmann constant, T represents the absolute temperature, N_A is Avogadro's number, e stands for the elementary charge, and I represents the ionic strength of the electrolytic buffer solution. It is obvious that an electrolytic solution of higher ionic strength (I) has a shorter λ_d, thus creating a more severe screening effect on the FET-based sensing measurements[212].

Table 8 *Debye-Hückel length calculated in different electrolytes*

Electrolytes	Ionic strength of the solutions (mM)	Ionic strength in the cell (mM)	Debye-Hückel length (λ_d) (nm)
PBS	163	81.5	1.07
Seawater	908	535 (454+81.5)	0.42

The Debye-Hückel length (λ_d) calculated from the equation eq.11 is given for the cesium detection measurements in the different electrolytes (Table 8). By using the crystalline structure of the cesium probe (Chapter 3), the distance between the DCOH-R lipid monolayer and the Cs^+ chelating area is estimated to be 0.96 nm (Figure 103(a)).

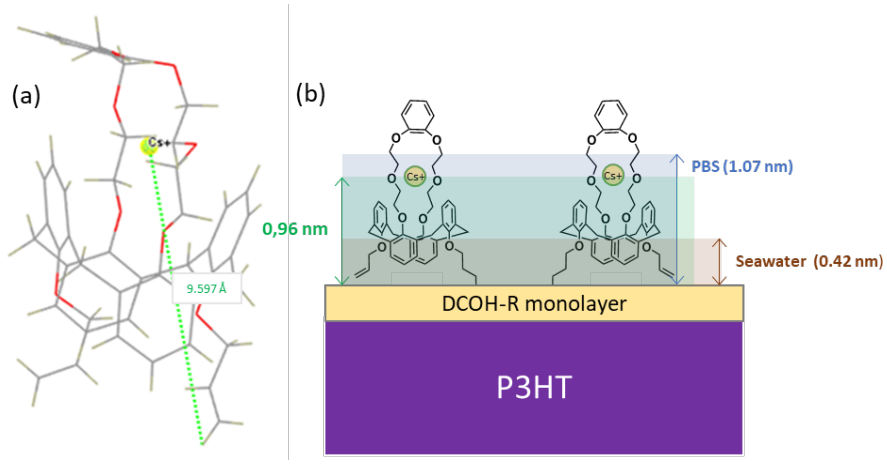

Figure 103 *(a) X-ray structure of the cali[4]arene based Cs^+ probe with the chelating area – allyl moieties measured distance (b) Schematic representation of the ionic screening effect in different electrolytes*

When λ_d is lower than 0.96 nm (in the case of cesium detection in pure seawater), the sensitivity of the measurements is drastically reduced. Indeed, the intense charge screening makes the Cs^+ complexation inefficient to alter the EDL and therefore the capacitance of the surface is not

[211] (Zhang, et al., 2008)
[212] (Chen, Li, & Chen, 2011)

changed. When λ_d is higher than 0.96 nm (in the case of cesium detection in PBS), the Cs^+ complexation affects the EDL and a surface capacitance variation occurs (Figure 103(b)).

IV.5. Conclusion

In summary, novel EGOFETs was developed by functionalizing transistor P3HT based channels with the engineered DCOH-R lipids monolayer. Besides the intrinsic EGOFETs advantage of working at low V_{TH}, the engineered lipids monolayer contributed to improving EGOFET operation performance by preventing the doping effect from electrolyte solution into the transistor channels. The ΔVth was negligibly small even after repeated operations in the electrolyte solution for a long time.

Further improving the stability performance of the transistor, lipids monolayer plays a key role in the versatility of the transistor. In fact, by modifying the head group of the lipids it has been possible to build a cesium sensor: the EG-OFET with DCOH-R lipids monolayer grafted with cesium probe showed an ultra-selectivity toward cesium in interfering medium such as seawater. The observed ultra-low detection limit (10^{-19} M) open new perspectives for our approach for the development of new sensor applications in chemical and biological fields.

V. Conclusion & Perspectives

A new super selective sensor for cesium detection has been developed (Figure 104). For this, an ultra-thin (2.5 nm), very dense (2.6 x 10^{14}/cm^2), polymerizable lipid layer with a modifiable head-group was used. This layer was deposited on a semiconducting regioregular polymer (P3HT) by using the vesicle fusion method. The lipids appeared to perfectly interlocks with the aliphatic chains of the polymer. The multiple Van der Waals interactions between the two layers plus the inter and intra chain cross-linking of the lipids after radical polymerization allowed to obtain a very stable organic interface verified by AFM force measurements. Subsequently, a calixarene-based probe was synthesized and attached. Cation affinity measurements by UV-vis and NMR showed a high selectivity of the probe towards cesium. The formation of this new, thin, stable, cesium-selective, all-organic, three-layer interface was monitored using a multifunction fluidic cell implemented in an FTIR in ATR mode. Once incremented in an electrolyte-gated field-effect transistor, the results showed that it is possible to detect cesium in seawater with a detection range of 10^{-17} M – 10^{-7} M and sensitivity of 7 mV/dec. We can, therefore, answer to the main question of this thesis: Is it possible to detect very low concentrations of cesium cation in seawater? Yes. Besides it is full-organic composition, the very low detection limit and the ultra-high selectivity toward Cs^+ are probably the two biggest advantages here of the developed new interface implemented in EGOFET.

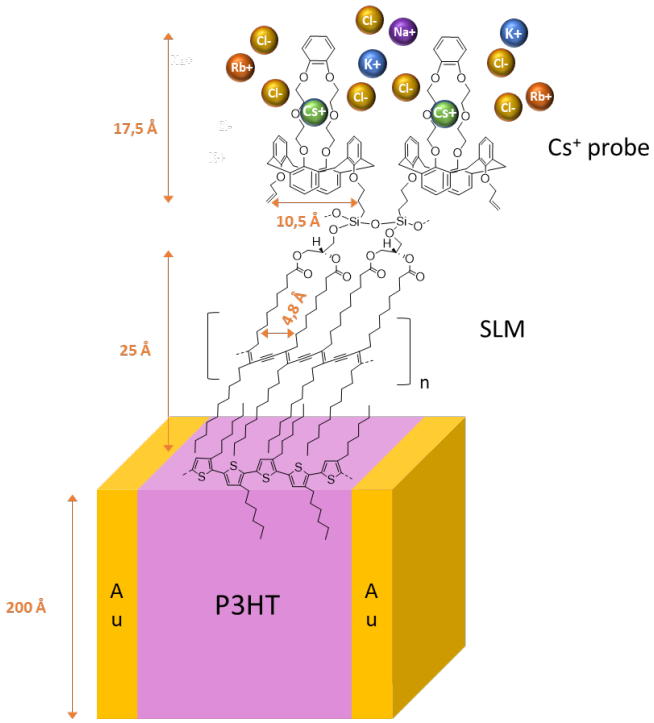

Figure 104 *Developed interface implemented in EGOFET for cesium detection*

The detection of cesium in seawater was focused on this thesis. However, the versatility of the lipids functionalization allows the application of the developed EGOFET in several fields. In fact, by modifying the cesium selective probe to a bio-selective probe, the EGOFET can be used in the biomolecule probing field for example. Another perspective concerns the tool developed to follow the different steps of the interface formation. Indeed, the FTIR ATR cell can be used to study the fundamental properties of new complex interfaces. Besides the advantages offered by the developed EGOFET sensor, one recurrent problem exists in these types of sensors: the desorption of the analyte. In our case, several methods have been attempted to desorb the cesium from the chelator but without success. In this way, the chelator molecular structure can be investigated and optimized to aim this goal. Despite of all, the developed sensor can be used as one-shot sensor due to its cheap material composition

VI. Experimental Techniques

VI.1. Protocole of the probe chemical synthesis

VI.1.1. Reactions

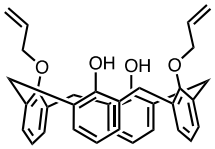

1

Synthesis of 1,3-diallyloxy calix[4]arene 1. Under an Argon atmosphere, a mixture of 2.00 g (4.72 mmol, 1 equiv) of commercially available calix[4]arene and 0.72 g (5.20 mmol, 1.1 equiv) of K_2CO_3 in 50 mL of anhydrous CH_3CN were stirred under reflux for 2h. Then 1.17 g (9.68 mmol, 2.05 equiv) of allyl bromide was added dropwise to the reaction mixture. Reflux was continued for 2 days. After cooling, the solvent was removed under reduce pressure. The obtained residue was taken up in $CHCl_3$ (100 mL) and the organic phase was washed twice with 40 mL of a 2M aqueous HCl solution followed twice with 40 mL of water. The organic phase was dried over $MgSO_4$, filtered and evaporated in *vacuo*. The compound was purified by column chromatography over SiO_2 (eluent petroleum ether: DCM 1:1) yielding the titled compound in 62% as a white solid.

^{1}H NMR (400 MHz, $CDCl_3$): δ= 7.98 (s, 2H, OH); 7.09 (d, 4H, ^{3}J= 7.5 Hz); 6.94 (d, 4H, ^{3}J= 7.5 Hz); 6.78 (t, 2H, ^{3}J= 7.5 Hz); 6.69 (t, 2H, ^{3}J= 7.5 Hz); 6.30 (ddd, 2H, ^{3}J= 22.2, 10.4, 5.1 Hz, vinyl); 5.81 (dd, 2H, ^{3}J= 17.2, 1.5 Hz, vinyl); 5.45 (dd, 2H, ^{3}J= 10.6, 1.3 Hz, vinyl); 4.59 (d, 4H, ^{3}J= 5.0 Hz, vinyl-CH_2-Ar); 4.36 (d, 4H, ^{3}J= 13.1 Hz, Ar-CH_2-Ar); 3.42 (d, 4H, ^{3}J= 13.1 Hz, Ar-CH_2-Ar). ^{13}C NMR (100 MHz, $CDCl_3$): δ= 153.8; 152.3; 134.0; 133.4; 129.6; 129.1; 128.7; 126.1; 119.6; 118.5; 77.3; 32.0.

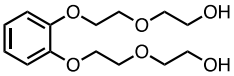

diol

Synthesis of 1,2-bis[2-(2-hydroxyethoxy)ethoxy]benzene. To a solution under Argon atmosphere of 5.00 g (45.00 mmol, 1 equiv) of commercially available catechol **3** in 150 mL of anhydrous DMF was successively added at room temperature 63.00 g (0.45 mol, 10 equiv) of K_2CO_3 and 22.50 g (180 mmol, 4 equiv) of 2-(2-chloroethoxy)ethanol. The reaction mixture was heated to 80°C overnight under stirring. After cooling down the solvent was removed under reduced pressure to dryness. The residue was taken up in 150 mL of $CHCl_3$ and the organic phase was washed three times with 40 mL of a 0.5M aqueous NaOH solution followed by three times with 40 mL of water. The organic phase was dried over Na_2SO_4 and the solvent was removed in vacuo. The compound was purified by column chromatography over SiO_2 (hexane 6:4 EtOAc) yielding the titled compound in 47% as an orange oil.

^{1}H NMR (400 MHz, $CDCl_3$): δ= 6.90 (d, 4H, ^{3}J= 1.9 Hz); 4.15 (dd, 4H, ^{3}J= 5.4, 3.5 Hz); 3.89 (m, 4H); 3.74-3.67 (m, 8H).

Synthesis of 1,2-bis[2-[2-[[(4-tolyl)sulfonyl]oxy]ethoxy]ethoxy]benzene 2.

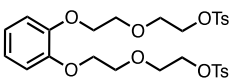

2

To a solution of 2.50 g (6.30 mmol, 1 equiv) of the **diol** in 6.25 mL of THF was added an aqueous solution of NaOH (1.23 g (30.00 mmol, 4.8 equiv) in 6.25 mL of water). The new solution was cooled down to 0°C and a solution of 3.67 g (19 mmol, 3 equiv) of p-toluenesulfonyl chloride in 8.75 mL of THF was added dropwise over a period of 1 hour. After addition, the reaction mixture was stirred a further hour at 0°C, then 25 mL of a 25% aqueous solution of HCl was added to quenched the reaction. The organic phase was extracted twice with 50 mL of DCM. The organic phase was then successively washed twice with 25 mL of water, twice of a 0.5M aqueous solution of $NaHCO_3$ and twice with 25 mL of water. The organic phase was dried over $CaCl_2$ and the solvent was removed under reduced pressure. The residue was purified by column chromatography over SiO_2 using a mixture of petroleum ether – EtOAc (80:20) as eluent.

^{1}H NMR ($CDCl_3$, 400 MHz) : δ 7.81 (d, 4H, ^{3}J= 8.2 Hz), 7.32 (d, 4H, ^{3}J= 8.1 Hz), 6.92 (m, 4H), 4.20 (t, 4H), 4.09 (t, 4H), 3.79 (q, 8H, ^{3}J= 5.7 Hz), 2.43 (s, 6H).

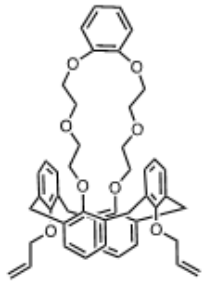

Synthesis of 1,3-alternate 25,27-bis-(1-allyloxy)-1,3-[1,2-bis[2-(2-oxyethoxy)ethoxy]phenylene]calix[4]arene, 3. To a solution, under Argon atmosphere, of 0.090 g (0,180 mmol, 1.0 equiv) of 1,3-diallyloxy calix[4]arene **1** in 30 mL of anhydrous CH_3CN was added, in one portion, 0.234 g (0.730 mmol, 4.0 equiv) of cesium carbonate. The reaction mixture was stirred under reflux for 2h prior adding dropwise a solution of 0.120 g (0,198 mmol, 1.1 equiv) of **2** in 9 mL of anhydrous CH_3CN. At the end of the addition the reflux was maintained for 2 days and then the reaction mixture was cooled down to room temperature. Solvent was removed under reduced pressure. The residue was taken up in 100 mL of CH_2Cl_2 and the organic phase was washed successively twice with 60 mL of a 2M aqueous HCl solution, then twice with 50 mL of brine and twice with 50 mL of water. The organic phase was dried over Na_2SO_4, filtered and the solvent was removed under vacuo. The residue was purified by column chromatography over SiO_2 (eluent: petroleum ether: EtOAc 8:2) yielding the titled compound in 61% as a colourless solid. Mp= 142°C uncorrected).

^{1}H NMR (400 MHz, $CDCl_3$): δ= 7.00 (d, 4H, ^{3}J= 7.5 Hz), 6.91 (dd, 8H, ^{3}J= 12.1, 4.8 Hz), 6.60 (td, 4H, ^{3}J= 7.5, 4.5 Hz), 5.65 (ddt, 2H, ^{3}J= 17.2, 10.6, 4.6 Hz), 4.97 (dd, 2H, ^{3}J= 10.7, 1.7 Hz), 4.84 (dd, 2H, ^{3}J= 17.3, 1.8 Hz), 4.09 (t, 4H, ^{3}J= 5.1 Hz), 4.03 (dd, 4H, ^{3}J= 4.1, 2.0 Hz), 3.60 (m, 20H). ^{13}C NMR (100 MHz, $CDCl_3$): δ= 138.23; 138.02; 131.16; 116.46; 115.64; 113.10; 112.21; 104.39; 104.29; 103.97; 97.95; 97.33; 52.93; 52.61; 52.34; 51.62 ppm. Elemental analysis for $C_{48}H_{50}O_8$+CH_3CN (%): calculated C, 75.45; H, 6.71; O, 16.08. Found C, 75.39; H, 6.67; O, 16,18.

Synthesis of 1,3-alternate 25-[(3-triethoxy)-silyl-1-propyloxy]-27-(1-allyloxy)-1,3-[1,2-bis-[2-(2-oxyethoxy)-ethoxy]phenylene]calix[4]arene, 4. To a solution, under Argon atmosphere, of 0.050 g (0.066 mmol, 1.0 equiv) of 3 in 2 mL of anhydrous was added 0.027 mL (0.145 mmol, 2.2 equiv) of triethoxysilane and the reaction mixture was stirred at room temperature for 20 min. The reaction vessel was placed in a glove box then 0.020 mL of the Karstedt's catalyst was added dropwise. The reaction was warmed up to 50°C and was stirred for 12h. The reaction mixture was cooled down to room temperature and filtered off through a pad of Celite. Excess of triethoxysilane and solvent were removed under reduced pressure. The product was used without further purification.

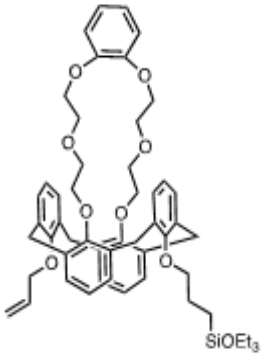

^{1}H NMR (400 MHz, $CDCl_3$): δ = 6.81 (m, 16H, H aromatics), 5.69 (m, 1H, H vinyl), 3.89 (m, 36H, CH_2), 1.25 (m, 9H, methyl), 0.94 (m, 2H, CH_2) NMR ^{29}Si ($CDCl_3$, 79 MHz) : δ -100 (s, 1Si).

VI.1.2. Materials

Regarding the materials, 2-(2-chloroethoxy)ethanol), Catechol and p-toluenesulfonyl chloride (TsCl) were purchased from TCI. Calix[4]arene and allyl bromide were purchased from Alfa Aesar. Karstedt's catalyst, Li^+, Na^+, K^+, Rb^+, Cs^+, and Mg^{2+} as chlorine salts, dimethylformamide (DMF), anhydrous acetonitrile (CH_3CN), methanol (MeOH), dichloromethane (DCM), tetrahydrofuran (THF), anhydrous toluene, anhydrous 1,4-dioxane, K_2CO_3, NaOH and Cs_2CO_3 were purchased from Sigma Aldrich. Column chromatography was performed using silica 60 M (0.04-0.063 mm) purchased from Macherey-Nagel.

VI.2. Protocole of the EGOFET fabrication

The top-gate and bottom-contact configurated EGOFET was fabricated as described below :

- Si(1,0,0) wafers with 200 nm thick SiO_2 is used as a substrate.

- Gold films 22 nm thick were thermally evaporated in a vacuum through a shadow mask (**Figure S1**) to pattern the substrates with source and drain electrodes. Two duplicates of 4 transistors is present in each chip. The length (L) is fixed to 2000 µm. The width (W) varies: 100 µm, 120 µm, 150µm and 200µm.

- The P3HT solution was prepared by dissolving P3HT (Sigma Aldrich, 90% regioregular) in chlorobenzene at 0.75% wt. The solution was heated at 60°C for 30 min to ease the dissolution of the polymer. After passing through filters with a 200 nm pore size, the homogeneous solution was slowly spin-coated onto the electrodes at 4000 rpm for 1 min. Subsequently, the P3HT film was annealed at 150 °C in a vacuum. This step helped to eliminate residual solvent and to improve the crystallinity of the P3HT films.

- A polydimethysiloxane (PDMS) well for use as electrolyte container was carefully sealed on top of the device.

- The gate bias voltage was applied by the immersion of an Au gate electrode in electrolyte solution.

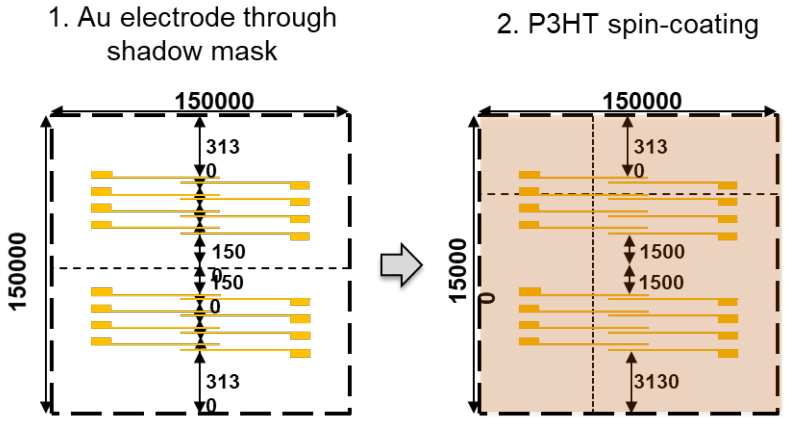

Figure S1 *Shadow mask for the OFET fabrication*

VI.3. Working parameters determination of the transistor

VI.3.1. OFET function principle

VI.3.1.a. FET and OFET in general

A field effect transistor (FET) is consists of three metallic conducting electrodes: source (S), drain (D) and gate (G), a semiconductor, where charge carriers flow, and a very thin insulating layer (**Figure S2**).

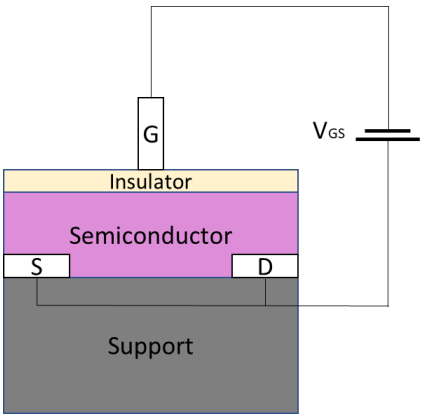

Figure S2 *Simplified FET/OFET scheme in top-gate bottom contact geometry*

The working principle of a FET is the following: a voltage applied to the gate modifies the charge carrier density in the semiconductor in between source and drain, which therefore modulates the source-drain current. There are two kinds of charge carriers: electrons (e) and hole (h) for n or p-type semiconductors, respectively. In organic FETs (OFETs), electron donating organic semiconductors have a high highest occupied molecular orbital (HOMO) level and therefore are good candidates for p-type semiconductors, while electron-accepting ones with low HOMO levels are used as n-type semiconductors. In OFETs, at least one of the functional layers is made of organic material. The OFET characteristics are greatly affected by the properties of the semiconductor-insulator interface.

VI.3.1.b. EGOFET

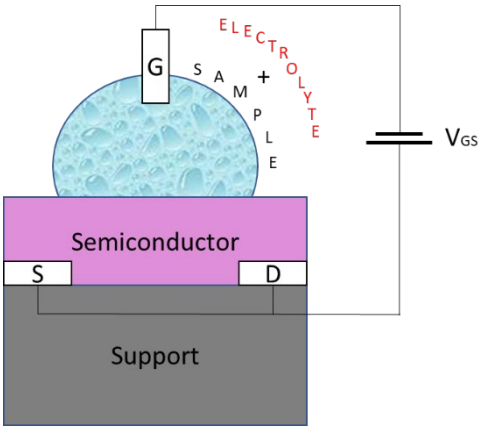

Figure S3 *Simplified EGOFET scheme in top-gate bottom contact geometry*

The working principle of the developed Ion Sensitive Organic Field Effect Transistor (OFET) is almost similar to electrolyte-gated OFETs (EGOFETs) which are a subclass of OFETs. The only difference is the addition of an inert and stable layer between the OSC/electrolyte interfaces. It is therefore important to understand EGOFETs. It is slightly different from classical OFETs (Figure S3). Indeed, the organic semiconducting layer is in direct contact with an electrolyte instead of a classical dielectric. In EGOFETs, the conductivity of the semiconducting channel is modulated by a solid or a liquid electrolyte put in between the semiconductor and the gate. EGOFETs display higher gate capacitance than other types of OFETs. As a consequence, biasing voltages used for EGOFETs are typically much smaller than those necessary for OFETs (<1 V, versus >10 V or even higher). The gate electrode is immersed in the electrolyte and source and drain electrodes, isolated from the electrolyte, provide electrical contact to the channel. Even if EGOFET looks like an OECT (organic electrochemical transistor), only capacitive processes occur for EGOFETs but no charge transfer. In an EGOFET made with a p-type semiconductor, upon negative polarization of the gate, the cations of the electrolyte accumulate at the electrolyte/gate interface while the anions accumulate at the electrolyte/OSC interface, resulting in the formation of an electrical double layer (EDL) at both interfaces. The EDL is composed of the Helmholtz layer (HL) and the diffuse layer (DL). The HL is a monolayer of ions, whereas the DL is simply more concentrated in ions (either cations or anions) than in the bulk electrolyte (Figure S4). In other words, the excess of ions decreases with the distance from the interface. Accumulation of anions at the electrolyte/semiconductor interface produces accumulations of holes in the topmost layer of the semiconductor[213,214] which causes the OSC to become conducting.

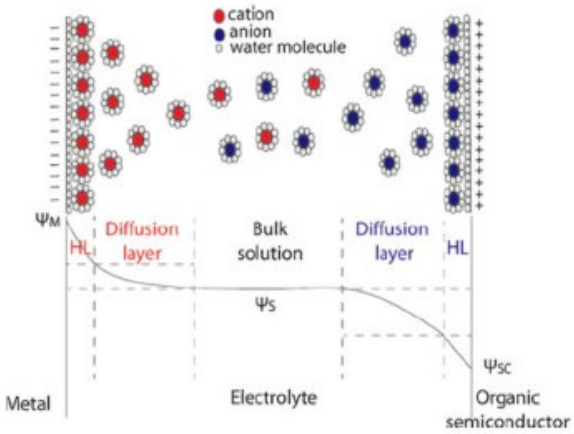

Figure S4 *Illustration of the Helmholtz and diffuse layer occurring in the different interface (Ref.223)*

In FET transistors, four electrical parameters are important to be defined: V_{DS} and I_{DS} (voltage and current between the drain and source electrodes), V_{GS} (voltage between the gate and source electrodes) and V_{TH} (threshold voltage required to have current flow in the semiconductor). These working parameters can be characterized by two types of I-V curves: the output curves and the transfer curves.

VI.3.2. Output characteristic

Output curves reflect the variation of the current (I_{DS}) regarding to the source-drain voltage (V_{DS}) at different gate-source voltage (V_{GS}) (Figure S5). Three regions are observable:

[213] (Stern, Klemic, Routenberg, Wyrembak, Turner-Evans, Hamilton, Lavan, Fahmy, Reed, 2007)
[214] (Stern, Wagner, Sigworth, Breaker, Fahmy, Reed, 2007)

- Cut-off region where $V_{GS} \leq V_{TH}$: No channel is formed and $I_{DS} = 0$.
- Linear region where $V_{GS} > V_{TH}$ and $V_{DS} < V_{GS} - V_{TH}$: the current I_{DS} flowing through the channel is linearly proportional to the applied voltage V_{GS} until a breakdown voltage is reached. In this region, the transistor shows some resistance to the flow of current.
- Saturation region where $V_{GS} > V_{TH}$ and $V_{DS} \geq V_{GS} - V_{TH}$: the channel is pinched off and the current I_{DS} flowing through the channel is constant with the V_{DS} and varies only with the V_{GS}

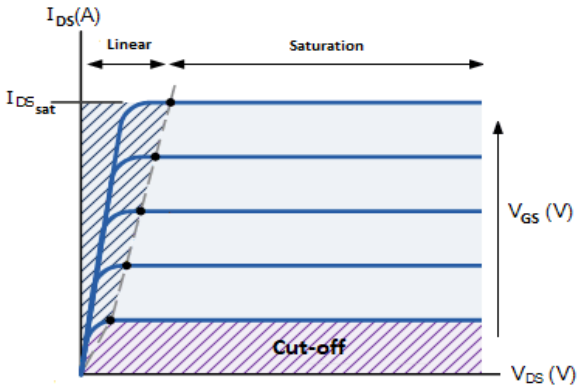

Figure S5 *Typical output curve of FET with the different regions*

The output curves are usually used to fix-out the V_{DS} in order to be at the saturation region. At the saturation region, the current I_{DS} is only controlled by V_{GS} according to the equation **eq.12**[215].

$$I_{DS} = \frac{W}{2L} \mu C_i (V_{GS} - V_{TH})^2 \qquad \textbf{eq. 12}$$

where W, L , µ and C*i* are respectively the width and length of the transistor channel, carrier mobility and the capacitance of the gate dielectric layer. From this equation, it is possible to extract the threshold voltage V_{TH} ,the most important parameter for the detection application. An extrapolation is required by using the transfer curve.

VI.3.3. Transfer characteristic and on/off ratio

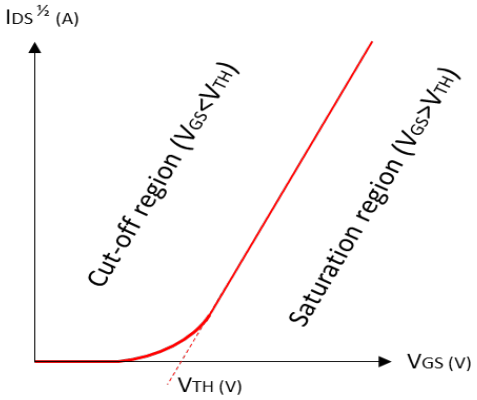

Figure S6 *Typical transfer curve of FET with the different regions*

The transfer characteristics describe the drain-source current I_{DS} versus the gate-source voltage V_{GS} at fixed V_{DS}. Along the cut-off region, the current is negligible. When V_{GS} cross the V_{TH}, a transition from weak to strong inversion is attained (**Figure S6**). The transfer curves are useful to determine the V_{TH} by using a quadratic extrapolation method[216] from the **eq.12**. at the saturation region. Practically, the intersection of the tangent line of the curve in the saturation region with the X-axis corresponds to the V_{TH}. Besides obtaining the V_{TH}, transfer curves are also used to get the on/off ratio of the transistor. By dividing the I_{DS} maximum by the I_{DS} minimum, it is possible to obtain information about the switching performance of the transistor.

[215] (Ishii, Kudo, Nakayama, & Ueno, 2015)
[216] (Loke, et al., 2010)

VI.4. Protocole of the DCOH lipids deposition and functionalization

In this thesis, modified vesicle fusion method was adapted and used for the immobilization of the lipids on solid substrate.

VI.4.1. Lipids cleavage

DCPC was mixed with deionized water (at pH 7.2) to form vesicles. Catalytic amount of phospholipase C from *Bacillus Cereus* was then added. The mixture was sonicated for 15 min and then slowly stirred at 55°C for 72h. Once the reaction achieved, the organic part was extracted three times with chloroform. The obtained solution was then dried with Mg_2SO_4 and filtrated. Purification with column chromatography with petroleum ether 8:2 ethyl acetate as eluent was performed. The obtained solution was evaporated under reduce pressure to obtain a white powder. Reaction yield was 85%.

VI.4.2. Lipids deposition an stabilization

DCOH lipids are stored in chloroform at -20°C to avoid any alteration.

- Evaporate the solvent slowly at 45°C. Once 97% of the solvent is evaporated, deionized water is added to obtain 0.27 mM of DCOH concentration.
- Sonicate the solution for 30 min.
- Perform extrusion by using polycarbonate 0.1 µm sized pore.
- On clean hydrophobic surface, do the deposition at 25°C and reduce quickly the temperature to 10°C, wait 10 min.
- Increase the temperature (1°C/min) to 30°C for P3HT or 32°C for SiH
- Add 0.5% concentrated AAPH solution. Rinse several time with this solution. Wait 10 min.
- Increase the temperature to 35°C and wait 10 min.
- Increase the temperature to 42°C and wait 60 min.
- Decrease the temperature to 35°C and wait 10 min.
- Rinse abundantly with DI water at 25°C and dry with N_2.

VI.4.3. Lipids functionalization

Functionalization of the DCOH-R lipids layer is performed by incubating 0.25 mM of the probe with silane anchor function diluted (compound **7**) in dioxane 1,4 and the DCOH-R lipids coated substrate for 30 min. Then, the sample is rinsed abundantly with dioxane 1,4, methanol and DI water.

VI.5. Protocole of the FT-IR ATR *in-situ* experimentation

VI.5.1. Setup of the cell

Big sized Si prism is required (2cm L x 1,5cm l). To setup the prism with the cell, follow the order presented on the pictures below (Figure S7). Use a pump to stabilize the prism. Put the thermocouple in contact with the Si prism at the end, before introducing it in the chamber. Test it before. The liquid will enter from the bottom and exit from the top of the cell by gravitation.

Tip 1 : to avoid leakage, enlarge the width of the canal after inserted in the holes of the chamber. Then pull it back and adjust it.

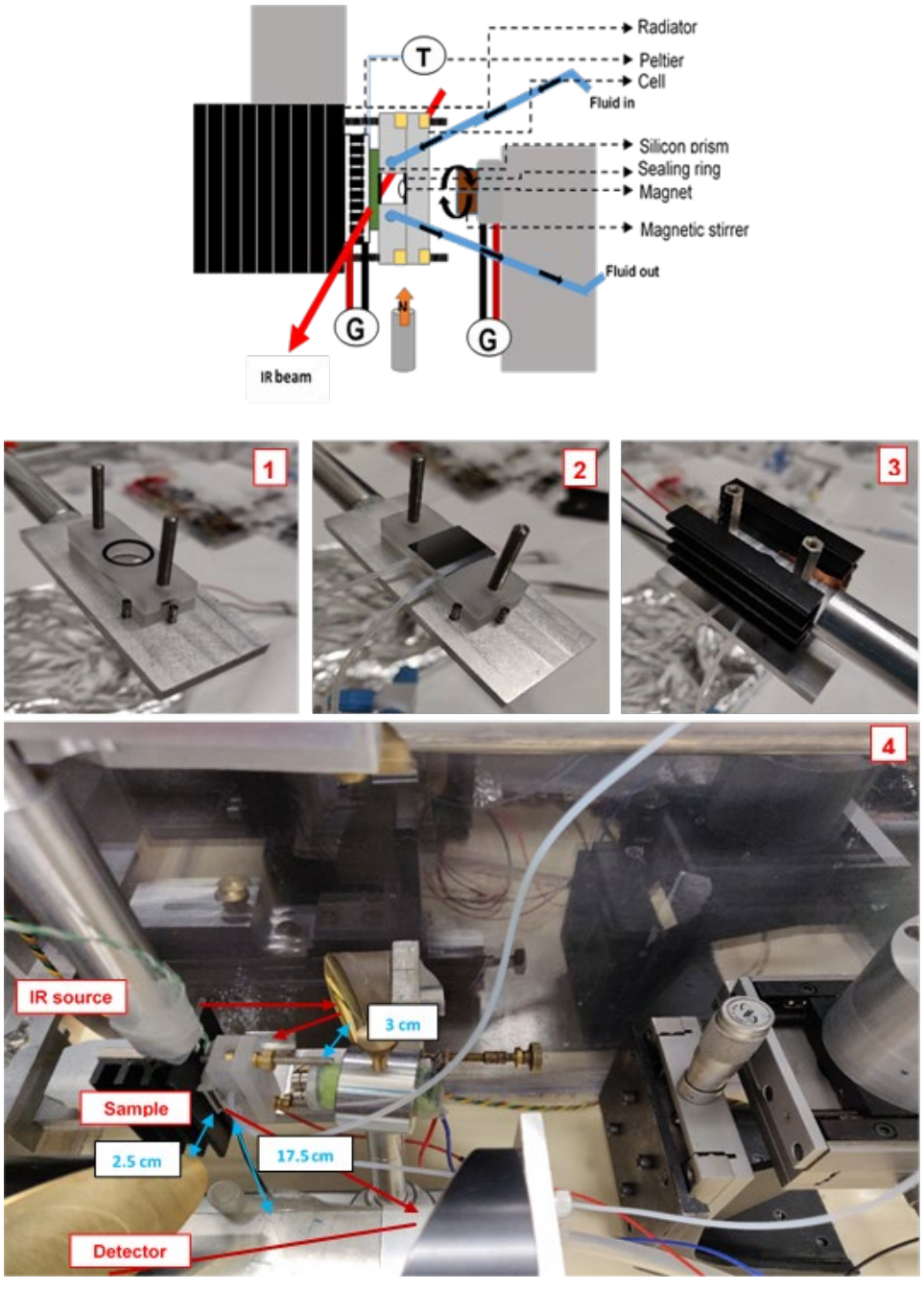

Figure S7 *Configuration of the ATR cell for FTIR measurements*

VI.5.2. Alignment of the IR beam to the prism

To obtain high intensity signals, the IR beam must be well aligned to go through the prism. First, increase the limit of the alignment setup. Value of the controller: H = 4 mm, = 17.5 mm, = 15 mm. For the sensor : = 9 mm , = 9.5 mm, = 9.5 mm

IR Intensity after alignment: around 1250 for SiO_2 substrate.

VI.5.3. Lipids introduction and measurements

VI.5.3.a. Measurements

After the cell was introduced in the N_2 purged chamber (to minimize H_2O vapor and CO_2 absorption) and the IR beam alignment achieved, measurements can be carried out. Spectra were averaged over 150 scans (4 cm^{-1} resolution) in the range of 1000-3200 cm^{-1} with the OPUS software.

Tip 2 : before starting measurements of the lipids deposition, do a reference in water. It is required at each step of the process (different temperatures) in order to normalize and obtain only the signal from the lipids.

Tip 3: before saving the reference, rinse the cell with hot water in order to remove residual waste from the sealing ring.

VI.5.3.b. Lipids solution preparation and introduction

Lipids solution: 300µL (2mg/mL) in 3,0 mL of DI water. Add 3% of chloroform for easy dissolution.

Tip 4 : use Eppendorf, no glass ! Lipids stuck on glass.

Sonication 30 min (open the bottle during sonication). Extrusion with 0.1 µm pore sized polycarbonate membrane.

Preheat lipids vesicles solution and substrate in air at 45°C before injection. After injection of 3 mL of the solution by syringe, reduce the temperature to 10°C. Wait 5 min. Increase back to 45°C, wait 3 min and reduce to 10 min for 5min. Start measurement. Always under stirring.

Tip 5 : rinse with methanol if you want to remove the lipids.

VI.5.4. Quantification method

In ATR-FTIR spectroscopy experiments, the IR beam is directed into an IR transparent element, the Si substrate here shaped as a prism (refractive index n_1 = 3.42) in contact with an external medium with lower refractive index (air or solution, n_2 ~1) (**Fig. S8**).

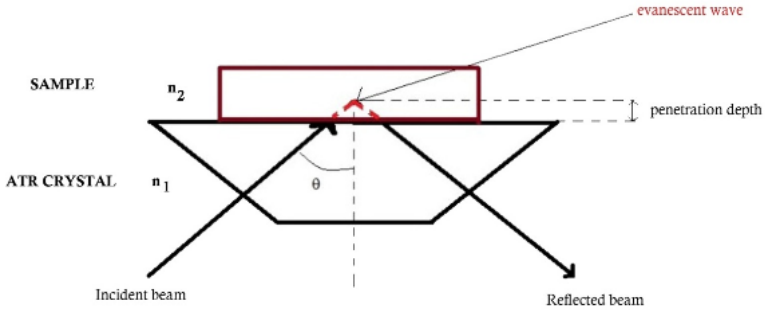

Figure S8 *Scheme of ATR working principle (Ref.224)*

Because of the difference of refractive index, the IR beam is totally reflected at the Si/air or solution interface giving rise to a propagation of the IR beam inside the material. At each reflexion, the evanescent part of the electromagnetic wave propagates in the outside medium over a distance δ (eq.13) (where v denotes the wavenumber of the IR light, n_1 and n_2 are the refractive index of the internal reflection element (Si) and the rarer medium (water or air), respectively, and θ is the angle of incidence) and may be absorbed by the dipoles present on or nearby the surface leading to a diminution of the intensity of the incident beam.

$$\delta = 1/[v2\pi(n_1{}^2 sin^2\theta - n_2{}^2)^{\frac{1}{2}}] \qquad \text{eq. 13}$$

In ATR geometry, the intensity of the signal associated with the infrared vibrational mode of an adsorbate dipole can be computed, provided that the infrared cross-section of the mode is known. This cross-section can be determined if the absorption of the considered mode can be measured in a liquid-phase experiment in the same geometry taking (i.e surrounded with the same modes when absorbed on the surface). Therefore, the number of absorbing dipoles parallel N// and perpendicular N⊥ can be determined from the measured absorbance in p and s polarization (Abs_p and Abs_s), the calculation of the intensity of the electromagnetic field I_x, I_y and I_z in the 3 directions of the space (eq.(14-16)) and calibrated absorbance ($Abs_s°$ measured for a given dipole concentration in solution C) taking into account the dielectric properties of the external medium (eq.14 to eq.19):

$$I_x = \frac{4n_1{}^2 cos^2\theta(n_1{}^2 sin^2\theta - n_2{}^2)}{n_2{}^4 cos^2\theta + n_1{}^4 sin^2\theta - n_1{}^2 n_2{}^2} \qquad \text{eq. 14}$$

$$I_y = \frac{4n_1{}^2 cos^2\theta}{n_1{}^2 - n_2{}^2} \qquad \text{eq. 15}$$

$$I_z = \frac{4n_1{}^4 sin^2\theta cos^2\theta}{n_2{}^4 cos^2\theta + n_1{}^4 sin^2\theta - n_1{}^2 n_2{}^2} \qquad \text{eq. 16}$$

$$\text{N}// = I_y^0 \left(\frac{C}{3}\right)\left(\frac{\delta}{abs_s^0}\right)\left(\frac{1}{I_y}\right)\left(\frac{n_1 cos\theta}{n_1^0 cos\theta^0}\right) abs_s \qquad \text{eq. 17}$$

$$\text{N}\perp = I_y^0 \left(\frac{C}{6}\right)\left(\frac{\delta}{abs_s^0}\right)\left(\frac{1}{I_y}\right)\left(\frac{1}{I_z}\right)\left(\frac{n_1 cos\theta}{n_1^0 cos\theta^0}\right)\left(\frac{n_{ML}}{n_2}\right)^4 (I_y abs_p - I_x abs_s) \qquad \text{eq. 18}$$

$$\text{N} = \text{N}\perp + \text{N}// \qquad \text{eq. 19}$$

C, $I_{x,y,z}°$ and $abs_s°$ correspond respectively to the dipole concentration in solution, the calculated intensity of the electromagnetic field and the absorbance measured in the calibration experiments. θ is the angle incidence of the IR beam. n is the refractive index of the medium (1 = prism index, 2 = solution index, *ML* = adsorbate index).

In the case of lipids quantification on P3HT surface (Figure S9), CH_2 symmetrical stretching dipole has been focused. Area of the absorbance from the dipoles C-H of the lipids aliphatic CH_2 chain correspondings both the crystal and the liquid lipids phases of the layer at 2850 and 2856 cm^{-1} respectively was extracted in p (abs_p) and s polarization (abs_s) and normalized with the numbers of reflexion R_n (eq.20).

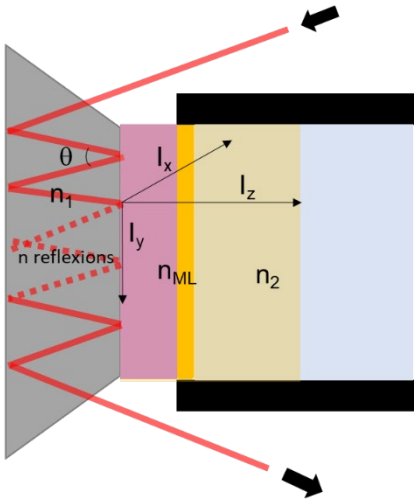

Figure S9 *Scheme of ATR in the case of lipids quantification on P3HT*

$$R_n = \frac{L}{e * tan\theta} \qquad \text{eq. 20}$$

with L the length of the prism (here the diameter of the cell (10 mm)), e the thickness of the prism (0.52 mm) and θ the angle of incidence (43°). R_n is divided by 2 as we work on one side of the prism. R_n = 19/2. Calibration was achieved with pure tetradecane. Absorbance of the CH_2 stretching symmetric mode in s (abs_s^0) polarization, incidence angle θ^0 (47.5°), reflexion index n_1^0 of Si (3.42) and intensity of the electromagnetic field $I_{x,y,z}^0$ (1.7594, 2.2118, 2.5918 respectively) obtained from the tetradecane quantification was inserted to the **eq.17** & **eq.18**. The absorption coefficient of the considered mode is proportional to the vibrator concentration in the layer with the same proportionality coefficient as that between the absorption coefficient and the vibrator concentration in the liquid (here tetradecane). We assume that $n_{ML} = n_{lipids} = n_{P3HT} = 1.47$. To have further detail about the ATR quantification method, please refer to the thesis of A. Faucheux[117, 118, 104].

VI.6. Other common techniques

VI.6.1. Atomic Force Microscopy (AFM)

VI.6.1.a. Imaging in tapping mode

The AFM consists of a cantilever with a sharp tip (probe) at its end that is used to scan the specimen surface (**Fig. S10**). For imaging, the reaction of the probe to the forces that the sample imposes on it can be used to form an image of the three-dimensional shape (topography) of a sample surface at a high resolution. In tapping mode, the cantilever is driven to oscillate up and down at or near its resonance frequency. This oscillation is commonly achieved with a small piezo element in the cantilever holder, the frequency and amplitude of the driving signal are kept constant, leading to a constant amplitude of the cantilever oscillation as long as there is no drift or interaction with the surface. The interaction of forces acting on the cantilever when the tip comes close to the surface (Van der Waals forces, dipole-dipole interactions, electrostatic forces, etc.) cause the amplitude of the cantilever's oscillation to change as the tip gets closer to the sample. This amplitude is used as the parameter that goes into the electronic servo that controls the height of the cantilever above the sample. The servo adjusts the height to maintain a set cantilever oscillation amplitude as the cantilever

is scanned over the sample. A tapping AFM image is therefore produced by imaging the force of the intermittent contacts of the tip with the sample surface[217].

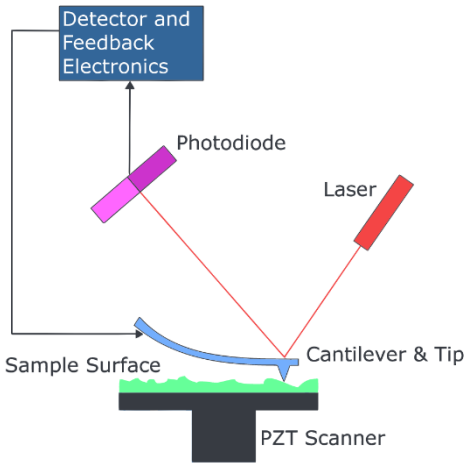

Figure S10 *Scheme of the AFM composition*

The AFM images presented in this thesis were obtained by using an NTEGRA branded AFM from NT-MDT in tapping mode. Silicon tips (MikroMash) with theoretical resonant frequency of 150 kHz and a spring constant of 5.4 N/m at 20°C were used.

VI.6.1.b. Force measurements

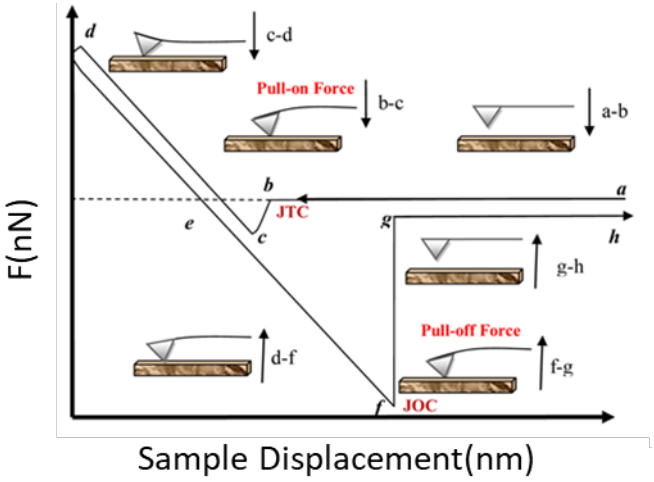

Figure S11 *Representation of a typical F vs sample displacement curve*

An AFM force-distance curve (**Fig. S11**) is a plot of the interaction forces between a tip and a sample versus the tip-sample distance. First (a-b) the tip approaches the sample surface; the force is zero. (b-c) the tip-surface contact occurs with predominant Van der Waals forces. A deflection of the cantilever happen and some repulsion force can exist. (c-d) by continuing to approach, the force applied on the surface increase and induces both indentations of the tip and/or bending of the cantilever. (d-f) retraction of the tip from the surface. Adhesive forces may impede the retraction of the tip. Capillaries forces represent the main adhesive forces. In the air, several nanometers of water is absorbed in the surface of the sample bridging the tip to the sample. Working in water is preferred

[217] (Geisse, 2009)

to avoid this problem. (f-g) pull-off force to take off the tip from the sample. (g-h) the tip is not anymore on the surface. The force is zero.

To obtain such curves, the sample (or the tip) is moved forward to the tip (or sample) in the z-direction then backward and the cantilever deflection is acquired along with the cantilever displacement. The deflection is the result of two contributions: the tip-sample interaction and the cantilever elastic force. At a given tip-sample distance, the cantilever bends until its elastic force is equal to the tip-sample interaction according to Hooke's law (**eq 24**):

$$F = k_c \delta_c \qquad \textbf{eq. 24}$$

with k_c the spring constant of the cantilever and δc the cantilever deflection. Force measurements were carried out in deionized water to avoid the effect of capillary force using AFM (NTEGRA from NT-MDT). Silicon tips CSC17 from MikroMash with a typical resonance frequency of 14 kHz in solution and tip radius in the range 8−10 nm were selected for this testing. The AFM tip radii were determined after imaging the tip by scanning electron microscopy. The spring constants in the range from 0.1 to 0.3 N/m were determined using the thermal noise method after obtaining the deflection sensitivity of the cantilever by pressing the AFM tip against a hard reference silicon surface. Cantilever deflection sensitivity measurements were performed before all sets of measurements.

VI.6.2. X-ray Photon Spectroscopy (XPS)

X-ray photoelectron spectroscopy (XPS) is a well-known technique to fathom around 10 nm of the surface and therefore qualify and quantify the molecular composition of the surface. XPS spectra are obtained by irradiating a material with a beam of X-rays while simultaneously measuring the kinetic energy and number of electrons that escape from the top 0 to 10 nm of the material being analyzed.

The measurements were performed on XPS at Clermont-Auvergne University by Guillaume Monier with Source X Omicron DAR 400 using Mg anode E=1253.6 eV; detector Omicron EA in constant analyser energy mode at 20 eV, angle of 55° between the detector and the X beam source. The sample holder is made of non-magnetic material (molybdenum).

VI.6.3. UV-vis spectroscopy

UV-vis spectroscopy is a quantitative measurement of the absorption/transmission or reflection of a material as a function of wavelength. Molecules containing bonding and non-bonding electrons (n-electrons) can absorb energy in the form of ultraviolet or visible light to excite these electrons to higher anti-bonding molecular orbitals. The more easily excited the electrons (i.e. lower energy gap between the HOMO and the LUMO), the longer the wavelength of light it can absorb.[218]

The absorbance of the different materials presented in this thesis was obtained by a Jasco V-670 spectrophotometer. The measurement range was 320-240 nm and a scan speed of 200 nm/min and data interval of 0.1 nm with 801 points was applied.

VI.6.4. Nuclear Magnetic Resonance (NMR)

NMR is a physical method to obtain physical, chemical, electronic and structural information about molecules. In a constant strong magnetic field, a compound possessing nuclei with non-zero nuclear spin (typically ^{1}H, ^{13}C) is placed. The magnetic field is then perturbed by a weak oscillating

[218] (Skoog, West, & Holler, 1999)

magnetic field. When the oscillation frequency matches the intrinsic frequency of the nuclei, which depends on the strength of the static magnetic field, the chemical environment, and the magnetic properties of the isotope involved, a response by producing an electromagnetic signal with a characteristic frequency is observed.

In this thesis, ^{1}H and ^{13}C NMR spectra were recorded on a JEOL ECS spectrometer at 400 MHz (^{1}H) and 100 MHz (^{13}C) at room temperature. NMR chemical shifts are given in ppm relative to Me_4Si with solvent resonances used as internal standards ($CDCl_3$: 7.26 ppm for ^{1}H and 77.2 ppm for ^{13}C).

VI.6.5. High resolution Mass spectroscopy (HRMS)

A mass spectrometer (MS) generates multiple ions from the sample under investigation, it then separates them according to their specific mass-to-charge ratio (m/z), and then records the relative abundance of each ion type. The first step in the mass spectrometric analysis of compounds is the production of gas phase ions of the compound, basically by electron ionization. This molecular ion undergoes fragmentation. Each primary product ion derived from the molecular ion, in turn, undergoes fragmentation, and so on. The ions are separated in the mass spectrometer according to their mass-to-charge ratio, and are detected in proportion to their abundance. A mass spectrum of the molecule is thus produced. It displays the result in the form of a plot of ion abundance versus mass-to-charge ratio. Ions provide information concerning the nature and the structure of their precursor molecule.

Here, MS (in electrospray ionization mode) analyses were performed on a SYNAPT G2 HDMS (waters) spectrometer at the "Spectropôle" of Aix-Marseille University[219]. This instrument was equipped with an electrospray ionization source (ESI) and a TOF mass analyzer. The sample was ionized in electrospray positive mode with a tension of 2.8 kV, the orifice tension was 50 V and the N_2 rate of flow was 100L/h.

VI.6.6. X-ray diffraction for crystal analysis (XRD)

X-ray crystallography is a method of determining the arrangement of atoms within a crystal, in which a beam of X-rays strikes a crystal and scatters into many different directions. From the angles and intensities of these scattered beams a three-dimensional picture of the density of electrons within the crystal can be produced. From this electron density, the mean positions of the atoms in the crystal can be determined, as well as their chemical bonds, their disorder and various other information.

The presented experiments were made at the Spectropôle by Michel Giorgi on a Rigaku Oxford Diffraction SuperNova diffractometer and measured at 203, 250, and 150 K, respectively, under Cu radiation (λ = 1.54184 Å). Data collection, reduction, and multiscan ABSPACK corrections were performed with CrysAlisPro (Rigaku Oxford Diffraction). Using Olex2[220],the structures were solved with the ShelXT structure solution program using Intrinsic Phasing and refined with ShelXL using least-squares minimization[221].

[219] (Spectropôle from Aix Marseille University, s.d.)
[220] (Dolomanov, Bourhis, Gildea, Howard, & Puschmann, 2009)
[221] (Sheldrick, 2015)

VII. Annexes

VII.1. NMR ^{1}H and ^{13}C of the cesium probe (*compound* 6)

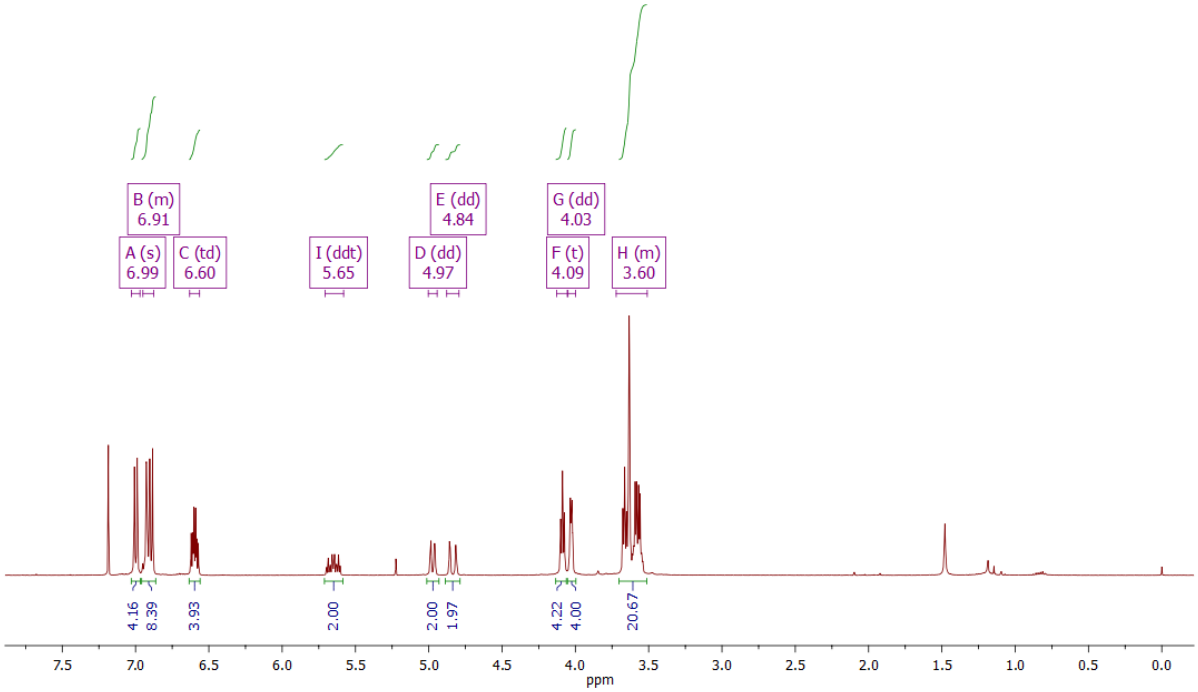

Figure S12 *NMR ^{1}H of the compound **6** (cesium probe) Analysis at 400 MHz in CDCl3 (δ= 7.00 (d, 4H, 3J= 7.5 Hz), 6.91 (dd, 8H, 3J= 12.1, 4.8 Hz), 6.60 (td, 4H, 3J= 7.5, 4.5 Hz), 5.65 (ddt, 2H, 3J= 17.2, 10.6, 4.6 Hz), 4.97 (dd, 2H, 3J= 10.7, 1.7 Hz), 4.84 (dd, 2H, 3J= 17.3, 1.8 Hz), 4.09 (t, 4H, 3J= 5.1 Hz), 4.03 (dd, 4H, 3J= 4.1, 2.0 Hz), 3.60 (m, 20H))*

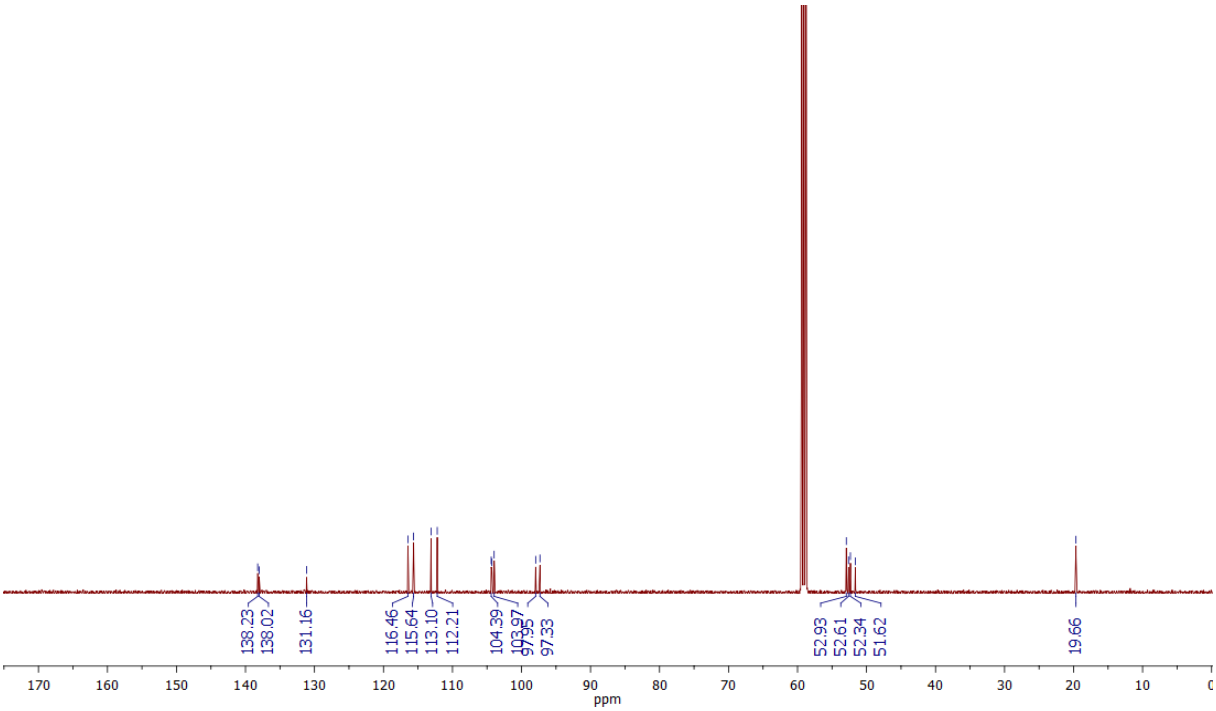

Figure S13 *NMR ^{13}C of the compound **6** (cesium probe). Analysis at 100 MHz in CDCl3 (δ= 138.23; 138.02; 131.16; 116.46; 115.64; 113.10; 112.21; 104.39; 104.29; 103.97; 97.95; 97.33; 52.93; 52.61; 52.34; 51.62 ppm*

VII.2. NMR ^{1}H and ^{29}Si of the cesium probe with the anchor function (*compound* 7)

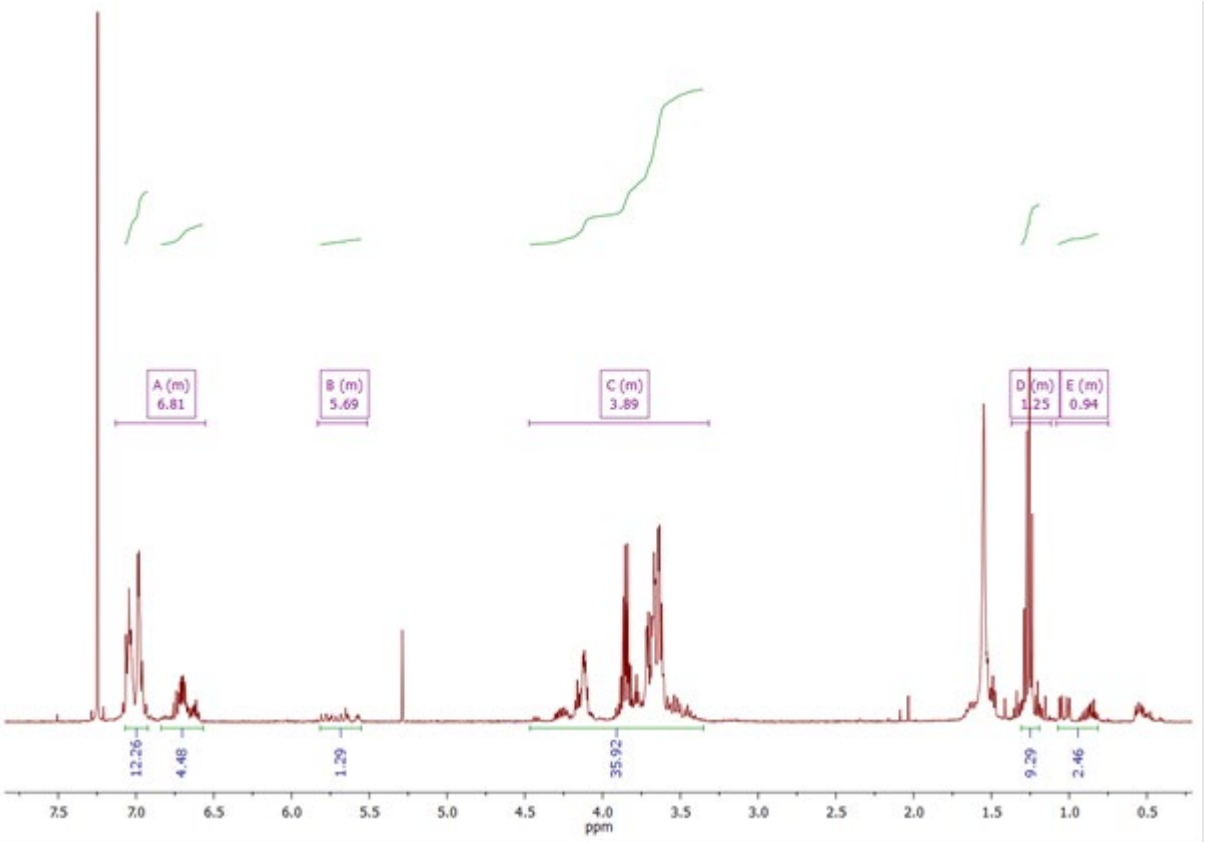

Figure S14 *NMR ^{1}H of the cesium probe with anchor function (compound **7**) Analysis at 400 MHz in CDCl3 (δ = 6.81 (m, 16H, H aromatics), 5.69 (m, 1H, H vinyl), 3.89 (m, 36H, CH2), 1.25 (m, 9H, methyl), 0.94 (m, 2H, CH2))*

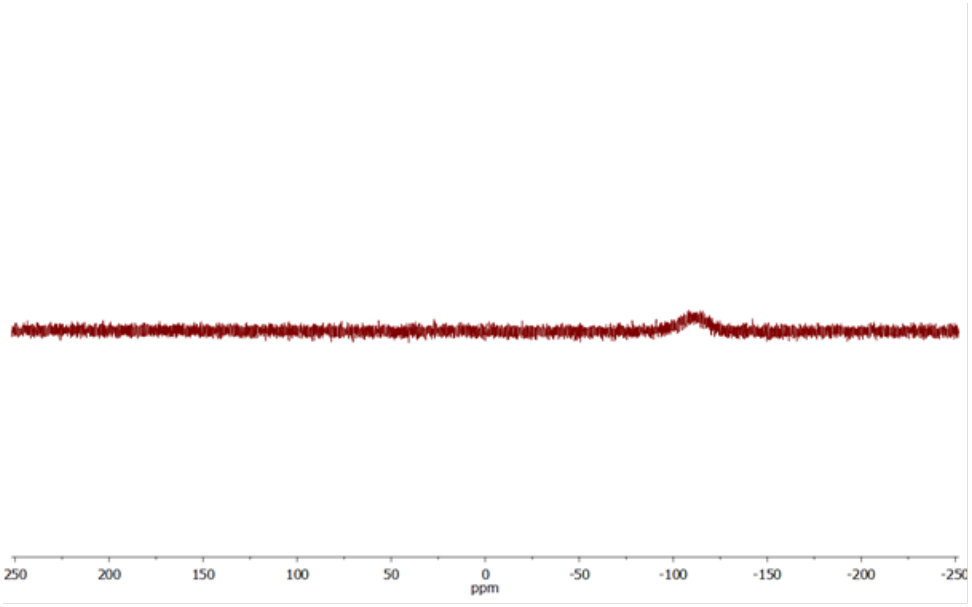

Figure S15 *NMR ^{29}Si of the probe **7** Analysis at 79 MHZ in CDCl3(δ = -100 (s, 1Si)*

VII.3. HRMS of the probe (*compound* 6)

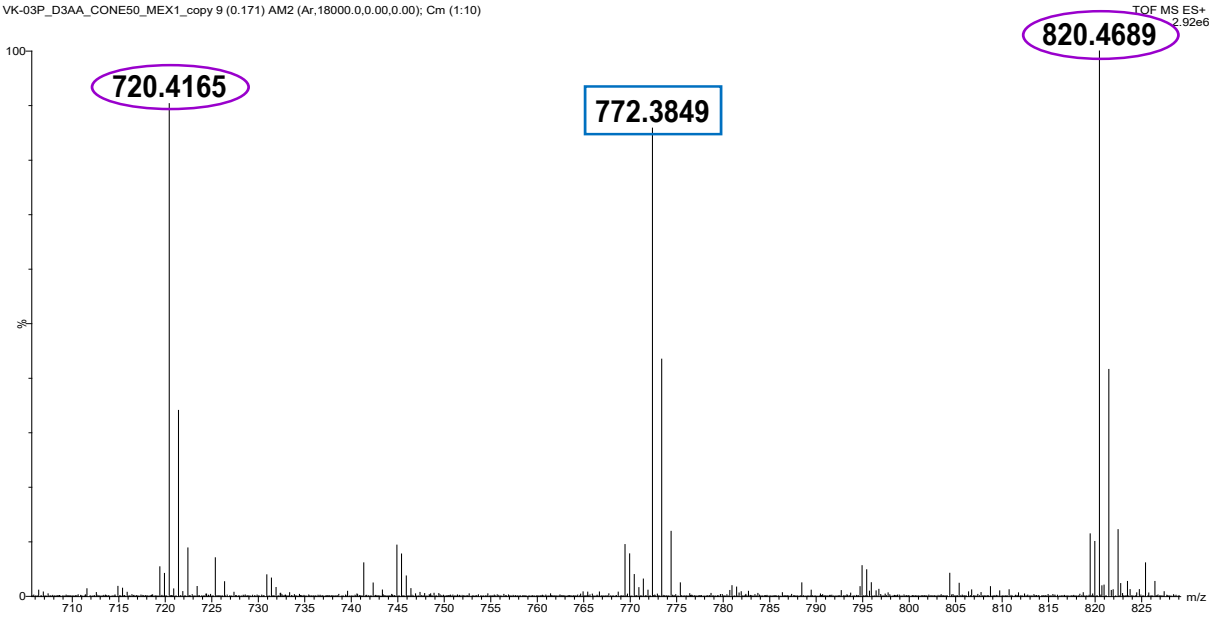

Figure S16 *High Resolution Mass Spectrum of the molecule **6** in electrospray positif mode. Targeted ion $(M+NH4)^+$ is detected at m/z 772.3849 and the peaks for the internal references (PMMA800) are observed at respectively m/z 720.4165 and m/z 820.4689* .This result is showing that the compound **6** has a molecular formula of $C_{48}H_{50}O_8$, an exact monoisotopic weight of 754.3506 Da and hold 24 insaturations with an error less than 1 ppm.

VII.4. Crystallographic parameter of the probe (*compound* 6) by XRD

Table 9 Crystallographic data of the compound **6** obtained by X-ray diffraction. Atomic coordinates, bond lengths and angles, and thermal parameters have been deposited at the Cambridge Crystallographic Data Centre (CCDC number: 1935509, DOI: 10.5517/ccdc.csd.cc22z1sx). Copies of the data can be obtained free of charge on application to CCDC, 12 Union road, Cambridge CB21EZ, UK. Email: deposit@ccdc.cam.ac.uk.

Bond precision:	C-C = 0.0056 A		Wavelength=1.54184
Cell:	a=11.3911(2)	b=10.4981(2)	c=17.4878(3)
	alpha=90	beta=106.375(2)	gamma=90
Temperature:	293 K		
	Calculated		Reported
Volume	2006.45(7)		2006.45(7)
Space group	P 21		P 1 21 1
Hall group	P 2yb		P 2yb
Moiety formula	C48 H50 O8		C48 H50 O8
Sum formula	C48 H50 O8		C48 H50 O8
Mr	754.88		754.88
Dx,g cm-3	1.250		1.249
Z	2		2
Mu (mm-1)	0.676		0.676
F000	804.0		804.0
F000'	806.43		
h,k,lmax	13,12,21		13,12,21
Nref	7757[4103]		7060
Tmin,Tmax	0.823,0.960		0.739,1.000
Tmin'	0.816		
Correction method= # Reported T Limits: Tmin=0.739			
Tmax=1.000 AbsCorr = MULTI-SCAN			
Data completeness= 1.72/0.91		Theta(max)= 71.213	
R(reflections)= 0.0428(6283)		wR2(reflections)= 0.1238(7060)	
S = 1.025	Npar= 505		

VII.5. Full scan NMR ^{1}H of the titration experiments

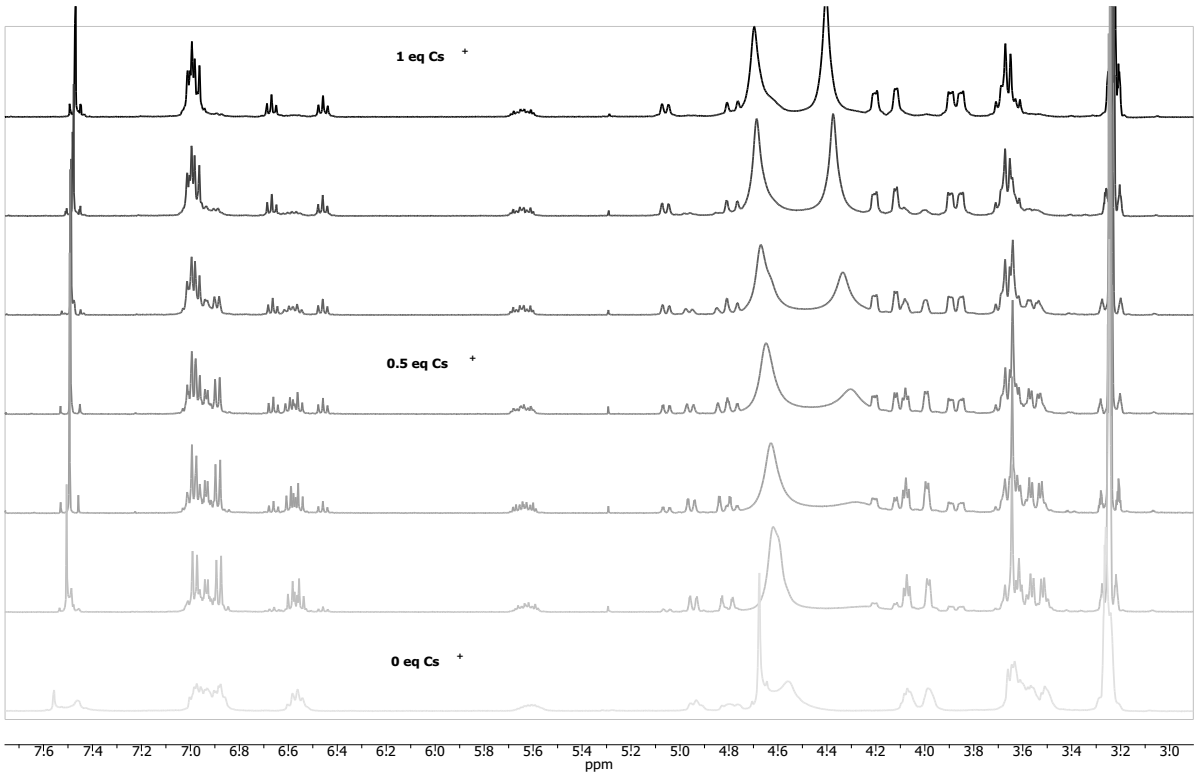

Figure S17 *1H NMR (400 MHz) titration experiments in MeOD/ CDCl3 (1:1) of the host molecule **6** with CsCl in D2O*

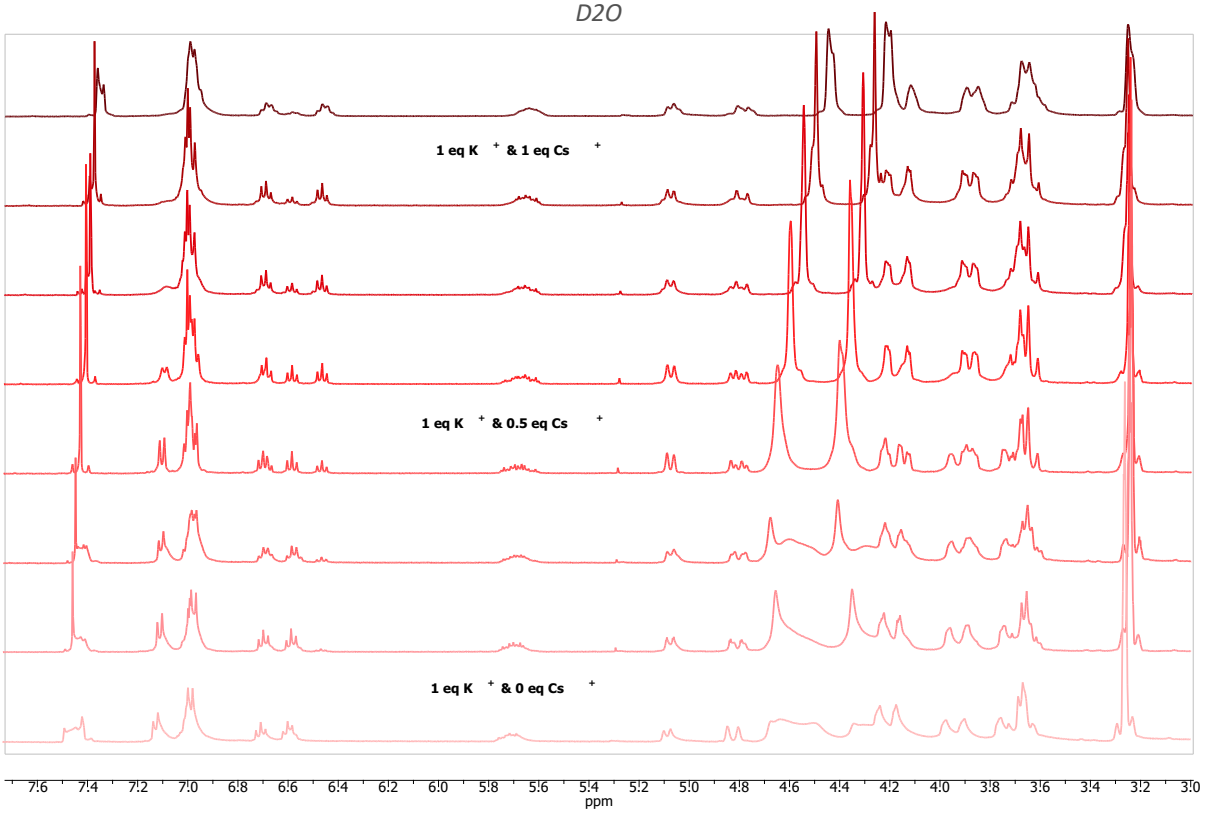

Figure S18 *1H NMR (400 MHz) titration experiments in MeOD/ CDCl3 (1:1) of the complex **6**/K+ with CsCl in D2O*

> *"The scientific man does not aim at an immediate result. He does not expect that his advanced ideas will readily taken up. His work is like that of the planter – for the future. His duty is to lay the foundation for those who are to come, and point the way. He lives and labors and hopes."*
>
> - *Nikola Tesla*

VIII. Summary in French

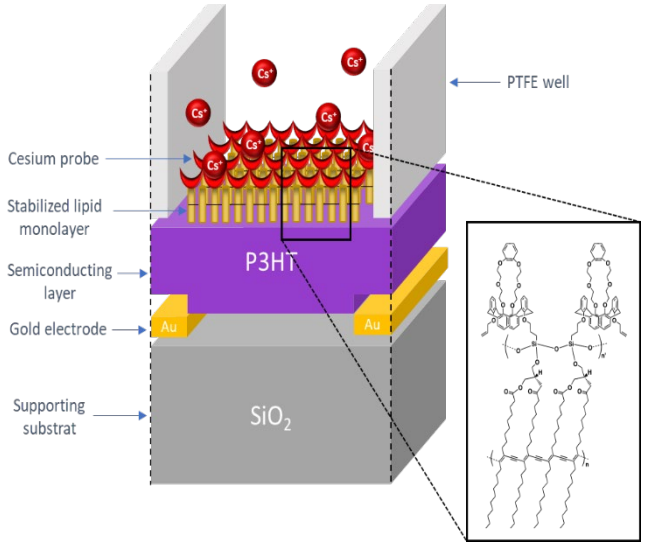

Figure R2 *Prototype du FET développé pour la détection du césium*

Dans cette thèse, j'aimerais présenter une nouvelle interface de détection pour les FET dédiée à la détection de trace de césium et composée de deux couches organiques ultra-minces : un poly(3-hexylthiophène) (P3HT) de 20 nm d'épaisseur comme couche semi-conductrice et une couche diélectrique de lipides artificiels de 2,5 nm d'épaisseur. Un tel assemblage présente un certain nombre d'avantages que je vais expliquer dans cette thèse. Après avoir étudiés les nano-diélectriques à base de lipides et leurs auto-assemblages sur la couche de P3HT, la synthèse et la caractérisation de la sonde sélective pour le césium à base de calixarène et son greffage sur la couche nano-diélectrique seront présentées. Pour finir, je montrerai la fabrication du FET avec l'interface organique développée. La performance du FET développé pour la détection du césium sera également étudiée dans la dernière partie comme preuve de concept (**Figure R1**).

VIII.1. La grille diélectrique à base de monocouches de lipides

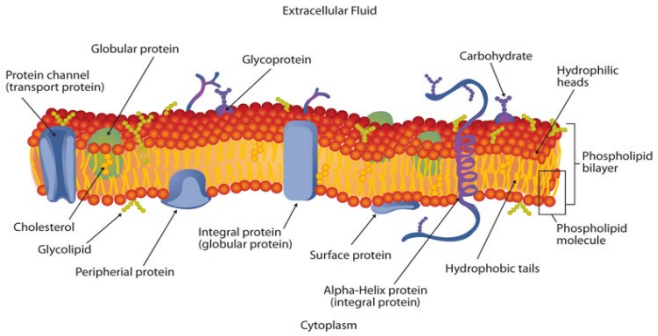

Figure R2 *Composition of cell membrane in human body (Lipid Bilayer Membranes, chem.libretexts.org)*

Dans le système vivant, le rôle de la membrane lipidique est de compartimenter les parties internes et externes des cellules. La membrane est un isolant naturel (**Figure R2**) qui joue un rôle efficace de barrière au transport ionique et électronique à travers la membrane, associé à une résistance électrique de l'ordre de plusieurs giga-Ohms de magnitude[77]. Parmi les lipides, les

phospholipides constituent la grande famille des lipides[78]. La flexibilité des paramètres tels que le groupe de tête, la longueur de la chaîne et le degré de saturation de la chaîne aliphatique offre une diversité structurelle au sein de chaque type de phospholipides. En raison de leur nature amphiphile, c'est-à-dire du groupe de tête hydrophile et des queues hydrophobes (une ou deux), les lipides s'auto-organisent spontanément en milieu aqueux en bicouches sous forme de vésicules. Dans les vésicules, les groupes de tête des lipides sont en contact avec le milieu aqueux tandis que les chaînes hydrophobes s'orientent vers l'intérieur des vésicules.

Les lipides peuvent également être utilisés pour former des couches supportées sur des substrats, sous la forme de monocouches, de bicouches ou de multicouches. Le type de couche et l'orientation des molécules à la surface (tête en haut ou en bas) sont directement corrélés aux propriétés hydrophobes du substrat. Une propriété intéressante des couches lipidiques est leur fluidité par rapport à la température. Pour chaque type de lipides, une transition de gel à fluide se produit à une température donnée[93]. Elle est principalement déterminée par la longueur des chaînes aliphatiques, le nombre de liaisons insaturées et le groupement chimique de tête[94]. Cette fluidité induit une instabilité dans l'air, lorsqu'ils sont exposés à un solvant ou sous l'application d'une force mécanique ou électrique. C'est la raison pour laquelle les lipides ont été mal exploités dans le développement de dispositifs électroniques.

Afin de stabiliser les lipides sur des substrats solides, plusieurs stratégies ont été développées[95,96]. Parmi ces stratégies, une méthode d'immobilisation et de stabilisation des lipides a été proposée par Charrier et *al :* en utilisant la polymérisation radicalaire des groupes acétylène présents dans la queue aliphatique des lipides de 1,2-bis-(10,12-tricosadiynoyl)-sn-glycéro-3-phosphocoline (DCPC), il a été possible d'obtenir des lipides réticulés avec des propriétés mécaniques, chimiques et diélectriques élevées sur un substrat de silicium hydrogéné (SiH) d'une épaisseur de 2,2 nm (+/-0,2)[73]. Ces couches où les lipides sont réticulés ont été utilisées comme une couche diélectrique ultrafine dans des transistors à effet de champ à base de silicium et comme une plate-forme capacitive pour la détection des ions métalliques (Figure R3).

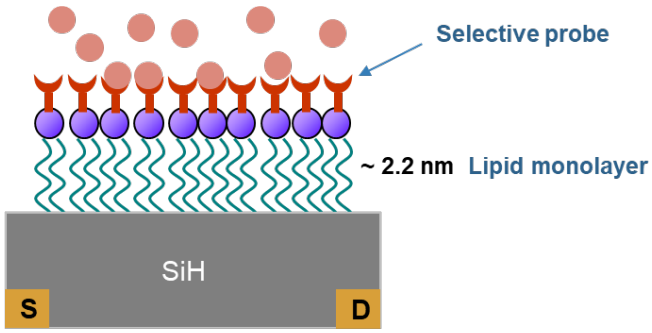

Figure R3 *Représentation schématique des lipides comme grille diélectrique*

Les lipides constituent donc des candidats idéals comme diélectrique de grille pour les FET organique (OFET) à basse tension de fonctionnement. Le succès d'une telle couche lipidique en tant que diélectrique de grille efficace dépend de plusieurs paramètres : tout d'abord, la couche doit être suffisamment dense pour être un bon isolant. Deuxièmement, la couche doit être mécaniquement robuste pour être utilisée dans des appareils. Troisièmement, l'interface lipide/couche semi-conductrice doit présenter un faible piégeage de charges interfaciales. Toutes ces exigences dépendent fortement de la qualité de la couche lipidique en termes d'organisation, de densité, de taux de réticulation qui dépendent tous en fin de compte de l'interaction entre les lipides et la couche semi-conductrice. En particulier, il a été démontré que pour obtenir une réticulation efficace, la disposition

des groupes diacétyléniques au sein de l'assemblage de la monocouche doit répondre à la même conformation spatiale que celle des cristaux[97]. Un exemple de monocouches lipidiques denses et lâches est illustré à la **Figure R4**.

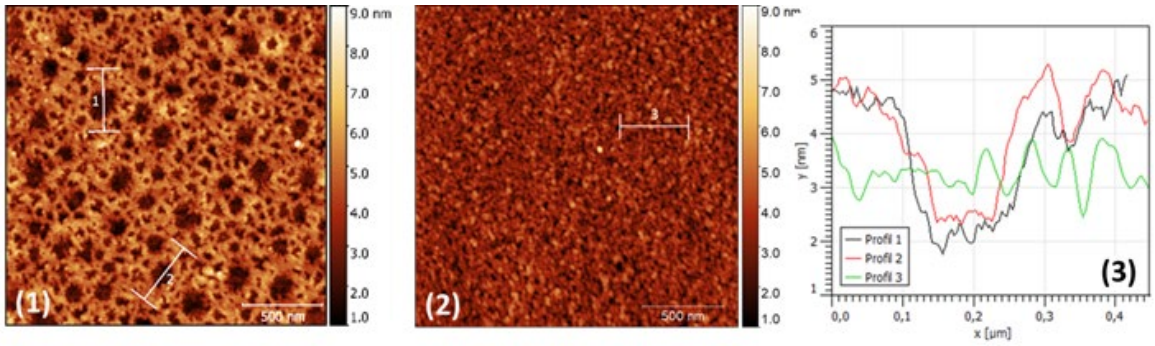

Figure R4 *Images topographiques AFM des monocouches de lipides DCOH sur P3HT (1) peu dense (2) et dense. (3) Profil des trous présents sur la surface de (1) & (2)*

Cette partie se concentre sur la formation des lipides réticulés utilisés comme grille diélectrique à la surface du polymère semi-conducteur P3HT dans le dispositif FET. Les groupes de tête de phosphatidylcholine du DCPC ont été clivés pour obtenir des lipides de glycérol (DCOH) qui ont été assemblés sur la couche P3HT en utilisant une version dérivée de la méthode de fusion des vésicules. La densité, la structure et l'organisation de l'assemblage des lipides ont été étudiées à l'aide de différentes méthodes, notamment la spectroscopie infrarouge à transformée de Fourier (ATR FTIR) en mode de réflectance totale atténuée *in situ*, la spectroscopie photoélectronique à rayons X (XPS) et la microscopie à force atomique (AFM). La stabilité mécanique de la couche lipidique sur des couches P3HT a été étudiée par des mesures d'indentation au moyen de l'AFM.

VIII.1.1. Clivage des têtes phosphatidylcholines des lipides DCPC

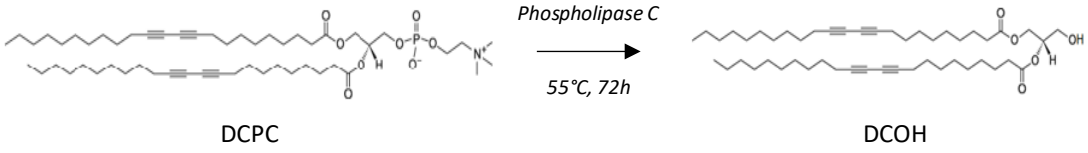

Figure R5 *Enzymatic cleavage reaction of DCPC*

La couche diélectrique qui compose notre transistor à effet de champ est basée sur des lipides et en particulier sur une version modifiée des lipides 1,2-bis-(10,12-tricosadiynoyl)-sn-glycéro-3-phosphocoline (DCPC) disponibles dans le commerce (Avanti Polar Lipid,Inc.) qui portent deux groupements diacétylène. Avant le dépôt sur la couche semi-conductrice, la modification de la DCPC est cruciale. L'élimination du groupe de tête initial de la phosphatidylcholine présent sur le DCPC laisse au groupe de tête des lipides une fonction hydroxyle (OH) qui sera utilisée ultérieurement pour greffer la sonde de césium et stabiliser davantage la couche. La description de la sonde et de sa greffe sur la couche diélectrique sera examinée en détail dans le chapitre suivant. A ce stade, il est intéressant de comprendre qu'un lipide contenant un groupe de tête hydroxyle est nécessaire pour les étapes futures de la fonctionnalisation et de la stabilisation de la couche diélectrique.la modification du DCPC par clivage du groupe de tête phosphatidylcholine pour obtenir le lipide de glycérol (DCOH) a été réalisée en utilisant une réaction enzymatique (**Figure R5**). Le protocole actuel basé sur les travaux précédents de Charrier et *al.*[70,71,72] a été optimisé pour augmenter le rendement (*Exp.Tech. partie VI.4.1.*). Le

succès du clivage des lipides pour obtenir du DCOH a été vérifié par résonance magnétique nucléaire (RMN) de ^{1}H et XPS.

VIII.1.2. Dépôt et stabilisation des monocouches lipidiques de DCOH

Comme présenté dans l'introduction de ce chapitre, la stabilité est le principal problème pour l'application des monocouches lipidiques comme couche diélectrique dans les dispositifs électroniques. Premièrement, ces couches sont très instables dans l'air ou lorsqu'elles sont rincées avec des solvants ; deuxièmement, elles ne supportent pas les forces mécaniques ou électriques. L'application d'un champ électrique entraîne une électroporation même à faible champ, ce qui conduit à la dégradation de ses propriétés diélectriques[98]. Afin de surpasser ce problème, la formation de la monocouche lipidique DCOH sur P3HT a été obtenue à l'aide d'un protocole dérivé de la méthode de fusion des vésicules. Une version compactée de ce protocole est ajoutée à la *partie VI.4.2 de l'Exp. Tech*. Comme cette technique est cruciale pour le projet, elle sera détaillée ici.

Les lipides DCOH sont stockés dans du chloroforme à -20°C pour éviter toute altération. La première étape consiste à évaporer lentement le solvant à 45°C pour éviter d'endommager les lipides. Une fois la plus grande partie du solvant évaporée, on ajoute de l'eau déionisée pour obtenir une solution de DCOH à 0,27 mM. À ce stade, des vésicules lipidiques multilamellaires se forment spontanément (**Figure R6**).

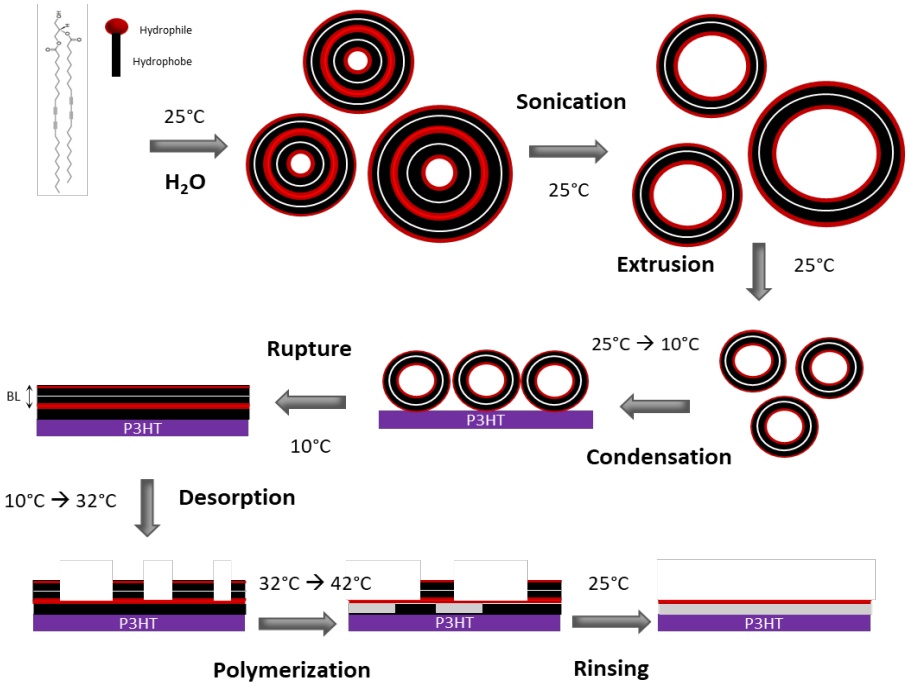

Figure R6 *Représentation schématique de la méthode de fusion des vésicules lipidiques dérivées pour la fabrication de la couche lipidique isolante utilisée dans l'OFET*

Les vésicules unilamellaires sont ensuite obtenues par sonication de la solution lipidique pendant 30 min. Ensuite, les vésicules sont filtrées plusieurs fois avec des membranes en polycarbonate de 0,1 µm de diamètre de pore afin de réduire leur taille. Il est important de réaliser ces étapes juste avant le dépôt. En effet, après ce processus, les vésicules ont une forte courbure qui les rend instables et plus faciles à casser. Les vésicules de lipides DCOH sont ensuite injectées dans un puits de PTFE sur une surface propre de P3HT à 25°C. Sous agitation manuelle, la température est brusquement réduite à 10°C, ce qui provoque la condensation des vésicules et la fusion des lipides sur le P3HT. Ce dépôt de lipides à basse température devrait produire des couches de haute densité. À cette étape, une

monocouche avec des plages supplémentaires de bicouches de 5 nm de hauteur est formée. Après être restée 10 min à cette température, la surface a été chauffée de 1°C/min jusqu'à 32°C, la température à laquelle les sur-couches se désorbent de la surface, laissant une monocouche homogène de DCOH sur le dessus du P3HT. La stabilisation de la monocouche a été obtenue par polymérisation radicalaire des lipides. Elle se produit dans les chaînes aliphatiques où se trouvent les groupes diacétylènes. L'initiateur de la polymérisation radicalaire est le dichlorhydrate de 2,2'-Azobis(2-amidinopropane) (AAPH) ajouté à 0,5 % dans la cellule. La température a ensuite été lentement portée à 35°C pendant 10 min puis à 42°C pendant 60 min. L'échantillon a ensuite été rincé avec de l'eau DI à 25°C sous agitation. À ce stade, la couche réticulée DCOH-R est suffisamment stable sur P3HT pour être rincée et séchée. Des images topographiques AFM de la surface P3HT avant et après la formation d'une couche stable de DCOH-R ont été obtenues (**Figure R7**).

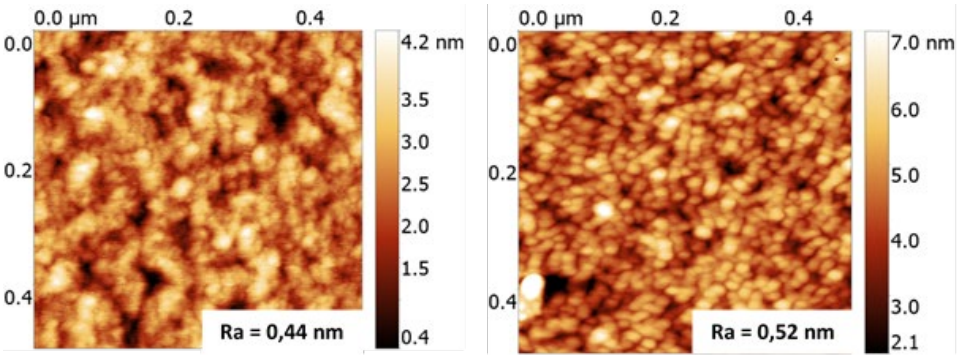

Figure R7 *Images topographiques AFM de P3HT nu (à gauche) et de DCOH-R (à droite) à l'air*

La rugosité moyenne a été légèrement augmentée de 0,44 nm à 0,52 nm avant et après la formation des couches lipidiques respectivement. Mais le principal changement s'est produit sur la structure. De petits domaines de forme arrondie d'environ 20 nm de diamètre sont observables après la formation du DCOH-R. L'angle de contact avant et après le dépôt de DCOH a également été étudié (**Figure R8**).

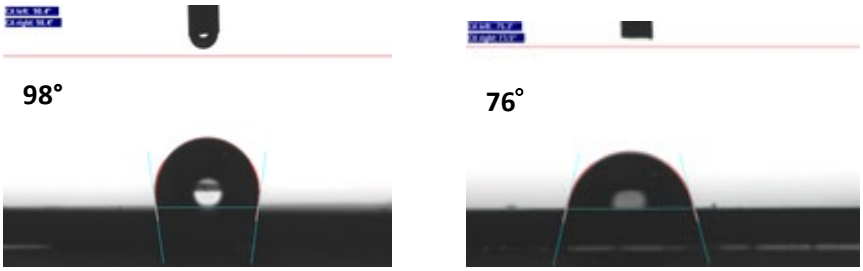

Figure R8 *Angle de contact de la goutte d'eau sur P3HT nu (à gauche) et DCOH-R (à droite) mesuré par un goniomètre*

La surface du P3HT nu a un angle de contact élevé de 98°, ce qui signifie qu'il s'agit d'un matériau hydrophobe. Après la formation du DCOH-R, on observe une diminution de l'angle de contact à 76° en raison des propriétés très polaires des groupes de tête hydroxyles du DCOH.

Ces résultats, obtenus à la fois par des mesures topographiques AFM et des mesures d'angle de contact, confirment le bon dépôt du DCOH-R sur P3HT en utilisant la technique de fusion de vésicules modifiée (**Figure R6**). Néanmoins, avec ces méthodes courantes, il n'est pas possible d'obtenir des informations quantitatives sur la densité, l'organisation et l'efficacité de la polymérisation des lipides. Une autre méthode doit être utilisée.

VIII.1.3. Caractérisation structurelle du diélectrique de grille

Afin d'obtenir des informations quantitatives et qualitatives supplémentaires sur la réticulation, la densité et l'organisation des lipides, la spectroscopie infrarouge à transformée de Fourier à réflectance totale atténuée (ATR-FTIR) a été utilisée. En effet, la FT-IR en mode ATR est une technique bien connue pour la caractérisation des couches minces : elle repose sur la présence d'une onde évanescente à l'interface de réflexion. À notre connaissance, le processus de fusion des vésicules sur les surfaces n'a été étudié que par résonance plasmonique de surface[106], voltampérométrie cyclique et spectroscopie d'impédance[107]. La FT-IR en mode ATR n'a jamais été utilisée pour étudier un processus dynamique se produisant à l'échelle du nanomètre. De ce fait, afin de suivre la formation de la monocouche lipidique, une nouvelle cellule in-situ a été construite pour les besoins de cette étude. Elle contient un système de chauffage/refroidissement, un système fluidique et un système d'agitation pour mélanger les solutions (**Figure R9**).

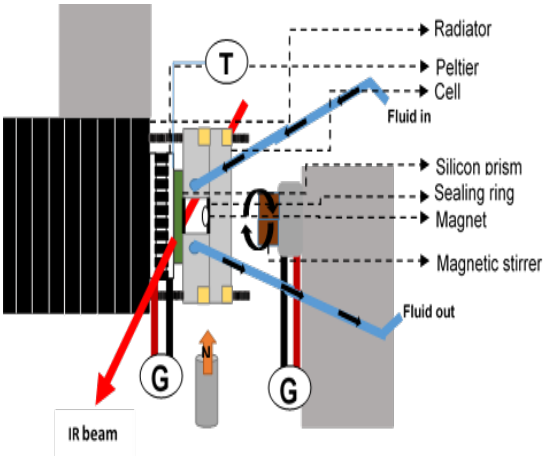

Figure R9 *Représentation schématique de l'installation conçue pour les mesures ATR FT-IR in-situ*

Une telle cellule implantée dans un dispositif expérimental ATR FT-IR présente plusieurs avantages en plus de celui apporté par le mode ATR :

- La réalisation d'expériences *in-situ* permet de soustraire le signal de l'échantillon de référence sans avoir le problème du changement de la ligne de base.

- La plaque Peltier, le système fluidique et l'agitateur magnétique permettent de jouer sur différents paramètres tels que la température, la concentration et l'agitation de la solution injectée.

- L'enregistrement des spectres peut être réalisé dans le temps, ce qui permet de suivre l'évolution de la cinétique des réactions se produisant à la surface du substrat.

- La cellule inerte à base de téflon et les tubes fluidiques évitent les réactions parasitaires.

Dans ce qui suit, tous les spectres ont été enregistrés (**Figure R10**) dans la plage de 1000-3200 cm^{-1} de nombres d'onde avec les polarisations p et s du faisceau IR. Plusieurs pics associés à la signature du DCOH sont visibles. Le signal du groupe ester du DCOH est observable (1154 cm^{-1} ; 1217 cm^{-1} ; 1241 cm^{-1} ; 1735 cm^{-1}). De même que le signal de la chaîne aliphatique des DCOH (2849 cm^{-1} ; 2917 cm^{-1} ; 2958 cm^{-1}). Comme les spectres sont normalisés avec des références dans l'eau, un pic négatif correspondant à la perte de volume d'eau après le dépôt de lipides est apparent à 1640 cm^{-1}.

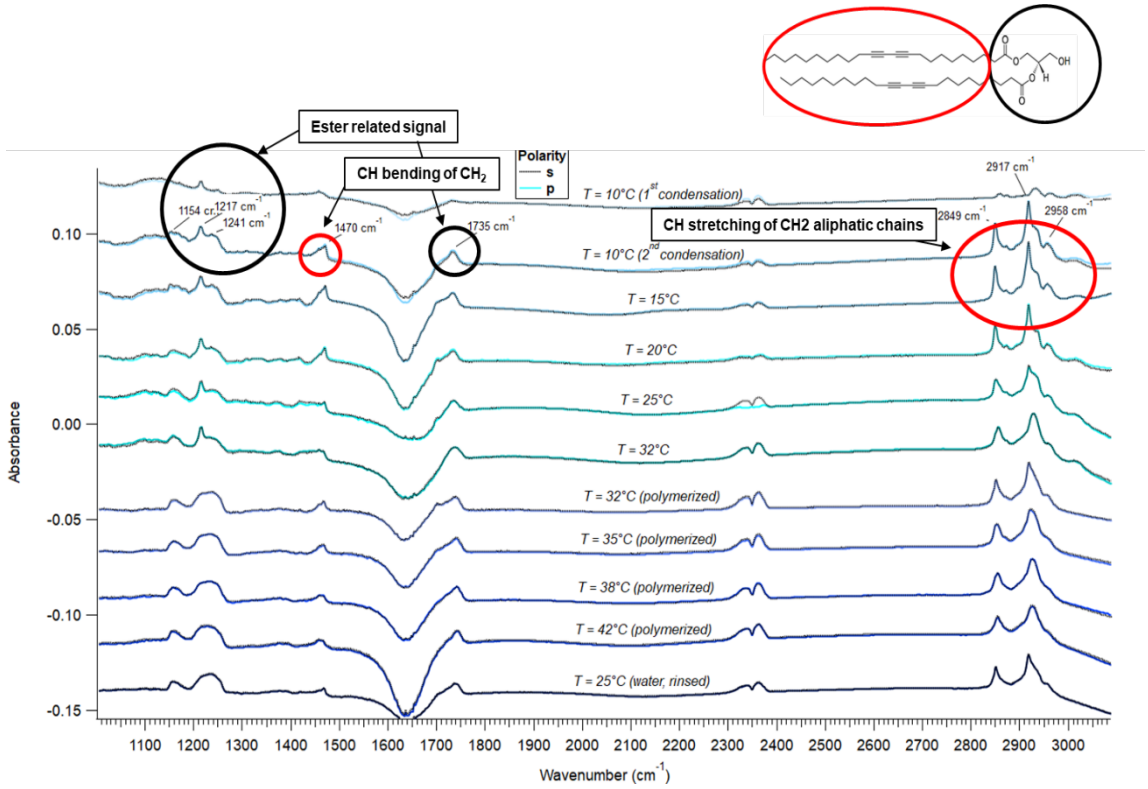

Figure R10 *Spectres IR complets enregistrés en mode ATR in-situ avec polarisation p & s du faisceau à différentes étapes du processus de formation du DCOH-R sur P3HT. Les spectres ont été normalisés avec P3HT en référence à l'eau pour ne garder que le signal des lipides DCOH dans l'eau.*

L'absence du pic lié au groupe acétylène médian (étirement se produisant dans la plage 2260-2100 cm^{-1})[108] avant la polymérisation peut être surprenante. Cependant, il a été démontré que dans certains cas, comme dans les alcynes substitués hautement symétriques, il peut ne pas apparaître du tout en raison de la faible polarité de la triple liaison associée à ces alcynes[109]. À partir de ces spectres, il est possible d'obtenir des informations qualitatives et quantitatives sur la polymérisation, la densité, l'organisation et l'inclinaison des lipides sur P3HT.

L'obtention et la discussion des différentes propriétés structurelles de la monocouche de lipides DCOH sur P3HT sont détaillées dans la version originale de la thèse. Le **Tableau R2** et la **Figure R11** résume les différents résultats obtenus.

Tableau R2 *Caractéristiques structurelles de la monocouche de lipides sur P3HT*

Densité	Orientation	Organisation
2,6. 10^{14} lipid/cm^2	26°	Cristalline

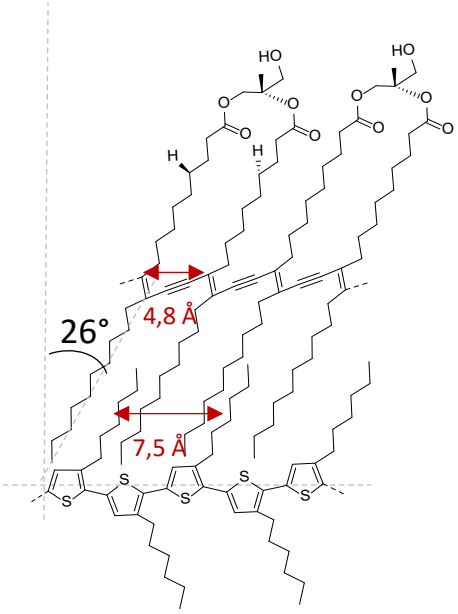

Figure R11 *Représentation moléculaire de DCOH-R enchevêtré sur P3HT*

Afin d'exploiter cette interface monocouche lipide/P3HT dans le développement de dispositifs pouvant être utilisés sur site, une grande robustesse mécanique de la monocouche lipidique sur P3HT est essentielle. Il est bien connu que les couches lipidiques sont très instables sur les substrats, en particulier lorsqu'elles subissent des traitements chimiques, lorsqu'elles sèchent ou lorsqu'elles sont exposées à un champ électrique ou à une contrainte mécanique. Il a été montré que les groupes diacétyléniques présents dans la chaîne aliphatique des lipides DCOH peuvent être polymérisés en introduisant l'agent de polymérisation AAPH à 30°C sur une monocouche bien organisée de lipides DCOH sur P3HT. Après avoir maintenu au moins 1h à 42°C, on peut obtenir des lipides réticulés ayant une résistance mécanique suffisante au lavage à l'eau. Cependant, la stabilité de la couche obtenue après ce processus peut ne pas être suffisante pour d'autres travaux de génie chimique rigoureux. Nous avons vu précédemment que le DCOH-R porte des groupements chimiques OH actifs sur ses groupements de tête. Le groupement de tête des lipides peut donc être utilisé pour une étape de réticulation supplémentaire afin d'améliorer la stabilité de la couche : en faisant réagir le groupe hydroxyle actif des lipides DCOH -R avec des molécules à base de siloxane (**Fig. R12**).

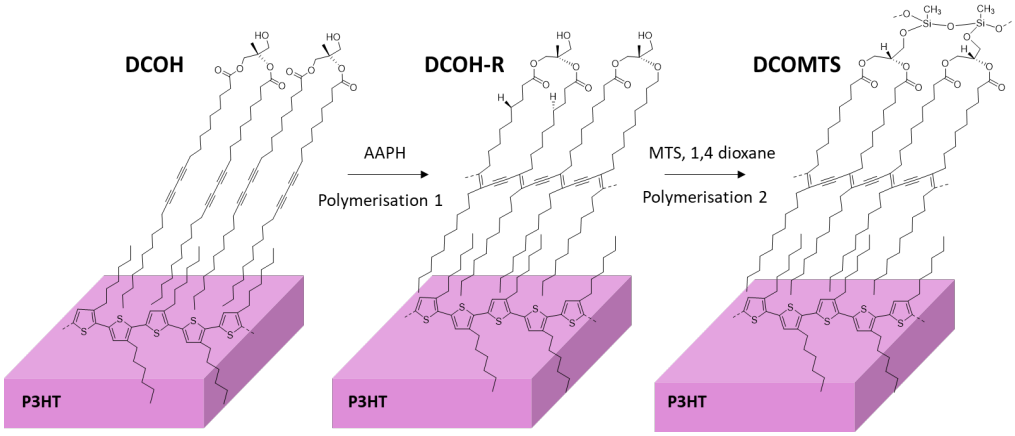

Figure R12 *Etapes de la réaction moléculaire pour obtenir une couche de lipides doublement réticulés (DCOMTS)*

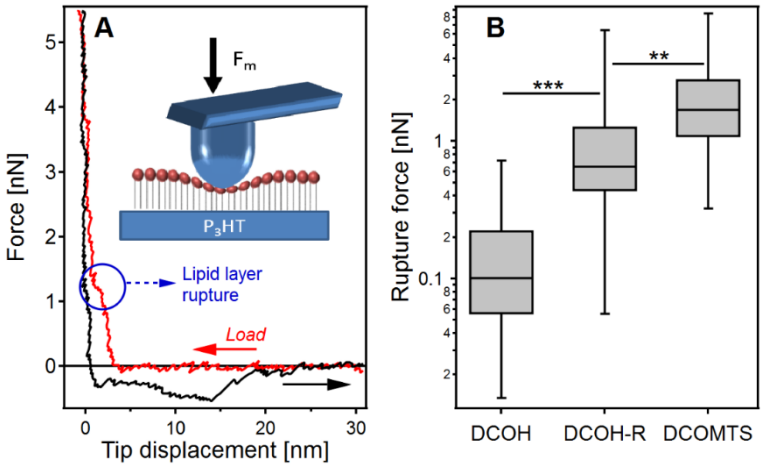

Figure R13 *(A) Experimental example of force vs tip displacement curve obtained on DCOH-R/P3HT force measurements (B) Comparison of the layer breakthrough force for DCOH/P3HT, DCOH-R/P3HT and DCOMTS/P3HT*

L'effet des deux réticulations successives décrites ci-dessus sur la stabilité mécanique de la monocouche de lipides supportée sur P3HT a été étudié à l'aide de mesures d'indentation par AFM[134].. De plus amples informations sont données dans la *partie VI.6.1.b de l'Exp.Tech*. Dans cette expérience, une force normale est exercée sur la couche lipidique par une pointe AFM jusqu'à la rupture de la couche lipidique (**Fig. R13, A**). Les forces de rupture obtenues sur des couches non réticulées formées sur P3HT (DCOH), après la réticulation des chaînes aliphatiques (DCOH-R) et après la réticulation des groupes de tête (DCOMTS) sont rapportées (**Fig. R13, B**). Pour chaque type de couche lipidique, environ 300 mesures ont été effectuées. La très faible force de rupture moyenne de ~0,1 nN obtenue avec la couche de DCOH augmente avec les réticulations jusqu'à 0,6 nN pour le DCOH-R et jusqu'à 1,8 nN pour le DCOMTS, ce qui montre un avantage considérable des réticulations. Cette stabilité améliorée est également marquée par le fait que le lipide doublement réticulé sur le substrat P3HT peut ensuite être rincé avec des solvants, séché et conservé pendant plusieurs semaines sans aucune trace de dommage.

Dans cette partie, nous avons montré la formation et la caractérisation de la grille isolante à base de lipides qui sera utilisée pour le développement du capteur OFET. En utilisant la cellule fluidique personnalisée pour les mesures ATR-FTIR *in-situ*, nous avons pu suivre la formation d'une interface basée sur l'assemblage d'une monocouche de lipides de 2,5 nm et d'un polymère semi-conducteur P3HT. Nous avons montré que les lipides déposés au départ sur la surface très plate de P3HT à 10°C, c'est-à-dire bien en dessous de la température de transition de phase gel/liquide du lipide, s'organisent en une monocouche super dense permettant une réticulation efficace des groupes diacétylènes dans les chaînes aliphatiques et une stabilisation de la couche. Nous avons montré qu'une réticulation supplémentaire au niveau des groupes de tête par silanisation augmente encore plus la stabilité mécanique de la couche. La couche finale a une densité étonnamment élevée de ~2,6 x 10^{14} lipides/cm², c'est-à-dire correspondant à une surface moléculaire de 38,5 Å², dans laquelle les lipides sont inclinés d'un angle de 26° par rapport à la normale à la surface. Nous pensons qu'un tel tassement des lipides est favorisé par leur interaction avec les chaînes aliphatiques de P3HT qui peuvent contrôler la distribution des lipides. Nous pensons que cette interface est très prometteuse pour une intégration plus poussée dans des dispositifs électroniques tels que les transistors à effet de champ.

VIII.2. Synthèse et caractérisation d'une sonde spécifique au césium à base de calix[4]arene

Une classe de molécules semble être parfaite pour la sonde au césium souhaitée : les calix[n]arenes. L'intérêt pour cette classe de matériaux moléculaires est basé sur leurs multiples applications potentielles, résultant des relations structure/propriétés, en catalyse, séparation et stockage par exemple, et des propriétés physiques que peuvent présenter certains de ces molécules : électronique, optique, magnétisme, conduction, etc.[151,152]. L'exploitation des calix[n]arenes (en particulier les calix[4]arenes) est favorisée par leur capacité particulière à adopter différentes conformations (cône, cône partiel, 1,2-alternée et 1,3-alternée), par la possibilité d'ancrer jusqu'à huit sites de coordination ou plus par la fonctionnalisation des groupements inférieurs et/ou supérieurs et également par la variation de la nature des groupes de liaison entre les unités phénoliques (ponts -CH_2- ou -S). Au cours des dernières décennies, une grande variété d'architectures utilisant le squelette du calixarène a été prévu pour la création de nouveaux systèmes supramoléculaires, basés sur les principes de la reconnaissance moléculaire et de la chimie host-guest[153-156]. La détection du césium a conduit au développement d'une variété de matériaux, notamment des sondes moléculaires, des matériaux absorbants (inorganiques, polymères), des composites organiques/inorganiques, des nanomatériaux de carbone, des semi-conducteurs et ainsi de suite, sur la base de diverses techniques et principes de détection. Les propriétés de détection sont fortement influencées à la fois par la surface spécifique et la nature de l'interaction entre l'analyte et les matériaux de détection.

VIII.2.1. Synthèse et caractérisation moléculaire de la sonde spécifique au césium

Parmi cette classe de molécule, les calix[4]arenes 1,3 alternées couplées d'un éther couronne ont retenu notre attention en raison de leurs structures bien définies présentant une cavité qui s'adapte parfaitement au rayon ionique du césium[157-159]. Les propriétés évidentes de sélectivité du césium du calix[4]arène et son intégration possible dans un matériau solide nous amènent à nous intéresser aux structures similaires pour la synthèse de la sonde de césium appliquée dans des transistors organiques à revêtement lipidique.

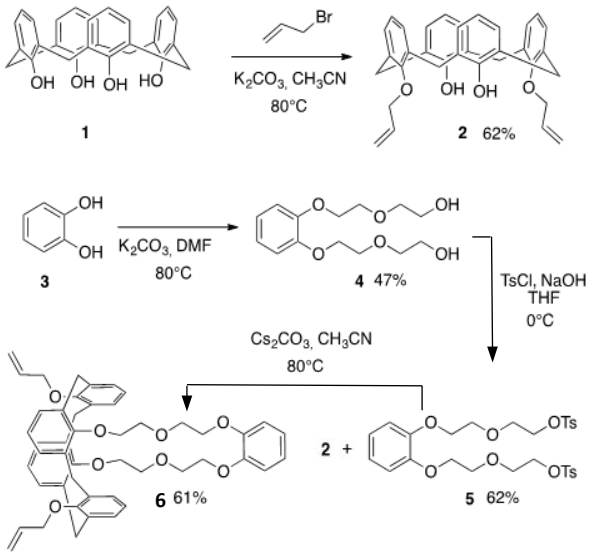

Schéma R1 *Voie de réaction chimique pour la synthèse de la sonde de césium*

La synthèse du chélateur cible **6** est décrite dans le Schéma R1. La RMN ^{1}H, la RMN ^{13}C, l'HRMS et l'analyse élémentaire confirment la formule moléculaire $C_{48}H_{50}O_8$ du composé **6** synthétisé. Veuillez-vous référer à *l'annexe VII.1* et *VII.3* pour plus de détails. Un examen plus approfondi de la taille de la cavité à partir de la structure cristallographique a révélé que les distances mesurées Cs+-O (3,31Å) et Cs+-Aromatique calix (3,44 Å) sont conformes à des systèmes similaires signalés, ce qui indique que la cavité de **6** est plus adaptée au Cs^+ par rapport aux autres cations.

VIII.2.2. Sélectivité de la sonde

Comme la détection se fera dans l'eau de mer, la sonde synthétisée doit avoir la plus grande sélectivité au césium. En effet, l'eau de mer est composée de nombreux cations et anions. Dans cette section, la sélectivité du chélateur **6** conçu sera vérifiée et testée. La constante d'affinité, le paramètre stœchiométrique et la compétition entre les ions seront étudiés à la fois par spectroscopie UV-visible et RMN ^{1}H.

Les propriétés d'absorption du chélateur **6** ont été étudiées dans un mélange de solvants MeOH : DCM (v/v, 1:1). Le spectre d'absorption UV-visible du récepteur **6** présente plusieurs bandes d'absorption dans la région 240-300 nm, attribuées à l'absorption des aromatiques du calix[4]arène et de la benzocouronne. Les propriétés de complexation du chélateur **6** ont été examinées par spectroscopie UV-visible avec 1 équivalent de plusieurs cations monovalents compétitifs présumés (Li^+, Na^+, K^+, Rb^+, Cs^+) et également avec un cation divalent (Mg^{2+}) (Figure R14).

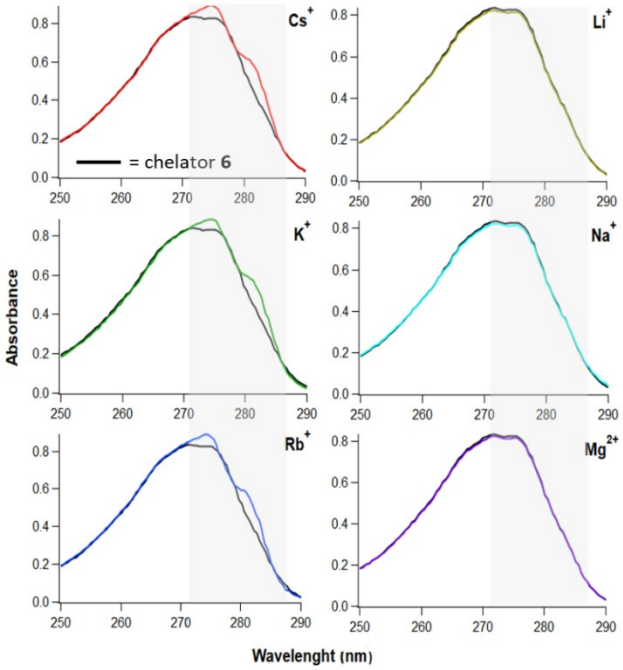

Figure R14 *Propriétés optiques du récepteur **6** après addition de 1 équivalent de cations Li^+(jaune), Na^+(turquoise), K^+(vert), Rb^+(bleu), Cs^+(rouge) et Mg^{2+}(violet)*

Les changements optiques les plus importants ont été observés pour Cs^+, K^+ et Rb^+ tandis que pour les autres cations (Na^+, Li^+ et Mg^{2+}), des variations beaucoup plus faibles sont observées. Lors de l'addition de Cs^+, K^+ ou Rb^+, une augmentation des bandes d'absorption centrées à 275 nm et 281 nm a été observée, mettant en évidence la formation des complexes **6**.X^+. Il a été prévu que la présence du cycle benzène dans la partie éther couronne pourrait entraîner une réduction de la flexibilité de la cavité, empêchant la complexation de cations plus petits tels que Na^+, Li^+ et Mg^{2+}. En effet, les rayons ioniques de Cs^+, K^+ ou Rb^+ dans la structure coordonnée **6** sont respectivement de 1,67 Å, 1,38 Å et 1,52 Å alors

que pour Na^+ et Li^+ ils sont respectivement de 0,76 Å et 1,02 Å . La structure résultante de **6** a montré que les distances Cs+-O (3,31 Å) et Cs+-Arcalix (3,44 Å) de la cavité de la couronne d'éther caractérisent bien l'interaction cation-π pour les cations Cs^+, K^+ et Rb^+.

Sur la base de ces résultats, la constante d'affinité et le paramètre stœchiométrique par respectivement la méthode de Benesi-Hildebrand et Job's sur les cations les plus compétitifs (Cs^+, Rb^+ et K^+) ont été calculés (**Tableau R3**). Le chélateur présente une meilleure affinité envers le cesium.

Tableau R3 *Caractéristique stœchiométrique et constante d'affinité entre les cations compétitifs et le chélateur*

Cation	Constante d'affinité (M^{-1})	Stochiométrie
Cs^+	6024	1:1
K^+	2825	1:1
Rb^+	2288	1:1

VIII.2.3. Greffage de la sonde sur une surface fonctionnalisé au DCOH-R

Les propriétés de détection intrinsèques du nouveau chélateur **6** par rapport au Cs^+, nous ont amenés à envisager son utilisation éventuelle dans un dispositif de détection tel qu'un Chem-OFET. Néanmoins, avant sa mise en œuvre dans un dispositif, il est nécessaire de le greffer efficacement sur une surface appropriée. Dans ce contexte, nous avons récemment démontré que les monocouches de lipides DCOH-R[70-72] peuvent être utilisées comme diélectrique organique efficace dans les dispositifs à transistors à effet de champ. Sur la base de ces faits pertinents, nous avons décidé de fonctionnaliser le chélateur **6** avec un groupe d'ancrage approprié afin de le greffer sur les monocouches lipidiques DCOH-R. Le groupe triéthoxysilane a été sélectionné et utilisé comme groupe d'ancrage. En effet, les groupes silanes sont bien connus pour être réactifs aux groupements hydroxyles (présents à la surface du DCOH-R). A partir de **6**, ce groupe fonctionnel peut être facilement introduit sur la partie allylique du groupement inférieur en une seule étape en utilisant le catalyseur de Karstedt (**Figure R15**)[184]. Le composé fonctionnalisé cible **7** a été obtenu à 59% et a été utilisé sans autre purification dans l'étape suivante (*Exp. Tech. partie VI.1.1*.). La sonde fonctionnalisée au silane obtenue a été caractérisée par RMN ^1H et RMN ^{29}Si (*Annexe partie VII.2*). Les résultats montrent le succès de la silanisation du chélateur **6**.

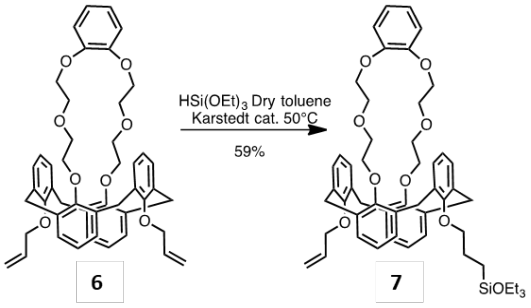

Figure R15 *Fonctionnalisation de la sonde avec un groupe d'ancrage*

Le greffage de la sonde **7** a été confirmé par ATR FTIR en utilisant la cellule développée (**Figure R9**). Pour cela, une monocouche de lipides DCOH-R a été assemblée sur un prisme en silicium avec une couche de P3HT en appliquant le protocole décrit précédemment. L'initiation et la propagation de la polymérisation au niveau du groupe de tête des lipides ont été initiées et assurées par la polycondensation du groupe triéthoxysilane avec le groupe ester à la tête des lipides de la monocouche DCOH-R (**Figure R16**).

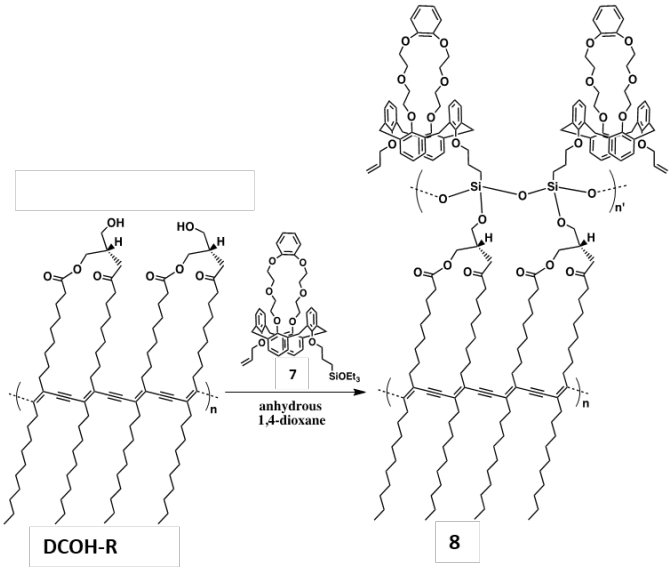

Figure R16 *Réaction chimique de greffage de la molécule **7** sur une monocouche lipidique de DCOH-R*

Elle a été réalisée en exposant les monocouches lipidiques DCOH-R à une solution de 0,25 mM de chélateurs substitués **7** dans du 1,4-dioxane anhydre pendant 1 heure. La surface a ensuite été abondamment rincée avec du 1,4-dioxane, du méthanol et de l'eau. La fonctionnalisation des molécules à base de silane n'est pas toujours simple, en raison de l'auto-polymérisation parallèle qui produit un film épais de polysiloxane recouvrant le substrat. En fait, la réaction de condensation est autocatalytique car les molécules d'eau activent l'ethoxysilane en silanols réactifs. L'excès d'eau, en l'absence d'humidité relative contrôlée, entraîne la compétition de la polycondensation de la molécule précurseur au lieu de la greffe de surface. Cependant, en utilisant une faible concentration de la sonde **7** avec une étape de rinçage avec des solvants, cet effet secondaire indésirable du processus de greffage est réduit.

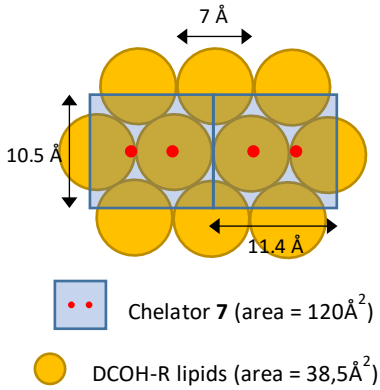

Figure R17 *Architecture moléculaire simplifiée de l'interface lipides DCOH-R/chélateur **7**. (Vue de dessus en 2D)*

La quantification directe de la quantité de chélateur greffé sur les monocouches de lipides DCOH-R n'est pas triviale. En effet, malgré la présence d'un site de greffage par lipide, l'encombrement moléculaire induit par le grand volume du chélateur (montré par les données cristallographiques du chélateur) rend le rapport de greffage 1:1 avec les lipides impossible à atteindre. Néanmoins, cette information peut être obtenue indirectement. Il a été démontré que la densité des lipides est d'environ $2,6 \times 10^{14}/cm^2$. En fixant deux hypothèses, on peut estimer le nombre de chélateurs greffés par lipides. Tout d'abord, nous considérons que le volume du chélateur **6** est à peu près équivalent au volume du

chélateur **7**. Deuxièmement, nous fixons que les lipides ont une configuration cristallin hexagonal. Par conséquent, en appliquant ces hypothèses et en utilisant l'aire de la surface du chélateur **7** (120 $Å^2$), on peut dessiner un modèle simplifié de l'interface monocouche de lipides DCOH-R/chélateur **7** (**Figure R17**). Sans tenir compte des angles des différentes architectures moléculaires, on estime un rapport de DCOH 5:1 chélateur **7**. Dans le cas d'un greffage total, la densité du chélateur de césium sur la surface va alors être égale à 5,2 x $10^{13}/cm^2$.

Nous avons étudié la synthèse et la caractérisation d'une sonde de césium à base de calix[4]arène. Nous avons montré le succès de sa mise en œuvre dans un substrat solide de P3HT fonctionnalisé avec une monocouche de lipide DCOH-R. La sonde possède une sélectivité remarquable vis-à-vis du Cs^+, par rapport à d'autres cations interférents. À partir du calcul de la densité des lipides réalisé dans le chapitre précédent et des paramètres cristallographiques de la sonde, nous avons estimé un rapport de 5 lipides pour un chélateur. Par conséquent, la densité maximale du chélateur est de 5,2 x $10^{13}/cm^2$. La sonde synthétisée a une grande sélectivité vis-à-vis du Cs^+ et nous avons montré la possibilité de greffer le chélateur sur les groupes de tête des lipides par une réaction de silanisation. Dans la prochaine partie, nous implanterons cette nouvelle interface sensible et sélective au cesium dans un transistor organique à effet de champ pour la détection sélective du Cs^+ dans l'eau de mer.

VIII.3. Développement du transistor à effet de champ à grille électrolytique (EGOFET)

Dans cette partie, je vais centrer la discussion sur l'intégration de l'interface prometteuse précédemment développé dans un transistor à effet de champ avec un électrolyte comme diélectrique de grille (EGOFET). Quelles sont les avantages de l'implémentation d'une telle interface dans un EGOFET ?

En ce qui concerne les applications de capteurs dans un environnement aqueux, les électrolytes liquides ont été largement utilisés comme grille diélectriques dans les transistors[44,187,188,189,190]. Il est important de noter que les EGOFET fonctionnent dans la gamme des millivolts. Cela est dû à la capacité élevée (1-20 $\mu F.cm^{-2}$)[191,192] d'une double couche électrique (EDL) formée à l'interface entre la solution d'électrolyte et le canal du semi-conducteur organique. Ceci conduit à une tension de seuil ultra basse (V_{TH}) inférieure à 1 V, efficace pour éviter toute réaction électrochimique dans la solution d'électrolyte[191,52]. Il convient de noter ici que la V_{TH} est très sensible aux charges de surface fournies par des analytes tels que les ions ou les biomolécules[75,188,193]. Par conséquent, une V_{TH} ultra-faible est avantageuse pour détecter les signaux même petits. En raison de ces caractéristiques, les EG-OFETs sont adaptés pour la détection d'ions dans un environnement aqueux.

Malgré les avantages procurés par les EGOFET, plusieurs obstacles nécessitent d'être surmontés pour avoir une meilleur performance de détection. Premièrement, la détection de ces analytes est généralement effectuée en présence d'ions interférents, par exemple le potassium et le sodium. Ces ions sont bien connus pour dégrader les performances des transistors car ils agissent comme des pièges électriques pour les OFET[191,192,194]. Le fonctionnement stable des EGOFET dans un tel environnement aqueux reste donc encore un défi[191,195,196]. Deuxièmement, des sondes de détection spécifiques devraient être fixées à la surface des canaux des transistors pour détecter des analytes tels que les ions et les protéines.

VIII.3.1. Fabrication de l'EGOFET

Un EGOFET développé et présenté ici a été appliqué comme un capteur de césium. Pour cela, la sonde sélective au césium à base de calixarène a été greffée sur la monocouche lipidique DCOH-R déposée sur la couche semi-conductrice P3HT. La **Figure R18** montre la conception de l'EGOFET développé. Les électrodes sont en or. L'épaisseur du P3HT régiorégulié à 90% est de 20 nm. L'épaisseur de la monocouche lipidique DCOH-R greffée avec le chélateur de césium à base de calixarène est estimée à 4,5 nm.

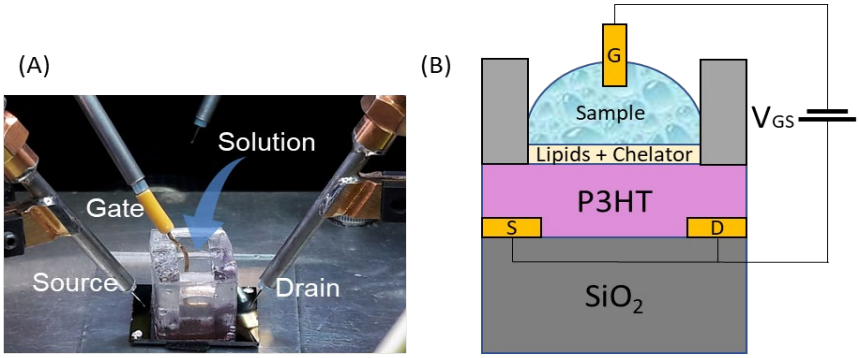

Figure R18 *Mise en place de la mesure de détection avec l'EGOFET développé. (A) Schéma de l'image réelle (B)*

Le choix du poly-3-hexylthiophène (P3HT) comme couche semi-conductrice dans le transistor a été fait du fait de ces propriétés intéressantes. En effet, le P3HT (**Figure R19**) est un semi-conducteur polymère de type p bien connu, qui présente une mobilité raisonnable des trous (~10^{-2} $cm^2.v^{-1}.s^{-1}$), ce qui présente un grand avantage pour former des couches planes homogènes avec une faible rugosité de surface. Facilement transformable et commercialement accessible, le P3HT est le candidat idéal pour assumer la fonction de couche semi-conductrice dans l'EGOFET développé.

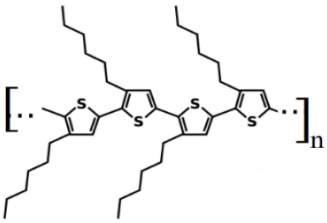

Figure R19 *P3HT molecular structure*

VIII.3.2. Influence du revêtement lipidique sur les performances de l'EGOFET

Le P3HT pur sans monocouche de lipides et le P3HT avec lipides DCOH-R implémenté dans l'EGOFET ont été comparés. Les courbes I-V ont été mesurées en utilisant un analyseur de paramètres à semi-conducteurs (Agilent B1500A) dans des conditions ambiantes. La solution tampon de phosphate (PBS) avec un pH fixe de 6,86 a été utilisée comme électrolyte pour évaluer la performance de l'EGOFET. La **Figure R20** montre les courbes de transfert de deux dispositifs : avec et sans revêtement DCOH-R. La tension de grille a été balayée de +0,4 V à -0,5 V avec une tension de drain fixe de -0,5 V. Le V_{TH} a été calculé avec l'équation **eq.12**.(*Exp. Partie VI.3.2*). Le transistor avec une largeur de canal de 100 µm a été utilisé pour les expériences. Le V_{TH} du transistor P3HT vierge a été estimé à +70 mV

(±27 mV). Le transistor avec la monocouche de lipides DCOH-R était quant à lui de -29 mV (±33 mV). La capacité estimée de la monocouche lipidique sur le film P3HT (16,25 μFcm^{-2}) était inférieure à celle du film P3HT vierge (20,5 μFcm^{-2}) en raison de la présence de la membrane lipidique. Les mobilités des charges ont été calculées comme étant respectivement de 7,2 x 10^{-3} $cm^2V^{-1}s^{-1}$ pour le P3HT vierge et de 4,3 x 10^{-3} $cm^2V^{-1}s^{-1}$ pour le P3HT avec DCOH-R[208]. Les mobilités des charges estimées sont comparables à celles rapportées dans les EGOFETs[187,191] à base de P3HT, ce qui suggère que les monocouches lipidiques ont eu un impact modéré sur le transport des charges. La monocouche de lipides déposées sur du P3HT a également un effet sur l'hystérésis des courbes de transfert. De nettes différences ont été observées dans les balayages de potentiels. Le P3HT vierge a montré une hystérésis autour de +0,4 à 0 V. En revanche, les EGOFETs couverts par le revêtement de monocouche de lipides ont montré une hystérésis négligeable lors de la mesure (**Figure R20**). L'hystérésis observée dans le P3HT vierge peut être attribuée au dopage ionique de la solution d'électrolyte dans le canal P3HT pendant les balayages de potentiel. Le revêtement de la monocouche de lipides a donc supprimé ces effets de dopage électrochimique.

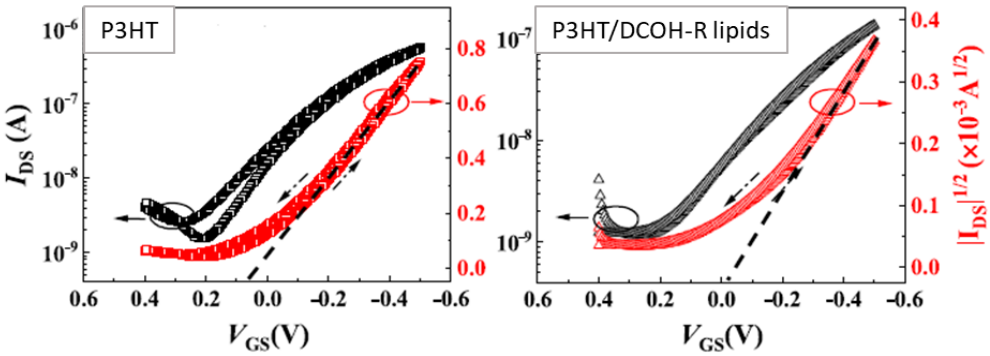

Figure R20 *Courbes de transfert du DCOH revêtu (à droite) et non revêtu (à gauche) P3HT*

L'avantage du revêtement de monocouche de lipides sur EG-OFET est plus prononcé dans l'opération à long terme. En effet, la stabilité du fonctionnement à long terme dans la solution d'électrolyte est crucial pour les applications de capteurs. La stabilité de fonctionnement de deux dispositifs (DCOH-R revêtu et non revêtu) a été évaluée en répétant des mesures de dix cycles pendant 10 min chacun dans une solution d'électrolyte PBS. Une diminution progressive du V_{TH} avec une déviation significative dans le P3HT EGOFET vierge a été observée (**Figure R21**).

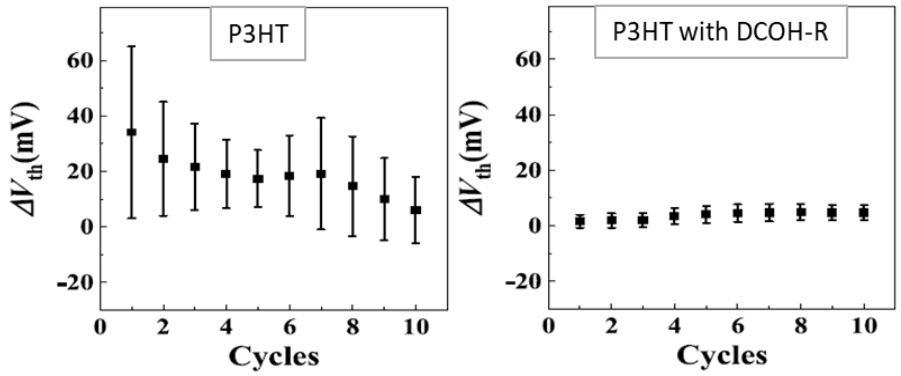

Figure R21 *Stability of the DCOH-R coated (right) and non-coated (left) P3HT EG-OFET over many electrical measurements cycles*

Le ΔV_{TH} a été défini par la différence entre les valeurs V_{TH} les plus basses et les autres valeurs V_{TH}. L'écart-type est calculé à partir de la moyenne des 5 transistors du ΔV_{TH}. Ce résultat peut s'expliquer

par le dopage de la solution d'électrolyte dans le canal du P3HT. En revanche, le P3HT revêtu d'une monocouche de lipides a amélioré la stabilité de l'EGOFET pour la mesure à long terme ; aucun décalage du V_{TH} n'a été observé, comme le montre la **Figure R21**. Les écarts à chaque cycle étaient également négligeables. Ces résultats indiquent également que le revêtement monocouche de lipides est efficace pour réduire le dopage ionique dans le canal P3HT. C'est un avantage évident pour le fonctionnement durable des EGOFET dans une solution d'électrolyte.

VIII.3.3. Mesures de détection : EGOFET appliqué comme capteur Cs^+

Dans cette partie, le dispositif développé a été utilisé comme capteur de Cs^+. Le chélateur est greffé à la monocouche lipidique réticulée via la fonction silane. Le V_{DS} a été fixé à -0,3 V et le V_{GS} varié de 0 à -0,3 V pour optimiser le temps de mesure. Les courbes de transfert ont été enregistrées en utilisant un analyseur de paramètres à semi-conducteurs (Agilent B1500A) dans des conditions ambiantes. La moyenne ΔV_{TH} de 5 transistors a été obtenue en normalisant le V_{TH} obtenu avec le V_{TH} sans cations ajoutés (concentration 0). Des expériences de détection ont été réalisées avec plusieurs électrolytes et cations.

Le but de mon projet est de pouvoir faire de la détection de césium dans l'eau de mer. Comme l'eau de mer est composée de multiples ions et notamment de potassium qui est également détecté par la sonde synthétisée, il a été décidé de réaliser une première expérience de détection dans un milieu interférent (PBS).

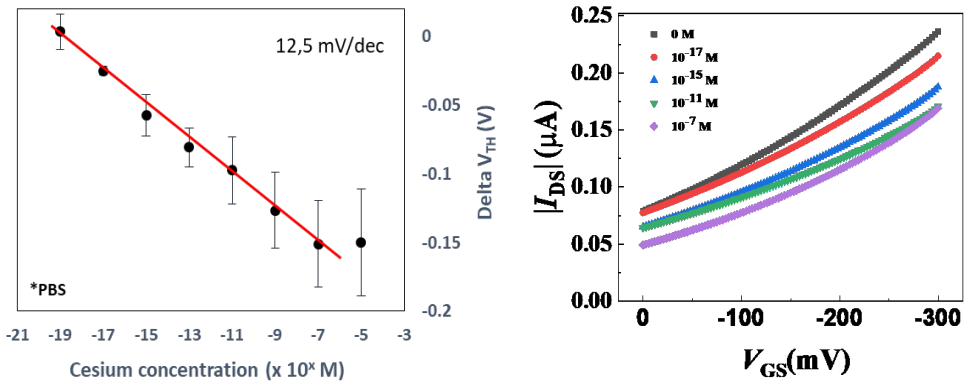

Figure R22 *Évolution de la V_{TH} en fonction de la concentration de césium dans le PBS (gauche) Courbes de transfert associées (droite)*

Les données obtenues (**Figure R22**) montrent un comportement linéaire du ΔV_{TH} dans une gamme de 10^{-19} M à 10^{-7} M de chlorure de césium. On peut attribuer une limite inférieure de détection à 10^{-19} M et une limite de saturation de détection à 10^{-7} M. La sensibilité calculée est de 12,5 mV/decade. Même si la sensibilité est faible, la super sélectivité du transistor doit être mise en évidence. En effet, les chélateurs de césium greffés sur la couche de lipides DCOH sont saturés avec le potassium K^+ présent dans la solution de PBS avant les mesures de détection. Ce qui est donc mesuré, c'est la modification de la charge de surface apportée par le passage du système de liaison chélateur/K^+ au système de liaison chélateur/Cs^+. Bien que Cs^+ et K^+ portent tous les deux une charge, le césium a un rayon plus grand et le masquage de la charge effective de Cs^+ dû aux ions dans l'électrolyte devrait être différent de celui de K^+. La charge de surface effective devrait donc être différente.

Après les résultats obtenus dans le milieu PBS interférent, l'expérience de détection du césium a été réalisée dans l'eau de mer. Le chlorure de césium à différentes concentrations a été dilué dans de l'eau de mer pure.

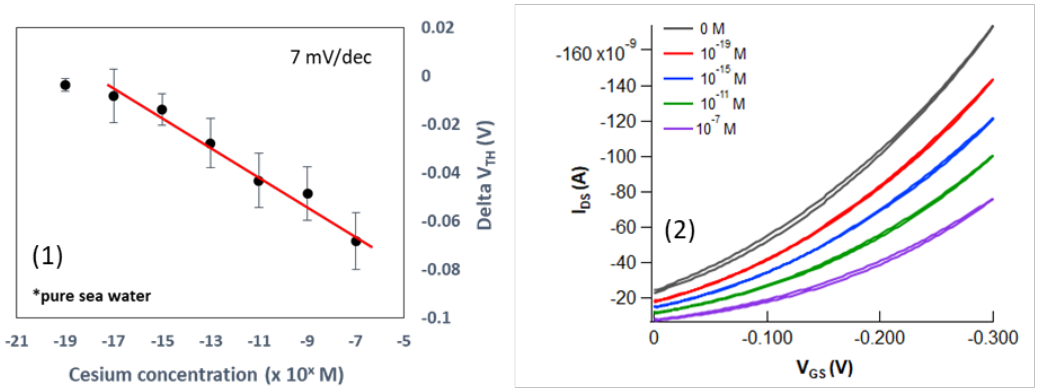

Figure R23 *(1) Evolution de la V_{TH} par rapport à la concentration en césium dans l'eau de mer pure. (2) Courbes de transfert à différentes concentrations de CsCl dans l'eau de mer*

Une diminution linéaire du ΔV_{TH} est à nouveau observée (**Figure R23**) avec une limite de détection de 10 aM. Par rapport à l'expérience dans le PBS, la sensibilité est réduite. Elle peut s'expliquer par l'augmentation du masquage de la charge dans l'eau de mer. En effet, dans les mesures de détection basées sur les FET, les charges dans l'électrolyte jouent un rôle important dans la détermination de la performance de détection. Dans les solutions contenant des concentrations élevées de sel (telles que l'eau de mer ou le PBS), le potentiel d'interaction entre le récepteur et l'analyte qui provoque le changement de conductance dans le capteur FET pourrait être partiellement masqué par la forte force ionique de la solution, réduisant ainsi les signaux obtenus à partir des mesures électriques.

Pour conclure, un nouveau capteur super sélectif pour la détection du césium a été développé. Pour cela, on a utilisé une couche lipidique polymérisable ultra-mince (2,5 nm), très dense (2,6 x 10^{14}/cm^2), avec un groupe de tête modifiable. Cette couche a été déposée sur un polymère régiorégulié semi-conducteur (P3HT) en utilisant la méthode de fusion des vésicules. Les lipides semblent s'imbriquer parfaitement dans les chaînes aliphatiques du polymère. Les multiples interactions de Van der Waals entre les deux couches ainsi que la réticulation inter et intra chaîne des lipides après polymérisation radicale ont permis d'obtenir une interface organique très stable vérifiée par des mesures de force AFM. Par la suite, une sonde à base de calixarène a été synthétisée et fixée. Les mesures de l'affinité des cations par UV-vis et RMN ont montré une forte sélectivité de la sonde vis-à-vis du césium. La formation de cette nouvelle interface à trois couches, mince, stable, sélective pour le césium et entièrement organique, a été contrôlée à l'aide d'une cellule fluidique multifonctionnelle mise en œuvre dans un FTIR en mode ATR. Une fois incrémenté dans un transistor à effet de champ à électrolyte, les résultats ont montré qu'il est possible de détecter le césium dans l'eau de mer avec une plage de détection de 10^{-17} M - 10^{-7} M et une sensibilité de 7 mV/dec. Nous pouvons donc répondre à la question principale de cette thèse : est-il possible de détecter de très faibles concentrations de cation césium dans l'eau de mer ? Oui. En plus de sa composition entièrement organique, la très faible limite de détection et la très haute sélectivité vis-à-vis du Cs^+ sont probablement les deux plus grands avantages de la nouvelle interface développée et mise en œuvre dans EGOFET.

IX. References

IX. References

[1] Pasternack, J. B., & Howell, R. W. (**2013**). RadNuc: A graphical user interface to deliver dose rate patterns encountered in nuclear medicine with a 137Cs irradiator. *Nucl. Med. Biol.*, 304-311.

[2] Yuan, S., Chen, D., Li, D., Zhong, J., & Xu, X. (**2018**). In Situ Crystallization Synthesis of CsPbBr3 Perovskite Quantum Dot-Embedded Glasses with Improved Stability for Solid-State Lighting and Random Upconverted . *ACS Appl. Mater. Interfaces 10* , 18918-18926 .

[3] Downs, J. D. (**2006**). Drilling and Completing Difficult HP/HT Wells With the Aid of Cesium Formate Brines-A Performance Review. *Society of Petroleum Engineers*.

[4] Markowitz, W., Glenn Hall, R., Essen, L., & Parry, J. (**1958**). Frequency of Cesium in Terms of Ephemeris Time. *Phys. Rev. Lett. 1*, 105.

[5] Unterweger, M., Hoppes, D., Schima, F., & Coursey, J. (**2009**). Radionuclide Half-Life Measurements Data. *National Institute of Standards and Technology*.

[6] Burger, A., & Lichtscheidl, I. (**2018**). Stable and radioactive cesium: A review about distribution in the environment, uptake and translocation in plants, plant reactions and plants' potential for bioremediation. *Sci. Total Environ. 618*, 1459 –1485.

[7] Murakami, M., Ohte, N., Suzuki, T., Ishii, N., Igarashi, Y., & Tanoi, K. (**2014**). Biological proliferation of cesium-137 through the detrital food chain in a forest ecosystem in Japan. *Sci. Rep. 4*, 3599.

[8] Melnikov, P., & Zanoni, L. Z. (**2009**). Clinical effects of cesium intake. *Biol. Trace Elem. Res. 135*, 1-9.

[9] Guy, R. H., Hostynek, J. J., Hinz, R. S., & Lorence Marcel Dekker, C. R. (**2000**). Metals and the Skin : Topical Effects and Systemic Absorption. *Applied Organometallic Chemistry*.

[10] Evans Analytical Group. (s.d.). *ICP-MS detection limit guidance.*

[11] Povinec, P., & Sanchez-Cabeza, J. (**2006**). International Conference on Isotopes and Environmental Studies 8.

[12] TEPCO. (**2011**). *Report of the Result of the Nuclide Analysis of the Seawater.* Récupéré sur http://www.tepco.co.jp/en/press/corp-com/release/betu11_e/images/110330e10.pdf

[13] Liezers, M., Farmer, O., & Thomas, M. (**2009**). Low-level detection of 135Cs and 137Cs in environmental samples by ICP-MS. *J. Radioanal. Nucl. Chem. 282*, 309.

[14] Ohno, T., & Muramatsu, Y. (**2014**). Determination of radioactive cesium isotope ratios by triple quadrupole ICP-MS and its application to rainwater following the Fukushima Daiichi Nuclear Power Plant accident. *J. Anal. Spectrom. 29* , 347-351.

[15] Zheng, J., Tagami, K., Bu, W., Uchida, S., Watanabe, Y., Kubo-ta, Y., Fuma, S., Ihara, S. (**2014**). 135Cs/137Cs Isotopic Ratio as a New Tracer of Radiocesium Released from the Fukushima Nuclear Accident. *Environ. Sci. Technol. 48*, 5433-5438 .

[16] Zheng, J., Bu, W., Tagami, K., Shikamori, Y., Nakano, K., Uchida, S., & Ishii, N. (**2014**). Determination of 135Cs and 135Cs/137Cs Atomic Ratio in Environmental Samples by Combining Ammonium Molybdophosphate (AMP)-Selective Cs Adsorption and Ion-Exchange Chromatographic Separation to Triple-Quadrupole Inductively Coupled Plasma-Mass Spectrometry. *Anal. Chem. 86*, 7103-7110.

[17] Russell, B., Warwick, P. E., & Croudace, I. W. (**2014**). Calixarene-based extraction chromatographic separation of ^{135}Cs and ^{137}Cs in environmental and waste samples prior to sector field ICP-MS analysis. *Anal. Chem. 86*, 11890-11896.

[18] Ji, Y.-Y., Lim, T., Hitomi, K., & Yajima, T. (**2020**). Spectrometric estimation of dose rate induced from radioactive cesium in the ground using a mobile gamma-ray spectrometry based on a LaBr3(Ce) Detector. *Health Phys. 118* , 215-225.

[19] Miura, K., Yamamoto, K., Yonetani, A., & Shirasaki, T. (**2013**). Determination of Cesium in Foods by Atomic Absorption Spectrometry Based on Background-correction Using Zeeman Splitted Spectrum. *Bunseki kagaku 62(1)*, 37-41.

[20] Temirov, J. P., Matveev, O. I., Smith, B. W., & Winefordner, J. D. (**2003**). Laser-enhanced ionization with avalanche amplification: detection of cesium at fg/mL levels. *Appl. Spectrosc. 57*, 729-732.

[21] Ohkoshi, S., Yoshikiyo, M., Namai, A., Nakagawa, K., Chiba, K., Fujiwara, R., & Tokoro, H. (**2017**). Cesium ion detection by terahertz light. *Scientific Reports 7*, 8088.

[22] Joffrion, J., Mills, D., & Clower, W. a. (**2017**). On-Chip Microplasmas for the Detection of Radioactive Cesium Contamination in Seawater. *Micromachines 8(9)*, 259.

[23] Ferdov, S., & Lin, Z. (**2010**). Selective Detection of Cs+ in Water Solutions via One-Step Formation of a New Type of Struvite-Like Phosphate. *Chem. Mater. 22*, 5345-5349.

[24] Qiu, J., Fu, L., Wang, H., Zou, R., Zhang, Y., Li, X., & Wu, A. (**2020**). Colorimetric detection of Cs+ based on the nonmorphological transition mechanism of gold nanoparticles in the presence of Prussian blue. *New J. Chem.*

[25] Li, C., & Shi, G. (**2013**). Polythiophene-Based Optical Sensors for Small Molecules. *ACS Appl. Mater. Interfaces 5*, 4503.

[26] Thomas, S., Joly, G., & Swager, T. (**2007**). Chemical Sensors Based on Amplifying Fluorescent Conjugated Polymers. *Chem. Rev. 107*, 1339.

[27] Radaram, B., Mako, T., & Levine, M. (**2013**). Sensitive and Selective Detection of Cesium via Fluorescence Quenching. *Dalton Transactions 42.46*, 16276-16278.

[28] Namgung, H., Gwon, Y. J., Kim, J., Jang, G., Pepper, S. E., Ogden, M. D., Whittle, K. R.; Harwood, L. M.; Lee, T. S. (**2018**). Synthesis of Prussian blue-embedded porous polymer for detection and removal of Cs ions. *Polym. 158*, 320-326.

[29] Kang, S.-M., Jang, S.-C., Haldorai, Y., Vilian, A. T., Rethinasabapathy, M., Roh, C., Han, Y.-K., Huh, Y. S. (**2017**). Facile fabrication of paper-based analytical devices for rapid and highly selective colorimetric detection of cesium in environmental samples. *RSC Advances 7*, 48374-48385.

[30] Akamatsu, M., Komatsu, H., Matsuda, A., Mori, T., Nakanishi, W., Sakai, H., Hill, J.P., Ariga, K. (**2017**). Visual detection of cesium ions in domestic water supply or seawater using a nano-optode. *Bull. Chem. Soc. Jpn. 90*.

[31] Kumar, N., Leray, I., & Depauw, A. (**2016**). Chemically derived optical sensors for the detection of cesium ions. *Coord. Chem. Rev. 310*, 1-15.

[32] Leray, I., & Valeur, B. (**2009**). Calixarene-Based Fluorescent Molecular Sensors for Toxic Metals. *Eur. J. Inorg. Chem. 24*, 3525-3535.

[33] Saadat, M., & Nezamzadeh-Ejhieh, A. (**2016**). Clinoptilolite nanoparticles containing HTDMA and Arsenazo III as a sensitive carbon paste electrode modifier for indirect voltammetric measurement of cesium ions. *Electrochim. Acta 217*, 163-170.

[34] Shamsipur, M., Asgari, M., Maragheh, M. G., & Matt, D. (**2015**). Impedimetric sensing of cesium ion based on a thiacalix[4]arene self-assembled gold electrode. *Sens. Actuator B-Chem. 2209*, 9-14.

[35] Alghamdi, N., Alqahtani, Z., & Grell, M. (**2019**). Sub-nanomolar detection of cesium with water-gated transistor. *J. Appl. Phys. 126(6)*, 064502/1-064502/8.

[36] Canali, C., Jacoboni, C., Nava, F., Ottaviani, G., & Quaranta, A. (**1975**). Electron drift velocity in silicon. *Phys. Rev. B12 4* , 2265-2284.

[37] Bergveld, P. (**1970**). Development of an ion-sensitive solid-state device for neurophysiological measurements. *IEEE Trans. Bio-Med. Eng. BME 17*, 70-71 .

[38] Chiang, J., Chou, J., & Chen, Y. (**2001**). Study of the pH-ISFET and EnFET for Biosensor Applications. *J. Med. Biol. Eng. 21*, 135–146.

[39] Voigt, H., Schitthelm, F., Lange, T., Kullick, T., & Ferretti, R. (**1997**). Diamond-like carbon-gate pH-ISFET. *Sens. Actuators B Chem. 44*, 441–445 .

[40] Lee, W., Kim, D., Rivnay, J., Matsuhisa, N., Lonjaret, T., Yokota, T., Yawo, H., Sekino, M., Malliaras, G. G., Someya, T. (**2016**). Integration of Organic Electrochemical and Field-Effect Transistors for Ultraflexible, High Temporal Resolution Electrophysiology Arrays. *Adv. Mater. 28*, 9722.

[41] Henning, S., Matt, B., & Ni, Z. (**2010**). Charge Transport Physics of Conjugated Polymer Field-Effect Transistors. *Adv. Mater. 22*, 3893.

[42] Collet, J., & Vuillaume, D. (**1998**). Nano-field effect transistor with an organic self-assembled monolayer as gate insulator . *Appl. Phys. Lett. 73* , 2681–2683.

[43] Collet, J., Tharaud, O., Chapoton, A., & Vuillaume, D. (**2000**). Low-voltage, 30 nm channel length, organic transistors with a self-assembled monolayer as gate insulating films. *Appl. Phys. Lett. 76* , 1941–1943 .

[44] Halik, M., Klauk, H., Zschieschang, U., Schmid, G., Ponomarenko, S., Kirchmeyer, S., & Weber, W. (**2003**). Relationship Between Molecular Structure and Electrical Performance of Oligothiophene Organic Thin Film Transistors. *Adv. Mater. 15* , 917–922.

[45] Park, Y., Kim, D., Jang, Y., Hwang, M., Lim, J., & Cho, K. (**2005**). Low-voltage polymer thin-film transistors with a self-assembled monolayer as the gate dielectric. *Appl. Phys. Lett. 87*, 1-3.

[46] Fukuda, K., Hamamoto, T., Yokota, T., Sekitani, T., Zschieschang, U., Klauk, H., & Someya, T. (**2009**). Effects of the alkyl chain length in phosphonic acid self-assembled monolayer gate dielectrics on the performance and stability of low-voltage organic thin-film transistors. *Appl. Phys. Lett. 95*, 203301 .

[47] Salinas, M., & Halik, M. (**2013**). Photoactive self-assembled monolayers for optically switchable organic thin-film transistors. *Appl. Phys. Lett. 102* , 203301.

[48] Casalini, A., Bortolotti, C., Leonardi, F., & Biscarini, F. (**2017**). Self-assembled monolayers in organic electronics. *Chem. Soc. Rev. 46*, 40.

[49] Wang, Y., Huang, X., Li, T., Li, L., Guo, X., & Jiang, P. (**2019**). Polymer-based Gate Dielectrics for Organic Field-effect Transistors. *Chem. Mater.*

[50] Tsumura, A., Koezuka, H., & Ando, T. (**1986**). Macromolecular electronic device: Field-effect transistor with a polythiophene thin film. *Appl. Phys. Lett. 49*, 1210–1212.

[51] Lin, P., & Yan, F. (**2012**). Organic Thin-Film Transistors for Chemical and Biological Sensing. *Advanced Materials 24*, 34-51 .

[52] Kergoat, L., Piro, B., Berggren, M., Pham, M., Yassar, A., & Horowitz, G. (**2012**). DNA detection with a water-gated organic field-effect transistor. *Org. Electron. 13*, 1.

[53] Mulla, M., Tuccori, E., Magliulo, M., Lattanzi, G., Palazzo, G., Persaud, K., & Torsi, L. (**2015**). Capacitance-modulated transistor detects odorant binding protein chiral interactions. *Nat. Commun. 6*, 1.

[54] Casalini, S., Leonardi, F., Cramer, T., & Biscarini, F. (**2013**). Organic field-effect transistor for label-free dopamine sensing. *Org. Electron. 14*, 156.

[55] Berto, M., Diacci, C., D'Agata, R., Pinti, M., Bianchini, E., Di Lauro, M., Casalini, S., Cossarizza, A., Berggren, M., Simon, D., Spoto, G., Biscarini, F., Bortolotti, C.A (**2017**). EGOFET Peptide Aptasensor for Label-Free Detection of Inflammatory Cytokines in Complex Fluids. *Adv. Biosyst.*, 1700072.

[56] Yaman, B., Terkesli, I., Turksoy, K., Sanyal, A., & Mutlu, S. (**2014**). Fabrication of a planar water gated organic field effect transistor using a hydrophilic polythiophene for improved digital inverter performance. *Org.Electron. 15*, 646.

[57] Porrazzo, R., Luzio, A., Bellani, S., Bonacchini, G., Noh, Y., Kim, Y., Lanzani, G., Antognazza, M.R, Caironi, M. (**2017**). Water-Gated n-Type Organic Field-Effect Transistors for Complementary Integrated Circuits Operating in an Aqueous Environment. *ACS Omega 2*, 1.

[58] Parkula, V., Maglione, M., Casalini, S., Zhang, Q., Greco, P., Bortolotti, C.A, Rovira, C., Mas-Torrent, M., Biscarini, F. (**2019**). EGOFET Gated by a Molecular Electronic Switch: A Single-Device Memory Cell. *Adv. Electron. Mater.*, 1800875.

[59] Schmoltner, K., Kofler, J., Klug, A., & List-Kratochvil, E. (**2013**). Electrolyte-Gated Organic Field-Effect Transistor for Selective Reversible Ion Detection. *Advanced Materials Communication 25(47)*, 6895-99.

[60] Melzera, K., Münzera, A., Jaworska, E., Maksymiuk, K., Michalska, A., & Scarpa, G. (**2014**). Polymeric ion-selective membrane functionalized gate-electrodes: Ion-selective response of electrolyte-gated poly (3-hexylthiophene) field effect transistors. *Organic Electronics 15*, 595-601.

[61] Chen, Y.-T., Sarangadharan, I., Sukesan, R., Hseih, C.-Y., Lee, G.-Y., Chyi, J.-I., & Wang, Y.-L. (**2018**). High-field modulated ion-selective field-effect-transistor (FET) sensors with sensitivity higher than the ideal Nernst sensitivity. *Scientific Reports 8*, 8300.

[62] Liao, C., & Yan, F. (**2013**). Organic semiconductors in organic thin-film transistor-based chemical and biological sensors. *Polym. Rev. 53*, 352–406.

[63] Herlogsson, L., Crispin, X., Robinson, N., Sandberg, M., Hagel, O., Gustafsson, G., & Berggren, M. (**2007**). Low-voltage polymer field-effect transistors gated via a proton conductor. *Adv. Mater. 19*, 97–101.

[64] Ono, S., Miwa, K., Seki, S., & Takeya, J. (**2009**). A comparative study of organic single-crystal transistors gated with various ionic-liquid electrolytes. *Appl. Phys. Lett. 94*, 063301.

[65] Xia, Y., Cho, J., Lee, J., Ruden, P., & Frisbie, C. (**2009**). Comparison of the mobility-carrier density relation in polymer and single-crystal organic transistors employing vacuum and liquid gate dielectrics. *Adv. Mater. 21*, 2174–2179.

[66] Lee, J., Panzer, M., He, Y., Lodge, T., & Frisbie, C. (**2007**). Ion gel gated polymer thin-film transistors. *J. Am. Chem. Soc. 129* , 4532–4533.

[67] Cho, J., Lee, J., Xia, Y., Kim, B., He, Y., Renn, M., Lodge, T.P., Frisbie, C. (**2008**). Printable ion-gel gate dielectrics for low-voltage polymer thin-film transistors on plastic. *Nat. Mater. 7*, 900–906.

[68] Facchetti, A. (**2008**). Dielectric materials: Gels excel. *Nat. Mater. 7* , 839–840.

[69] Belkhir, A. (**2009**). *Ph.D. Thesis: Contribution à la Modélisation des Transistors Organiques.* Reims, France: The University of Reims Champagne-Ardenne.

[70] Charrier, A., Mischki, T., & Lopinski, G. (**2010**). Direct Stabilization of a Phospholipid Monolayer on H-Terminated Silicon. *Langmuir 26(4)*, 2538–2543.

[71] Dumas, C., El Zein, R., Dallaporta, H., & Charrier, A. (**2011**). Autonomic Self-Healing Lipid Monolayer: A New Class of Ultrathin Dielectric. *Langmuir 27, 22*, 13643-13647 .

[72] El Zein, R., Dallaporta, H., & Charrier, A. (**2012**). Supported Lipid Monolayer with Improved Nanomechanical Stability: Effect of Polymerization. *J. Phys. Chem. B 116*, 7190−7195.

[73] Kenaan, A., El Zein, R., Kilinc, V., Lamant, S., Raimundo, J.-M., & Charrier, A. (**2018**). Ultrathin Supported Lipid Monolayer with Unprecedented Mechanical and Dielectric Properties. *Adv. Funct. Mater.*, 1801024.

[74] Nguyen, T. D., El Zein, R., Raimundo, J.-M., Dallaporta, H., & Charrier, A.-M. (**2013**). Label free femtomolar electrical detection of Fe(III) ions with a pyridinone modified lipid monolayer as the active sensing layer. *J. Mater. Chem. B 1* , 443-446.

[75] Nguyen, T. D., Labed, A., El Zein, R., Lavandier, S., Bedu, F., Ozerov, I., Dallaporta, H., Raimundo, J.-M., Charrier, A.-M. (**2014**). A field effect transistor biosensor with a γ-pyrone derivative engineered lipid-sensing layer for ultra sensitive Fe3+ ion detection with low pH interference. *Biosens. & Bioelectron. 54*, 571-577.

[76] Kenaan, A., Nguyen, T. D., Dallaporta, H., Raimundo, J.-M., & Charrier, A.-M. (**2016**). Sub-picomolar iron sensing platform based on functional lipid monolayer microarrays. *Anal. Chem. 88,* 3804−3809.

[77] Jung, S., Choi, S., Kim, Y., & Jeon, T. (**2012**). Storable droplet interface lipid bilayers for cell-free ion channel studies. *Bioprocess Biosyst. Eng. 35*, 241-246.

[78] Berg, J., Tymoczko, J., & Stryer, L. (**2002**). There Are Three Common Types of Membrane Lipids. *Biochemistry 5*.

IX. References

[79] Langmuir, I., & Schaefer, V. (**1938**). Activities of Urease and Pepsin Monolayers. *J. Am. Chem. Soc. 60*, 1351.

[80] Brian, A., & McConnell, H. (**1984**). Allogeneic stimulation of cytotoxic T cells by supported planar membranes. *Proc. Natl Acad. Sci. USA 81* , 6159 .

[81] McConnell, H., Watts, T., Weis, R., & Brian, A. (**1986**). Supported planar membranes in studies of cell-cell recognition in the immune system. *Biochim. Biophys. Acta 95*, 864.

[82] Tamm, L., & McConnell, H. (**1985**). Supported phospholipid bilayers. *Biophys. J. 47*, 105.

[83] Rossetti, F., Bally, M., Michel, R., Textor, M., & Reviakine, I. (**2005**). Interactions between titanium dioxide and phosphatidyl serine-containing liposomes: formation and patterning of supported phospholipid bilayers on the surface of a medically relevant material. *Langmuir 21*, 6443.

[84] Reimhult, E., Hook, F., & Kasemo, B. (**2003**). Intact Vesicle Adsorption and Supported Biomembrane Formation from Vesicles in Solution: Influence of Surface Chemistry, Vesicle Size, Temperature, and Osmotic Pressure. *Langmuir 19*, 1681.

[85] Yang, J., & Kleijn, J. (**1999**). Order in phospholipid Langmuir-Blodgett layers and the effect of the electrical potential of the substrate. *Biophys. J. 76*, 323.

[86] Lahiri, J., Kalal, P., Frutos, A., Jonas, S., & Schaeffler, R. (**2000**). Method for Fabricating Supported Bilayer Lipid Membranes on Gold. *Langmuir 16*, 7805.

[87] Salamon, Z., Wang, Y., Tollin, G., & Macleod, H. (**1994**). Assembly and molecular organization of self-assembled lipid bilayers on solid substrates monitored by surface plasmon resonance spectroscopy. *Biochim. Biophys. Acta Biomembranes 267*, 1195.

[88] Puu, G., & Gustafson, I. (**1997**). Planar lipid bilayers on solid supports from liposomes--factors of importance for kinetics and stability. *Biochim. Biophys. Acta Biomembranes 149*, 1327.

[89] Castellana, E., & Cremer, P. (**2006**). Solid supported lipid bilayers: from biophysical studies to sensor design. *Surf. Sci. Rep. 61, 10* , 429-444.

[90] Nuzzo, N., & Allara, D. (**1983**). Adsorption of bifunctional organic disulfides on gold surfaces. *J. Am. Chem. Soc. 105*, 4481.

[91] Plant, A., Brighamburke, M., Petrella, E., & Oshannessy, D. (**1995**). Phospholipid/alkanethiol bilayers for cell-surface receptor studies by surface plasmon resonance. *Anal. Biochem. 226*, 342.

[92] Rao, N., Plant, A., Silin, V., Wight, S., & Hui, S. (**1997**). Characterization of biomimetic surfaces formed from cell membranes. *Biophys. J. 73*, 3066.

[93] Hardy, G., Nayak, R., & Zauscher, S. (**2013**). Model cell membranes : Techniques to form complex biomimetic supported lipid bilayers via vesicle fusion. *Curr.Opin.Colloid Interface Sci. 18, 5*, 448-458.

[94] Lodish, H., Berk, A., & Zipursky, S. (**2000**). Biomembranes : structural organization and basic functions. *Molecular Cell Biology 4*.

[95] Magliulo, M., Mallardi, A., Mulla, M., Cotrone, S., Pistillo, B., Favia, P., Vikholm-Lundin, I., Palazzo, G., Torsi, L. (**2013**). Electrolyte-Gated Organic Field-Effect Transistor Sensors Based on Supported Biotinylated Phospholipid Bilayer. *Advanced Materials Communication 25, 14*, 2090-2094.

[96] Misra, N., Martinez, J., Huang, S.-C., Wang, Y., Stroeve, P., Grigoropoulos, C., & Noy, A. (**2009**). Bioelectronic silicon nanowire devices using functional membrane proteins. *Proc. Natl. Acad. Sci 106, 33*, 13780-13784.

[97] Hu, S.-K., Hsiao, S.-W., Mao, H., Chen, Y.-M., Chang, Y., & Chao, L. (**2013**). Using crosslinkable diacetylene phospholipids to construct two-dimensional packed beds in supported lipid bilayer separation platforms. *Sci. Technol. Adv. Mater. 14*, 044408.

[98] Heurtault, B., Saulnier, P., Pech, B., Proust, J.-E., & Benoit, J.-P. (**2003**). Physico-chemical stability of colloidal lipid particles. *Biomaterials 24* , 4283–4300.

[99] Tero, R., Takizawa, M., Li, Y., Yamazaki, M., & Urisu, T. (**2004**). Lipid membrane formation by vesicle fusion on silicon dioxide surfaces modified with alkyl self-assembled monolayer islands. *Langmuir 20, 18*, 7526-7531.

[100] Khan, M., Dosoky, N., Williams, J. (**2013**). Engineering Lipid Bilayer Membranes for Protein Studies. *Int. J. Mol. Sci. 14, 11*, 21561-21597.

[101] McColl, J., Yakubov, G., & Ramsden, J. (**2007**). Complex desorption of mucin from silica. *Langmuir 23, 13*, 7096-7100.

[102] Almeida, P., Vaz, W., & Thompson, T. (**1992**). Lateral Diffusion in the Liquid Phases of Dimyristoylphosphatidylcholine/ Cholesterol Lipid Bilayers: A Free Volume Analysis. *Biochemistry 31* , 6739-6747.

[103] Sun, W.-J., Tristram-Nagle, S., Suter, R., & Nagles, J. (**1996**). Structure of Gel Phase Saturated Lecithin Bilayers: Temperature and Chain Length Dependence. *Biophysical Journal 71*, 885.

[104] Goormaghtigh, E., Raussens, V., & Ruysschaert, J. (**1999**). Attenuated total reflection infrared spectroscopy of proteins and lipids in biological membranes. *Biochimica et Biophysica Acta 1422* , 105-185.

[105] Mirabella, F. (**1993)**. *Internal reflection spectroscopy: Theory and applications.* Practical Spectroscopy Series, Marcel Dekker.

[106] Hubbard, J., Silin, V., & Plant, A. (**1998**). Self-assembly driven by hydrophobic interactions at alkanethiol monolayers: mechanisms of formation of hybrid bilayer membranes. *Biophys. Chem. 75*, 163.

[107] Peng, Z., Tang, J., Han, X., Wang, E., & Dong, S. (**2002**). Formation of a Supported Hybrid Bilayer Membrane onGold: A Sterically Enhanced Hydrophobic Effect. *Langmuir 22*, 4834.

[108] Coates, J. (**2006**). *Encyclopedia of Analytical Chemistry R.A. , Interpretation of Infrared Spectra, A Practical Approach.* Meyers (Ed.), John Wiley & Sons Ltd.

[109] Smith, B. (**1999**). *Infrared Spectral Interpretation: A Systematic Approach.* New York: CRC Press.

[110] Parikh, A., Beers, J., Shreve, A., & Swanson, B. (**1999**). Infrared Spectroscopic Characterization of Lipid−Alkylsiloxane Hybrid Bilayer Membranes at Oxide Substrates. *Langmuir 15*, 5369.

[111] Batchelder, D., Evans, S., Freeman, T., Haussling, L., Ringsdorf, H., & Wolf, H. (**1994**). Self-assembled monolayers containing polydiacetylenes. *J. Am. Chem. Soc. 116*, 1050.

[112] Porter, M., Bright, T., Allara, D., & Chidsey, C. (**1987**). Spontaneously organized molecular assemblies. 4. Structural characterization of n-alkyl thiol monolayers on gold by optical ellipsometry, infrared spectroscopy, and electrochemistry. *J. Am. Chem. Soc. 109*, 3559.

[113] Golden, W., Snyder, C., & Smith, B. (**1982**). Infrared reflection-absorption spectra of ordered and disordered arachidate monolayers on aluminum. *J. Phys. Chem 86, 2700*, 2700.

[114] Nuzzo, R., Dubois, L., & Allara, D. (**1990**). Fundamental Studies of Microscopic Wetting on Organic Surfaces. 1. Formation and Structural Characterization of a Self-Consistent Series of Polyfunctional Organic Monolayers *J. Am. Chem. Soc. 112*, 558.

[115] Baughman, R., & Yee, K. (**1978**). Solid-state polymerization of linear and cyclic acetylenes. *Macromol. Rev. 13*, 219.

[116] Menzel, H., Mowery, M., Cai, M., & Evans, C. (**1999**). Fabrication of noncovalent and covalent internal scaffolding in monolayer assemblies using diacetylenes. *Macromolecules 32*, 4343.

[117] Faucheux, A., Gouget-Laemmel, A., Henry de Villeneuve, C., Boukherroub, R., Ozanam, F., Allongue, P., & Chazalviel, J.-N. (**2006**). Well-Defined Carboxyl-Terminated Alkyl Monolayers Grafted onto H-Si(111): Packing Density from a Combined AFM and Quantitative IR Study. *Langmuir 22*, 153-162.

[118] Faucheux, A. (**2005**). *Thesis : Nouvelles fonctionnalités de l'interface silicium/diélectrique pour la microélectronique.* Palaiseau: Ecole Polytechnique.

[119] Baek, S., Phan, M., Lee, J., & Shin, K. (**2016**). Packing effects on polymerization of diacetylene lipids in liposomes and monolayers matrices. *Polymer Journal 48 (4)*, 457-463.

[120] Walsh, S., & Lando, J. (**1994**). Fabrication of alternating diacetylenic multilayers and the role of subphase conditions. *Langmuir 10, 1*, 246-251.

[121] Tamm, L. (**1997**). Infrared spectroscopy of proteins and peptides in lipid bilayers. *Quaterly Reviews of Biophysics 30, (4)*, 365-429.

[122] Scheibe, C. (**2018**). Orientation of lipids in solid supported lipid bilayers studied by polarized ATR-FTIR spectroscopy. *Biomedical Spectroscopy and imaging 7*, 17-24.

[123] Fringeli, U. (**1992**). In Situ Infrared Attenuated Total Reflection (IR ATR) Spectroscopy: A Complementary Analytical Tool for Drug Design and Drug Delivery. *Chimia 46* , 200-214 .

[124] Johnston, D., Sanghera, S., Pons, M., & Chapman, D. (**1980**). Phospholipid Polymers: Synthesis and Spectral Characteristics. *Biochimica et Biophysica Acta 602* , 57-69.

[125] Nuzzo, R., Fusco, F., & Allara, D. (**1987**). Spontaneously organized molecular assemblies. 3. Preparation and properties of solution adsorbed monolayers of organic disulfides on gold surfaces. *J. Am. Chem. Soc. 109, 8* , 2358-2368.

[126] Strong, L., & Whitesides, G. (**1988**). Structures of self-assembled monolayer films of organosulfur compounds adsorbed on gold single crystals: electron diffraction studies. *Langmuir, 4, 3*, 546-558.

[127] Verploegen, E., Miller, C., Schmidt, K., Bao, Z., & Toney, M. (**2012**). Manipulating the morphology of P3HT–PCBM bulk heterojunction blends with solvent vapor annealing. *Chemistry of Materials 24, (20)*, 3923-3931.

[128] Yamamoto, T., Komarudin, D., Ara, M., Lee, B.-L., Suganuma, H., Asakawa, N., Inoue, Y., Kubota, K., Sasaki, S., Fukuda, T., Matsuda, H. (**1998**). Extensive studies on p-stacking of poly(3-alkylthiophene-2,5-diyl)s and poly(4-alkylthiazole-2,5-diyl)s by optical spectroscopy, NMR analysis, light scattering analysis, and Y-ray crystallography. *J. Am. Chem. Soc. 120*, 2047-2058.

[129] Menzel, H., Horstmann, S., Mowery, M., Cai, M., & Evans, C. (**2000**). Diacetylene polymerization in self-assembled monolayers: influence of the odd/even nature of the methylene spacer. *Polymer 41*, 8113-8119 .

[130] Yavlovich, A. S. (**2011**). A novel class of photo-triggerable liposomes containing DPPC:DC(8,9)PC as vehicles for delivery of doxorubicin to cells. *Biochim Biophys Acta. 1808*, 117-26.

[131] Punnamaraju, S., You, H., & Steckl, A. (**2012**). Triggered Release of Molecules across Droplet Interface Bilayer Lipid Membranes using Photopolymerizable Lipids. *Langmuir 22;28(20)*, 7657-64.

[132] Bower, D. M. (**1989**). *The vibrational spectroscopy of polymers.* Cambridge: Cambridge University Press.

[133] Porter, M., Bright, T., Allara, D., & Chidsey, C. (**1987**). Spontaneously organized molecular assemblies. 4. Structural characterization of n-alkyl thiol monolayers on gold by optical ellipsometry, infrared spectroscopy, and electrochemistry. *J. Am. Chem. Soc. 109*, 3559.

[134] Florin, E., Moy, V., & Gaub, H. (**1994**). Adhesion forces between individual ligand-receptor pairs . *Science 264(5157)*, 415-417.

[135] Hakim Elahi, S., Abbaszadegan, M., & Conroy-Ben, O. (**2019**). Engineered proteoliposome transporter for treatment of cesium contaminated water . *Sci. Total Environ. 704*, 135317.

[136] Song, K., Lee, H., Moon, H., & Lee, K. (**1997**). Simultaneous removal of the radiotoxic nucleides Cs137 and I129 from aqueous solution. *Separation Purif. Technol.12(3)* , 215-227.

[137] Miura, H., Yamagishi, I., & Akiba, K. (**1989**). Removal of radioactive cesium and strontium by zeolites. *Nippon Kagaku Kaishi 3*, 621-627.

[138] Miyake, T., Miyake, F., & Sano, M. (**2019**). Removal of Cs+ using zeolite rho. *Sci. Technol. Rep. Kansai Univ. 61* , 11-18.

[139] Cheng, J., Liang, J., Dong, L., Chai, J., Zhao, N., Ullah, S., Wang, H., Zhang, D., Imtiaz, S., Shan, G., Zheng, G. (**2018**). Self-assembly of 2D-metal-organic framework/graphene oxide membranes as highly efficient adsorbents for the removal of Cs+ from aqueous solutions. *RSC Advances 8*, 40813-40822.

[140] Yu, H.-R., Hu, J.-Q., Liu, Z., Ju, X.-J., Xie, R., Wang, W., & Chu, L.-Y. (**2017**). Ion-recognizable hydrogels for efficient removal of cesium ions from aqueous environment . *J. Hazard. Mater. 323 (Part B)*, 632-640.

[141] Kasprzak, A., & Sakurai, H. (**2019**). Site-selective cation- π interaction as a way of selective recognition of the caesium cation using sumanene-functionalized ferrocene. *Dalton Trans. 48* , 17147-17152.

[142] Makrlik, E., Sykora, D., Bohm, S., & Vanura, P. (**2017**). [2,2,2]Paracycophane as a receptor for the cesium cation in the gas phase. *Mol. Phys. 115*, 2553-2557.

[143] Deng, X. Y., Chen, K., Chen, M.-D., Lue, L. B., & Tao, Z. (**2019**). Recognition of Different Metal Cations by a trans-4-[4-(Dimethylamino)styryl]-1-methylpyridinium Iodide@Tetramethylcucurbit[6]uril Probe. *Eur. J. Inorg. Chem.*, 1212-1219.

[144] Jung, S. H., Hyun, T. K., Kim, J.-Y., & Jung, J. H. (**2015**). High selective fluorescence imaging of cesium distribution in Arabidopsis using a bis(trihydroxyphenyl)-appended fluorescent probe with a turn-on system. *RSC Advances 5*, 26662-26665.

[145] Akamatsu, M., Komatsu, H., Mori, T., Adams, E., Shin, R., Sakai, H., Abe, M., Hill, J.P., Ariga, K. (**2014**). Intracellular imaging of cesium distribution in Arabidopsis using cesium green. *ACS Appl. Mater. Interfaces 6* , 8208-8211.

[146] Luo, Q., Tang, D., & Wu, G. (**2008**). Ribose-protected thioguanosine-based 1H NMR spectroscopic probe for the detection of cesium from solid cesium-containing sources in acetonitrile. *Inorg. Chem. Commun. 11* , 1359-1362.

[147] Lin, S., Yang, C., Mao, Z., He, B., Wang, Y.-T., Leung, C.-H., & Ma, D.-L. A. (**2016**). G-pentaplex-based assay for Cs+ ions in aqueous solution using a luminescent Ir(III) complex. . *Biosens. Bioelectron. 77* , 609-612.

[148] Shamsipur, M., Gilani, N. S., & Rofouei, M. K. (**2011**). 133Cs NMR study of Cs+ ion complexes with aza-18-crown-6, diaza-18-crown-6 and dibenzyldiaza-18-crown-6 in binary acetonitrile-nitromethane mixtures. . *J. Sol. Chem. 40*, 40-47.

[149] Rabiul Awuala, M., Yaita, T., Taguchi, T., Shiwaku, H., Suzuki, S., & Okamoto, Y. (**2014**). Selective cesium removal from radioactive liquid waste by crown ether immobilized new class conjugate adsorbent. *Journal of Hazardous Materials 278*.

[150] Ji, H.-F., Brown, G. M., & Dabestani, R. (**1999)**. Calix[4]arene-based Cs+ selective optical sensor. *Chem. Commun. 7* , 609-610.

[151] Blake, A., Champness, N., Hubberstey, P., Li, W., Withersby, M., & Schröder, M. (**1999**). Inorganic crystal engineering using self-assembly of tailored building-blocks. *Coord. Chem. Rev. 183*, 117–138.

[152] Long, J., & Yaghi, O. (**2009**). The pervasive chemistry of metal–organic frameworks. *Chem. Soc. Rev. 38* , 1213–1214 .

[153] Shinkai, S. (**1993**). Calixarenes - the third generation of supramolecules. *Tetrahedron 49*, 8933–8968.

[154] Gutsche, C. (**1998**). *Calixarenes Revised: Monographs in Supramolecular Chemistry, vol.6.* Cambridge: The Royal Society of Chemistry .

[155] Asfari, Z., Böhmer, V., Harrowfield, J., & Vicens, J. (**2001**). *Calixarenes.* Dordrecht: Kluwer Academic.

[156] Neri, P., Sessler, J., & Wang, M. (**2016**). *Calixarenes and Beyond.* Springer International Publishing.

[157] Ungaro, R., Casnati, A., Ugozzoli, F., Pochini, A., Dozol, J.-F., Hill, C., & Rouquette, H. (**1994**). 1,3-Dialkoxycalix[4]arenecrowns-6 in 1,3-alternate conformation: Cesium-selective ligands that exploit cation-arene interaction. *Angew. Chem. Int. Ed. 33*, 1506-1509.

[158] Lamare, V., Dozol, J.-F., Fuangswasdi, S., Arnaud-Neu, F., Thuéry, P., Nierlich, M., Asfari, Z., Vicens, J. (**1999**). A new calix[4]arene-bis(crown ether) derivative displaying an improved caesium over sodium selectivity : molecular dynamics and experimental investigation of alkali-metal ion complexation. *J. Chem. Soc. Perkin Trans 2*, 271-284.

[159] Kim, S. K., Vargas-Zunica, G. I., Hay, B. P., Young, N. J., Delmau, L. H., Masselin, C., Lee, C. H., Kim, J. S., Lynch, V. M., Moyer, B. A., Sessler, J. L. (**2012**). Controlling Caesium Cation Recognition via Cation Metathesis Within an Ion Pair Receptor. *J. Am. Chem. Soc. 134*, 1782-1792.

[160] Roper, E., Talanov, V. S., Gorbunova, M. G., Bartsch, R. A., & Talanova, G. G. (**2007**). Optical Determination of Thallium(I) and Cesium(I) With a Fluorogenic Calix[4]arenebis(crown-6-ether) Containing One Pendent Dansyl Group. *Anal. Chem. 79*, 1983-1989.

[161] Yeon, Y., Leem, S., Wagen, C., Lynch, V. M., Kim, S. K., & Sessler, J. L. (**2016**). 3-(Dicyanomethylidene)indan-1-one-Functionalized Calix[4]arene–Calix[4]pyrrole Hybrid: An Ion-Pair Sensor for Cesium Salts. *Org. Lett. 18* , 4396-4399.

[162] Kumar, N., Pham-Xuan, Q., Depauw, A., Hemadi, M., Ha-Duong, N.-T., Lefevre, J. P., Ha-Thi, M.-H., Leray, I. (**2017**). New sensitive and selective calixarene-based fluorescent sensors for the detection of Cs+ in an organoaqueous medium. *New. J. Chem. 41*, 7162-7170.

[163] Pham-Xuan, Q., Jonusauskaite, L., Depauw, A., Kumar, N., Lefevre, J. P., Perrier, A., Ha-Thi, M. H., Leray, I. (**2018**). New water-soluble fluorescent sensors based on calix[4]arene biscrown-6 for selective detection of cesium. *J. Photochem. Photobiol. A 364*, 355-362.

[164] Jung, S. H., Park, J. S., Choi, Y., Kim, S. K., & Jung, J. H. (**2017**). Calix[4]arene-based fluorescent probe and the adsorption capacity of its electrospun nanofibrous film for the cesium cation as an adsorbent. *Supramol. Chem. 29* , 139-145.

[165] Ahmadzadeh, S., Rezayi, M., Kassim, A., & Aghasi, M. (**2015**). Cesium selective polymeric membrane sensor based on p-isopropylcalix[6]arene and its application in environmental samples. *RSC Advances 5* , 39209-39217.

[166] Ji, H.-F., Finot, E., Dabestani, R., Thundat, T., Brown, G. M., & Britt, P. F. (**2000**). A novel self-assembled monolayer (SAM) coated microcantilever for low level caesium detection. *Chem. Commun. 6* , 457-458.

[167] Thundat, T., Finot, E., Ji, H.-F., Dabestani, R., Britt, P. F., Bonnesen, P. V., Brown, G.M, Warmack, R. J. (**1999**). Highly selective microcantilever sensor for cesium ion detection. *Proc. Electrochem. Soc. , 99-23(Chemical Sensors IV)*, 314-319.

[168] Kim, J. S., Cho, M. H., Yu, I. Y., Pang, J. H., Kim, E. T., Suh, I. H., Oh, M.R., Ra, D.Y., Cho, N. S. (**1997**). Calix[4]arene dibenzocrown ethers as cesium ionophore. *Bull. Kor. Chem. Soc. 18*, 677-680.

[169] Kim, J. S., Yu, I. Y., Pang, J. H., Kim, J. K., Lee, Y.-I., Lee, K. W., & Oh, W.-Z. (**1998**). New calix[4]arene dibenzocrown ethers for selective sensing of cesium ion in an aqueous environment. *Microchem. J. 58* , 225-235.

[170] Ji, H. F., Dabestani, R., Brown, G. M., & Hettich, R. L. (**2001**). Synthesis and sensing behavior of cyanoanthracene modified 1,3-alternate calix[4]benzocrown-6: a new class of Cs+ selective optical sensors. *J. Chem. Soc., Perkin Trans 2*, 585-591.

[171] Wright, K., Melandri, F., Cannizzo, C., Wakselman, M., & Mazaleyrat, J. P. (**2002**). New crown-carrier Cα,α-disubstituted glycines derived from α-methyl-(L)-DOPA. *Tetrahedron 58*, 5811-5820.

[172] Deutman, A. B., Smits, J. M., de Gelder, R., Elemans, J. A., Nolte, R. J., & Rowan, A. E. (**2014**). Strong induced-fit binding of viologen and pyridine derivatives in adjustable porphyrin cavities. *Chem. Eur. J. 20*, 11574-11583.

[173] Weber, E. (**1983**). Neutralliganden mit Tensidstruktur – Synthese, Komplexierung, Ionentransfer. *Liebigs Ann. Chem. 5*, 770-801.

[174] Surowiec, M., Custelcean, R., Surowiec, K., & Bartsch, R. A. (**2009**). Mono-ionizable calix[4]arene-benzocrown-6 ligands in 1,3-alternate conformations: synthesis, structure and silver(I) extraction. *Tetrahedron 65* , 7777-7783.

[175] Sessler, J. L., Kim, S., Gross, D., Lee, C., Kim, J., & Lynch, V. (**2008**). Crown-6-calix[4]arene-capped calix[4]pyrrole: an ion-pair receptor for solvent-separated CsF ions. *J. Am. Chem. Soc. 130*, 13162-13166.

[176] *Database of Ionic Radii, Imperial College of London*. (s.d.) http://abulafia.mt.ic.ac.uk/shannon/ptable.php

[177] Benesi, H., & Hildebrand, J. (**1949**). A Spectrophotometric Investigation of the Interaction of Iodine with Aromatic Hydrocarbons. *J. Am. Chem. Soc. 71*, 2703.

[178] Ravikumar, I., & Ghosh, P. (**2011**). Zinc(II) and PPi selective fluorescence OFF-ON-OFF functionality of a chemosensor in physiological conditions. *Inorg. Chem. 50*, 4229.

[179] Hofmeister, F. (**1888**). Zur Lehre von der Wirkung der Salze. *Arch. Exp. Pathol. Pharmakol. 24*, 247.

[180] Lo Nostro, P., & Ninham, B. W. (**2012**). Hofmeister phenomena: an update on ion specificity in biology. *Chem. Rev. 112* , 2286.

[181] Yoe, J. H., & Jones, A. L. (**1944**). Colorimetric Determination of Iron with Disodium-1,2-dihydroxybenzene-3,5-disulfonate. *Anal. Chem. 16*, 111.

[182] Job, P. (**1971**). *Spectrochemical Methods of Analysis.* New York: Wiley Interscience.

[183] Smith, R., Pillai, K., Chow, T., & Folsom, T. (**1965**). Determination of Rubidium in Sea Water. *Limnol. Oceanog. 10.*

[184] Kim, Y.-J., Jung, H.-S., Lim, J., Ryu, S.-J., & Lee, J.-K. (**2016**). Rapid Imaging of Latent Fingerprints Using Biocompatible Fluorescent Silica Nanoparticles. *Langmuir 32*, 8077.

[185] Parikh, A., Schivley, M., Koo, E., Seshadri, K., Aurentz, D., Mueller, K., & Allara, D. (**1997**). n-Alkylsiloxanes: From Single Monolayers to Layered Crystals. The Formation of Crystalline Polymers from the Hydrolysis of n-Octadecyltrichlorosilane. *J. Am. Chem. Soc. 119*, 3135–3143.

[186] Small, D. (**1984**). Lateral chain packing in lipids and membranes. *Journal of Lipid Research 25* , 1490.

[187] Kergoat, L., Herlogsson, L., Braga, D., Piro, B., Pham, M. C., Crispin, X., & Berggren, M. a. (**2010**). A water-gate organic field-effect transistor. *Adv. Mater. 22*, 2565.

[188] Lai, S., Demelas, M., Casula, G., Cosseddu, P., Barbaro, M., & Bonfiglio, A. (**2013**). Ultralow Voltage, OTFT-Based Sensor for Label-Free DNA Detection. *Adv. Mater. 25*, 103.

[189] Buth, F., Donner, A., Sachsenhauser, M., Stutzmann, M., & Garrido, J. A. (**2012**). Biofunctional electrolyte-gated organic field-effect transistors. *Adv. Mater. 24* , 4511.

[190] Nguy, T. P., Hayakawa, R., Kilinc, V., Petit, M., Raimundo, J.-M., Charrier, A.-M., & Wakayama, Y. (**2019**). Stable operation of water-gated organic field-effect transistor depending on channel flatness, electrode metals and surface treatment. *Jpn. J. Appl. Phys. 58*, SDDH02.

[191] Cotrone, S., Ambrico, M., Toss, H., Angione, M., Magliulo, M., Mallardi, A., Berggren, M., Palazzo, G., Horowitz, G., Ligonzo, T., Torsi, L. (**2012**). Phospholipid film in electrolyte-gated organic field-effect transistors. *Org. Electron. 13*, 638.

[192] Buth, F., Kumar, D., Stutzmann, M., & Garrido, J. A. (**2011**). Electrolyte-gated organic field-effect transistors for sensing applications. *Appl. Phys. Lett. 98*, 2009.

[193] Minamiki, T., Hashima, Y., Sasaki, Y., & Minami, T. (**2018**). An electrolyte-gated polythiophene transistor for the detection of biogenic amines in water. *Chem. Commun. 54*, 6907.

[194] Knopfmacher, O., Hammock, M. L., Appleton, A. L., Schwartz, G., Mei, J., Lei, T., Pei, J., Bao, Z. (**2014**). Highly stable organic polymer field-effect transistor sensor for selective detection in the marine environment. *Nat. Commun. 5*, 2954.

[195] Porrazzo, R., Bellani, S., Luzio, A., Lanzarini, E., Caironi, M., & Antognazza, M. R. (**2014**). Improving mobility and electrochemical stability of a water-gated polymer field-effect transistor. *Org. Electron. 15*, 2126.

[196] Cramer, T., Campana, A., Leonardi, F., Casalini, S., Kyndiah, A., Murgia, M., & Biscarini, F. (**2013**). Water-gated organic field effect transistors – opportunities for biochemical sensing and extracellular signal transduction. *J. Mater. Chem. B 1*, 3728.

[197] Piliego, C., Jarzab, D., Gigli, G., Chen, Z., Facchetti, A., & Loi, M. A. (**2009**). High Electron Mobility and Ambient Stability in Solution-Processed Perylene-Based Organic Field-Effect Transistors. *Adv. Mater. 21*, 1573 .

[198] Crone, B., Dodabalapur, A., Gelperin, A., Torsi, L., Katz, H. E., Lovinger, A. J., & Bao, Z. (**2001**). Electronic Sensing of Vapors with Organic Transistors. *Appl. Phys. Lett. 78*, 2229 .

[199] Facchetti, A., Yoon, M. H., & Marks, T. J. (**2005**). Gate Dielectrics for Organic Field-Effect Transistors: New Opportunities for Organic Electronics. *Adv. Mater. 17* , 1705.

[200] Tsao, H. N., Cho, D., Andreasen, J. W., Rouhanipour, A., Breiby, D. W., Pisula, W., & Müllen, K. (**2009**). The Influence of Morphology on High-Performance Polymer Field-Effect Transistors. *Adv. Mater. 21*, 209.

[201] Liu, C., Xu, Y., Li, Y., Scheideler, W., & Minari, T. (**2013**). Critical Impact of Gate Dielectric Interfaces on the Contact Resistance of High-Performance Organic Field-Effect Transistors. *J. Phys. Chem. C 117*, 12337.

[202] Kline, R., McGehee, M., Kadnikova, E., Liu, J., & Frechet, J. (**2003**). Controlling the field-effect mobility of regioregular polythiophene by changing the molecular weight. *Adv. Mater. 15*, 1519.

[203] McCullough, R. D., Lowe, R. D., Jayaraman, M., & Anderson, D. L. (**1993**). Design, synthesis, and control of conducting polymer architectures: structurally homogeneous poly(3-alkylthiophenes). *J. Org. Chem. 58*, 904.

[204] Chen, T.-A., Wu, X., & Rieke, R. D. (**1995**). Regiocontrolled synthesis of poly(3-alkylthiophenes) mediated by Rieke zinc: their characterization and solid-state properties. *J. Am. Chem. Soc. 117*, 233.

[205] Fell, H. J.-N., & Mardalen, J. (**1995**). Unexpected orientational effects in spin-cast, sub-micron layers of poly(alkylthiophene)s: A diffraction study with synchrotron radiation. *Solid State Commun. 94*, 843.

[206] Sirringhaus, H., Brown, P., Friend, R., Nielsen, M., Bechgaard, K., Langeveld-Voss, B., Spiering, A., Janssen, R.A., Meijer, E., Herwig, P. (**1999**). Two-dimensional charge transport in self-organized, high-mobility conjugated polymers. *Nature 401*, 685.

[207] Alberga, D., Mangiatordi, G., Torsi, L., & Lattanzi, G. (**2014**). Effects of annealing and residual solvents on amorphous p3ht and pbttt films. *J. Phys. Chem. C 118*, 8641.

[208] Nguy, T. P., Hayakawa, R., Kilinc, V., Petit, M., Yemineni, S. H., Raimundo, J.-M., Charrier, A. M., Wakayama, Y. (**2020**). Electrolyte-gated-organic field effect transistors functionalized by lipid monolayer with tunable pH sensitivity for sensor applications. *Appl. Phys. Express 13*, 011005.

[209] Picca, R., Manoli, K., Macchia, E., Tricase, A., Di Franco, C., Scamarcio, G., Cioffi, N., Torsi, L. (**2019**). A Study on the Stability of Water-Gated Organic Field-Effect-Transistors Based on a Commercial p-Type Polymer. *Front. Chem. 7*, 667.

[210] Zhang, Q., Leonardi, F., Casalini, S., Temiño, I., & Mas-Torrent, M. (**2016**). High performing solution-coated electrolyte-gated organic field-effect transistors for aqueous media operation. *Sci. Rep. 6*, 39623.

[211] Zhang, G., Zhang, G., Chua, J., Chee, R., Wong, E., Agarwal, A., Buddharaju, K.D., Singh, N., Gao, Z.Q., Balasubramanian, N. (**2008**). DNA sensing by silicon nanowire: charge layer distance dependence. *Nano Lett. 8*, 1066.

[212] Chen, K.-I., Li, B.-R., & Chen, Y.-T. (**2011**). Silicon nanowire field-effect transistor-based biosensors for biomedical diagnosis and cellular recording investigation. *Nano Today 6* , 131-154.

[213] Stern, E., Klemic, J., Routenberg, D., Wyrembak, P., Turner-Evans, D., Hamilton, A., Lavan, D.A., Fahmy, T.M., Reed, M. (**2007**). Label-free immunodetection with cmos-compatible semiconducting nanowires. *Nature 445*, 519.

[214] Stern, E., Wagner, R., Sigworth, F., Breaker, R., Fahmy, T., & Reed, M. (**2007**). Importance of the Debye screening length on nanowire field effect transistor sensors. *Nano Lett. 7*, 3405.

[215] Ishii, H., Kudo, K., Nakayama, T., & Ueno, N. (**2015**). Electronic Processes in Organic Electronics: Bridging Nanostructure, Electronic States and Device Properties. *Oxford University Press*.

[216] Loke, A. L., Wu, Z., Moallemi, R., Cabler, C., Lackey, C., Wee, T., & Doyle, B. (**2010**). Constant-Current Threshold Voltage Extraction in HSPICE for Nanoscale CMOS Analog Design. *Synopsys Users Gr. 1*.

[217] Geisse, N. A. (**2009**). AFM and Combined Optical Techniques. *Materials Today. 12 (7–8)*, 40–45.

[218] Skoog, D., West, D., & Holler, F. (**1999**). *Analytical Chemistry: An Introduction 7th Ed.*

[219] *Spectropôle from Aix Marseille University*. (s.d.). https://fr-chimie.univ-amu.fr/spectropole

[220] Dolomanov, O., Bourhis, L. J., Gildea, R. J., Howard, J. A., & Puschmann, H. (**2009**). OLEX2: A Complete Structure Solution, Refinement and Analysis Program. *J. Appl. Crystallogr. 42* , 339-341.

[221] Sheldrick, G. (**2015**). SHELXT – Integrated space-group and crystal-structure determination. *Acta Crystallogr., Sect. A: Found. Adv. 71*, 3-8.

[222] Kurta, R. P., Grodd, L., Mikayelyan, E., Gorobtsov, O. Y., Zaluzhnyy, I. A., Fratoddi, I., Venditti, I., Russo, M. V., Sprung, M., Vartanyants, I.A., Grigorian, S. (**2015**). Local structure of semicrystalline P3HT films probed by nanofocused coherent X-rays. *Physical Chemistry Chemical Physics 11*.

[223] Wang, D., Noël, V., & Piro, B. (**2016**). Electrolytic Gated Organic Field-Effect Transistors for Application in Biosensors - A Review. *Electronics 5*, 9.

[224] Simonescu, C. (s.d.). *Advanced Aspects of Spectroscopy. Akhyar Farrukh M (ed.). InTech2012*. http://www.intechopen.com/books/advanced-aspects-of-spectroscopy

Abstract

Le césium est un métal alcalin de haute réactivité, utilisé dans les cellules photoélectriques et les horloges, et agit également comme catalyseur pour favoriser les réactions organiques. Bien que le césium soit légèrement toxique de nature, ses isotopes radioactifs, émetteurs gamma, sont des éléments particulièrement dangereux que l'on trouve dans la nature. Leur grande solubilité dans l'eau entraîne des effets néfastes à la fois sur l'environnement et sur la santé humaine. Avec l'essor de l'activité industrielle et nucléaire ces dernières années, une augmentation de la pollution des eaux par le cesium a été observé. Il est donc souhaitable de développer des techniques pour la détection rapide des ions césium dans des systèmes environnementaux complexes. Dans ce but, les transistors à effet de champ répondent aux exigences requises dans le domaine des technologies de capteurs électriques et offrent des caractéristiques uniques telles que la miniaturisation, le faible coût, la facilité d'utilisation, la spécificité, la sélectivité et des capacités de surveillance en temps réel. Le développement de tels dispositifs nécessite des transducteurs efficaces présentant des spécificités et des sélectivités élevées. Dans cette thèse, des monocouches lipidiques auto-assemblées (SLM) sont utilisées comme diélectrique ultra-fin, conduisant à des propriétés de détection avec des limites de détection jusqu'au femtomole dans les capteurs Chem-FET lorsqu'ils sont fonctionnalisés avec des sondes spécifiques. Une interface innovante à base de poly(3-hexylthiophène) comme semiconducteur et de SLM fonctionnalisée avec un nouvel chélateur à base de calix[4]arène 1,3-alterné, présentant une grande sélectivité élevée vis-à-vis du Cs+ , a été assemblé et caractérisé. Après l'implémentation cette nouvelle interface toute organique, les propriétés du Chem-FET tels que la sensibilité, la sélectivité et les limites de détection ont été étudiées pour la détection de césium dans l'eau de mer.

Cesium is a highly reactive alkali metal used in photocells and clocks, and also acts as a catalyst to promote organic reactions. Although cesium is slightly toxic by nature, its radioactive isotopes, gamma emitters, are particularly dangerous elements found in nature. Their high solubility in water causes adverse effects on both the environment and human health. With the growth of industrial and nuclear activity in recent years, an increase in cesium pollution of water has been observed. It is therefore desirable to develop techniques for the rapid detection of cesium ions in complex environmental systems. To this end, field-effect transistors meet the requirements of electrical sensor technologies and offer unique features such as miniaturization, low cost, ease of use, specificity, selectivity and real-time monitoring capabilities. The development of such devices requires efficient transducers with high specificity and selectivity. In this thesis, self-assembled lipid monolayers (SLMs) are used as an ultra-thin dielectric, leading to detection properties with detection limits down to femtomole in Chem-FET sensors when functionalized with specific probes. An innovative interface based on poly(3-hexylthiophene) as a semiconductor and SLM functionalized with a novel calix[4]arene 1,3-alternate chelating agent having a high selectivity towards Cs+ has been assembled and characterized. After the implementation of this new all-organic interface, the properties of the Chem-FET such as sensitivity, selectivity and detection limits were studied for the detection of cesium in seawater.